

ELECTROMAGNETIC ANALYSIS OF 2.5D STRUCTURES IN OPEN LAYERED MEDIA

THÈSE N° 3183 (2005)

PRÉSENTÉE À LA FACULTÉ SCIENCES ET TECHNIQUES DE L'INGÉNIEUR

Institut de transmissions, ondes et photonique

SECTION DE GÉNIE ÉLECTRIQUE ET ÉLECTRONIQUE

ÉCOLE POLYTECHNIQUE FÉDÉRALE DE LAUSANNE

POUR L'OBTENTION DU GRADE DE DOCTEUR ÈS SCIENCES

PAR

Daniel LLORENS del RÍO

ingénieur en télécommunications, Université de Malaga, Espagne
et de nationalité espagnole

acceptée sur proposition du jury:

Prof. J. R. Mosig, directeur de thèse

Prof. M. Kunt, rapporteur

Prof. D. Schaubert, rapporteur

Prof. J. Zapata Ferrer, rapporteur

Lausanne, EPFL
2005

Ô bruit doux de la pluie
Par terre et sur les toits !
Pour un cœur de grenouille
Ô le chant de la pluie !

Paul VERLAINE

Abstract

This thesis presents a specialization of the integral equation (IE) method for the analysis of three-dimensional metallic and dielectric structures embedded in laterally unbounded (open) layered media. The method remains basically spatial but makes use of extensive analytical treatment of the vertical dependence of the problem in the 2D Fourier-transformed domain. The analytical treatment restricts somewhat the class of structures that can be analyzed. Still, the field of applicability remains very large, and includes most printed circuit and integrated circuit structures.

The method is developed in full numerical detail, from first principles down to the properties of new Green's functions and the computation of particular types of convolution integrals. We show how the memory and time complexity are considerably reduced when compared to the requirements of the analysis of general 3D structures.

With the newly developed tool, it is possible to deal with some peculiar characteristics of microwave and millimeter-wave circuits and antennas. Most noteworthy among these is the presence of thick metallizations (either electrically, or relative to circuit features). A novel full-wave analysis of arbitrarily shaped apertures in thick metallic screens is presented. This is compared to other methods, both full-wave and approximate, and demonstrated to offer excellent accuracy. Comparison with measured data, obtained from specially constructed prototypes, further validates the new technique. A second application is to the analysis of airbridges in coplanar waveguide (CPW) and slotline (SL) circuits. Comparison of measured and simulated data validates again our technique and provides valuable information about the behavior of CPW-fed slot loop antennas.

Among the more specific applications, particular attention is devoted to the analysis and design of submillimeter-wave integrated dielectric lens feeds. These were object of study in the frame of a European Space Agency project, *Integrated Front-End Receivers* (IFER), which our Laboratory carried out in cooperation with a team at University of Toronto. The analysis method developed in this work encompasses and extends all previous work done at our Laboratory (LEMA) related with the analysis of this kind of feed. Together with the advanced 3D ray-tracing code developed at University of Toronto, it is possible to gain a high degree of insight into the behavior of these integrated receivers.

Resumé

Cette thèse présente une spécialisation de la méthode de l'équation intégrale (IE) pour l'analyse de structures tridimensionnelles métalliques et diélectriques situées dans des milieux multicouches latéralement illimités (ouverts). La méthode demeure fondamentalement spatiale mais se sert du traitement analytique de la dépendance verticale du problème dans le domaine transformé de Fourier 2D. Le traitement analytique limite légèrement la classe des structures qui peuvent être analysées. Toutefois, le champ de l'applicabilité demeure très grand, et inclut la plupart des structures de circuits imprimés et de circuits intégrés.

La méthode est développée de manière très détaillée, des premiers principes aux propriétés de nouvelles fonctions de Green et au calcul des types particuliers d'intégrales de convolution. Nous montrons comment la complexité de mémoire et de temps est considérablement réduite lorsqu'on la compare aux exigences d'analyse de structures 3D générales.

Avec l'outil nouvellement développé, il est possible de traiter certaines caractéristiques particulières des circuits et antennes de micro-ondes et d'ondes millimétriques. La plus remarquable parmi ces dernières est la présence des métallisations épaisses (que cela soit électriquement, ou relative aux dispositifs du circuit). Une nouvelle analyse full-wave des ouvertures avec une forme quelconque dans des écrans métalliques épais est présentée. Ceci est comparé à d'autres méthodes, full-wave et approximées, et il est démontré que la nouvelle méthode offre une précision excellente. La comparaison avec des données mesurées, obtenues à partir des prototypes spécialement construits, valide la nouvelle technique. Une deuxième application est l'analyse d'« airbridges » dans des circuits de guides d'onde coplanaires (CPW) et circuits de lignes à fentes (SL). La comparaison des données mesurées et simulées valide encore notre technique et fournit des informations valables au sujet du comportement des antennes de boucle à fentes alimentées par CPW.

Parmi les applications plus spécifiques, une attention particulière est consacrée à l'analyse et la conception d'alimentations avec lentilles diélectriques intégrées pour la bande d'ondes sub-millimétriques. Ces alimentations étaient l'objet d'étude dans le cadre d'un projet de l'Agence Spatiale Européenne (ESA), *Integrated Front-End Receivers* (IFER), que notre laboratoire a effectué en coopération avec une équipe de l'Université de Toronto. La méthode d'analyse développée dans ce travail entoure et prolonge tous les travaux précédents faits au LEMA en relation avec l'analyse de ce genre d'alimentation. Ensemble avec le code 3D « ray-tracing » avancé développé à Toronto, il est possible de gagner un degré élevé de connaissances dans le comportement de ces récepteurs intégrés.

Resum*

Aquesta tesi presenta una especialització del mètode de l'equació integral (IE) per a l'anàlisi d'estructures metàl·liques i dielèctriques en tres dimensions incloses a medis multi-capac lateralment il·limitats (oberts). El mètode és bàsicament espacial, però utilitza un tractament analític extensiu de la dependència vertical del problema en el domini transformat de Fourier en 2D. El tractament analític restringeix d'alguna manera la classe d'estructures que poden ser analitzades. Tot i així, el camp d'aplicació roman molt ampli, i inclou la majoria de circuits impresos i estructures de circuits integrats.

El mètode es desenvolupa amb tot detall numèric, des dels principis bàsics fins a les propietats de noves funcions de Green i el càlcul de tipus particulars d'integrals de convolució. Mostrem com la memòria i el temps de computació són reduïts considerablement comparant-los amb els requeriments de l'anàlisi d'estructures generals en 3D.

Amb la nova eina desenvolupada, és possible tractar algunes característiques peculiars de circuits de microones i ones mil·limètriques i antenes. El més remarcable entre ells, és la presència de metallitzacions amples (ja sigui elèctricament o amb relació a paràmetres de circuit). Es presenta una nova anàlisi full-wave d'obertures de forma arbitrària situades a pantalles metàl·liques amples. Això ha estat comparat a d'altres mètodes, tant full-wave com aproximats, i s'ha demostrat que el nou mètode ofereix una precisió excel·lent. La comparació amb les mesures, que s'han obtingut de prototips construïts especialment, també valida la nova tècnica. Una segona aplicació és per a l'anàlisi d'«airbridges» a circuits de guia d'ona coplanar (coplanar waveguide, CPW) i de línies amb ranures (slotline, SL). La comparació de les mesures i les simulacions valida un altre cop la nostra tècnica i proporciona una informació valuosa sobre el comportament de les antenes de llaç alimentades per CPW.

Entre les aplicacions més específiques, es dedica una particular atenció a l'anàlisi i disseny d'alimentacions amb lents dielèctriques integrades per a la banda d'ones submil·limètriques. Aquestes van ser objecte d'estudi en el marc d'un projecte de l'Agència Espacial Europea (ESA), *Receptors «Front-End» Integrats* (IFER), que el nostre laboratori ha efectuat en col·laboració amb un equip de la Universitat de Toronto. El mètode d'anàlisi desenvolupat en aquesta tasca comprèn i estén tots els treballs precedents fets al LEMA relacionats amb l'anàlisi d'aquest tipus d'alimentació. Juntament amb el codi avançat «ray-tracing» 3D desenvolupat a Toronto, és possible de guanyar un alt grau de coneixement sobre el comportament d'aquests receptors integrats.

*Traducció de Maria Eugènia Cabot.

Resumen

Esta tesis presenta una especialización del método de la ecuación integral (IE) para el análisis de estructuras metálicas y dieléctricas en tres dimensiones inmersas en un medio estratificado abierto, es decir, un medio cuyos parámetros varían exclusivamente en una dirección. El método es básicamente espacial, pero hace uso de un tratamiento analítico extensivo de la dependencia vertical del problema (de acuerdo con la estratificación) en el dominio transformado de Fourier. Aunque los requisitos de este tratamiento analítico restringen en cierta medida el tipo de estructuras que pueden ser analizadas, el campo de aplicación es muy amplio, e incluye la mayor parte de circuitos impresos y de circuitos integrados.

Se empieza por desarrollar el método con todo detalle, desde las ecuaciones de base hasta las propiedades de las funciones de Green y el cálculo de ciertas integrales de convolución. Se ponen de relieve las dificultades numéricas. Se muestra cómo la memoria y el tiempo de análisis se ven reducidos gracias al precálculo de la dependencia vertical del problema, en comparación con las exigencias de un método que fuera capaz de tratar una estructura 3D arbitraria.

Una vez que las bases de la nueva técnica han quedado establecidas, se considera su aplicación a ciertas características de los circuitos impresos de alta frecuencia. Entre éstas, la más destacable es el análisis de metalizaciones gruesas. Se presenta un nuevo método de onda completa para el análisis de aperturas de forma arbitraria en pantallas metálicas gruesas. Se ha comparado este método con otros, tanto de onda completa como aproximados, así como con medidas, y se ha demostrado una precisión excelente. Una segunda aplicación es el análisis del efecto de puentes (*air-bridges*) en circuitos basados en línea de ranura (SL) y línea coplanar (CPW). La comparación de medidas y simulaciones proporciona información valiosa sobre el comportamiento de las antenas de lazo alimentadas por línea coplanar.

La aplicación final es al análisis y diseño de antenas primarias para lentes dieléctricas. Nuestro Laboratorio colaboró con un equipo de la Universidad de Toronto en el proyecto de la Agencia Espacial Europea *Integrated Front-End Receivers* (IFER), dedicado al estudio de este tipo de sistemas. El método de análisis que aquí se presenta permite, junto con las nuevas técnicas de trazado de rayos desarrolladas en Toronto, una mejor comprensión de su comportamiento.

Acknowledgements

Unhappy that I am, I cannot heave my heart into my mouth.

William SHAKESPEARE

In this work I had the help of the people of LEMA who are acknowledged by name in the references or in the text. Michael Mattes, Ivica Stevanović and Francisco Núñez were generally helpful and supporting.

There are three exceptional contributions. M^a Eugenia Cabot helped with the figures and the translations. Pedro Crespo gave me the idea of modelling the thick screen as a parallel-plate medium, which has proved thesis-making. J.-F. Zürcher built all the prototypes I designed for testing, including many that I do not show.

Outside LEMA, I am indebted to Dr. Lin of ESA/ESTEC, Earth Observation Programs, and to Andrew Pavacic and George Eleftheriades of the University of Toronto.

On a personal note, I want to thank my sister, Natalia, for her happy emails, my mother, for expecting the best from me despite heavy evidence, and Tomasz, for letting me weep on his shoulder. Finally, I thank Juan Mosig for being the best of advisors.

Contents

| | |
|--|-----------|
| Introduction | 1 |
| 1 Principles | 7 |
| 1.1 Field equations | 7 |
| 1.2 Medium and structure | 8 |
| 1.3 Principles of equivalence | 9 |
| 1.4 Integral equation method | 10 |
| 1.5 Spectral vs spatial | 10 |
| 1.6 Method of moments solution by subsectional basis expansion | 11 |
| 2 Layered medium | 13 |
| 2.1 Plane wave solution | 15 |
| 2.2 Solution for elementary sources | 17 |
| 2.3 Potentials | 18 |
| 2.4 Transmission line Green's functions | 20 |
| 2.5 Integrated transmission line Green's functions | 26 |
| 2.6 Quasistatic and singular behavior | 32 |
| 2.7 Numerical inversion | 43 |
| 2.8 Examples | 46 |
| 2.9 Conclusion | 48 |
| 3 Surface equivalence | 53 |
| 3.1 Discretization | 54 |
| 3.2 Metallic scatterers | 54 |
| 3.3 Apertures | 66 |
| 3.4 Piecewise homogeneous dielectric bodies | 77 |
| 3.5 Examples | 78 |
| 3.6 Conclusion | 80 |
| 4 Volume equivalence | 83 |
| 4.1 Dielectric bodies | 83 |
| 4.2 Discretization | 83 |
| 4.3 Solution by the Method of Moments | 85 |
| 4.4 Layered medium | 88 |
| 4.5 Examples | 90 |
| 4.6 Assessment | 96 |
| 5 Applications | 99 |
| 5.1 Apertures in thick metallic screens | 99 |
| 5.2 Airbridges in CPW and SL circuits | 110 |

5.3 Integrated antennas in substrate lenses 117

6 Perspectives 125

A Vector relations 127

B Ancillary 131

C Gaussian rules 137

D Documentation for TM 143

List of Figures 151

List of Tables 155

References 157

Index 167

Introduction

This thesis has been motivated to a great extent by a research project (IFER) which the European Space Agency awarded to the Laboratoire d'Électromagnétisme et d'Acoustique (LEMA) in 2000, and which was completed in 2004 to the satisfaction of all partners involved. A discussion of the details and results of this project can be found in the official documentation [47, 64, 65, 67, 90, 102, 103, 104]. The challenge offered to our Laboratory in the frame of this project was the electrodynamic full-wave analysis of various structures embedded in stratified media, including horizontal and vertical structures (in a layered or stratified medium, horizontal means 'parallel to the layers') as well as slots in thin or thick metallic screens, and (if time and resources permitted) the inclusion of dielectric inhomogeneities of arbitrary dielectric contrast (fig. 1). The electromagnetic model was to lead to an operational software tool.

Starting with the work of the director of this thesis, there is a long tradition of work on the integral equation method in the Laboratoire d'Electromagnétisme et Acoustique (LEMA). The first target of the method was the microstrip patch, somewhen around the misty dawn of the nine-hundred eighties [91]. In [11], the complete multilayered, multislot printed circuit antenna was analyzed; all unknowns were horizontal.

Thus, our wonted answer to these type of antenna and circuit problems has been an integral equation approach, where the unknowns are 2D vector functions defined on the metallizations and/or the apertures. Following in the steps of these developments, it was decided to explore whether, with the adequate upgrades and improvements, the traditional techniques would remain competitive for the more involved aspects of the problems posed by the IFER project, compared to brute-force approaches like FEM or FDTD. In this spirit of extending the integral equation method, vertical metallizations were included in [39], and that work was later improved with a first attempt at a semi-spectral method in [45].

In the presence of vertical metallic parts (vias, airbridges), the lack of vertical symmetry of the layered medium, which need not be taken into account when only horizontal layers are used, becomes an essential issue. But there is an inner structure that can be used to our advantage and that is best revealed by working in the 2D Fourier transformed domain. For that reason, a careful consideration of the spectral dyadic Green's functions was deemed necessary, and it was decided that our first task was to be a reappraisal of the derivation of field and potential Green's functions in layered media. This reappraisal led us a very general and compact formulation that includes several original features. It was at this point that the direction of all further work was set.

The salient feature of a planar stratified medium is that its properties change along a single coordinate axis (z). The structures embedded in it can be seen either as an evolution of those analyzed by vintage 2D electromagnetic analysis software, or as a simplification and restriction of more general 3D structures. The title of this dissertation comes, then, from a limitation, but a limitation that is the result of an opportunity and a choice. A 2.5D structure is a structure that is made up of some parts that are horizontal, and these parts can be connected with other parts that are *strictly* vertical (fig.1). The construction of a 2.5D structure is easier to specify

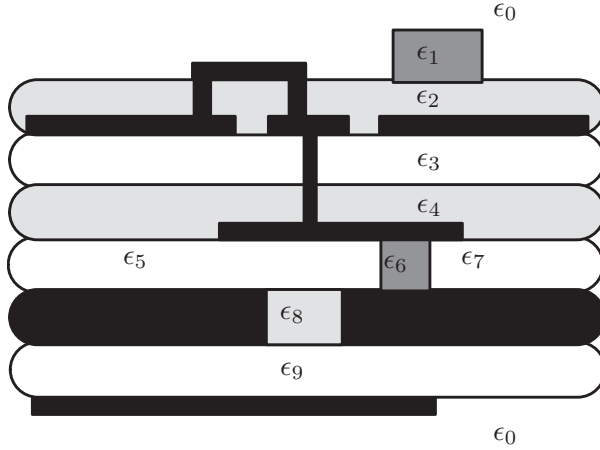


Figure 1: A complex 2.5D structure embedded in an open layered medium, including vertical and horizontal metalizations, dielectric inclusions and thick metallic screens.

and to normalize, which is why nowadays most of us live and work inside 2.5D structures. Printed circuit structures are built by laying layers one on top of another and thus correspond, approximately, to this description. There is clearly a niche for methods of electromagnetic analysis specially tailored to 2.5D printed circuits and antennas; and where a need is fulfilled, what is not needed is not seen as a limitation.

A specialization of the integral equation technique for the analysis of 2.5D scatterers in layered media is presented in this work. Many methods are available that can deal with much more general structures, and some of them are very fast and accurate. However, the integral equation is still recognized as the most efficient way to analyze scatterers in open media, because, being a boundary method, the computational resources are concentrated only on the features of the problem that are of interest.

And the special constitution of the layered medium (indeed, its being ‘layered’) makes it possible, if the limitation to 2.5D scatterers is accepted, to precompute the vertical component of the problem, and to reuse it for any other scatterer with the same vertical structure. This precomputation takes place in the Fourier transformed domain and, with a suitable choice of approximation functions for the unknown currents on the scatterer, can be done analytically. Therefrom results a simplification of the analysis of an order of magnitude, and the calificative that has been given to this method of ‘mixed spectral/spatial’ [140].

The original contributions of this work may thus be listed:

- A very general solution of the TL model equations makes it possible to implement vertical integration in the spectral domain on any Green’s function automatically; in fact, independently of the particular field or potential Green’s function, as the operations depend only on some factors of the transmission line Green’s functions (§2.4).
- The extraction of quasistatic parts, both in the spectral and the spatial part of the method, is extended to the new integrated Green’s functions (§§2.6, 3).
- The inclusion of magnetic currents, together with the extraction of quasistatic parts mentioned above, gave the idea and the possibility of a new way of modeling arbitrarily shaped apertures in thick metallic screens. This model treats the aperture as a parallel plate waveguide (§5.1).

At the end of this thesis-time, our Laboratory possesses a new computer code, able to meet most of the challenges formulated at the beginning and which enlarges the scope of problems

and geometries amenable to an efficient full-wave analysis. Although inevitably some aspects of the computer implementation fall short of the original goals, other new (one may say collateral) applications were made possible, quite unexpectedly, during the development.

An important part of this work, which would be difficult to quantify, has consisted in writing and debugging this code. A description of one of its most important pieces has been included as an appendix. However, it has been decided that the dissertation should concentrate on explaining the principles of electromagnetic analysis the code is based on, rather than on describing the code itself.

In any case, the code has opened new possibilities to our Laboratory, and it is for instance being used today to help define and analyze EM simulation benchmarks after the ‘Software Initiative’ of the European Network of Excellence ACE (2004-2005) in which the LEMA participates actively.

Outline

I refer to chapters and sections in a uniform way: §1 is **Chapter 1, Principles**, and §2.1 is section **2.1 Plane wave solution**.

In §1 we present the basic principles in which the rest of the work is based: the field equations, the equivalence principles, the mechanics of the method of moments. The purpose of these short explanations is to allow us to go right to the subject matter in each of the subsequent chapters, which often deal with more material than what their title alone would indicate. Some ancillary matters, such as the solution of a linear system of equations, the principle of the computation of a radiation pattern, and so on, are also covered here.

§2 presents the layered medium and the computation of the associated Green’s function. The exposition begins by the computation the response of the medium to an elementary plane wave excitation, directly from the Maxwell equations. The Green’s function is then obtained through an inverse Fourier transform. The exponential dependence of the Green’s function on the vertical coordinates (in the spectral domain) is obtained by direct calculation on a transmission line model. We show how this dependence can be integrated with simple basis and test functions, and which are the characteristics of the resulting ‘integrated’ Green’s functions. This is the marrow of the pseudospectral-2.5D method of analysis. An section on the numerical inversion of these spectral Green’s functions (§2.7) follows, with a section of examples (Green’s functions for various media and relative positions of source and observer) to illustrate the theory.

The original contribution of this chapter is the development of the 2.5D method. The subject is covered extensively, from the derivation of convenient transmission-line model equations and the vertical integration in the spectral domain to the numerical inversion and the extraction of quasistatic parts of the new integrated Green’s functions. Implementation notes are also given.

§3 is devoted to the analysis of metallic antennas and scatterers embedded in layered media, using the surface equivalence principle. We also deal here with apertures in metallic ground planes, and, in free space or ground-plane bounded homogeneous half-spaces, with homogeneous dielectric bodies. The Mixed Potential treatment of every kind of interaction in the frame of the 2.5D method is original. Here, the quasistatic parts obtained in §2 are used to extend the singularity extraction technique, traditionally used for the computation of potential and field integrals, to the new integrated Green’s functions, which for the most part present logarithmic singularities.

§4 is devoted to the analysis of dielectric bodies embedded in layered media. We begin with a description of the volume integral equation in free space, which is then extended to a layered medium using the pseudospectral method. Although, unlike for surface patches, a full implementation is still lacking, we present results for dielectrics in free space, and compare the

results of traditional 3D integration with those of the 2.5D method.

In §5, the results of the surface formulation of §3 are applied to two special problems: 1) the analysis of apertures in thick metallic screens and 2) the analysis of CPW and SL circuits with metallic air bridges. The analysis of apertures in thick ground planes benefits especially from the 2.5D method, which for the first time provides an efficient technique of analysis for arbitrarily shaped apertures, with no approximation as to the thickness. We compare our results to measurements and, for some cases, to two other more limited numerical techniques.

§A and §B collect key expressions and calculations that were not be presented in full in the course of the text for lack of opportunity.

§C describes the numerical integration technique used to integrate the regular part of the Green's functions over various subdomains (triangles, parallelograms, tetrahedra, parallel wedges, and parallel hexahedra) and lists abscissas and weights for optimal Gaussian rules that have been obtained from a variety of sources.

§D is a summary description of TM, a software package developed to implement and demonstrate the content of this thesis. A great deal of effort was spent in it. Indeed, every equation and figure of this work has its weight many times in lines of code. Some technical issues that are thought to be important or interesting but that find no place in the development of the theory are discussed here.

Finally, there is a bibliography, and an index.

Notation and conventions

- Equations are numbered within chapters.
- According to general convention, source points are primed.
- For two-dimensional vectors and distances, we do not use $\rho, \boldsymbol{\rho}, P$ but p, \mathbf{p}, P .
- Vectors are set bold (\mathbf{A}) and dyadics with a double bar above ($\bar{\bar{A}}$). Normalized vectors carry a caron ($\hat{\mathbf{a}}$).
- The orientation of $\hat{\mathbf{z}}$ may vary depending on the context, but in absence of other indication, it is, in layered media, normal to the layers.
- Only a few dyadics are used by name in this work. These are: the Green's functions for the electric/magnetic fields produced by an electric/magnetic dipole ($\bar{\bar{E}}^J, \bar{\bar{E}}^M, \bar{\bar{H}}^J, \bar{\bar{H}}^M$), the Green's functions for the potentials ($\bar{\bar{A}}, \bar{\bar{F}}, \bar{\bar{\Phi}}, \bar{\bar{W}}$), the idemfactor ($\bar{\bar{I}}$), a generic reflection dyadic ($\bar{\bar{R}}$) and a generic projection dyadic ($\bar{\bar{P}}$). A particular kind of $\bar{\bar{P}}$ is $\bar{\bar{I}}_t = \bar{\bar{I}} - \hat{\mathbf{z}}\hat{\mathbf{z}}$. A generic Green's function is $\bar{\bar{G}}$ or perhaps $\bar{\bar{g}}$. The distinction between spectral and spatial quantities should always be obvious from the arguments of the functions or from context.
- In integrals, the symbol dx (or dS, dV) is dropped when the integration variable is clear from context.
- Symbols $\text{grad}, \text{curl}, \text{div}$ are used, rather than $\nabla, \nabla \times, \nabla \cdot$. $\text{grad}_s, \text{curl}_s, \text{div}_s$ are the two-dimensional operators. All these imply derivation respect to observer (or field) coordinates; derivation respect to source coordinates is indicated by $\text{grad}', \text{curl}', \text{div}'$.
- A convolution is indicated with $*$, ie $f * g = \int f(\mathbf{r}, \mathbf{r}')g(\mathbf{r}')dv'$. If f is a dyadic and g a vector or both are vectors, a dot product is implied. If both f and g are dyadics, a double dot product is implied.
- A time factor $e^{+j\omega t}$ is assumed and suppressed.

- An effort is made to present every plot and table in normalized dimensions, ie, the speed of light and the constitutive parameters of empty space become 1 (cf the ‘natural’ units in [99, table I-2, pp. 466]), frequency (ω) becomes 1, and distances are multiplied by $k_0 = \omega/c_0$. For this reason, the permittivity $\epsilon_0 = 8.85 \cdot 10^{-12} \text{ Fm}^{-1}$ and the permeability $\mu_0 = 4\pi \cdot 10^{-7} \text{ Hm}^{-1}$ will not appear in what follows, and ϵ_0 and μ_0 will be used to denote some relative permittivity and permeability, with no different meaning than, say, ϵ_7 . or $\mu_{\text{orichalcum}}$.
- Some paragraphs contain important ideas or points that are referenced later in the text. These are marked and numbered: **P1**, **P2**...

1 Principles

The engineering solution of any EM problem is a rather complex process that starts from the EM field basic equations (Maxwell equations) and ends in the prediction of some measurable quantity, like a received power or an input impedance.

Many paths are possible, ranging from purely analytical approximations (like variational expressions) to direct, brute-force numerical solution of Maxwell equations) (finite differences, finite elements), followed by some post-processing of the primary result —the fields.

This thesis uses systematically an integral equation approach [86] based on the application of equivalence principles [50, §3.5] to transform the Maxwell equations in a set of coupled integral equations. The method of moments [51] is applied on these equations to produce a linear system that can be solved by computer using standard algorithms.

Although these steps are nowadays well known, they are briefly described in this chapter, for the sake of completeness and to set up some notation and conventions to be assumed in the following chapters.

1.1 Field equations

The electromagnetic field behaves according to Maxwell equations, which in differential, time-harmonic form are [50, (1-48)]

$$\text{curl } \mathbf{E} + j\omega\mu\mathbf{H} = -\mathbf{M} \quad (1.1a)$$

$$\text{curl } \mathbf{H} - j\omega\epsilon\mathbf{E} = +\mathbf{J} \quad (1.1b)$$

A *medium* is a particular pair $\epsilon(\mathbf{r}), \mu(\mathbf{r})$. If $\epsilon(\mathbf{r})$ and $\mu(\mathbf{r})$ are constant everywhere, this is an *unbounded homogeneous medium*. The *free space* is an unbounded homogeneous medium where $\epsilon(\mathbf{r}) = 1$ and $\mu(\mathbf{r}) = 1$, but we may occasionally write about free-space with other constants. A *open layered medium* has $\epsilon = \epsilon(z)$ and $\mu = \mu(z)$. If ϵ, μ are scalars, the medium is *isotropic*. This will always be the case in this work.

We deal with two problems posed by (1.1). The first is to find the *total field* \mathbf{E}, \mathbf{H} when the medium is *excited* with some known sources. This is the *scattering problem*. If the source is an elementary dipole, the solution is called the *Green's function* for the medium. As (1.1) are linear and both field and source are represented by vectors, the Green's function is a linear vector function—a dyadic $\bar{\bar{G}}(\mathbf{r}, \mathbf{r}')$; \mathbf{r} is the position where the field is computed, and \mathbf{r}' the position of the source. If the Green's function for a given medium is known, the linearity of (1.1) guarantees that the field produced by any excitation can be obtained by superposition, viz

$$\begin{aligned} \mathbf{E} &= \bar{\bar{E}}^J * \mathbf{J} + \bar{\bar{E}}^M * \mathbf{M} \\ \mathbf{H} &= \bar{\bar{H}}^J * \mathbf{J} + \bar{\bar{H}}^M * \mathbf{M} \end{aligned} \quad (1.2)$$

where, for example, $\bar{\bar{E}}^J$ is the dyadic Green's function that gives the electric field vector (\mathbf{E}) produced by an arbitrarily oriented electric dipole (\mathbf{J}). In (1.2), the scattering problem has been reduced to the computation of an integral.

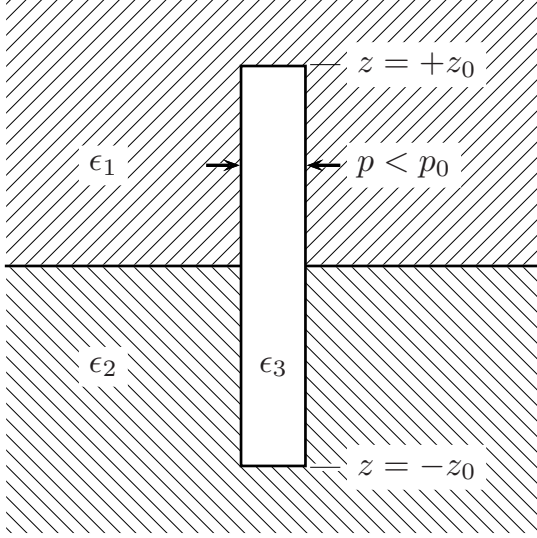


Figure 1.1: A complicated medium with no embedded structure.

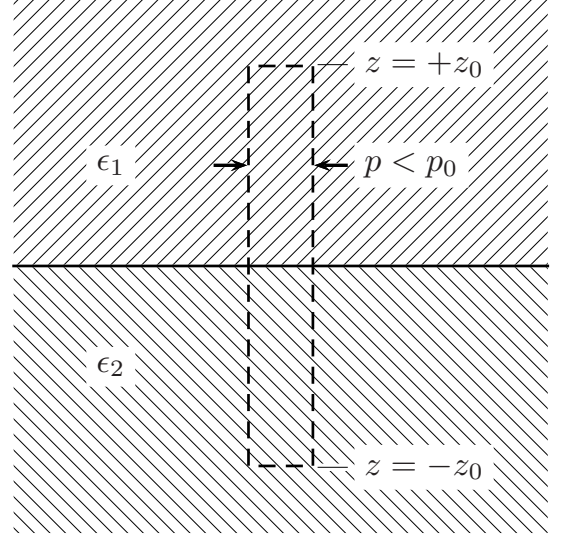


Figure 1.2: A manageable medium with an embedded structure.

The second problem is that of finding the sources when a (sufficient) condition on the fields has been given. This problem arises on application of the equivalence principle (§1.3) to simplify the medium (§1.2).

1.2 Medium and structure

Imagine a metallic stake crossing a dielectric interface, for example, half buried in earth. We may well imagine that this is a medium defined by (fig. 1.1)

$$\mu(\mathbf{r}) = 1$$

$$\epsilon(\mathbf{r}) = \begin{cases} \epsilon_1, & z > z_0, \text{ or } z > 0 \text{ and } p > p_0 \\ \epsilon_2, & z < -z_0, \text{ or } z < 0 \text{ and } p > p_0 \\ \epsilon_3, & p < p_0, |z| < z_0 \end{cases}$$

and try to compute the Green's function for it. This is perfectly possible and sometimes useful (see for instance [100]). Most often, however, it is advisable to try to compute the Green's function for a simpler medium, just (fig. 1.2)

$$\mu(\mathbf{r}) = 1$$

$$\epsilon(\mathbf{r}) = \begin{cases} \epsilon_1, & z > 0 \\ \epsilon_2, & z < 0 \end{cases}$$

The part of the medium that has been extracted can be accounted for representing it as unknown sources using the equivalence principle and enforcing additional conditions on the field, but it is no longer included in the Green's function. We have then a restriction on the definition of 'medium' given above, which is: we call something medium if we use its Green's function. Everything else, which is indeed part of the medium but is not handled with a Green's function, is called the *structure* or perhaps the *scatterer*.

The *incident field* is the field produced by known sources through the Green's function of the (restricted) medium, in absence of scatterers. The incident field could also be given without reference to known sources; most often this is a the plane wave, a sourceless solution of 1.1 for free space. In any case, the problem consists in finding another field (the *scattered field*) so that the sum of both fulfills (1.1) in the complete medium, in the presence of scatterers.

1.3 Principles of equivalence

We consider two principles of equivalence. The surface equivalence principle [50, §3.5] is based on the unicity theorem [131, §9.2]. According to this theorem, the field inside a bounded, sourceless region is completely determined by the tangential fields on the boundary of the region; this follows in turn from Green's theorem. If we place sources in this boundary that produce the same tangential fields, the fields inside do not change. This principle has at least three distinct applications.

The first is to the analysis of homogeneous dielectric bodies. The dielectric interface is covered on each side with electric and magnetic sources. The problem is divided in two by the interface; on each side's problem we assume null fields on the *other* side. Therefore the currents of each side reproduce a field ($i = 1, 2$)

$$\mathbf{J}_i = \hat{\mathbf{n}}_i \times \mathbf{H}_i, \quad \mathbf{M}_i = -\hat{\mathbf{n}}_i \times \mathbf{E}_i \quad (1.3)$$

which, by the unicity theorem above, completely determine the field. [By (1.3), the currents on the *other* side produce no field in *our* side]. We are then free to extend our own medium to the other side, effectively removing the dielectric interface. The equivalent currents on both sides (and both problems) are linked by the continuity conditions [131, (9.23)]

$$\hat{\mathbf{n}}_i \times (\mathbf{E}_1 - \mathbf{E}_2) = 0, \quad \hat{\mathbf{n}}_i \times (\mathbf{H}_1 - \mathbf{H}_2) = 0 \quad (1.4)$$

which must be enforced separately.

The second application is to the analysis of metallic structures. It is the same as above, save that in one of the media the fields are *really* zero. For this reason there is only one problem to solve and not two. The tangential electric field on the surface of the conductor is zero, so $\mathbf{M} = 0$, and this is the condition (ie, $\mathbf{E} \times \hat{\mathbf{n}} = 0$) to be enforced.

The third application is to the analysis of apertures on perfectly conducting bodies [53, §2.2]. In principle, this is similar to the analysis of a homogeneous dielectric object. However, instead of using the Green's function of the medium that results when the scatterer is removed, we use the Green's function that includes the presence of the metallic body, with its apertures closed. A tangential electric current does not radiate if placed on a perfectly conducting surface, and so equivalent electric currents disappear from the problem. Magnetic currents are only required where tangential \mathbf{E} is not actually known to be zero, that is, on the aperture. The complication in this case is that the Green's function in the presence of the metallic scatterer must be known, but there are instances where it may be obtained quite trivially. The standard example is an infinite ground plane, whose Green's function can be obtained through image theory.

The volume equivalence principle is much simpler in concept than the surface equivalence principle, because it is based on a straightforward algebraic manipulation. It is discussed in §4.

In all these equivalence principles, the equivalent sources are not known. The integral equation method, described in the next section, will be used to find them.

1.4 Integral equation method

The integral equation method is an essential tool in the solution of electromagnetic problems in open media: its principal advantage over other (differential-equation based) methods is that it automatically incorporates the boundary conditions at infinity (Sommerfeld conditions) through the medium's Green function.

We have seen above (§1.3) that the application of the equivalence principle produced

- some unknown equivalent sources;
- a set of conditions for the field.

The integral equation is the statement of that set of conditions for the total field,

$$\begin{aligned}\mathbf{E} &= \mathbf{E}^i + \mathbf{E}^s \\ \mathbf{H} &= \mathbf{H}^i + \mathbf{H}^s\end{aligned}\tag{1.5}$$

It is an integral equation because the scattered field $\mathbf{E}_s, \mathbf{H}_s$ is a function of the equivalent sources through (1.2). For example, for a metallic scatterer, the integral equation will read

$$(\bar{\bar{E}}^J * \mathbf{J} + \bar{\bar{E}}^M * \mathbf{M}) \times \hat{\mathbf{n}} = -\mathbf{E}^i \times \hat{\mathbf{n}}\tag{1.6}$$

enforced on the metallic surface, and for a homogeneous dielectric object, it will read

$$(\bar{\bar{E}}_1^J * \mathbf{J} + \bar{\bar{E}}_1^M * \mathbf{M} - \bar{\bar{E}}_2^J * \mathbf{J} + \bar{\bar{E}}_2^M * \mathbf{M}) \times \hat{\mathbf{n}} = -\mathbf{E}^i \times \hat{\mathbf{n}}\tag{1.7a}$$

$$(\bar{\bar{H}}_1^J * \mathbf{J} + \bar{\bar{H}}_1^M * \mathbf{M} - \bar{\bar{H}}_2^J * \mathbf{J} + \bar{\bar{H}}_2^M * \mathbf{M}) \times \hat{\mathbf{n}} = -\mathbf{H}^i \times \hat{\mathbf{n}}\tag{1.7b}$$

enforced on the dielectric interface. If the equivalence principles have been used more than once, then we shall have to deal with a set of coupled integral equations.

If the Green's functions $\bar{\bar{E}}^J$, etc. are used directly in (1.6) or (1.7), the integral equation is called an electric or magnetic field integral equation (EFIE/MFIE) depending on the field whose continuity is being enforced. For example, of (1.7), (1.7a) is an EFIE while (1.7b) is a MFIE. It is possible, however, to express these equations in terms of vector and scalar potentials, making use of

$$\mathbf{E} = -j\omega\mathbf{A} - \text{grad } \Phi - \frac{1}{\epsilon} \text{curl } \mathbf{F}\tag{1.8}$$

and similarly for the magnetic field. The resulting Green's functions $\bar{\bar{A}}, G_\Phi, \bar{\bar{F}}$, etc, have weaker singularities and are generally easier to work with. In addition, the number of components necessary to describe the fields completely is usually smaller in terms of potentials. This is true both in an homogeneous and in layered media [86, §3.2]. The EFIE (1.6), written with potentials $\bar{\bar{A}}, G_\Phi$, is called the mixed potential integral equation, or MPIE. This name may, less strictly perhaps, be applied to (1.7), if $\bar{\bar{H}}^M$ is written in terms of $\bar{\bar{F}}$ and G_W (magnetic mixed potentials) and $\bar{\bar{E}}^J$ in terms of $\bar{\bar{A}}$ and G_Φ .

1.5 Spectral vs spatial

An essential step in the application of the integral equation method is the computation of the Green's functions for the particular medium at hand. But these Green's functions are known in closed form (in terms of elementary and not-too-special functions) for little more than free space. However, if a one-, two- or three-dimensional Fourier transform is applied to Maxwell equations, the Green's function in the spectral variables is available in closed form (or is easier

to compute) for a much greater variety of media. Resorting to transform techniques is therefore an almost unavoidable step in the computation of the Green's functions. But once this is done, there are two possibilities:

- To solve the integral equation completely in the transformed variables, and only come back to the spatial domain (reverse the Fourier transformation) once the solutions (the equivalent currents \mathbf{J} , \mathbf{M}) are known. This is the *spectral domain approach*.
- To convert the Green's function to the spatial domain as soon as it is known, and to carry out all the remaining steps for the solution in the spatial coordinates. This is the *spatial domain approach*.

The respective limitations of the methods come from the point where they return to the spatial domain. The spatial domain approach is typically more flexible, and can handle arbitrarily shaped structures if the medium has symmetries that ease the (Fourier) inversion of the Green's function. The spectral domain approach is limited in this respect by the need to invert the final solution.

1.6 Method of moments solution by subsectional basis expansion

The generic integral equation, that covers as particular cases (1.7) and (1.7) among many others, can be written in terms of a linear functional L as [51, §1.1]

$$L(\mathbf{f}) = \mathbf{g} \quad (1.9)$$

where \mathbf{f} represents the unknown equivalent currents, and \mathbf{g} the incident field. One method to solve (1.9) is as follows [52, §III].

Expansion The equivalent sources are written as a finite linear combination of *basis functions* with unknown coefficients. If each of these were defined over the whole domain of the equivalent sources, they would be called *entire-domain* basis functions. Instead, they are defined over a part of this domain, and so they are called *subsectional* or *subdomain* bases. Their definition must enforce certain continuity and boundary conditions so that the physical quantity they represent is well approximated: for example, in an open metallic surface, the electric current normal to the border must vanish, and so must the normal component of the basis functions on that border. Thus we have

$$L(\mathbf{f}) = L\left(\sum_{j=0}^{n-1} \alpha_j \mathbf{b}_j\right) = \sum_{j=0}^{n-1} \alpha_j L(\mathbf{b}_j) = \mathbf{g} \quad (1.10)$$

Test We form the inner product [51, §1.2] of (1.10) with each of a list of *test functions*, of which there are as many as basis functions; in this way we obtain

$$\sum \alpha_j \langle \mathbf{t}_i, L(\mathbf{b}_j) \rangle = \langle \mathbf{t}_i, \mathbf{g} \rangle, \quad i = 0..n-1 \quad (1.11)$$

The purpose of the test is to enforce the integral equation in an approximate way. The set of test functions should cover the domain of the equivalent currents, because there is also where the integral equation is enforced. If $\mathbf{t}_i = \mathbf{b}_i$, $i = 0..n-1$, the method of moments is called *Galerkin's method* and this choice will be tacitly assumed hereafter. The inner product is chosen so that the

matrix elements are *reaction terms*. The reaction between two source distributions $a = \{\mathbf{J}_a, \mathbf{M}_a\}$ and $b = \{\mathbf{J}_b, \mathbf{M}_b\}$ is [115, (1)].

$$\|a, b\| \equiv \int (\mathbf{J}_b \cdot \mathbf{E}(\mathbf{J}_a, \mathbf{M}_a) - \mathbf{M}_b \cdot \mathbf{H}(\mathbf{J}_a, \mathbf{M}_a)) dv \quad (1.12)$$

The reciprocity theorem [50, §3.8] states that $\|a, b\| = \|b, a\|$. For each of the particular cases

$$\mathbf{M}_a = \mathbf{M}_b = 0$$

$$\mathbf{J}_a = \mathbf{J}_b = 0$$

$$\mathbf{J}_a = \mathbf{M}_b = 0$$

particular reciprocity relations result:

$$\|\mathbf{J}_b, \mathbf{J}_a\| = \|\mathbf{J}_a, \mathbf{J}_b\| \quad (1.13a)$$

$$\|\mathbf{M}_b, \mathbf{M}_a\| = \|\mathbf{M}_a, \mathbf{M}_b\| \quad (1.13b)$$

$$\|\mathbf{J}_b, \mathbf{M}_a\| = \|\mathbf{M}_a, \mathbf{J}_b\| \quad (1.13c)$$

These are important when the symmetry of the matrix $\langle \mathbf{t}_i, L(\mathbf{b}_j) \rangle$ of (1.11) comes into play. Specifically, they give the reason for selecting the inner product of (1.11) according to (1.12).

Solution (1.11) is a linear system of equations in the coefficients α_j . It is solved by any conventional technique, such as Gauss-Jordan elimination. With some care in the choice of the inner product and the test functions, it is possible to obtain a linear system with a symmetric (indefinite) matrix. A system with a symmetric matrix can be solved with special algorithms that take advantage of the symmetry to save half the storage space, such as the Bunch-Kaufman method [130, §3.2.5]; see p.147 for an implementation note. Otherwise, it is well known that these methods have unacceptably high complexity for electrically large problems. We shall only be concerned with small problems.

2 Layered medium

In this chapter, we introduce a systematic approach to compute Green's functions in a layered planar medium. Source and observer are both at an arbitrary height and within any layer. Particular attention is devoted to the 'vertical' (z, z') dependences, and an exhaustive analytical treatment is provided for an efficient integration along these vertical coordinates.

The layered medium is depicted in fig. 2.1. Each layer $i = 0..n - 1$ is homogeneous and isotropic. The medium extends to infinity in every horizontal direction. In the vertical direction, it may extend to infinity or be closed by an impedance boundary on either end, or on both.

The study of layered media is a standard topic in electromagnetics since the early development of the technique of radiocommunication and the study of long distance wave propagation over the earth's surface [141, §1]. A strong interest has long existed in optics, ever since the first interesting solution of a layered media problem was stated in 1621 [15, p.xxvi], and more recently for multilayer filters, antireflection coatings, and the similar structures.

The wave we still ride began at the end of the 1970's, when the first microstrip antennas were developed. Microstrip antennas, or antenna elements (in arrays), are mostly of the compact kind, their size rarely exceeding a free space wavelength. They have proved very resistant to simplified modelling, much more so than other microwave and millimeter wave structures that are not supposed to radiate. For this reason, their apparition stimulated the development of computational methods for the calculation of every property of the layered medium and of structures embedded on it. These methods are much more powerful (and computer intensive) than those applied in optics, where the multilayered medium is on its own and is rarely excited

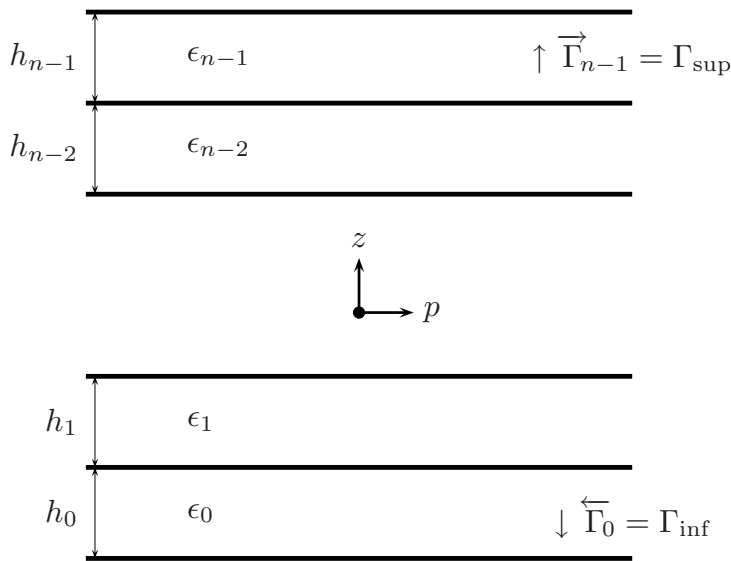


Figure 2.1: Layered medium.

with something other than rays or plane waves; their true source is in the works of George Green (on his function, and on the proper formulation of the equivalence principle) and Arnold Sommerfeld (on the fields of a dipole over a dielectric interface). The names of these two people will appear many many times in this chapter.

Some milestones in the specific context of this work are:

- In 1980, a transmission line (TL) model was applied to the computation of layered media Green's functions [55].
- In 1982, the Method of Moments was combined with interpolation of the spatial Green's functions and applied to the study of arbitrarily shaped planar antennas [91].
- In 1990, the spatial domain technique was improved to allow analysis of arbitrarily shaped 3D metallic scatterers embedded in layered media [80, 82]. This analysis, which at least theoretically had closed that problem, remained computationally very expensive, while further development continued on the analysis of arbitrarily shaped antennas on multilayer structures [12], including slots [49, 122] and cavities.
- Problems with arbitrarily oriented magnetic surface currents, for the analysis of homogeneous dielectric objects, were tackled by [32] and also by [20].
- Meanwhile a thorough reference appeared on the derivation and use of the Green's functions in multilayered media [78].

Also, all since [81] was published, effort has gone on in two directions:

- On one hand, to accelerate the computation of the layered media Green's function, either by approximating it [135] or by devising efficient three-dimensional interpolation schemes [20].
- On the other hand, to develop restricted approaches that allow more efficient analysis of special types of 3D structures.

One of these restricted approaches involves the spectral treatment of the vertical dependence of the Green's functions, that is eliminated from the spatial domain method of moments. Thus, 3D interpolation becomes unnecessary. This is the main subject matter of this chapter and indeed of this whole dissertation. The restriction is that the expansion functions for the electric and magnetic unknowns (§1.6) must have *separable* dependence on the coordinate axis normal to the stratification (ie z). The meaning of this separability is precised in §2.5, but, in practice, it means that the structures to be analyzed cannot include oblique parts, that are neither parallel to the stratification nor normal to it —what we call a 2.5D structure.

This 2.5D technique has evolved from the limited application of [136], to a general formulation of the *idea* in [57] and full realization in [140]. While [136] and [140] used mixed EFIE-MPIE formulations, that of [57] was fully MPIE. All these works dealt only with electric currents.

The main advantage of a mixed potential formulation over a pure electric field formulation lies in the reduced singularity of the Green's function in the former case. For this reason the plain EFIE is not normally used in the solution of surface integral equations. The treatment of the vertical dependence of the Green's functions in the spectral domain weakens that singularity, however, and the plain EFIE becomes usable. But it is still necessary to deal with (in layered media) a full dyadic (9 cartesian components, though not accounting for symmetry) while in mixed potential form there are just 7 components (5 for the magnetic vector potential dyadic and 2 for the scalar potential, not accounting for symmetry) to compute. The EFIE has the advantage only for some interactions (for example, the interaction between two vertical elements

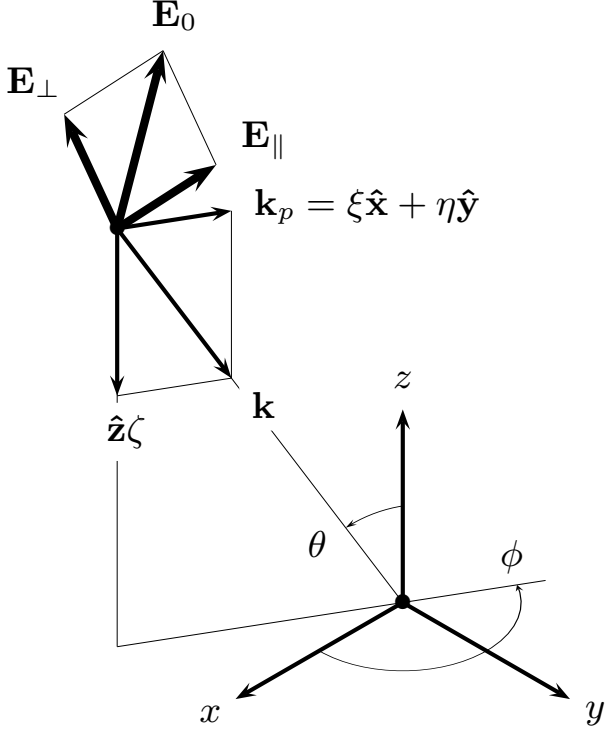


Figure 2.2: Characteristic parameters of a plane wave.

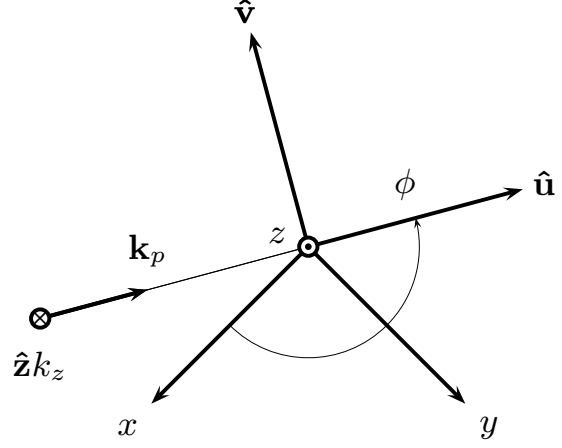


Figure 2.3: Projection of fig.(2.2) showing the natural axes for the modal representation.

requires up to four components for the EFIE, once the vertical dependences are integrated, and five for the MPIE). In addition, the quasistatic terms are simpler in mixed potential form. For these reasons only the mixed potential forms are used in this work for $\bar{\bar{E}}^J$ and $\bar{\bar{H}}^M$.

Our contribution is threefold. First, the transmission line model is solved to yield expressions that are particularly convenient for the automatic computation of the specially treated Green's functions. Second, the quasistatic parts of the specially treated Green's functions are analyzed in order to enable the application of singularity extraction procedures in the spatial domain part of the method. Third, in addition to electric currents, magnetic currents on ground planes are also considered. This will enable the analysis of various patch-slot structures in layered media [66, 69]; see §5.1.

2.1 Plane wave solution

Consider the incidence of a plane wave

$$\begin{aligned}\mathbf{E} &= \mathbf{E}_0 e^{-j\mathbf{k}\cdot\mathbf{r}} \\ \mathbf{H} &= Y \hat{\mathbf{k}} \times \mathbf{E}_0 e^{-j\mathbf{k}\cdot\mathbf{r}}\end{aligned}\tag{2.1}$$

on a dielectric interface at $z = 0^+$ (fig. 2.2). The plane determined by \mathbf{k} and $\hat{\mathbf{z}}$ is the *plane of incidence*. For (\mathbf{E}, \mathbf{H}) to be a solution of Maxwell's equations, $\mathbf{k} \cdot \mathbf{E}_0 = 0$. Therefore \mathbf{E} can be split into two components, one parallel to $\hat{\mathbf{z}} \times \mathbf{k}$, normal to the plane of incidence, and another normal to both \mathbf{k} and $\hat{\mathbf{z}} \times \mathbf{k}$, parallel to the plane of incidence. The first field is variously called *perpendicularly polarized*, *horizontally polarized* [108, §15.4], *TE to z*, *H-polarized* [26, §1.2], or

simply *h*. The second field is called *parallel polarized*, *TM to z*, *E-polarized*, or simply *e*. In a cartesian coordinate system (u, v, z) oriented according to the direction of arrival of the plane wave (fig. 2.3), the h-wave has components H_u, E_v, H_z . The e-wave has components E_u, H_v, E_z .

The boundary conditions \mathbf{E} and \mathbf{H} at dielectric interfaces [108, §13.4.1] ensure that an H-polarized field remains H-polarized when refracted and reflected in either one or many parallel dielectric interfaces. The same is obviously true also for an E-polarized wave. Even more, the same continuity conditions force the field to depend on u according to $e^{-jk_p u}$, with the *same* \mathbf{k}_p on every layer. In other words, $\mathbf{E} = \hat{\mathbf{v}}e^{-jk_p u}$ or $\mathbf{H} = \hat{\mathbf{v}}e^{-jk_p u}$ are eigenfunctions of the system of fig. 2.1, and for that reason the dependence on u can be factored out of the field equations.

Now, both fields are independent of the v coordinate —indeed, it is precisely because of this that they can be separated in e- and h-fields at all [26, §2.1.2]. Therefore, the problem of finding the response of a system of parallel dielectric interfaces to the incidence of an arbitrarily polarized plane wave has been reduced to the solution of two one-dimensional problems; as it happens, of two transmission line problems.

This can be formalized quite briefly. Assume fields and sources $\mathbf{F} = (\mathbf{E}, \mathbf{H}, \mathbf{J}, \mathbf{M})$ satisfying everywhere

$$\frac{\partial \mathbf{F}}{\partial v} = 0 \quad (2.2a)$$

$$\frac{\partial \mathbf{F}}{\partial u} = -jk_p \mathbf{F} \quad (2.2b)$$

Using (2.2a) in (1.1),

$$\begin{aligned} \text{curl}_v \mathbf{H} &= +j\omega D_v + J_v & \text{curl}_v \mathbf{E} &= -j\omega B_v - M_v \\ -\frac{\partial E_v}{\partial z} &= -j\omega B_u - M_u & -\frac{\partial H_v}{\partial z} &= +j\omega D_u + J_u \\ +\frac{\partial E_v}{\partial u} &= -j\omega B_z - M_z & +\frac{\partial H_v}{\partial u} &= +j\omega D_z + J_z \end{aligned} \quad (2.3a) \quad (2.3b)$$

(2.3a) describe an H-polarized field, and (2.3b), an E-polarized field (cf [26, (1.15, 1.16)]). They are restated applying (2.2b) as

$$\begin{aligned} \frac{\partial E_v}{\partial z} - j\omega\mu H_u &= +M_u \\ -\frac{\partial H_u}{\partial z} + \left[j\omega\epsilon + \frac{k_p^2}{j\omega\mu} \right] E_v &= -J_v - \frac{k_p}{\omega\mu} M_z \end{aligned} \quad (2.4a)$$

$$\begin{aligned} \frac{\partial H_v}{\partial z} + j\omega\epsilon E_u &= -J_u \\ \frac{\partial E_u}{\partial z} + \left[j\omega\mu + \frac{k_p^2}{j\omega\epsilon} \right] H_v &= -M_v + \frac{k_p}{\omega\epsilon} J_z \end{aligned} \quad (2.4b)$$

A comparison of (2.4) with the telegraphist's equations

$$\frac{dV}{dz} + j\zeta ZI = v \quad (2.5a)$$

$$\frac{dI}{dz} + j\zeta YV = i \quad (2.5b)$$

leads to the equivalences

$$\begin{aligned}
V^h &\equiv E_v & V^e &\equiv E_u \\
I^h &\equiv -H_u & I^e &\equiv H_v \\
v^h &\equiv +M_u & v^e &\equiv -M_v + \frac{k_p}{\omega\epsilon} J_z \\
i^h &\equiv -J_v - \frac{k_p}{\omega\mu} M_z & i^e &\equiv -J_u \\
Z^h &\equiv \frac{\omega\mu}{\zeta} & Z^e &\equiv \frac{\zeta}{\omega\epsilon}
\end{aligned}
\tag{2.6a}$$

Note that v, i are here generators in the transmission line model [the free term in (2.5)] and this v should not be confused with the planewave coordinate v .

From (2.3), the vertical components (H_z, E_z) are given in terms of the transmission line parameters:

$$H_z = \frac{1}{j\omega\mu} (+jk_p V^h - M_z) \tag{2.7a}$$

$$E_z = \frac{1}{j\omega\epsilon} (-jk_p I^e - J_z) \tag{2.7b}$$

Naturally $k_p^2 + \zeta^2 = k^2 = \omega^2\mu\epsilon$ (cf fig. 2.2). If the medium is bounded at z_{inf} and/or z_{sup} by isotropic boundary conditions [36, §5.7]

$$\hat{\mathbf{z}} \times Z_s \mathbf{H} = \hat{\mathbf{z}} \times (\mathbf{E} \times \pm \hat{\mathbf{z}}) \tag{2.8a}$$

with the sign above for z_{inf} , the equivalent transmission line model condition may be obtained from (2.6) as

$$\begin{aligned}
Z_s I^e &= \mp V^e \\
Z_s I^h &= \mp V^h
\end{aligned}
\tag{2.8b}$$

This transmission line model is the same as that in [78, §III]. A notable alternative is offered by [87, §9-10], where the role of the vertical component and the transversal component of the fields is reversed in the derivation, ie, the latter are expressed in terms of the first [cf with (2.7)]. However, the final expressions differ only in the choice of constants, and they are not obtained as straightforwardly as here.

2.2 Solution for elementary sources

In §2.1, it has been shown how to obtain the field components produced by sources that satisfy the separability conditions (2.2); they are given by (2.6) and (2.7) after solving twice the transmission line equations (2.5), once with TE parameters (2.6a) and again with TM parameters (2.6b). If the sources are not eigenfunctions, then they are written as a superposition of them, the pair (2.5), (2.6) is solved for each term, and the total field is recovered again from superposition. The required expression is the two-dimensional Fourier transform [36, §5.2], [62, §7.1]

$$f(\mathbf{p}, z) = \frac{1}{(2\pi)^2} \iint_{\infty^2} F(\mathbf{k}_p, z) e^{-j\mathbf{k}_p \cdot \mathbf{p}} d\xi d\eta \tag{2.9a}$$

$$F(\mathbf{k}_p, z) = \iint_{\infty^2} f(\mathbf{p}, z) e^{+j\mathbf{k}_p \cdot \mathbf{p}} dx dy \tag{2.9b}$$

For example, a concentrated source $\mathbf{J}(\mathbf{r}) = \hat{\mathbf{z}}\delta(\mathbf{r} - \mathbf{r}')$ can be written as

$$\hat{\mathbf{z}}\delta(z - z')e^{+j\mathbf{k}_p \cdot \mathbf{p}'} = \iint_{\infty^2} \hat{\mathbf{z}}\delta(\mathbf{r} - \mathbf{r}')e^{+j\mathbf{k}_p \cdot \mathbf{p}} dx dy \quad (2.10)$$

In the transmission line model, this source becomes a generator [cf (2.6b)]

$$v^e = \frac{k_p}{\omega\epsilon} \delta(z - z')e^{+j\mathbf{k}_p \cdot \mathbf{p}'} \quad (2.11)$$

and if substituted into (2.7b), we obtain, after solving (2.5) for I^e and using (2.9a),

$$\begin{aligned} E_{zz}^J(\mathbf{r}, \mathbf{r}') &\equiv E_z(\mathbf{J} = \hat{\mathbf{z}}\delta(\mathbf{r} - \mathbf{r}') \text{ and } \mathbf{M} = 0) \\ &= \frac{1}{(2\pi)^2} \iint_{\infty^2} \left[\frac{1}{j\omega\epsilon} \left(-j \frac{k_p^2}{\omega\epsilon'} I^e - \delta(z - z') \right) \right] e^{-j\mathbf{k}_p \cdot (\mathbf{p} - \mathbf{p}')} d\xi d\eta \end{aligned} \quad (2.12)$$

and so forth for the other components of the Green's dyadics $\bar{\bar{E}}^J$, $\bar{\bar{E}}^M$, $\bar{\bar{H}}^J$ and $\bar{\bar{H}}^M$. The term inside square brackets in (2.12) is called the *spectral* Green's function. It has been shown that this is no more than a planewave field with implicit $e^{-jk_p u}$ dependence. (The Green's function has evident translational symmetry

$$G(\mathbf{p}, \mathbf{p}', z, z') = G(\mathbf{p} - \mathbf{p}', 0, z, z')$$

so the factor $e^{+j\mathbf{k}_p \cdot \mathbf{p}'}$ is not taken as part of the spectral function; in other words, the sources are always supposed to be placed at $\mathbf{p}' = 0$.) The whole lot of spectral Green's dyadics is listed in [78, (28-31)]; a table with all the cartesian components can be found in [45, p. 157] or [87, §11].

2.3 Potentials

The magnetic vector potential is computed from its definition $\mu\mathbf{H} = \text{curl } \mathbf{A}$; taking for \mathbf{H} the spectral Green's function $\bar{\bar{H}}^J$ [78, (29)]

$$\bar{\bar{H}}^J = \hat{\mathbf{u}}\hat{\mathbf{v}}I_i^h - \hat{\mathbf{v}}\hat{\mathbf{u}}I_i^e - \hat{\mathbf{z}}\hat{\mathbf{v}}\frac{k_p}{\omega\mu}V_i^h + \hat{\mathbf{v}}\hat{\mathbf{z}}\frac{k_p}{\omega\epsilon'}I_v^e, \quad (2.13)$$

making use of (2.2) on $\text{curl } \mathbf{A}$ and equating components for each orientation of the source,

$$-\mu I_i^e = \frac{\partial A_{uu}}{\partial z} + jk_p A_{zu} \quad (2.14a)$$

$$\hat{\mathbf{u}}\mu I_i^h - \hat{\mathbf{z}}\frac{k_p}{\omega}V_i^h = -\hat{\mathbf{u}}\frac{\partial A_{vv}}{\partial z} - \hat{\mathbf{z}}jk_p A_{vv} \quad (2.14b)$$

$$\frac{\mu k_p}{\omega\epsilon'} I_v^e = \frac{\partial A_{uz}}{\partial z} + jk_p A_{zz} \quad (2.14c)$$

The only certainty given by these equations is

$$A_{vv} = \frac{V_i^h}{j\omega}, \quad (2.15a)$$

which is given twice by (2.14b), once directly and again through (2.5a). To obtain the other components it is necessary to make choices. *Sommerfeld's choice* [126, §33 (2)] produces the simplest possible dyadic $\bar{\bar{A}}$:

- A_{uu} is set equal to A_{vv} .
- A_{vz} and A_{zv} are set to zero [they do not appear in (2.14) at all].
- A_{uz} is set to zero.

With this, and substituting (2.15a) in (2.14a)

$$A_{zu} = \frac{\mu}{jk_p}(I_i^h - I_i^e) \quad (2.15b)$$

and from (2.14c),

$$A_{zz} = \frac{\mu}{j\omega\epsilon'} I_v^e \quad (2.15c)$$

The Lorenz gauge gives the scalar potential

$$-j\omega\mu\epsilon\Phi = \operatorname{div} \mathbf{A} \quad (2.16a)$$

and its Green's function is defined in a homogeneous medium by

$$\Phi = G^\Phi * \frac{-\operatorname{div}' \mathbf{J}}{j\omega} \quad (2.16b)$$

Therefore it would be natural to define

$$\frac{1}{\mu\epsilon} \operatorname{div} \mathbf{A} = G^\Phi * \operatorname{div}' \mathbf{J} \quad (2.16c)$$

It is apparent that, with the choice of \bar{A} given by (2.15), G^Φ cannot be independent of the orientation of \mathbf{J} , in other words, G^Φ cannot be a scalar. We shall abide by that choice, and would write (cf [21, §II.B]),

$$\frac{1}{\mu\epsilon} \operatorname{div} \bar{A} * \mathbf{J} = \bar{\Phi} * \operatorname{grad}' \mathbf{J} \quad (2.17)$$

To obtain a relationship between \bar{A} and $\bar{\Phi}$ it is necessary to factor out the dependence on the source. Integration by parts on (2.17) yields

$$\frac{1}{\mu\epsilon} \operatorname{div} \bar{A} * \mathbf{J} = \int_{\partial V'} (\bar{\Phi} \cdot \mathbf{J}) \cdot \hat{\mathbf{n}} - (\operatorname{div}' \bar{\Phi}) * \mathbf{J} \quad (2.18)$$

At this stage it would be difficult to say whether the boundary integral vanishes or not. In fact, as it will be seen during the development of the various integral equations, it does not, at least it does not unless the medium is homogeneous. Therefore it will prove better to follow [80, (12)], [21, (6)], put (2.17) aside, *define* instead the scalar potential Green's function by

$$\frac{1}{\mu\epsilon} \operatorname{div} \bar{A} = -\operatorname{div}' \bar{\Phi} \quad (2.19)$$

and leave the boundary integral for later (§3.2). (2.19) furnishes at most three scalar conditions on $\bar{\Phi}$. Therefore the form $\bar{\Phi} = \Phi_u \hat{\mathbf{u}}\hat{\mathbf{u}} + \Phi_v \hat{\mathbf{v}}\hat{\mathbf{v}} + \Phi_z \hat{\mathbf{z}}\hat{\mathbf{z}}$ is postulated. Equating u components in (2.19) produces

$$-jk_p A_{uu} + \frac{\partial A_{zu}}{\partial z} = +j\mu\epsilon k_p \Phi_u \quad (2.20a)$$

wherefrom substitution of (2.15) and application of (2.5) gives

$$\Phi_u = \frac{j\omega}{k_p^2} (V_i^e - V_i^h) \quad (2.20b)$$

Equating v components in (2.19) gives $0 = 0$, so we naturally decide in favor of $\Phi_v = \Phi_u$. Last, equating z components,

$$\frac{1}{j\omega\epsilon\epsilon'} \frac{\partial I_v^e}{\partial z} = -\frac{\partial \Phi_z}{\partial z'} \quad (2.20c)$$

Using (2.5b) in (2.20c)

$$\frac{\partial \Phi_z}{\partial z'} = \frac{1}{\epsilon'} V_v^e \quad (2.20d)$$

Now $V_v(z, z') = -I_i(z', z)$ by circuit-level reciprocity [cf (2.31)]. Also, on the exchange $z \leftrightarrow z'$, (2.5a) reads

$$\frac{\partial V_i^e(z', z)}{\partial z'} = -\frac{j\zeta'^2}{\omega\epsilon'} I_i^e(z', z) \quad (2.20e)$$

Comparing (2.20d) to (2.20e), and using again circuit-level reciprocity $V_i(z, z') = V_i(z', z)$ [80, (32)]

$$\Phi_z = \frac{\omega}{j\zeta'^2} V_i^e \quad (2.20f)$$

To conclude this section, a table has been prepared (table 2.1) with the spectral potential Green's functions. The dual of (2.13), viz [78, (30)]

$$\bar{E}^M = -\hat{\mathbf{u}}\hat{\mathbf{v}}V_v^e + \hat{\mathbf{v}}\hat{\mathbf{u}}V_v^h + \hat{\mathbf{z}}\hat{\mathbf{v}}\frac{k_p}{\omega\epsilon}I_v^e - \hat{\mathbf{v}}\hat{\mathbf{z}}\frac{k_p}{\omega\epsilon'}V_i^h, \quad (2.21)$$

that will be used in later chapters, has also been included.

Two steps remain to arrive at the Green's functions for layered media. The first is the solution of the transmission line model. This is addressed in §2.4 ff. The second is the computation of the numerical inversion (2.9a), so that the Green's functions can be used in a spatial-domain method of moments formulation. This is addressed in §2.7.

2.4 Transmission line Green's functions

Here we shall only be concerned with piecewise constant $\epsilon(z), \mu(z)$, therefore piecewise constant $\zeta(z), Z(z)$ in (2.5). A (rather large) number of algorithms has been published to solve the problem of finding V and I at an arbitrary point z of the TL structure, when a generator (voltage or current) is placed at another arbitrary point z' , that is, the solution of (2.5) when v or $i = \delta(z - z')$. These are the four transmission line Green's functions (TLGF's),

$$\begin{array}{ll} V_i(z, z') & V_v(z, z') \\ I_v(z, z') & I_i(z, z') \end{array} \quad (2.22)$$

Actually some researchers do not work with parameters V and I as we have defined them in the TL model [78, §IV] or the 'modal network representation' [36, §2.4] ('modal' meaning 'spectral'). Instead they handle directly the fields (the matrix method in [142, §4.11, 4.13] and [86, §4.1]; also [22, §2]). In either case the results are comparable. The problem with expressions such

| <i>component</i> | <i>TL expression</i> | <i>reference</i> |
|-------------------|--|------------------|
| <i>potentials</i> | | |
| A_{uu} | $\frac{V_i^h}{j\omega}$ | (2.15a) |
| A_{zu} | $\frac{\mu}{jk_p}(I_i^h - I_i^e)$ | (2.15b) |
| A_{zz} | $\frac{\mu}{j\omega\epsilon'}I_v^e$ | (2.15c) |
| Φ_u | $\frac{j\omega}{k_p^2}(V_i^e - V_i^h)$ | (2.20b) |
| Φ_z | $\frac{\omega}{j\zeta'^2}V_i^e$ | (2.20f) |
| <i>fields</i> | | |
| E_{uv}^M | $-V_v^e$ | (2.21) |
| E_{vu}^M | $+V_v^h$ | (2.21) |
| E_{zv}^M | $+\frac{k_p}{\omega\epsilon'}I_v^e$ | (2.21) |
| E_{vz}^M | $-\frac{k_p}{\omega\epsilon'}V_i^h$ | (2.21) |

Table 2.1: Field and potential spectral Green's functions to be used in this work.

as [78, (67)] is that, although they do indeed provide an excellent way to compute the TLGF's for *fixed* z, z' , they fall short when trying to manipulate analytically the dependence on z, z' . Only when z and z' are in the same layer is this dependence made readily apparent [78, (66)]. Similarly, the expressions of [57, Appendix] are restricted to the same-layer case, which is noteworthy because the (otherwise truly excellent) work developed in that paper explicitly requires TLGF's 'cast into a specific form, where z and z' dependences are factored out'.

On the other hand, the algorithm given in [24] cleanly factors out these dependences in every case; but it would be desirable to have simple, easy-to-use, plainly stated expressions for every TLGF. Even if these expressions can indeed be obtained from that work, it is only after some digging.

Therefore this section is devoted to the development of a direct and complete solution of the TL model where z and z' dependences are factored out in the simplest possible way for *any* position of z and z' . The pertinent notation is given in the following table.

| <i>symbol</i> | <i>meaning</i> |
|---|--|
| γ, γ' | propagation constants [$j\zeta(z), j\zeta(z')$ in (2.5)] |
| i, i' | indices of observer and source layers |
| z, z' | relative to bottom of layer unless obviously not |
| h, h' | layer thicknesses |
| Z, Z' | characteristic impedances of layer |
| Y, Y' | characteristic admittances of layer |
| \vec{Z}, \vec{Z} | impedances looking up (from top of layer) |
| $\overleftarrow{Z}, \overleftarrow{Z}$ | idem looking down (from bottom of layer) |
| $\vec{\Gamma}, \vec{\Gamma}'$ | wave reflection coefficient looking up (from top of layer) |
| $\overleftarrow{\Gamma}, \overleftarrow{\Gamma}'$ | idem looking down (from bottom of layer) |
| I_g | strength of current source |
| V_g | strength of voltage source |

Table 2.2: Notation for the TL model (§2.4).

I define wave coefficients according to [24]. These do *not* represent incident or reflected power (for those which do, see eg [61]).

$$\begin{aligned} V &= a + b \\ ZI &= a - b \end{aligned} \quad (2.23a) \quad \begin{aligned} a &= V/2 + ZI/2 \\ b &= V/2 - ZI/2 \end{aligned} \quad (2.23b)$$

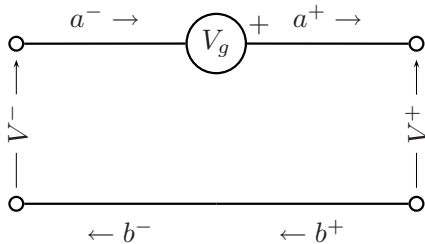
Consequently,

$$\vec{\Gamma}_i = \frac{\vec{Z}_{i+1} - Z_i}{\vec{Z}_{i+1} + Z_i} \quad (2.24a) \quad \overleftarrow{\Gamma}_i = \frac{\overleftarrow{Z}_{i-1} - Z_i}{\overleftarrow{Z}_{i-1} + Z_i} \quad (2.24b)$$

save for $\overleftarrow{\Gamma}_0$ and $\vec{\Gamma}_{n-1}$, which are given by (2.8b); clearly, $\overleftarrow{\Gamma}_0$ or $\vec{\Gamma}_{n-1}$ are zero if the medium is unbounded in that direction.

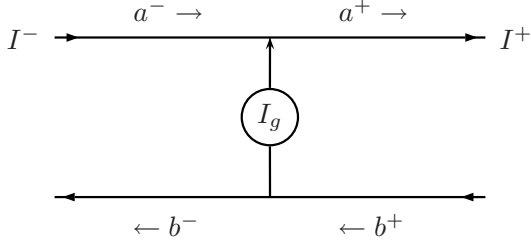
$$\vec{\Gamma}_{n-1} = \frac{Z_{s, \sup} - Z_{n-1}}{Z_{s, \sup} + Z_{n-1}} \quad (2.24c) \quad \overleftarrow{\Gamma}_0 = \frac{Z_{s, \inf} - Z_0}{Z_{s, \inf} + Z_0} \quad (2.24d)$$

Voltage and current generators induce discontinuities in the wave coefficients as follows. Note that the sign of the discontinuity induced by a current generator depends on the direction of the waves.



$$\begin{aligned} a^- + b^- &= a^+ + b^+ - V_g \\ a^- - b^- &= a^+ - b^+ \end{aligned} \quad (2.25a)$$

$$\begin{aligned} a^+ &= a^- + V_g/2 \\ b^+ &= b^- + V_g/2 \end{aligned} \quad (2.25b)$$



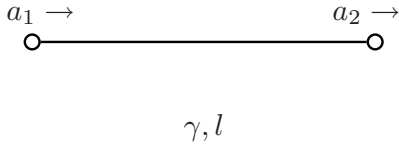
$$\begin{aligned} a^- + b^- &= a^+ + b^+ \\ a^- - b^- &= a^+ - b^+ - Z' I_g \end{aligned} \quad (2.26a)$$

$$\begin{aligned} a^+ &= a^- + Z' I_g / 2 \\ b^+ &= b^- - Z' I_g / 2 \end{aligned} \quad (2.26b)$$

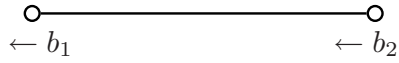
Two source parameters s, s' are defined by:

$$\left. \begin{aligned} s &= +V_g/2 \\ s' &= +V_g/2 \end{aligned} \right\} \text{ for a voltage source} \quad \left. \begin{aligned} s &= +Z' I_g/2 \\ s' &= -Z' I_g/2 \end{aligned} \right\} \text{ for a current source} \quad (2.27)$$

The wave coefficients travel along a constant-parameter transmission line section according to

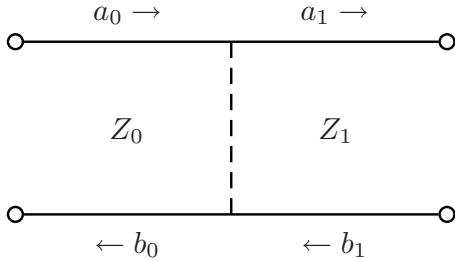


$$\begin{bmatrix} a_1 \\ b_1 \end{bmatrix} = T \begin{bmatrix} a_2 \\ b_2 \end{bmatrix} \quad (2.28a)$$



$$T = \begin{bmatrix} e^{+\gamma l} & 0 \\ 0 & e^{-\gamma l} \end{bmatrix} \quad (2.28b)$$

and cross layers (cf [24, (8-9)]) according to



$$\begin{bmatrix} a_0 \\ b_0 \end{bmatrix} = T(0 \leftarrow 1) \begin{bmatrix} a_1 \\ b_1 \end{bmatrix} \quad (2.29a)$$

$$T(0 \leftarrow 1) = \frac{1}{2} \begin{bmatrix} 1 + \frac{Z_0}{Z_1} & 1 - \frac{Z_0}{Z_1} \\ 1 - \frac{Z_0}{Z_1} & 1 + \frac{Z_0}{Z_1} \end{bmatrix} \quad (2.29b)$$

(2.29b) comes from using (2.23a) with $Z \rightarrow Z_1$ and then (2.23b) with $Z \rightarrow Z_0$. From (2.28)

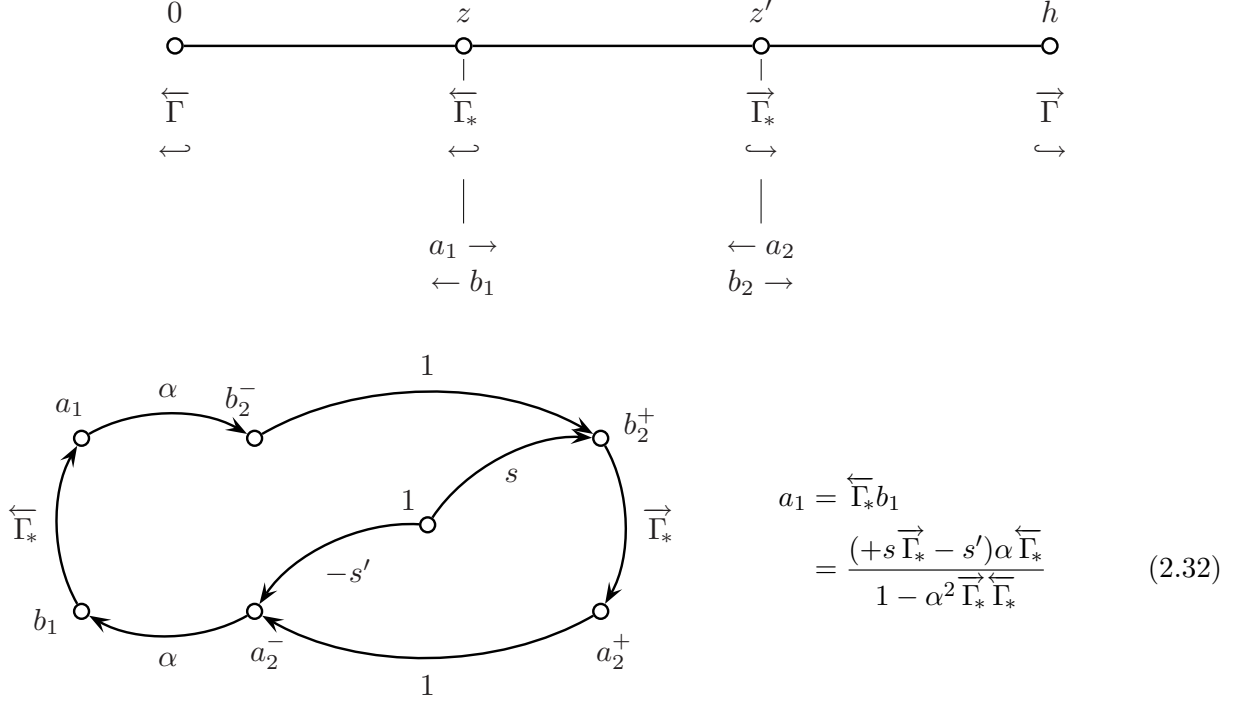
$$\vec{\Gamma}_i(0) = \vec{\Gamma} e^{-2\gamma h} \quad \overleftarrow{\Gamma}_i(h) = \overleftarrow{\Gamma} e^{-2\gamma h} \quad (2.30)$$

It is assumed that $z' > z$; the other case will be obtained at the end of this development by application of the reciprocity properties [84, ch. 2], [78, (24)]

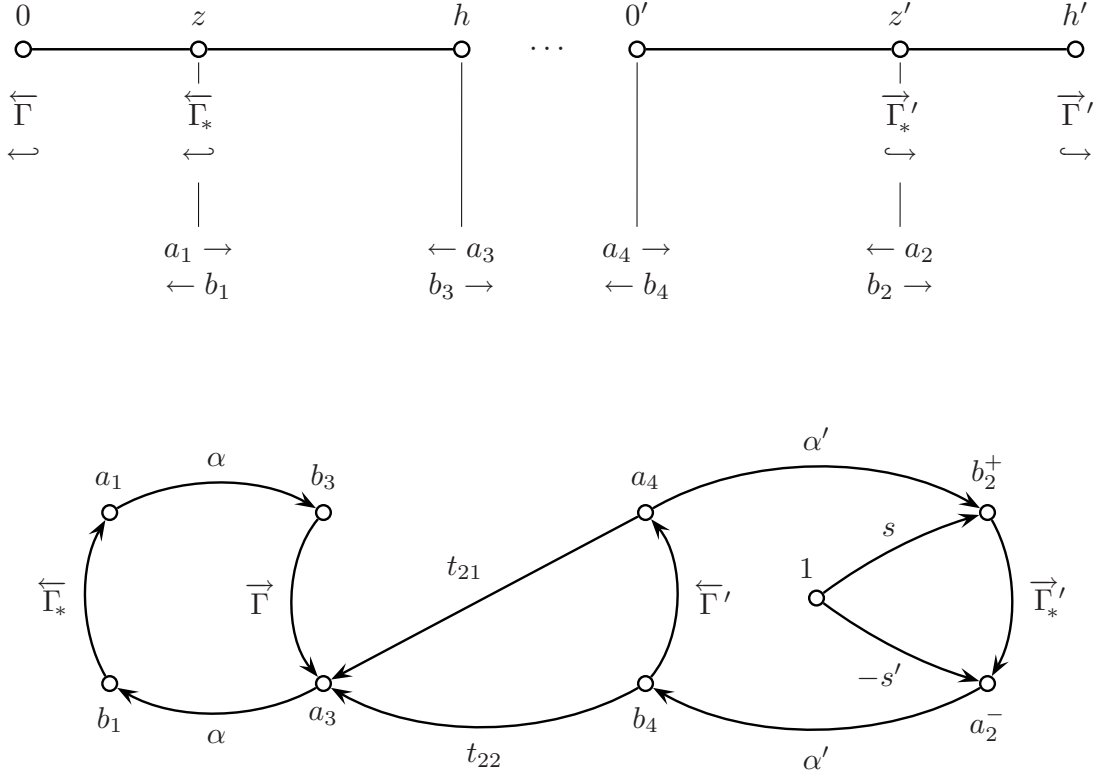
$$\begin{aligned} V_i(z, z') &= V_i(z', z) & V_v(z, z') &= -I_i(z', z) \\ I_v(z, z') &= I_v(z', z) & I_i(z, z') &= -V_v(z', z) \end{aligned} \quad (2.31)$$

In what follows, z and z' are taken relative to the base of their layers.

If source and observer are in the same layer, the wave coefficients at the observer can be related to the wave coefficients at the source by [with $\alpha = e^{-\gamma(z'-z)}$, $\overleftarrow{\Gamma}_* = \overleftarrow{\Gamma} e^{-2\gamma z}$, $\vec{\Gamma}_* = \vec{\Gamma} e^{-2\gamma(h-z')}$]:



If source and observer are in different layers, the wave coefficients at the observer are related to the wave coefficients at the closest boundary layer above, and the wave coefficients at the source are related to the wave coefficients at the closest boundary layer below. These are then linked together with (2.28) and (2.29). Here $\alpha = e^{-\gamma(h-z)}$, $\alpha' = e^{-\gamma'z'}$, $\overleftarrow{\Gamma}_* = \overleftarrow{\Gamma} e^{-2\gamma z}$ and $\overrightarrow{\Gamma}' = \overrightarrow{\Gamma}' e^{-2\gamma'(h'-z')}$. The relationship between a_2^\pm and b_2^\pm is similar to that of (2.32) and it has already been simplified in the following graph.



The source and observer sections can be solved separately.

$$a_4 = \overleftarrow{\Gamma}' b_4 = \frac{+s \overrightarrow{\Gamma}' \alpha' \overleftarrow{\Gamma}' - s' \alpha' \overleftarrow{\Gamma}'}{1 - (\alpha')^2 \overrightarrow{\Gamma}' \overleftarrow{\Gamma}'} \quad (2.33a)$$

$$\begin{bmatrix} b_3 \\ a_3 \end{bmatrix} = \begin{bmatrix} t_{11} & t_{12} \\ t_{21} & t_{22} \end{bmatrix} \begin{bmatrix} a_4 \\ b_4 \end{bmatrix} \quad (2.33b)$$

$$\begin{bmatrix} t_{11} & t_{12} \\ t_{21} & t_{22} \end{bmatrix} = T(i \leftarrow i+1) \prod_{j=i+1}^{i'-1} T_j T(j \leftarrow j+1) \quad (2.33c)$$

$$a_1 = \overleftarrow{\Gamma}_* b_1 = \overleftarrow{\Gamma}_* \alpha a_3 \quad (2.33d)$$

Putting together (2.32) and (2.33), we arrive at $\{a(z, z'), b(z, z')\} \equiv \{a_1, b_1\}$.

$$q_{ii'} \equiv \begin{cases} \frac{1}{1 - \overleftarrow{\Gamma}' \overrightarrow{\Gamma}' e^{-2\gamma' h'}}, & i = i' \\ \frac{e^{-\gamma h} (t_{21} \overleftarrow{\Gamma}' + t_{22})}{1 - \overleftarrow{\Gamma}' \overrightarrow{\Gamma}' e^{-2\gamma' h'}}, & i \neq i' \end{cases} \quad (2.34a)$$

$$\begin{aligned} A_{ii'} &\equiv q_{ii'} \overrightarrow{\Gamma}' e^{-2\gamma' h'} \\ B_{ii'} &\equiv q_{ii'} \\ C_{ii'} &\equiv q_{ii'} \overrightarrow{\Gamma}' \overleftarrow{\Gamma}' e^{-2\gamma' h'} \\ D_{ii'} &\equiv q_{ii'} \overleftarrow{\Gamma}' \end{aligned} \quad (2.34b)$$

$$\begin{aligned} a(z, z') &= s C_{ii'} e^{-\gamma z + \gamma' z'} - s' D_{ii'} e^{-\gamma z - \gamma' z'} \\ b(z, z') &= s A_{ii'} e^{+\gamma z + \gamma' z'} - s' B_{ii'} e^{+\gamma z - \gamma' z'} \end{aligned} \quad (2.34c)$$

An interpretation of the meaning of coefficients $\{A, B, C, D\}$ is given later on another context (fig.2.5). Basically, A and B are waves that come from above to the observer, and C and D , that come from below. The direct wave is contained in B , because the source is assumed to be above the observer.

The transmission line Green's functions may now be obtained, using (2.27) in (2.34c) and the result in (2.23a). The final expressions are $[V_g = I_g = 1, (\text{absolute}) z < z', e^{\sigma\sigma'} \equiv e^{\sigma\gamma z + \sigma'\gamma' z'}]$:

$$\begin{aligned} V_i(z, z') &= \frac{Z'}{2} (+C_{ii'} e^{-+} + D_{ii'} e^{--} + A_{ii'} e^{++} + B_{ii'} e^{+-}) \\ I_v(z, z') &= \frac{1}{2Z} (+C_{ii'} e^{-+} - D_{ii'} e^{--} - A_{ii'} e^{++} + B_{ii'} e^{+-}) \\ V_v(z, z') &= \frac{1}{2} (+C_{ii'} e^{-+} - D_{ii'} e^{--} + A_{ii'} e^{++} - B_{ii'} e^{+-}) \\ I_i(z, z') &= \frac{Z'}{2Z} (+C_{ii'} e^{-+} + D_{ii'} e^{--} - A_{ii'} e^{++} - B_{ii'} e^{+-}) \end{aligned} \quad (2.35a)$$

Application of (2.31) gives the TLGFs for (absolute) $z > z'$. Here it is important to remember that i, Z and γ are functions of absolute z , so the exchange of absolute z and absolute z' implies

not only $z \leftrightarrow z'$ but also $i \leftrightarrow i'$, $\gamma \leftrightarrow \gamma'$ and $Z \leftrightarrow Z'$.

$$\begin{aligned}
V_i(z, z') &= \frac{Z}{2} (+C_{i'i}e^{+-} + D_{i'i}e^{--} + A_{i'i}e^{++} + B_{i'i}e^{-+}) \\
I_v(z, z') &= \frac{1}{2Z'} (+C_{i'i}e^{+-} - D_{i'i}e^{--} - A_{i'i}e^{++} + B_{i'i}e^{-+}) \\
V_v(z, z') &= \frac{Z}{2Z'} (-C_{i'i}e^{+-} - D_{i'i}e^{--} + A_{i'i}e^{++} + B_{i'i}e^{-+}) \\
I_i(z, z') &= \frac{1}{2} (-C_{i'i}e^{+-} + D_{i'i}e^{--} - A_{i'i}e^{++} + B_{i'i}e^{-+})
\end{aligned} \tag{2.35b}$$

Coefficients $\{A, B, C, D\}$ depend only on f (frequency), k_p , and the layer indices i, i' . (From (2.35) we see that the case $i > i'$ need never be considered.) Therefore the most efficient procedure for the computation of the spectral Green's functions is (in the order given)

P1 Outline of computation of Green's functions

1. Find the layers $\{i\}$ where the levels $\{z\}$ of the functions to be computed are located; also, note if any of the $\{z\}$ falls exactly on a dielectric interface.
2. Select f and normalize the physical dimensions h_i and $\{z\}$.
3. Select P (skip if the spatial Green's functions are not required). The Fourier inversion is performed at this step on each of the spectral Green's functions computed below. The required inversion formulae depend on the azimuthal variation of the particular Green's function and are given in P21 on page 131. Details on the numerical inversion are given in §2.7.
4. Select k_p .
 - (a) Compute the layer parameters: $\gamma_i, Z_i, \vec{\Gamma}_i, \overleftarrow{\Gamma}_i$. All of them ($i = 0..n_l-1$) are necessary, even if the structure is confined to a single layer.
 - (b) Compute $\{A, B, C, D\}_{ii'}$ for all i, i' with $0 \leq i \leq i' < n_l$. This step, which consists essentially in the application of (2.33c), is the most expensive, its complexity (to the first order) being $\sim O(n^2)$. Naturally if the structure to be analyzed does not span all layers, a restricted set of $\{A, B, C, D\}_{ii'}$ may be computed.
5. For each required pair (z, z') , compute the transmission line Green's functions using (2.35).
6. Finally, obtain the spectral Green's functions [the kernels $F(k_p, z, z')$ in (2.9)] as explained in §2.2, or using tables 2.1, [45, 6.1, p.157 and 6.2, p.169] or [78, (28–31) and (52–57)] or [87, (54–57, 77)].

The idea behind this arrangement is to avoid as much as possible the solution of the transmission line problem (step 4) by moving the computations that depend of z, z' to the innermost loop.

2.5 Integrated transmission line Green's functions

With equations (2.35) and the recipe given in P1, the computation of the spectral Green's functions seems to be over. However, when we deal with a structure with vertical components, it will be necessary to compute the Green's functions at many points in both z and z' . Although the order of the steps in P1 has been chosen precisely to maintain efficiency in that case, a still better possibility exists, namely, to make use of the analytical dependence of the Green's

functions on z, z' , which is evident in 2.35, and to produce new Green's functions where the dependence on z, z' has been eliminated. That is the purpose of this section.

A generic (spatial domain) field integral using the Green's functions computed in the last section is

$$\mathbf{F} = \bar{\bar{G}} * \mathbf{B} = \int_{V'} d\mathbf{r}' \bar{\bar{G}}(\mathbf{r}, \mathbf{r}') \cdot \mathbf{B}(\mathbf{r}')$$

where \mathbf{B} is one of the basis functions used to expand the current distribution; they are described in §1.6. The Green's function is to be computed from a spectral representation; thus, from (2.9)

$$= \frac{1}{(2\pi)^2} \int_{V'} d\mathbf{r}' \mathbf{B} \cdot \int d\mathbf{k}_p \bar{\bar{g}}^T(\mathbf{k}_p, z, z') e^{-j\mathbf{k}_p \cdot \mathbf{P}} \quad (2.36a)$$

This field is to be tested against another current distribution \mathbf{T} ; the full (still generic) expression is

$$\begin{aligned} \langle \mathbf{T}, \mathbf{F} \rangle &= \int_V d\mathbf{r} \mathbf{T}(\mathbf{r}) \cdot \mathbf{F}(\mathbf{r}) \\ &= \frac{1}{(2\pi)^2} \underbrace{\int_V d\mathbf{r} \mathbf{T} \cdot \int_{V'} d\mathbf{r}' \mathbf{B}}_{\text{spatial part}} \cdot \underbrace{\int d\mathbf{k}_p \bar{\bar{g}}^T(\mathbf{k}_p, z, z') e^{-j\mathbf{k}_p \cdot \mathbf{P}}}_{\text{spectral part}} \end{aligned} \quad (2.36b)$$

(2.36b) is representative not only of the form of full reaction terms, but also of potential terms and of each of their (eg cartesian) components separately. It is certainly not necessary to insist on the cost and difficulty of computing (2.36b) and in fact a sizeable portion of this dissertation will be devoted to dissect various sorts of (2.36b). We begin by looking at some means of general simplification.

In free space the Green's function is available in closed form. It is tempting to try and work in stratified media on the same principle, that is, to have $\bar{\bar{G}}$ readily available at any required $(\mathbf{r}, \mathbf{r}')$. Direct inversion of the spectral Green's function is extremely time consuming (§2.7), so on-demand computation of the spectral part of (2.36b) is out the question. There are only two sensible approaches:

- To develop an approximation of $\bar{\bar{G}}$ that is more amenable to repeated computation. Depending on the type of approximation, we have rational function expansion for the spectral part [94, 95], plane wave expansions [9] and, last and foremost, the popular method of complex images [5, 23, 25, 29, 34, 57, 77, 135]. The issues with these approaches are the validity of the approximation for varying parameters (type of substrate, say, thin layer vs thick layer; distance source-observer; frequency) or different Green's functions (for electric/magnetic sources/fields; for horizontal/vertical sources/fields). We see this clearly in the history of the method: the first articles dealt only with horizontal dipoles and thin layers, and broke down in other cases; the present incarnation is a quite general and quite complicated procedure. Besides, some precise knowledge of the Green's function that has to be approximated is usually required: the exact form of the quasistatic part and the location of the poles of the modal representation. While some of this information is useful later, in the computation of the spatial integrals (ie the quasistatic part), most of it is not.
- To compute a table of $\bar{\bar{G}}$ at some (well chosen) points $(\mathbf{r}_i, \mathbf{r}_j)$ and later, during the computation of the spatial part of (2.36b), to interpolate into this table. Because the

table can be reused with different structures, the initial cost of computing it may become negligible, particularly in applications where many related structures must be analyzed (eg optimization of circuit/antenna dimensions).

The compute-tables-and-interpolate technique was fairly popular back when the analysis of 3D structures was not well developed; for example, because of the symmetry of the Green's functions, the analysis of a coax-fed planar microstrip patch only required (and requires, of course) a couple of one-dimensional tables and some extra values for the (cleverly approximated) interactions in the excitation region [92].

But a general 3D structure needs 3D tables, because every spatial Green's function depends on three coordinates, $\bar{G} \equiv \bar{G}(P, z, z')$. Not only the size of the tables grows appreciably: 3D lookup and interpolation is also more costly, and, because of the behaviour of the Green's function across layers or whenever z and z' cross, the interpolation grid in z and z' has to be chosen with particular care. Notwithstanding, this is the only truly general technique, and it has been implemented with success [32], [20].

The path taken in this work, however, is to realize that the factorization of the TLGF's (2.35) makes it possible to change the order of the integrations in (2.36b). Assuming that z and z' remain within the same layer, any spectral Green's function component g is a sum of up to four terms

$$g(\mathbf{k}_p, z, z') = L_A e_A + L_B e_B + L_C e_C + L_D e_D \quad (2.37a)$$

where $L_X(\mathbf{k}_p)$ contains precisely one of $\{A, B, C, D\}$ as a factor (these depend on \mathbf{k}_p only through k_p), and the $e_X(k_p, z, z')$ are the exponential functions

$$\begin{aligned} e_A &= e^{+\gamma z + \gamma' z'} & e_C &= e^{\sigma(-\gamma z + \gamma' z')} \\ e_B &= e^{\sigma(+\gamma z - \gamma' z')} & e_D &= e^{-\gamma z - \gamma' z'} \end{aligned} \quad (2.37b)$$

if z and z' are in different layers ($i \neq i'$; $\sigma = \text{sgn } i' - i$), or of

$$\begin{aligned} e_A &= e^{+\gamma(z+z')} & e_C &= e^{+\gamma|z-z'|} \\ e_B &= e^{-\gamma|z-z'|} & e_{C'} &= \text{sgn}(z - z') e^{+\gamma|z-z'|} \\ e_{B'} &= \text{sgn}(z - z') e^{-\gamma|z-z'|} & e_D &= e^{-\gamma(z+z')} \end{aligned} \quad (2.37c)$$

if z and z' are in the same layer ($i = i'$); the functions $e_{B'}$ and $e_{C'}$ are needed in V_v and I_i , whose terms with B_{ii} and C_{ii} change sign from (2.35a) to (2.35b). By definition, these two functions must be discontinuous at the source, ie when $z = z'$.

Now comes the justification for the '2.5D' in the title of this work: if the test \mathbf{T} and source \mathbf{B} functions are *separable*, ie, if they have components whose vertical and horizontal dependences are separable:

$$T(\mathbf{r}) = T_z(z) T_p(\mathbf{p}) \quad B(\mathbf{r}') = B_z(z') B_p(\mathbf{p}') \quad (2.38)$$

then, upon introduction of (2.37a) into (2.36b), we obtain terms like

$$\begin{aligned} & \frac{1}{(2\pi)^2} \int_V d\mathbf{r} T \int_{V'} d\mathbf{r}' B \int d\mathbf{k}_p e^{-j\mathbf{k}_p \cdot \mathbf{P}} L_X(\mathbf{k}_p) e_X(k_p, z, z') \\ &= \underbrace{\frac{1}{(2\pi)^2} \int_S d\mathbf{p} T_p \int_{S'} d\mathbf{p}' B_p \int d\mathbf{k}_p e^{-j\mathbf{k}_p \cdot \mathbf{P}} L_X(\mathbf{k}_p)}_{\text{spatial part}} \underbrace{\int_\tau dz T_z \int_{\tau'} dz' B_z e_X(k_p, z, z')}_{\text{spectral part}} \end{aligned} \quad (2.39)$$

where τ, τ' designate the vertical domains (z_0, z_1) and (z'_0, z'_1) of, respectively, T and B . These τ, τ' will hereafter be called *slices* (there is, to my knowledge, at least one precedent for this designation, [35, §II]). In (2.39), as it happens, the following has been accomplished:

P2 Advantages of z -integration in the spectral domain

1. The dimension of the spatial domain integrations has been reduced. (2.39) shows the case of volume source and test functions, where this reduction always takes place. (It will not if neither T or B do depend on z, z , as it happens, for example, in the interaction between two horizontal surface patches.) The advantages of an integral of reduced dimension should be obvious from a computational point of view, both the range of numerical techniques available and in the faster calculation.
2. If the spectral part of (2.39) is precomputed and stored in tables, there will be one such table for each pair (τ, τ') . Within this table, only 1D interpolation (in P) is necessary to compute the spatial integrals. There is no need for 3D interpolation.
3. With sensibly chosen expansion functions T_z, B_z , the integral

$$\int_{\tau} dz T_z \int_{\tau'} dz' B_z e_X(k_p, z, z') \quad (2.40)$$

can be computed in closed form.

4. As it will become apparent later, the Fourier inversion in (2.39) is easier to compute than that in (2.36b). At this point we may note that z -integration of $e_X(k_p, z, z')$ will produce, in the integrand of the spectral part, inverse powers of $\gamma = \sqrt{k_p^2 - k^2}$ that will accelerate the decay of that integrand with increasing k_p . The inversion requires an integration along the real axis of the k_p plane from some point up to $k_p \rightarrow \infty$, and the decay has a direct influence on the convergence of this integral.
5. The kernel of the spatial domain integrals in (2.39) has weaker singularities than that of (2.36b). The reason is that the singular behaviour as $P \rightarrow 0$ in the spatial domain is related to the decay in the spectral domain as $k_p \rightarrow \infty$; a faster decay means a weaker singularity (see §2.6.1).

Enticing as these advantages seem, the limitations forced on the structure by resorting to (2.39) may seem great: all of its elements must form an angle of 90° or 0° with the axis of stratification. However, this is to a very good approximation the case of most printed circuit structures, because of constraints of the fabrication process. This is a class of structures of great practical importance in which the complications of a full 3D method are wasted.

To apply efficiently the reordering in (2.39), the discretization of the structure must meet the following conditions.

P3 Conditions on slices

1. Different slices must never overlap. Allowing this would complicate needlessly the exponential integrals (2.40); indeed, it would be necessary to split them in exactly-overlapping and non-overlapping parts, so that is what is exacted beforehand.
2. An observer point is never inside a source slice, nor is ever a source point inside an observer slice. This condition may be considered as included in the previous one if the *layers* (z coordinates of horizontal unknowns) are considered slices of zero height. Again, this could be allowed, but at the cost of having to split the slice integrals at the position of the offending layer.
3. A slice never crosses a dielectric boundary, ie they must be entirely confined in a single dielectric layer. Otherwise (2.37a) becomes invalid, because the $\{A, B, C, D\}$ come to depend on z, z' .

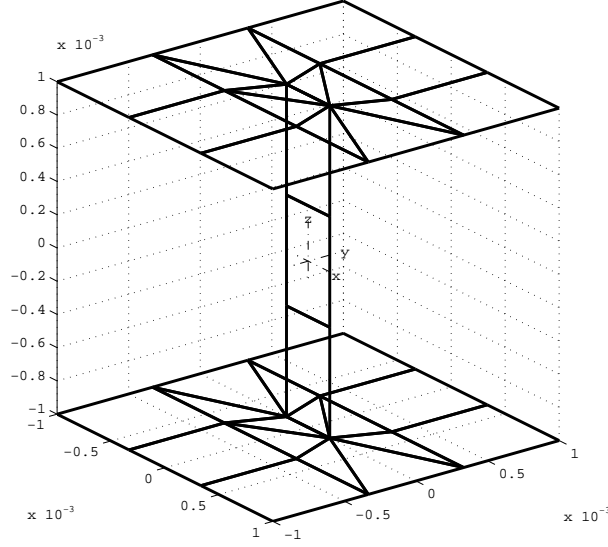


Figure 2.4: A 2.5D structure with three slices of equal height and two horizontal layers.

We stress the fact that these conditions do not limit the class of structures that can be analyzed any more than (2.38) did. Vertical unknowns may still cross dielectric layers and an horizontal layer may still cross or join a vertical wall at any height. P3 restrict only the possible *discretization* of the structure.

2.5.1 Closed form integration of TLGF vs linear variation along z

In this work, the expansion functions for the application of the Method of Moments will be exclusively linear rooftops, for either volume or surface supports. Whatever the support of the function, these rooftops always have the form ($\mathbf{f} \equiv \mathbf{T}, \mathbf{B}$)

$$\mathbf{f}(\mathbf{r}) = K(\mathbf{r} - \mathbf{r}_0) \cdot \bar{\bar{P}} \quad (2.41)$$

where \mathbf{r}_0 , K and $\bar{\bar{P}}$ are constants, and $\bar{\bar{P}}$ is either the unit dyadic $\bar{\bar{I}}$ or a proper projection dyadic. If such a \mathbf{f} is to be separable and is defined within a slice $\tau = (z_0, z_1)$ (and let $h = z_1 - z_0 > 0$), it can only depend on z according to

$$f_z(z) = \begin{cases} 1 \\ (z - z_0)/h \\ (z_1 - z)/h \end{cases} \quad (2.42)$$

(f_z is in (2.42), as in (2.38), the z -dependent factor of any component of \mathbf{f} , and not $\mathbf{f} \cdot \hat{\mathbf{z}}$.) Indeed it is easy to see that the orientation of \mathbf{f} is also restricted, so that if $f_z(z) = 1$, $\bar{\bar{P}}$ in (2.41) must be $\bar{\bar{I}} - \hat{\mathbf{z}}\hat{\mathbf{z}}$, and in the other two cases, $\bar{\bar{P}} = \hat{\mathbf{z}}\hat{\mathbf{z}}$. Consequently, the number of integrals (2.40) that are needed is relatively small; they have been collected in table 2.3. We have assumed that $z_0 = 0$; a constant factor $e^{\pm\gamma z_0/1}$ or $e^{\pm\gamma' z_0'/1}$ can always be taken out of the integrals. The functions are then

$$f_z(z) = \begin{cases} 1 \\ u(z) = z/h \\ d(z) = 1 - u(z) \end{cases} \quad (2.43)$$

| once | | | | |
|-----------------------|--------|---------|--|--|
| case | T_z | | e_X | $\int_{\tau} dz T_z e_X$ |
| I | 1 | | $e^{\sigma\gamma z}$ | $\frac{1}{\sigma\gamma}(e^{\sigma\gamma h} - 1)$ |
| II | $u(z)$ | | $e^{\sigma\gamma z}$ | $\frac{1}{\sigma\gamma}e^{\sigma\gamma h} - \frac{1}{\gamma^2 h}(e^{\sigma\gamma h} - 1)$ |
| III | $d(z)$ | | $e^{\sigma\gamma z}$ | [I]-[II] |
| twice, $\tau = \tau'$ | | | | |
| case | T_z | B_z | e_X | $\int_{\tau} dz T_z \int_{\tau'} dz' B_z e_X$ |
| IV | 1 | 1 | $e^{\sigma\gamma z-z' }$ | $\frac{2}{\gamma^2}(e^{\sigma\gamma h} - 1) - \frac{2h}{\sigma\gamma}$ |
| V | 1 | $u(z')$ | $e^{\sigma\gamma z-z' }$ | [IV]/2 |
| VI | $u(z)$ | 1 | $e^{\sigma\gamma z-z' }$ | [V] |
| VII | $u(z)$ | $u(z')$ | $e^{\sigma\gamma z-z' }$ | $-\frac{2h}{3\sigma\gamma} - \frac{1}{\gamma^2} + e^{\sigma\gamma h} \frac{2}{\sigma\gamma^3 h} - (e^{\sigma\gamma h} - 1) \frac{2}{\gamma^4 h^2}$ |
| VIII | 1 | 1 | $\text{sgn}(z - z')e^{\sigma\gamma z-z' }$ | 0 |
| IX | 1 | $u(z')$ | $\text{sgn}(z - z')e^{\sigma\gamma z-z' }$ | $-\frac{2}{\gamma^2} + (e^{\sigma\gamma h} - 1) \left\{ \frac{2}{\sigma\gamma^3 h} - \frac{1}{\gamma^2} \right\}$ |
| X | $u(z)$ | 1 | $\text{sgn}(z - z')e^{\sigma\gamma z-z' }$ | -[IX] |
| XI | $u(z)$ | $u(z')$ | $\text{sgn}(z - z')e^{\sigma\gamma z-z' }$ | 0 |

Table 2.3: Single and double integrals of exponential TLGF dependence vs linear rooftop (basis and test function) dependence. $\sigma = \pm 1$.

Not all possible double integrals $\int_{\tau} dz T_z \int_{\tau'} dz' B_z e_X$ have been included in the table; however, all can be readily obtained from it by one of the two following devices:

1. to form a product of two single integrals I, II and III. In this way all double integrals with $\tau \neq \tau'$ may be formed, because in that case the difference $z - z'$ never changes sign in the integrand and the dependences on z and z' are separable. If the exponential function is e_A or e_D in (2.37a), then (2.40) is separable even when $\tau = \tau'$.
2. to substitute d by $1 - u$ and develop the products. For example, if we put $u' = u(z')$, $u = u(z)$, etc,

$$dd' = (1 - u)(1 - u') = 1 + uu' - u - u'$$

and therefore, say,

$$\int_{\tau} dz d \int_{\tau} dz' d' e^{\sigma\gamma|z-z'|} = [\text{IV}] + [\text{VII}] - [\text{V}] - [\text{VI}]$$

and so on.

When, in addition to the pointwise Green's functions, the integrated TLGF's or integrated Green's functions described in this section must be computed, the algorithm P1 on page 26 can be easily modified to accomodate them; it suffices to consider the required pairs (τ, τ') , (τ, z') , (z, τ') in steps 5 and 6. The actual computation of the TLGF's is carried out simply by substituting the exponential functions (2.37a) in (2.35) by their integrals, as listed in table 2.3.

2.6 Quasistatic and singular behavior

The singular behavior of the Green's functions is intimately related to that of their quasistatic parts. The knowledge of this behavior is of paramount importance for the efficient inversion of the spectral Green's functions (§2.7) and for the computation of the spatial domain reaction integrals (§§3–4). In free space this behavior is

To take the quasistatic approximation is to let $\omega \rightarrow 0$. There is however no absolute measure of frequency in Maxwell's equations, so that is meaningless unless ω is compared with something. This something is the physical size of the system, given by the distance between source and observer R . In the spatial domain, then, to take the quasistatic approximation means to let $kR \rightarrow 0$.

This quasistatic field region (actually, $kP \rightarrow 0$: $|z - z'| \rightarrow 0$, of course, is clearly represented as just that in the spectral domain) is linked to the spectral domain asymptotic region $k_p/k \rightarrow \infty$ through the Fourier transform pair (2.9). Thanks to relation (B.1d), the azimuthal (k_ϕ) dependence of the spectral Green's function can be transferred to the spatial domain (on ϕ); it is then enough to consider instead 1D transforms of the type (B.2)

$$\mathcal{S}_n[f_p] \equiv \frac{1}{2\pi} \int_0^\infty dk_p k_p J_n(k_p P) f_p(k_p) \quad (2.44)$$

(2.44) is called the Sommerfeld inverse transform of order n of f_p . The transforms of various orders are associated with functions whose fastest azimuthal (ϕ) variation is $\cos(n\phi)$ or $\sin(n\phi)$. For example, from table 2.1, E_{uv}^M and E_{vu}^M require a transform of second order, E_{zv}^M , E_{vz}^M and A_{zu} , a transform of first order, and the rest, that are rotationally symmetric, a transform of zeroth order.

A fundamental formula is *Sommerfeld's identity*, which gives the relationship between the spatial and spectral potential Green's functions for free space:

$$\mathcal{S}_0 \left[\frac{e^{-\gamma|z-z'|}}{2\gamma} \right] = \frac{e^{-jkR}}{4\pi R} \equiv \Psi \quad (2.45)$$

The quasistatic version of this is obtained by letting $k_p/k \rightarrow \infty$ on the left; with $\gamma = \sqrt{k_p^2 - k^2}$, $\gamma \rightarrow k_p$,

$$\mathcal{S}_0 \left[\frac{e^{-k_p|z-z'|}}{2k_p} \right] = \frac{1}{4\pi R} \quad (2.46)$$

which is an instance of the formula [43, (6.611)], [124, p. 59], valid for $\text{Re}(n) > -1$,

$$\int_0^\infty dk_p e^{-k_p|Z|} J_n(k_p P) = P^{-n} \frac{(R - |Z|)^n}{R} \quad (2.47)$$

The following will also prove useful (cf [111, tab. 9.1-(6)]):

$$\mathcal{S}_0 \left[\frac{e^{-k_p|Z|}}{k_p^2} \right] = -\frac{1}{2\pi} \log(R + |Z|) \quad (2.48)$$

Naturally (2.46) gives the singular behavior of the free-space potential Green's functions. Now it is our objective to obtain the singular behavior of the 'integrated Green's functions'

$$\int_\tau dz T_z g(k_p, z, z') \quad \int_{\tau'} dz' B_z g(k_p, z, z') \quad \int_\tau dz T_z \int_{\tau'} dz' B_z g(k_p, z, z')$$

either in the spectral or in the spatial domain, so that the same quasistatic part extraction techniques (or singularity extraction techniques) that are usually applied to the computation both of the spatial and of the spectral part of (2.36b) may still be used in (2.39).

2.6.1 Free space

In free space this is easy enough. For $A_{uu} = \mu \frac{e^{-\gamma|z-z'|}}{2\gamma}$, the integrals along z, z' in the spectral domain are given directly by table (2.3). Indeed, from case #I there, $[z' > \tau = (z_0, z_1)]$

$$\int_\tau dz A_{uu} = \mu \frac{e^{-\gamma z'}}{2\gamma} \cdot \frac{1}{\gamma} (e^{+\gamma z_1} - e^{+\gamma z_0}) \quad (2.49a)$$

that does not have closed form inverse. But the quasistatic limit, $k_p \gg k$, can be computed as was done in passing from (2.45) to (2.46). The result

$$\int_\tau dz A_{uu} \xrightarrow{k_p \gg k} \mu \left[\frac{e^{-k_p|z_1-z'|}}{2k_p^2} - \frac{e^{-k_p|z_0-z'|}}{2k_p^2} \right] \quad (2.49b)$$

does have a closed form inverse [cf (2.48)]

$$\mathcal{S}_0 \left[\int_\tau dz A_{uu} \right] \Big|_{k_p \gg k} = \frac{\mu}{4\pi} [-\log(R_1 + |Z_1|) + \log(R_0 + |Z_0|)] \quad (2.49c)$$

If $z' < \tau = (z_0, z_1)$, the negative of (2.49c) is obtained, so that the general solution (recalling that the case $z_0 < z' < z_1$ is explicitly excluded from our consideration by rule #2 in 2 on page 29) is

$$\mathcal{S}_0 \left[\int_\tau dz A_{uu} \right] \Big|_{k_p \gg k} = \frac{\mu}{4\pi} |\log(R_1 + |Z_1|) - \log(R_0 + |Z_0|)| \quad (2.49d)$$

Actually the identity (2.48) used to invert (2.49b) has been obtained by integrating inside the quasistatic Sommerfeld identity (2.46), so the same results could have been obtained by simply integrating $(\int_\tau dz)$ the spatial domain quasistatic function $A_{uu}^{\text{qs}}(R) = \mu/(4\pi R)$.

The source-integrated quasistatic function can be computed in a similar way, yielding

$$\mathcal{S}_0 \left[\int_{\tau'} dz A_{uu} \right] \Big|_{k_p \gg k} = \frac{\mu}{4\pi} |\log(R_1 + |Z_1|) - \log(R_0 + |Z_0|)| \quad (2.50)$$

[(2.50) and (2.49d) look the same only by effect of the shorthand notation: here $Z_1 = z - z'_1$, and there $Z_1 = z_1 - z'_1$.]

We note that either (2.49d) or (2.50) are strictly singular only when either Z_1 or Z_0 vanish. The singularity in that case is like $-\log P$. When the weighting function (T_z or B_z in table 2.3) is u , u' , d or d' , the leading quasisingular term is the same as in (2.50) up to a constant factor. These results have been collected in table 2.4.

When a double integration $\int_{\tau} dz \int_{\tau'} dz'$ is performed on the Green's function, the results are particularly interesting and perhaps a bit surprising. The two representative cases are 1) $\tau = \tau'$ (same slice); 2) $z_1 = z'_0$ (source slice exactly over observer slice; the converse $z'_1 = z_0$ is identical). For the first case, the leading term $+2h/\gamma$ (case #IV in table 2.3 with $\sigma = -1$) indicates a singular space domain behavior $-2h \log P$. Space domain integration confirms it:

$$\int_{\tau} dz \int_{\tau'} dz' \frac{1}{R} = 2P - 2R_h - 2h \log \frac{P}{R_h + h} \quad (2.51)$$

For the second case, the integrals in z and z' are separable. We see by forming a product of two cases #I (table 2.3) that the result will decay as k_p^{-3} when $k_p \gg k$. In the spatial domain, this is never strictly singular. Namely,

$$\begin{aligned} \frac{1}{\gamma} \int_0^{h'} dz' e^{\gamma z'} \int_{h'}^{h+h'} dz e^{-\gamma z} &= \int_0^{h'} dz' \int_{h'}^{h+h'} dz \frac{1}{R} = \\ \frac{1}{\gamma^3} [-e^{-\gamma h} - e^{-\gamma h'} + e^{-\gamma(h+h')} + 1] &+ R_h - h \log[R_h + h] \\ \text{and } \gamma \rightarrow k_p &+ R_{h'} - h' \log[R_{h'} + h'] \\ &- R_{h+h'} + (h + h') \log[R_{h+h'} + (h + h')] \\ &- P \end{aligned} \quad (2.52)$$

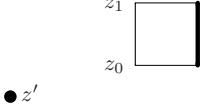
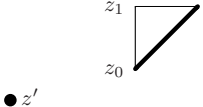
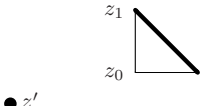
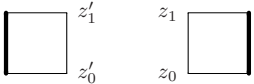
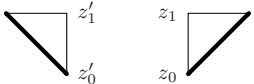
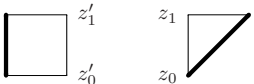
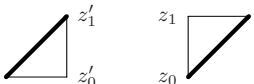
The cases involving other weighting functions behave comparably; the leading asymptotic or quasisingular behavior has again been collected, for reference, in table 2.4.

2.6.2 Layered medium

In general layered media, the quasistatic approximation cannot usually be computed in the same way as in homogeneous media due to the lack of a manageable closed form expression for the Green's function (which always exists—but is too cumbersome for anything more than, perhaps, two dielectric layers). Still, for the direct contribution from the source and the closest images, it can be obtained easily enough. For point sources, the procedure is described in the standard references [86, §7.1], [79], but most notably in papers devoted to the complex images approximation technique, where the knowledge of the quasistatic terms, which cannot be approximated by a decaying exponential series, is a requirement. For example [5, §B] extract up to *six* quasistatic terms from Φ_u in a two-layer microstrip medium.

We begin with a review of eqs. (2.34a–2.35). These are valid for any number of layers and any position of observer and source. If the restriction is allowed us: that observer and source are *in the same layer*, then the simpler expression for q_{ii} in (2.34a) is valid,

$$q_{ii} = \frac{1}{1 - \overleftrightarrow{\Gamma} \overleftarrow{\Gamma} e^{-2\gamma h}} \quad (2.53)$$

| <i>once, $\tau > z'$</i> | | | |
|---|---|--------------------------------|------------------------|
| <i>case</i> | <i>relative position</i> | $\gamma \rightarrow k_p$ | $kR \rightarrow 0$ |
| $c \cdot$ |  | $\frac{e^{-k_p Z_0 }}{k_p^2}$ | $-\log(R_0 + Z_0)$ |
| $u \cdot$ |  | $-\frac{e^{-k_p Z_1 }}{k_p^2}$ | $+\log(R_1 + Z_1)$ |
| $d \cdot$ |  | $\frac{e^{-k_p Z_0 }}{k_p^2}$ | $-\log(R_0 + Z_0)$ |
| <i>twice, $\tau = \tau'$</i> | | | |
| <i>case</i> | <i>relative position</i> | $\gamma \rightarrow k_p$ | $kR \rightarrow 0$ |
| cc' |  | $\frac{2h}{k_p^2}$ | $-2h \log P$ |
| uu' |  | $\frac{2h}{3k_p^2}$ | $-\frac{2}{3}h \log P$ |
| uc'^a |  | $\frac{h}{k_p^2}$ | $-h \log P$ |
| ud' |  | $\frac{h}{3k_p^2}$ | $-\frac{h}{3} \log P$ |

^aThis case is actually never used in the mixed potential integral equation for free space, because the vector potential is diagonal and the scalar potential is only applied to constant functions.

Table 2.4: Asymptotic and (quasi)singular behavior of the integrated free space potential Green's function. Factors of $\frac{1}{2}$ (spectral) and $\frac{1}{4\pi}$ (spatial) have been omitted. For the quasisingularities, only the leading term is shown. The cases uu' and ud' for $\tau > \tau'$ are even better behaved than cc' and these quasistatic parts need not be treated either in the spectral or the spatial domain.

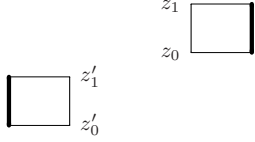
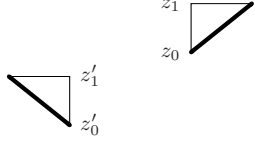
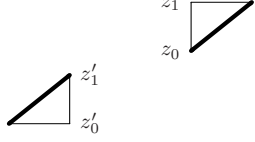
| <i>twice, $\tau > \tau'$</i> | | | |
|--|---|----------------------------------|--|
| <i>case</i> | <i>relative position</i> | $\gamma \rightarrow k_p$ | $kR \rightarrow 0$ |
| cc' |  | $\frac{e^{-k_p Z_{01} }}{k_p^3}$ | $-R_{01} + Z_{01} \log(R_{01} + Z_{01})$ |
| uu' |  | \dots | \dots |
| ud' |  | \dots | \dots |

Table 2.4: Singularities of integrated free space Green's function. (cont.)

Now, in the quasistatic limit, (2.53) is a convergent geometric series, because $|\overleftarrow{\Gamma} \overrightarrow{\Gamma} e^{-2h\gamma}|$ will eventually be < 1 when $\gamma \rightarrow k_p \rightarrow \infty$. Writing this out

$$q_{ii} \xrightarrow{k_p \rightarrow \infty} \sum_{n=0}^{\infty} (-\overleftarrow{\Gamma} \overrightarrow{\Gamma})^n e^{-2hnk_p} \quad (2.54)$$

The coefficients $\{A, B, C, D\}$ of (2.34b) read, when multiplied by their associated exponential functions (2.37c) —the k_p factor is omitted:

$$\begin{aligned} A_{ii}e_A &= \overrightarrow{\Gamma} e^{-(h-z)-(h-z')} \sum_{n=0}^{\infty} (-\overleftarrow{\Gamma} \overrightarrow{\Gamma})^n e^{-2hn} \\ B_{ii}e_B &= e^{-|z-z'|} \sum_{n=0}^{\infty} (-\overleftarrow{\Gamma} \overrightarrow{\Gamma})^n e^{-2hn} \\ C_{ii}e_C &= \overleftarrow{\Gamma} \overrightarrow{\Gamma} e^{-(2h-|z-z'|)} \sum_{n=0}^{\infty} (-\overleftarrow{\Gamma} \overrightarrow{\Gamma})^n e^{-2hn} \\ D_{ii}e_D &= e^{-z-z'} \overleftarrow{\Gamma} \sum_{n=0}^{\infty} (-\overleftarrow{\Gamma} \overrightarrow{\Gamma})^n e^{-2hn} \end{aligned} \quad (2.55)$$

(To compute V_v and I_i , $B_{ii}e_{B'}$ and $C_{ii}e_{C'}$ would be required instead of $B_{ii}e_B$ and $C_{ii}e_C$. The reader is reminded that z and z' are relative to the bottom of the layers i, i' and hence always positive). These are four series of quasistatic images. The distance of each image to the observer point is given by the negative of its exponent; for example, the direct image is the first term of $B_{ii}e_{B'}$. The whole set is ordered by index n , not strictly, because it is possible that images corresponding to different n be at the same distance. Fig. 2.5 illustrates the physical meaning of the first four $\{A_0, B_0, C_0, D_0\}$. The other images $\{A_n, B_n, C_n, D_n\}$ are the result of further (or previous) n double reflections.

Different image terms collapse (have the same exponent, and are at the same distance from the source) in the following circumstances:

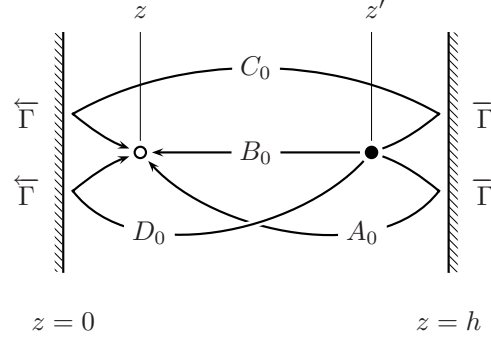


Figure 2.5: The first four quasistatic images of the set (2.55)

P4 Collapse of different quasistatic image terms into one

1. If $z = 0$ or $z' = 0$, image B_i collapses with image D_i .
2. If $z = h$ or $z' = h$, image B_i collapses with image A_i .
3. If $z = z'$, image C_i collapses with image B_{i+1} .
4. If $z = 0$ and $z' = h$, or vice versa, all four images $\{A_i, B_i, C_i, D_i\}$ collapse into one.

If any image collapses with the direct image term B_0 , the leading singular or quasisingular term of the Green's functions will change. Therefore, to be able to manipulate this term analytically, it is important that such situations (primarily cases #1 and #2 in P4, but perhaps, if h is very small, also #4) be recognized and that the correct associated factor be known. Although it is more or less clear how the factor of each of the terms of (2.55) could be computed automatically using the equations of the TL model, a direct solution is convenient for other reasons, for example to check the quasistatic behavior of those functions which were not present in a homogeneous medium, like A_{zu} .

For cases #1 and #2, of P4, this can be accomplished by neglecting $\overrightarrow{\Gamma}_i(z=0)$ and $\overleftarrow{\Gamma}_i(z=h)$ for all layers [cf (2.30)]. Therefore no interface can see each other and the sections of the TL model become decoupled. The impedances \overrightarrow{Z} and \overleftarrow{Z} in (2.24) are then equal to the characteristic impedances of the adjacent layers, and the coefficients $\overleftarrow{\Gamma}$, $\overrightarrow{\Gamma}$ become [substituting (2.6) in (2.24)]

$$\begin{aligned} \overrightarrow{\Gamma}^h &= \frac{\mu_{i+1} - \mu_i}{\mu_{i+1} + \mu_i} & \overrightarrow{\Gamma}^e &= \frac{\epsilon_i - \epsilon_{i+1}}{\epsilon_i + \epsilon_{i+1}} \\ \overleftarrow{\Gamma}^h &= \frac{\mu_{i-1} - \mu_i}{\mu_{i-1} + \mu_i} & \overleftarrow{\Gamma}^e &= \frac{\epsilon_i - \epsilon_{i-1}}{\epsilon_i + \epsilon_{i-1}} \end{aligned} \quad (2.56)$$

Note that (2.55) is a weaker approximation than (2.56), and actually independent of it. The limiting cases (2.24c) and (2.24d) are not contemplated here, because a proper knowledge of the cover impedances $Z_{s, \sup}$ and $Z_{s, \inf}$ is required. (The common case of a ground plane, $Z_s = 0$, is trivial).

Effectively, the multilayered medium is being approximated by two half spaces at each interface. Under such an approximation, there is only one quasistatic image term in addition to the direct term. Indeed, the TL equations (2.35) give, for a two half-space medium [with z, z' over the interface, ie $i = i' = 1$ in fig. (2.6)]

$$A = 0 \quad B = 1 \quad C = 0 \quad D = \overleftarrow{\Gamma}$$

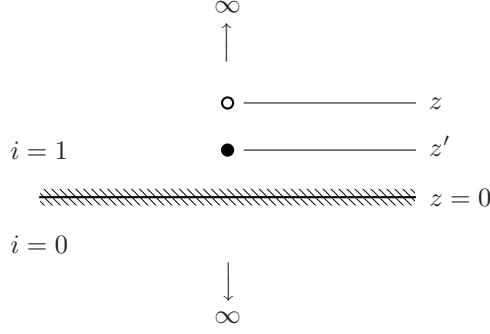


Figure 2.6: Medium with two dielectric half spaces [cf (2.57, 2.58)].

and

$$\begin{aligned}
 V_i &= \frac{Z'}{2} (\overleftarrow{\Gamma} e^{-z-z'} + e^{-|z-z'|}) \\
 I_v &= \frac{Y}{2} (-\overleftarrow{\Gamma} e^{-z-z'} + e^{-|z-z'|}) \\
 I_i &= \frac{1}{2} (\overleftarrow{\Gamma} e^{-z-z'} + \text{sgn}(z-z') e^{-|z-z'|})
 \end{aligned} \tag{2.57}$$

which through table (2.1), and replacing $\gamma \rightarrow k_p$ everywhere, yield

$$\begin{aligned}
 A_{uu} &= \frac{\mu}{2k_p} (+\overleftarrow{\Gamma}^h e^{-z-z'} + e^{-|z-z'|}) \\
 A_{zz} &= \frac{\mu}{2k_p} (-\overleftarrow{\Gamma}^e e^{-z-z'} + e^{-|z-z'|}) \\
 A_{zu} &= j \frac{\mu}{2k_p} (\overleftarrow{\Gamma}^e - \overleftarrow{\Gamma}^h) e^{-z-z'} \\
 \Phi_u &= \frac{1}{2\epsilon k_p} (+\overleftarrow{\Gamma}^e e^{-z-z'} + e^{-|z-z'|}) + \frac{\omega^2 \mu}{2k_p^3} (+\overleftarrow{\Gamma}^h e^{-z-z'} + e^{-|z-z'|}) \\
 \Phi_z &= \frac{1}{2\epsilon k_p} (+\overleftarrow{\Gamma}^e e^{-z-z'} + e^{-|z-z'|})
 \end{aligned} \tag{2.58}$$

The interpretation of (2.58) is, mostly, straightforward. A_{uu} , being purely TE, is not aware of a dielectric interface. The scalar potential Φ_z shows an image in agreement with the standard static solution [99, §3.5, fig. 3.3]. The image of A_{zz} has sign opposite to that of Φ_z . Φ_u agrees with Φ_z for the static part but adds a rapidly decaying dynamic term. Actually this term is meaningless because the approximation $\gamma = \sqrt{k_p^2 - k^2} = k_p - k^2/2 + \dots \rightarrow k_p$ cannot give terms of order k_p^{-3} in Φ_z (cf the more precise analysis in [107, §IV], which is restricted to planar sources/fields. They expand the Green's functions in series of ω , which is done by taking more terms in the Taylor expansion of γ).

The interesting bit is A_{zu} . Its behavior has been investigated, using a formulation that is essentially the same as ours, by [18, p. 371], and further by [83, §2], who provide plots of $A_{zp}(P)$. (B.1d) gives the inversion formula for A_{zu}

$$A_{zp} \hat{\mathbf{P}} = -j \mathcal{S}_1 [A_{zu} \hat{\mathbf{u}}] \tag{2.59}$$

with $A_{zp} = (A_{zx} \hat{\mathbf{x}} + A_{zy} \hat{\mathbf{y}}) \cdot \hat{\mathbf{P}}$. If *both* source and observation points are at the interface,

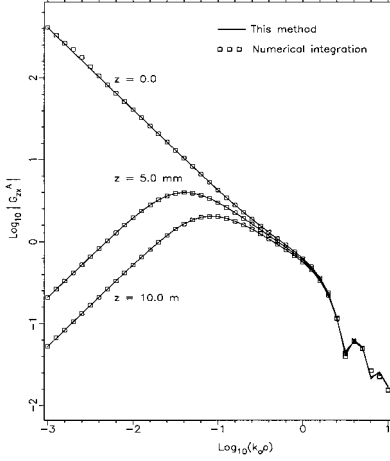


Figure 2.7: Half space: $\epsilon_0 = 10$, $\epsilon_1 = 1$, $f = 300$ MHz, source at interface $z = 0$. The 10.0 m figure is a mistake for 10.0 mm. (Reproduced from [83, f. 3].)

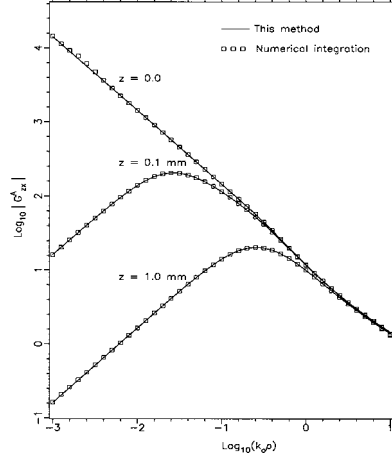


Figure 2.8: One-layer microstrip: $\epsilon_0 = 12.6$, $h_0 = 1$ mm, $\epsilon_1 = 1$, $f = 10$ GHz, source at interface $z = h_0$. (Reproduced from [83, f. 4].)

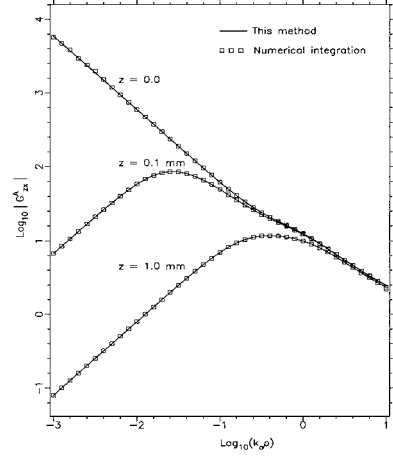


Figure 2.9: Two-layer microstrip: $\epsilon_0 = 12.6$, $h_0 = .75$ mm, $\epsilon_1 = 2.1$, $h_1 = 1.5$ mm, $\epsilon_2 = 1$, $f = 10$ GHz, source at interface $z = h_0$. (Reproduced from [83, f. 5].)

using [43, (6.511.1)]

$$A_{zp}(P, z = 0, z' = 0) = \frac{\mu}{4\pi} (\bar{\Gamma}^e - \bar{\Gamma}^h) \int_0^\infty dk_p J_1(k_p P) = \frac{1}{P} \quad (2.60)$$

Otherwise the more general formula given above (2.47) can be applied, with $n = 1$,

$$A_{zp}(P, z > 0, z' > 0) = \frac{\mu}{2\pi} (\bar{\Gamma}^e - \bar{\Gamma}^h) \frac{R_+ - Z_+}{PR_+} \quad (2.61a)$$

where I have written $Z_+ = z + z'$ and $R_+ = \sqrt{P^2 + Z_+^2}$. Multiplying above and below by $R_+ + Z_+$, which is always > 0 ,

$$= \frac{\mu}{2\pi} (\bar{\Gamma}^e - \bar{\Gamma}^h) \frac{P}{R_+^2 + Z_+ R_+} \quad (2.61b)$$

In the limit $P \rightarrow 0$, because $Z_+ > 0$, $R_+ \rightarrow Z_+$ and this becomes

$$= \frac{\mu}{2\pi} (\bar{\Gamma}^e - \bar{\Gamma}^h) \frac{P}{2Z_+^2} \quad (2.61c)$$

(2.61c) is in disagreement with [18, (24)] by a factor of Z_+^{-1} . But figs. 3, 4 and 5 from [83], reproduced here as figs. 2.7–2.9, corroborate (2.61c). First, the slope of the curves for $z = z'$ at an interface is one $|A_{zp}|$ -decade per P -decade. This confirms the $\sim P^{-1}$ behavior. Then, the two other z curves are separated by .6, 2. and 2. $|A_{zp}|$ -decades, respectively, for ratios between the two $|z|$ values of each graph of .3 = $\log_{10}(10 \text{ mm}/5 \text{ mm})$, 1. and 1. $|z|$ -decades. This confirms the $\sim Z_+^{-2}$ behavior.

We can study now the case in which source and observer are in adjacent layers. Instead of going back to the general equations of the TL model, we shall simplify the problem directly

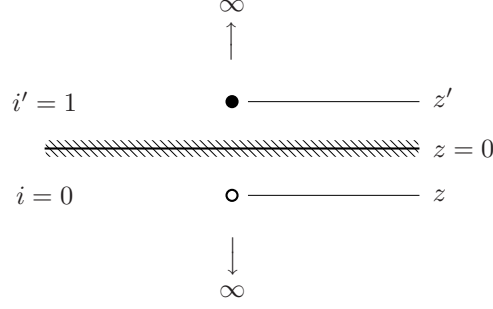


Figure 2.10: Source and observer on different sides of a dielectric interface [cf (2.64, 2.65)].

to that of a single dielectric interface, and postulate, on the basis of the remarks after P4 on page 37, that this will give the right factor for the closest quasistatic images, and thus for the correction, if there is one, to the singular behavior of the Green's functions.

The situation is that of fig. 2.10, and allows the analysis of case P4/1 directly and of case 2 by analogy. Case 4 would require at least a two-interface model, like a dielectric slab or a microstrip substrate. Here we must use the second form of $q_{ii'} = q_{01}$. The product of (2.33c) has a single factor $T(0 \leftarrow 1)$; this yields

$$\begin{aligned} t_{21}^h &= \frac{\mu_1 - \mu_0}{2\mu_1} & t_{21}^e &= \frac{\epsilon_0 - \epsilon_1}{2\epsilon_0} \\ t_{22}^h &= \frac{\mu_1 + \mu_0}{2\mu_1} & t_{22}^e &= \frac{\epsilon_0 + \epsilon_1}{2\epsilon_0} \end{aligned} \quad (2.62)$$

and, through $q_{01} = t_{21} \overleftarrow{\Gamma}' + t_{22}$,

$$q_{01}^h = e^{-\gamma h} \frac{2\mu_0}{\mu_0 + \mu_1} \quad q_{01}^e = e^{-\gamma h} \frac{2\epsilon_1}{\epsilon_0 + \epsilon_1} \quad (2.63)$$

From (2.34b), A , C and D will be 0. Therefore the relevant TLGF's are, from (2.35)

$$\begin{aligned} V_i &= \frac{Z'}{2} q_{01} e^{+z-z'} \\ I_v &= \frac{Y}{2} q_{01} e^{+z-z'} \\ I_i &= -\frac{Z'Y}{2} q_{01} e^{+z-z'} \end{aligned} \quad (2.64)$$

In a typical computer implementation, there is a finite h for every layer, there are no unbounded half-spaces; this is easily accomplished by terminating the structure on either end with a fictitious cover that has no reflection coefficient. In this way eqs. (2.33c–2.35) are always valid. Here, the term $\gamma(h - z)$ that appears in the exponents of (2.64) after multiplication with (2.63) must be interpreted as γ times the positive distance from the observer to the interface.

In the same way that led to (2.58) from (2.57), the following expressions are now from (2.64)

obtained for the case of fig. (2.10)

$$\begin{aligned}
A_{uu} &= \frac{e^{-z'-(h-z)}}{2k_p} \mu_1 \frac{2\mu_0}{\mu_0 + \mu_1} \\
A_{zz} &= \frac{e^{-z'-(h-z)}}{2k_p} \mu_0 \frac{2\epsilon_0}{\epsilon_0 + \epsilon_1} \\
A_{zu} &= \frac{e^{-z'-(h-z)}}{2k_p} j\mu_0 \left[\frac{2\mu_1}{\mu_0 + \mu_1} - \frac{2\epsilon_0}{\epsilon_0 + \epsilon_1} \right] \\
\Phi_u &= \frac{e^{-z'-(h-z)}}{2k_p} \left[\frac{2}{\epsilon_0 + \epsilon_1} + \frac{\omega^2}{k_p^2} \frac{2\mu_0\mu_1}{\mu_0 + \mu_1} \right] \\
\Phi_z &= \frac{e^{-z'-(h-z)}}{2k_p} \frac{2}{\epsilon_0 + \epsilon_1}
\end{aligned} \tag{2.65}$$

Comparing now this result to (2.58), we see that the coefficients of the various Green's functions correspond to the sum of the coefficients of the two images that we had when the observer was above the interface, after they collapse into one image when the observer is *at* the interface [$z = 0$ in (2.58) and $z = h$ in (2.65)]. The result for the charge (Φ_z) is well known in electrostatics [99, §3.5]. Otherwise they are observer-continuous, as predicted by the TL model. (The TLGF's are always observer-continuous; for the Green's functions, this is determined by the factors in table 2.1.)

The results of this section have been summarized in table 2.5. A necessary remark is that the results for a perfect conductor boundary cannot in general be obtained by letting $|\epsilon| \rightarrow \infty$. This is most clearly seen in A_{uu} , which vanishes if the source is placed on such a boundary, although this cannot be seen from (2.58) and (2.65). In such a case, both $\vec{\Gamma}_i^h = \vec{\Gamma}_i^e$ and $\overleftarrow{\Gamma}_i^h = \overleftarrow{\Gamma}_i^e$ are -1 and there is an extra image in the quasistatic expression for A_{uu} . A similar instance of such a situation (that $|\epsilon| \rightarrow \infty$ is not equivalent to PEC; it is also necessary to let $|\mu| \rightarrow 0$ [$\mu_{i\pm 1}$ in our case] at the same time) is to be found in [50, §6.9].

On another note, the results of table 2.5 can be applied to the magnetic scalar and vector potentials W and \mathbf{F} through the duality relations

$$\epsilon_i \longleftrightarrow \mu_i \quad \Gamma_i^e \Big|_{k_p \gg k} \longleftrightarrow -\Gamma_i^h \Big|_{k_p \gg k} \tag{2.66}$$

2.6.3 Integrated Green's functions and layered medium

Here we shall find the necessary modifications to the free-space results summarized in table 2.4 so that they hold also in layered media. One possible way is 1) to obtain the integrated functions in the spectral domain with the help of table 2.3, 2) apply the quasistatic approximation to these functions; 3) perform the Fourier inversion.

An alternative, which we think sufficiently justified after the development in §2.6.1 and §2.6.2, is to integrate in the spatial domain each of the image terms obtained in the quasistatic expansion for point sources (2.55). The accuracy of this assumption will later be checked by numerical experiment. Only three cases need actually be considered.

1. When source (z' or τ') and observer (z or τ) are in the same layer, and neither z' nor z is at a dielectric interface. (It does not matter whether τ' or τ do.) In that case only the quasistatic image term B_0 (fig.(2.5)) can become singular, and its singularity will be the same as in free space save for a factor that depends on the particular Green's function.

| <i>image(s)</i> | <i>A</i> | <i>D</i> | <i>C A D</i> |
|---|---|---|--|
| <i>coefficient(s)</i> | $\vec{\Gamma}_i$ | $\overleftarrow{\Gamma}_i$ | $\overleftarrow{\Gamma}_i \vec{\Gamma}_i \vec{\Gamma}_i \overleftarrow{\Gamma}_i$ |
| <i>collapse(s)</i> <i>with B when</i> | $z \rightarrow h$ $z' \rightarrow h$ | $z \rightarrow 0$ $z' \rightarrow 0$ | $z' \rightarrow h$ and $z \rightarrow 0$ $z' \rightarrow 0$ and $z \rightarrow h$ |
| <i>collapsed residual</i> <i>for A_{uu}</i> | $\frac{2\mu_i\mu_{i+1}}{\mu_i + \mu_{i+1}}$ | $\frac{2\mu_i\mu_{i-1}}{\mu_i + \mu_{i-1}}$ | $\mu_i(\vec{\Gamma}_i^h \overleftarrow{\Gamma}_i^h + \vec{\Gamma}_i^h + \overleftarrow{\Gamma}_i^h + 1)$ |
| <i>collapsed residual</i> <i>for Φ_u, Φ_z</i> | $\frac{2}{\epsilon_i + \epsilon_{i+1}}$ | $\frac{2}{\epsilon_i + \epsilon_{i-1}}$ | $\frac{1}{\epsilon_i}(\vec{\Gamma}_i^e \overleftarrow{\Gamma}_i^e + \vec{\Gamma}_i^e + \overleftarrow{\Gamma}_i^e + 1)$ |
| <i>collapsed residual</i> <i>for A_{zz}</i> | $\frac{\mu}{\epsilon'} \frac{2\epsilon_i\epsilon_{i+1}}{\epsilon_i + \epsilon_{i+1}}$ | $\frac{\mu}{\epsilon'} \frac{2\epsilon_i\epsilon_{i-1}}{\epsilon_i + \epsilon_{i-1}}$ | $\frac{\mu}{\epsilon'}(\vec{\Gamma}_i^e \overleftarrow{\Gamma}_i^e - \vec{\Gamma}_i^e - \overleftarrow{\Gamma}_i^e + 1)^a$ |

^aDiscontinuous by $\mu(\epsilon')$, when $z(z')$ moves from i to either $i+1$ or $i-1$.

Table 2.5: Singular images for point-source Green's functions when source and observer are in the same layer. The asymptotic reflection coefficients $\vec{\Gamma}_i, \overleftarrow{\Gamma}_i$ are defined in (2.56), and are -1 if the layer is bounded by a ground plane. The residuals are the factors that multiply the free-space singular behavior $\sim 1/(4\pi R)$. For the third case $C|A|D$, they were computed using a dielectric-slab approximation. Note that the residual for this case correctly agrees with $\Phi_z = 0$ if $\vec{\Gamma}_i^e$ or $\overleftarrow{\Gamma}_i^e = -1$. It can be checked against the complete expansion in [107, (43)].

2. When the Green's function has been integrated in z and the z' is at a dielectric interface; τ and z' are in the same layer. An equivalent situation is when the Green's function has been integrated in z' , z is at a dielectric interface, and τ' and z are in the same layer. In either case there are two singular images (B_0 and A_0 or B_0 and D_0) and each of them produces the same singularity as in free space save for a constant medium-dependent factor for each particular Green's function.
3. When the Green's function has been integrated both in z' and in z , only the B_0 term can ever become singular, because for the other terms source and observer do not overlap, and if there is no overlapping there is no singularity when $P \rightarrow 0$ [this was demonstrated in (2.52) and is shown in the cases $\tau > \tau'$ of table 2.4]. The knowledge of the quasisingular terms is less valuable here than in the case of point Green's functions, because the quasisingularity is much weaker.

Table 2.6 summarizes these cases. A particular case concerns the singularity of integrated A_{zp} . It can be confirmed by direct integration of (2.61a)

$$\int_{\tau} \frac{R-Z}{PR} = \frac{Z-R}{P} \quad (2.67)$$

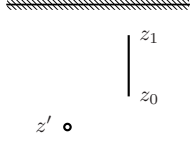
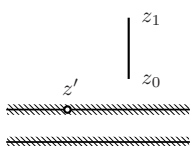
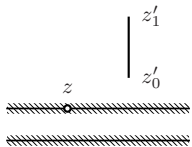
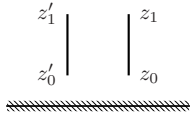
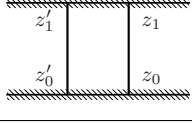
| <i>case</i> | <i>relative position</i> | <i>singular images</i> | <i>singularity</i> |
|---------------------------------|--|------------------------|--|
| z, z' in layer |  | B_0 | $\log(R_0 + Z_0)$ |
| z' at interface |  | B_0, D_0 | $(1 \pm \overleftarrow{\Gamma}) \log(R_0 + Z_0)$ |
| z at interface |  | B_0, D_0 | $(1 \pm \overleftarrow{\Gamma}) \log(R_0 + Z_0)$ |
| $\tau = \tau'$ in layer |  | B_0 | $K \log P$ |
| $\tau = \tau'$ at interfaces |  | B_0 | $K \log P$ |

Table 2.6: Singular cases for integrated Green's functions in layered media. In the once-integrated cases, the singularity is actually $\log P$ when τ and z' , or τ' and z , are in contact. There are equivalent cases where $z = h$ or $z' = h$ and image A_0 , instead of D_0 , becomes singular. These are the singularities of the TLGF's: they must still be multiplied by constant factors depending on the particular Green's function at hand. The factor K for the doubly integrated functions is given in table 2.4.

that the integrated function is never singular, not even when z' is at an interface and τ touches it, or vice versa. As for the components of $\bar{\bar{E}}^M$, the treatment of their singularities will be done completely in the space domain. This is possible because magnetic currents will only be allowed on ground planes, where the singular behavior of the Green's function is the same as in free space, as can easily be verified with the methods used all along this chapter.

2.7 Numerical inversion

As shown in P21 on page 131, the azimuthal dependence of the spectral Green's functions can be transferred in closed form to the spatial domain and eliminated from the Fourier inversion integral. Therefore the inversion can be written in terms of integrals of the cylindrical coordinates (P, k_p) alone [36, (5.2.8a)] as a Sommerfeld integral

$$f(P, z, z') = \frac{1}{2\pi} \int_0^\infty F(k_p, z, z') k_p J_n(k_p P) dk_p \quad (2.68)$$

or a combination of them. This integral will be computed numerically. To do this efficiently, it is necessary to consider

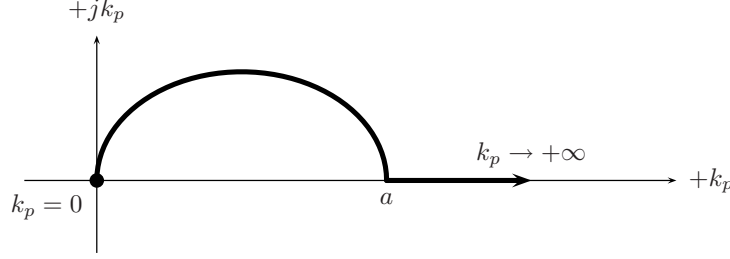


Figure 2.11: Integration path for (2.68)

- the range of values of p ,
- the range of values of $z - z'$,
- the behavior of $F(k_p, z, z')$ when $k_p \rightarrow \infty$,
- special features of $F(k_p, z, z')$, such as evenness,
- the characteristic points of $F(k_p, z, z')$: poles, branch points.

The integration path used in the computation of (2.68) can be considered as consisting of two parts. If it runs along the real axis, the part near the origin and up to $|k_{\max}|$ (where $k_{\max} = k_0 \max_i \sqrt{\epsilon_i \mu_i}$) contains all the surface wave poles and/or parallel plate modes of the layered medium, and up to two branch points if the structure is open [36, §5.3a]. This part accounts for the far field. The part from $|k_{\max}|$ and up to $k_p \rightarrow \infty$ is related to the near field and the singular behavior of the Green's function.

The problems studied in this work are electrically small. We are also interested in obtaining general results. While it is relatively easy to extract the contributions of the characteristic modes of a half space, a slab or a single-layer medium, and in so doing both to simplify the evaluation of the remaining integral and to obtain valuable physical insight, the substantial efforts this requires for the general multilayered medium (for example [114]) are not warranted in our case.

We shall address the first section of the path with the method both direct and simple presented in [39], where the integration path takes a detour to a region in the first quadrant of the k_p plane, away from singularities and branch points, and comes back to the real axis at $k_p = a$ (fig. 2.11). This method is impractical for P/λ larger than about 10, because the integrand becomes rapidly oscillating, but it will suffice to cover our applications. A typical choice for a is $|k_{\max}| + k_0$.

On the other hand, it is impossible to neglect the near field behavior of the Green's function, which is essential to the computation of reaction terms. To handle this behavior, an accurate integration of the tail of the integral (the interval $[a, +\infty)$ in fig. 2.11) is necessary. The method of weighted averages [85, §A.7], [86, §8.3] will be used. This is an extrapolation technique that depends on a certain amount of knowledge about the asymptotic behavior of the integrand. Specifically, it is designed to handle integrals of the type

$$\int_a^\infty dk_p q(k_p) k_p^\alpha e^{-k_p |Z|} \quad (2.69)$$

where $q(k_p)$ is a periodic or asymptotically periodic function when $k_p \rightarrow \infty$.

It comes as no surprise that all the integrands that have appeared in this chapter have this asymptotic form, either for point sources [cf (2.35), table 2.1] or for integrated sources [cf (2.3)].

The Bessel function fits here, too, because the first term of its large-argument asymptotic expansion is [4, (9.2.1)], [43, (8.451)]

$$J_{\pm n}(x) \sim \sqrt{\frac{2}{\pi x}} \cos\left(x \mp n\frac{\pi}{2} - \frac{\pi}{4}\right) \quad (2.70)$$

The $x^{-1/2} = (k_p P)^{-1/2}$ is particularly important. To apply the algorithm, then, α and $|Z|$ of (2.69) must be known. This α can be obtained from tables (2.3) or (2.4) or directly from equation (2.35) and table 2.1. For example, all functions that exhibit a potential-type singularity ($1/P$) have $\alpha = -.5$ (k_p^{-1} for the Green's function times k_p^{+1} for the factor in the Sommerfeld integral times $k_p^{-.5}$ for the Bessel function), and those with a logarithmic singularity, $\alpha = -1.5$. In [86, §8.3], the algorithm is tested with $\alpha = -.5$, and this seems to have been the only application of the technique for a long time. In the review article [76, (56), fig. 14], good performance is demonstrated for $\alpha = +.5$ and $|Z| = 0$ (a strongly singular case).

The asymptotic period of the Bessel function, which is also required, is given simply by $T = 2\pi/P$, according to (2.70) and (2.68). The weighted averages algorithm uses the half-period to split the tail in intervals where the partial integral is computed with a separate method (like Gauss-Legendre rules) and actually tries to extrapolate the sum of these intervals. When the oscillating function is not present (when $P = 0$), or if the period is very large, the intervals must be formed according to another rule. A most practical one is to compare $|Z|$ to P and choose as size of the interval the shortest of $\pi/|Z|$ and π/P . [76, p. 1414] suggests the use of $\pi/|Z|$ only when $P = 0$, but this seems too conservative. (He also notices that the weighted averages algorithm does not improve when the intervals are chosen according to the zeros of the Bessel function, which is a good characteristic, because it is easier to have equal-sized intervals.) Last, if $\pi/|Z|$ is chosen, α should be up by $+.5$, because the Bessel function is taken as constant for the purposes of extrapolation.

1. If $|Z| > 0$, the integral will eventually converge whatever the value of α , and the faster the larger $|Z|$ is. Trying to form intervals according to $P \rightarrow 0$ would only make it difficult to achieve any accuracy in the integration of each ever longer interval, thereby increasing computation time and in the end producing (probably) spurious convergence.
2. If $|Z| = 0$, there are two possibilities.
 - (a) Either the function is singular at $P = 0$; then computation time will increase without bound as $P \rightarrow 0$, because of the problem of achieving accuracy in the integral of each interval as explained above. It appears that the first interval $(a, a + T)$ is the most delicate. [75, §6.2.1] recommends a Romberg method here, but a Gauss-Kronrod method such as implemented in [60, 101] is more efficient. (In my experience, Romberg integration has a tendency to produce excessive accuracy with excessive number of function evaluations.) It is clear that in this case the intervals cannot be chosen as $\pi/|Z|$. The best bet is, if the singular behavior of the function is known (say, the principal quasistatic terms are known), to extrapolate towards the origin with the help of some points computed at reasonable $P > 0$ and then avoid numerical inversion.
 - (b) Or the function is bounded at $P = 0$. Then the integral of the tail will converge. But the function does not decrease exponentially, because $|Z| = 0$, nor does it alternate, because $P = 0$. Therefore, the intervals must be chosen on other grounds and the weighted averages method will be of little if of any help.

Fortunately, the need for values of the Green's functions at $R = 0$ or, for singular functions, at small P , can be circumvented in most cases by choosing with some care the spatial domain

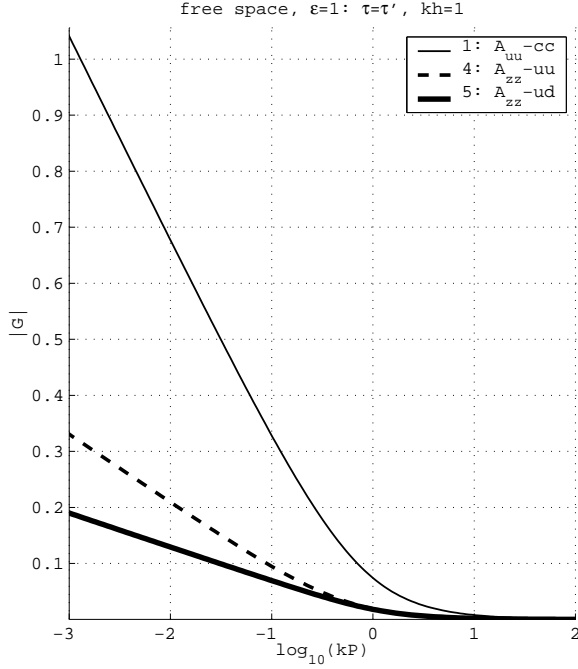


Figure 2.12: Twice integrated singular free space potential Green's functions. In free space $\int_{\tau} \int_{\tau'} cc \Phi_u$ (or $\int_{\tau} \int_{\tau'} cc \Phi_z$) is also used, and it is identical to $\int_{\tau} \int_{\tau'} cc A_{uu}$. The slope of $\int_{\tau} \int_{\tau'} cc A_{uu}$ when $P \rightarrow 0$ is (in this plot) $-2kh \frac{\log_e 10}{4\pi} = .367$, which agrees with table 2.4, as do the other two.

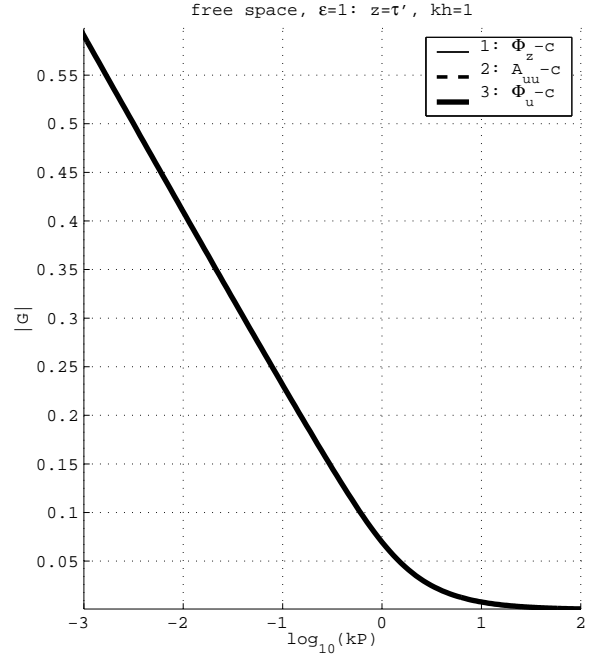


Figure 2.13: Once (z') integrated singular free space potential Green's functions. The slope of $\int_{\tau'} \Phi_u$ when $P \rightarrow 0$ is $-\frac{\log_e 10}{4\pi} = .183$, which agrees with table 2.4.

integration rules. (A list of optimal Gaussian-type rules for various regions has been compiled in §C).

2.8 Examples

In this section, a set of Green's functions will be computed with the general methods developed along this chapter. This will serve as justification for the properties we have claimed for them, and also as a reference, because as far as I know no plots of the integrated functions (§2.5) have appeared in the literature, and only a light reference to their properties [140, §C].

2.8.1 Free space

In free space, where the Green's function is known in closed form and there is no need of interpolation, it does not make any sense to apply the 2.5D formulation studied here. The integrated functions are interesting, nonetheless, as comparison and check material, and as a first step in the computation of the layered media Green's functions. Not even in free space do the integrated functions exist in closed form; they were computed with the same exact procedure that will be used to compute them in layered media, ie numerical Sommerfeld transform, as explained in §2.7.

Only the functions that could actually be used are shown. For example, because $\bar{\bar{A}}$ is diagonal, functions $\int_{\tau} \int_{\tau'} cu A$ are not needed.

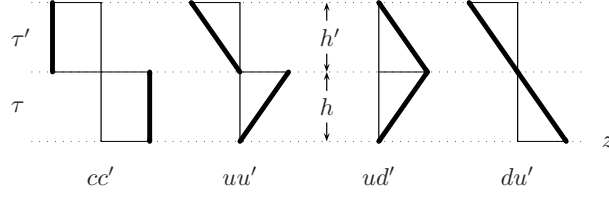


Figure 2.14: Key for figs. 2.15–2.16.

As shown in table 2.4, the only singular case for twice integrated functions is when $\tau = \tau'$. This is shown in fig. 2.12. In fig. 2.13, an horizontal layer touches a slice $[\tau' = (z'_0, z'_1)]$ and $z = z'_0$. This is first case (c') of table 2.4, with $R_0 = 0$.

The non-singular cases appear in 2.15 and 2.16. The first corresponds to the cases $\tau > \tau'$ in table 2.4 (actually $\tau' > \tau$, so they are mirrored: ud' in fig. 2.15 $\rightarrow du'$ in the table, etc; this symmetry is, of course, dependent also on the medium) with $R_{10} = 0$ (R_{01} in table 2.4). The second figure is the reciprocal of case c' , with $R_0 = \sqrt{P^2 + h^2}$ (see fig. 2.14).

Finally we show the transforms needed to compute the field dyadic $\bar{\bar{E}}^M$ when the test cell is vertical. These are given in table 3.2 as cases II (G1-c to G4-c in the plots) and III (G-u and G-d in the plots). The cartesian components of $\bar{I}_t \cdot \bar{\bar{E}}^M$ are obtained from these through formulas (B.4). Note that at most a potential-type singularity (P^{-1}) appears as a result of (B.4) from fig. 2.18, while all components of $\bar{\bar{E}}^M$ from 2.19 are regular at $P = 0$.

2.8.2 Layered medium

All the examples presented for the layered medium are based on the template of fig. 2.20. Up to five different layers and/or slices are allowed; for each medium (I, II...), the permittivity of each layer is listed in the table.

The first example uses media I and II (fig 2.20) and is both a check of table 2.6 and a symmetry test when $\tau = \tau'$ (the singular case for twice-integrated Green's functions) in fig. 2.22. Comparison between $\int_{\tau} \int_{\tau'} udA_{zz}$ and $\int_{\tau} \int_{\tau'} duA_{zz}$ is, on the other hand, a true reciprocity test on each of the media separately (fig.2.22). These media are reflected around the midline of τ_2 . There is only one slice and it is also τ_2 . On fig.2.23 the two scalar potentials have been represented. As can be seen, their first-order singular behavior (dominated by the real part) is the same, but they are very different far from the source. (Because they are integrated with cc , they are the same for either of media I and II).

A plot of the components of $\bar{\bar{E}}^M$ in a layered medium (figs. 2.24–2.25: these use medium IV from fig. 2.20) reveals some interesting features. First of all, the two curves G3-c $\equiv \int_{\tau} \mathcal{S}_1\{k_p^{-1} E_{uv}^M\}$ and G4-c $\equiv \int_{\tau} \mathcal{S}_1\{k_p^{-1} E_{vu}^M\}$ are different (this is easier to appreciate when source and observer are farther away in z , fig. 2.25) and this difference produces a non-zero component in the diagonal of $\bar{\bar{E}}^M \cdot \bar{I}_t$, which is not antisymmetric in a general layered medium. This component (related to the difference of G3-c and G4-c) is nonsingular at $R \rightarrow 0$ if \mathbf{M} is on a ground plane, which is the only case treated here. (For the general case, some information may be obtained from [32, §C], but further study is clearly warranted).

On the other hand, the behavior at $P \rightarrow 0$ of all the functions appearing in the singular case ($z_0 = z'$, fig.2.24) is the same as in free space; this is the justification for the singularity extraction procedure developed in §§3.3.5–3.3.6 for the reaction integrals involving them.

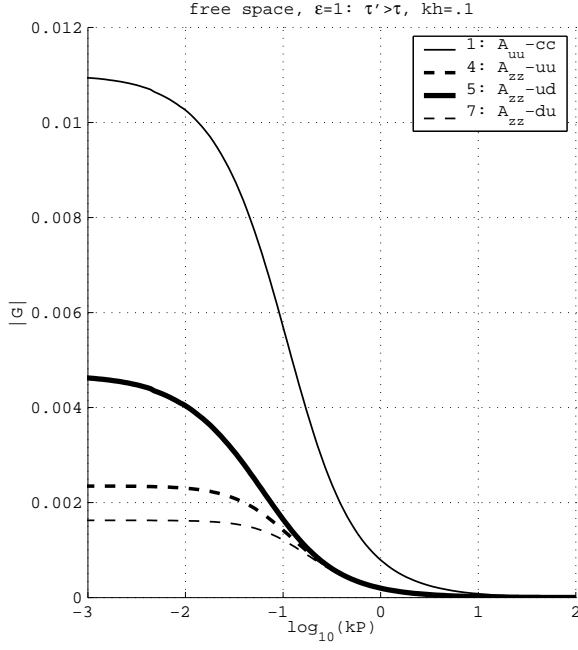


Figure 2.15: Twice integrated non-singular free space potential Green's functions. The values at $P = 0$, not shown because of the logarithmic kP axis, are $(\cdot 10^{-2})$: $1.095 - j.0794$ | $.466 - j.0199$ | $.234 - j.0199$ | $.1615 - j.0198$.

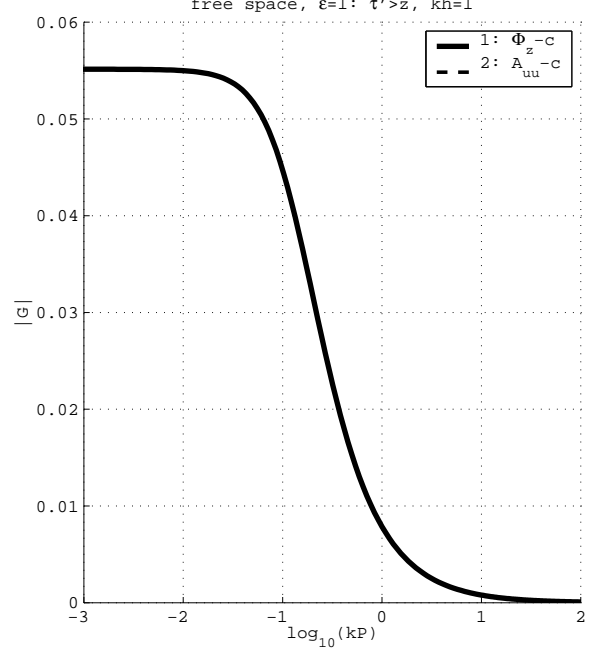


Figure 2.16: Once (z') integrated non-singular free space potential Green's functions. Only $\int_{\tau'} cf$ is actually used in free space, because only \hat{z} -directed currents have u or d -type variation, and these do not interact with horizontal currents in free space save through the associated charge. The value at $P = 0$ is $(5.456 - j.7927) \cdot 10^{-2}$.

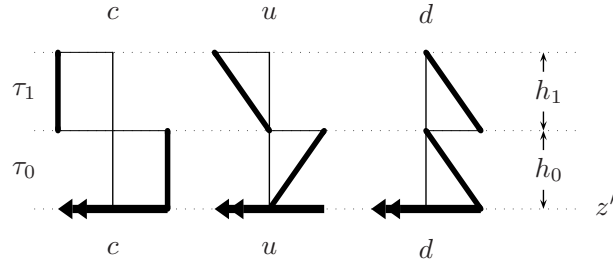


Figure 2.17: Key for figs. 2.18–2.19.

2.9 Conclusion

In this chapter, the derivation of the spatial domain field and potential Green's functions has been carried out, starting from Maxwell equations, by dint of a plane wave (modal, spectral) decomposition. In the spectral domain, the exponential dependence of these functions on the vertical coordinate has been made manifest, and then eliminated through integration with the linearly varying basis and test functions normally used in a method of moments procedure.

An idea that comes easily to mind is that of using higher order functions whose product with an exponential could also be integrated analytically. Two obstacles can be foreseen:

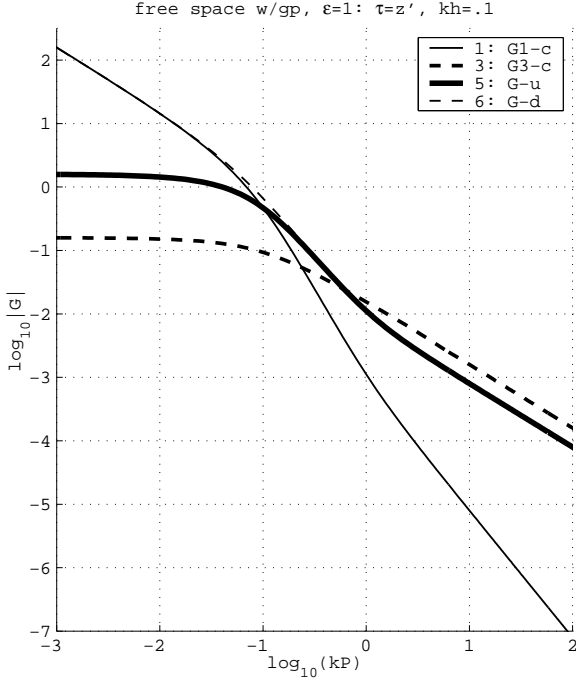


Figure 2.18: Once (z) integrated components of $\bar{\bar{E}}^M$ in PEC-bounded free space, when observer slice is τ_0 in fig. 2.17. Some of the components are singular, because source and observer actually touch when $P \rightarrow 0$: note in particular that $\int_{\tau} dE_{zx}^M$ (G-d) is singular (P^{-1}), while $\int_{\tau} uE_{zx}^M$ (G-d) is not. G2-c and G4-c are equal in modulus, respectively, to G1-c and G3-c in free space.

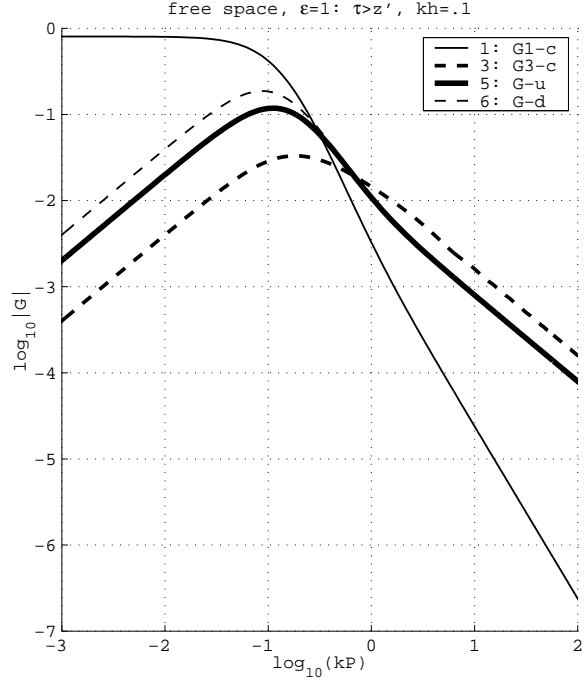
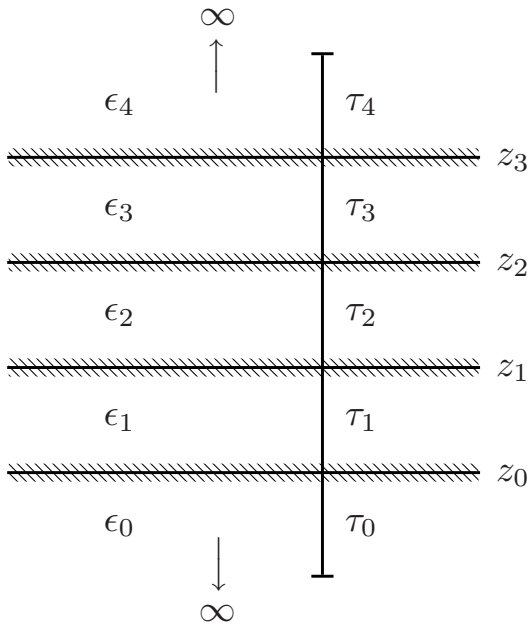


Figure 2.19: Once (z) integrated components of $\bar{\bar{E}}^M$ in PEC-bounded free space, when observer slice is τ_1 in fig. 2.17. Note that all components go to zero (like P) when $P = 0$, save G1,2-c= $S_0\{E_{uv}^M\}$, $S_0\{E_{vu}^M\}$ (these are equal in modulus in free space). Its value at the origin is $.8037 - j.7937 \cdot 10^{-3}$.



| medium | I | II | III | IV |
|--------------|---|----|-----|-----|
| ϵ_4 | 4 | 1 | 1 | 1 |
| ϵ_3 | 4 | 1 | 1 | 1 |
| ϵ_2 | 1 | 1 | 4 | 4 |
| ϵ_1 | 1 | 4 | 4 | PEC |
| ϵ_0 | 1 | 4 | 4 | PEC |

Figure 2.20: Key to examples of layered media z -integrated Green's functions. For all slices τ_0 - τ_4 , $kh = .1$.

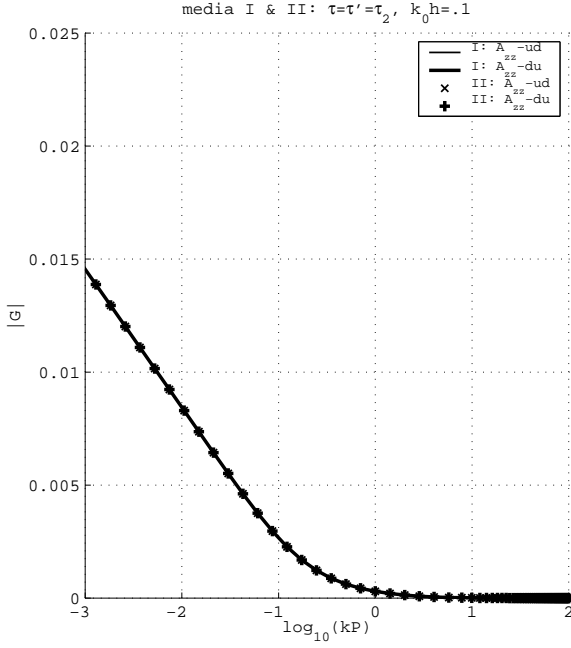


Figure 2.21: $\int_{\tau} \int_{\tau'} ud' A_{zz}$ and $\int_{\tau} \int_{\tau'} du' A_{zz}$ for $\tau = \tau' = \tau_2$; these are equal on each of the media I and II, fulfilling required reciprocity.

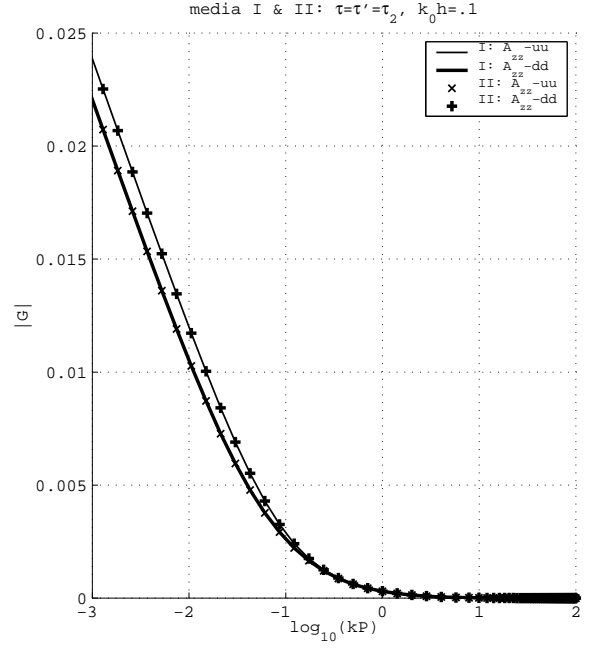


Figure 2.22: Twice integrated A_{zz} for $\tau = \tau' = \tau_2$. $\int_{\tau} \int_{\tau'} uu' A_{zz}$ on medium I equals $\int_{\tau} \int_{\tau'} dd' A_{zz}$ on medium II, and viceversa. The slope at $P \rightarrow 0$ is the same for all four functions. (Also, not shown here, $\int_{\tau} \int_{\tau'} cc' A_{zz}^I = \int_{\tau} \int_{\tau'} cc' A_{zz}^{II}$.)

- the increase in the number of integrated Green's function types, that will require a particularly careful implementation;
- the treatment of the quasistatic and singular parts, relatively simple when working with linear functions (all $1/R$ singularities are reduced to logarithmic type, and can be treated uniformly), will become more complicated. In the absence of analitically available quasistatic terms, spatial domain integration is also more complicated, and in practice slower.

However, for especially restricted structures (single-layer circuits including vias, very thin layers of highly conducting materials analyzed with a polarization current approach, etc) it is very possible that the advantages would outweigh the difficulties.

Another possibility, that was not fully explored here, is to have vertical magnetic current slices (and, in general, magnetic currents in any position, not only on ground planes). Indeed, the bases are already laid out, as the spectral domain integration (table 2.3) has been developed in a general way for all transmission line Green's functions. However, before a computer implementation is possible, a detailed study of the quasistatic parts of the individual components of \vec{E}^M , similar to what was done for the potentials, is necessary. This would make possible the analysis of 2.5D dielectric homogeneous bodies in layered media using the surface equivalence principle (see §3.4; a full 3D approach, using 3D interpolation, is described in [20, 21]).

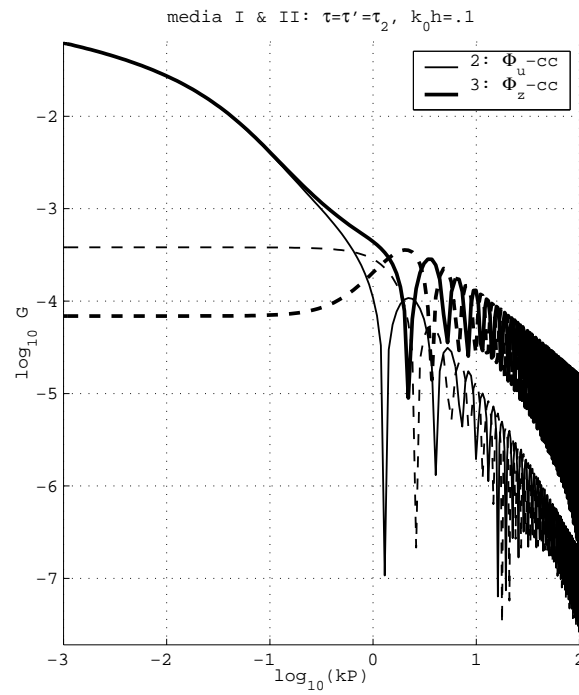


Figure 2.23: Twice integrated singular Φ_z and Φ_u for media I and II and $\tau = \tau' = \tau_2$ (see fig. 2.20) Real part in continuous line, imaginary part dashed line. These functions are $\sim -\log P$ near the origin; they have been represented in log axes in order to appreciate their features with $kP \approx 1$ and beyond.

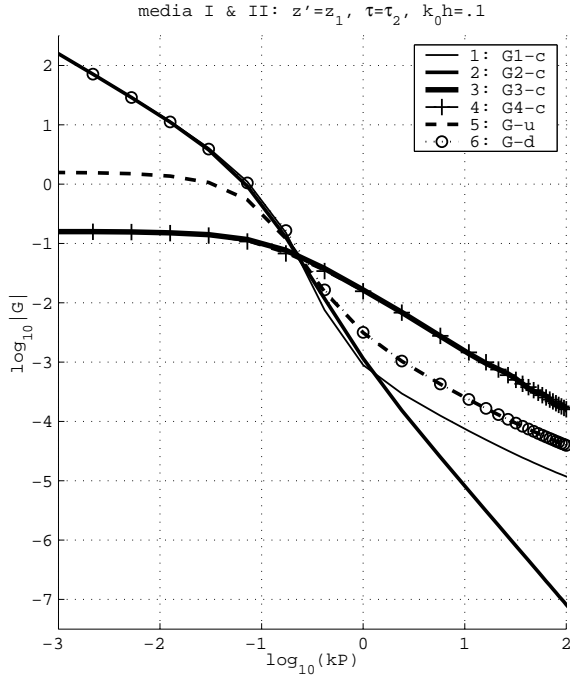


Figure 2.24: Source integrated components of $\bar{\bar{E}}^M$ in microstrip medium: singular case. This is in medium IV (fig. 2.20), $z' = z_1$, $\tau = \tau_2$. The singularity of G1-c, G2-c and G-d is the same (and the same as in free space, cf fig 2.18), while G3-c, G4-c and G-u are regular, but also behave at $P \rightarrow 0$ in the same way as in free space. Although it can not be appreciated in this plot, G3-c and G4-c are different at $P > 0$, giving raise to a non-zero $\bar{\bar{E}}_{xx}^M$.

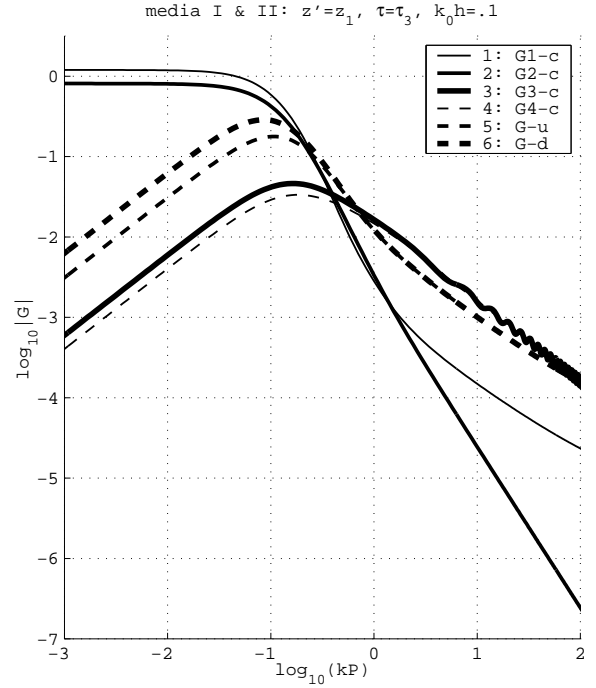


Figure 2.25: Source integrated components of $\bar{\bar{E}}^M$ in microstrip medium: nonsingular case. Same as fig. 2.24, but now $\tau = \tau_3$. Unlike in free space, all six components are distinct.

3 Surface equivalence

There are mainly two formulations that can be used to solve a scattering problem by application of the equivalence principle on the surfaces of conductors, apertures and homogeneous dielectric bodies: the Müller formulation and the PMCHWT (Poggio, Miller et al.) formulation [73, §1]. The former results in a second order integral operator, and is in general better behaved, particularly for low-contrast objects [73, §6]. For high-contrast bodies and conductors, the two behave rather similarly [150]. In this work, only the PMCHWT formulation is used.

The discretization of the unknown equivalent currents will be in terms of linear functions (rooftops) defined on arbitrarily oriented triangular and rectangular cells. These are treated on a similar way, and, in homogeneous media, all the results of this chapter are valid for either kind, or for any combination of them.

We begin by discussing the analysis of metallic bodies in stratified media (§3.2). For the particular case of perfectly conducting bodies, if the bodies are open (ie, have surface, but no volume) it is possible to obtain valid solutions by enforcing the boundary condition for the electric field alone. This condition is that the tangential electric field be zero on the surface of the conductor; magnetic current unknowns are therefore unnecessary.

In layered media, the condition of separability (2.5 on page 28) must be enforced on the structure, so that the 2.5D method can be applied. In this case, vertical elements can only be meshed using rectangles, and triangles can only be horizontal. Depending on the relative orientation of source and test cells, different Green's functions are needed. All the different cases (§§3.2.1–3.2.9) are examined with a view to implement them in a computer code. The knowledge of the quasistatic parts of the Green's functions (§2.6) is applied to a tailored singularity extraction procedure that results in an efficient computation of the reaction integrals.

Then we present the analysis of arbitrarily shaped apertures in metallic ground planes (§3.3), using the same discretization and integral equation approach as for metallic scatterers. In contrast to the analysis of metallic scatterers, here it is only necessary to use the equation for the continuity of the magnetic field. In some aspects, the formulation required by this problem is dual to that required for the analysis of open metallic scatterers. The different types of interactions between magnetic currents (always horizontal) and variously oriented electric current cells are considered.

The range of problems solvable using a surface formulation is completed with the analysis of arbitrarily shaped piecewise homogeneous dielectric bodies, either in free space or a ground-plane bounded homogeneous half-space (§3.4). This is a well known technique, to which the 2.5D formulation has not been applied; both electric and magnetic currents are used in the discretization of the body's surface. The established results it provides will be used in the next chapter (§4) to verify an alternative formulation using volume currents.

To conclude, a series of illustrative cases is showed in §3.5. In addition, all the results of §5, that are supported by our own measurements, have been obtained by applying the theory presented in this chapter.

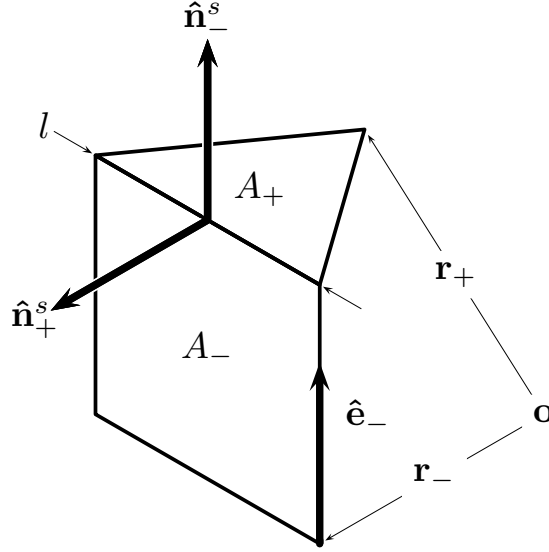


Figure 3.1: Parameters of the surface RWG function (3.2).

3.1 Discretization

To discretize a surface current distribution, either electric or magnetic, we shall use the classic linear RWG functions defined on triangular or rectangular (parallelogram) cells. These functions are the composition of two *half functions* defined over adjacent cells, ie cells that share an edge of the mesh (the *common edge*).

$$\mathbf{b} = \mathbf{b}_+ - \mathbf{b}_- \quad (3.1)$$

The definition of the half functions is (fig. 3.1)

$$\mathbf{b}_\pm(\mathbf{r}) = \frac{l}{2A_\pm}(\mathbf{r} - \mathbf{r}_\pm) \quad \text{on triangles,} \quad (3.2a)$$

$$\mathbf{b}_\pm(\mathbf{r}) = \frac{l}{A_\pm}(\mathbf{r} - \mathbf{r}_\pm) \cdot \hat{\mathbf{e}}_\pm \hat{\mathbf{e}}_\pm \quad \text{on parallelograms.} \quad (3.2b)$$

In the parallelogram, $\hat{\mathbf{e}}_\pm$ is a vector along the edge of the cell adjacent to the common edge. These functions have two fundamental properties [113]:

1. They have constant divergence.
2. Their component normal to the edge of the cell is zero, save on the common edge, where it is 1. This normal component is, therefore, continuous across half functions.

The normal to the cell itself is $\hat{\mathbf{n}}_{i\pm}$, or $\hat{\mathbf{n}}_{j\pm}$. The normal to the *edge* of the cell, on the plane of the cell, is $\hat{\mathbf{n}}_{i\pm}^s$, or $\hat{\mathbf{n}}_{j\pm}^s$.

3.2 Metallic scatterers

The electric field integral equation (EFIE) for conductors embedded in an open layered medium is

$$(\mathbf{E}^s + \mathbf{E}^i) \times \hat{\mathbf{n}} = 0 \quad (3.3a)$$

which must be enforced on the surface of the conductor. A good but imperfect conductor can be accomodated with the approximation [cf (2.8)]

$$(\mathbf{E}^s + \mathbf{E}^i) \times \hat{\mathbf{n}} = Z_s \mathbf{J} \times \hat{\mathbf{n}} \quad (3.3b)$$

with a surface impedance

$$Z^s = (1 + j) \sqrt{\frac{\mu_0 f}{\pi \sigma}} \quad (3.4)$$

The EFIE (3.3a) is not appropriate for closed bodies (cavities) because it does not guarantee the unicity of the solution at the resonant frequencies of the cavity [72]. This problem, which is particular to the lossless case, will not be considered, and (3.3a) will be used anyway.

Proceeding, then, with the application of the method of moments to (3.3) according to §1.6,

$$\mathbf{J} = \sum_{j=0}^{n-1} \alpha_j \mathbf{b}_j \quad (3.5)$$

and

$$\mathbf{E}^s = \sum_{j=0}^{n-1} \alpha_j \mathbf{E}_j \quad (3.6)$$

where [cf (2.16–2.19)]

$$\mathbf{E}_j = -j\omega \mathbf{A}_j - \text{grad } \Phi_j \quad (3.7)$$

When substituted in (3.3) or (3.3b), (3.7) will produce the mixed potential form of the EFIE, which is called the MPIE. For each of the terms of the field expansion (3.6), we have

$$\begin{aligned} \mathbf{A}_j &= \bar{\bar{A}} * \mathbf{b}_j \\ \Phi_j &= \frac{1}{j\omega} (\text{div}' \bar{\bar{\Phi}}) * \mathbf{b}_j \end{aligned} \quad (3.8)$$

Integrating by parts the scalar potential [cf (2.18)]

$$\Phi_j = -\frac{1}{j\omega} \bar{\bar{\Phi}} * \text{grad}' \mathbf{b}_j + \frac{1}{j\omega} \int_{\partial S'} (\bar{\bar{\Phi}} \cdot \mathbf{b}_j) \cdot \hat{\mathbf{n}}^s \quad (3.9)$$

The subdomain S' is composed of two cells S'_+ and S'_- . The boundary is then $\partial S' = \partial S'_+ + \partial S'_-$. The line integral of (3.9) becomes

$$\int_{\partial S'_+} (\bar{\bar{\Phi}} \cdot \mathbf{b}_{j+}) \cdot \hat{\mathbf{n}}_+^s - \int_{\partial S'_-} (\bar{\bar{\Phi}} \cdot \mathbf{b}_{j-}) \cdot \hat{\mathbf{n}}_-^s \quad (3.10)$$

In a homogeneous space or in a PC grounded half-space, $\bar{\bar{\Phi}}$ is simply $G^\Phi \bar{\bar{I}}$ and this is continuous in \mathbf{r}' . The RWG basis functions satisfy $\mathbf{b}_{j+} \cdot \hat{\mathbf{n}}_+^s = \mathbf{b}_{j-} \cdot \hat{\mathbf{n}}_-^s = 1$ on the common border of $\partial S'$, 0 elsewhere on $\partial S'$ (§3.1). For these reasons (3.10) is zero [113].

In a layered medium, only strictly vertical or horizontal $\mathbf{b}_{i\pm}$ will be considered. Because $\bar{\bar{\Phi}} = \bar{\bar{I}}_t \Phi_u + \hat{\mathbf{z}} \hat{\mathbf{z}} \Phi_z$, this condition allows $(\bar{\bar{\Phi}} \cdot \mathbf{b}_{j\pm}) \cdot \hat{\mathbf{n}}_\pm^s$ to be written as $\Phi_{u/z}(\mathbf{b}_{j\pm} \cdot \hat{\mathbf{n}}_\pm^s)$,

and to restrict the integration domain of (3.10) to the common edge. Indeed, (3.10) can now be written (cf [21, (10)])

$$\begin{aligned} & \int_{\partial S'+} (\Phi_u \mathbf{b}_{j+} + (\Phi_z - \Phi_u) \mathbf{b}_{j+} \cdot \hat{\mathbf{z}} \hat{\mathbf{z}}) \cdot \hat{\mathbf{n}}_+^s \\ & - \int_{\partial S'-} (\Phi_u \mathbf{b}_{j-} + (\Phi_z - \Phi_u) \mathbf{b}_{j-} \cdot \hat{\mathbf{z}} \hat{\mathbf{z}}) \cdot \hat{\mathbf{n}}_-^s \end{aligned} \quad (3.11)$$

Φ_u is source continuous everywhere [cf (2.20b)], but Φ_z is discontinuous when \mathbf{r}' crosses a dielectric interface [cf (2.20f)]. We write Φ_z^+ or Φ_z^- for Φ_z on either S_+ or S_- , and (3.11) can be simplified into

$$\int_{\partial S'} \Phi_u (\mathbf{b}_{j+} \cdot \hat{\mathbf{n}}_+^s - \mathbf{b}_{j-} \cdot \hat{\mathbf{n}}_-^s) \quad (3.12a)$$

$$+ \int_{\partial S'} (\Phi_z^+ - \Phi_u) \mathbf{b}_{j+} \cdot \hat{\mathbf{z}} \hat{\mathbf{z}} \cdot \hat{\mathbf{n}}_+^s - (\Phi_z^- - \Phi_u) \mathbf{b}_{j-} \cdot \hat{\mathbf{z}} \hat{\mathbf{z}} \cdot \hat{\mathbf{n}}_-^s \quad (3.12b)$$

(3.12a) is always zero. To lighten the notation, the symbol

$$\lambda_{j\pm} \equiv \hat{\mathbf{n}}_{j\pm}^s \cdot \hat{\mathbf{z}} \hat{\mathbf{z}} \cdot \hat{\mathbf{n}}_{j\pm}^s \quad (3.13)$$

is introduced. Its meaning is straightforward: it is 0 for half-bases directed perpendicularly to $\hat{\mathbf{z}}$, and 1 for half-bases directed along $\hat{\mathbf{z}}$. We enumerate the cases in which (3.12b) will differ from zero:

P5 Cases in which source line integral is $\neq 0$

1. Precisely one of $\lambda_{j\pm} = 0$; the other is then 1. Put in words, the cell couple is a ‘corner’ basis function [46]
2. None of $\lambda_{j\pm} = 0$, in which case both are 1, and $\Phi_z^+ \neq \Phi_z^-$; this is a vertical basis function that straddles a dielectric interface.

In both cases, the result is a line integral whose integrand is the difference of two scalar potential Green’s functions evaluated at the same source points. It has been shown (§P4) that the singular behavior of all these functions is the same, which means that this integrand is regular.

To summarize, the general form of the scalar potential in layered media is restated from (3.9) and (3.12b) (cf [80, (14)])

$$\begin{aligned} \Phi_j &= -\frac{1}{j\omega} \bar{\bar{\Phi}} * \text{grad}' \mathbf{b}_j \\ &+ \frac{1}{j\omega} \int_{\partial S'} (\Phi_z^+ - \Phi_u) \lambda_{j+} - (\Phi_z^- - \Phi_u) \lambda_{j-} \end{aligned} \quad (3.14)$$

with the caveat that the line integral term, which appears in non-trivial layered media, is valid only for strictly vertical and horizontal source currents.

Testing of (3.3b) produces

$$\sum_{j=0}^{n-1} \alpha_j \langle \mathbf{t}_i, \mathbf{E}_j \rangle = -\langle \mathbf{t}_i, \mathbf{E}^i \rangle + Z_s \langle \mathbf{J}_i, \mathbf{J}_i \rangle, \quad i = 0..n-1 \quad (3.15)$$

where

$$\langle \mathbf{t}_i, \mathbf{E}_j \rangle = -j\omega \langle \mathbf{t}_i, \mathbf{A}_j \rangle - \langle \mathbf{t}_i, \text{grad } \Phi_j \rangle \quad (3.16)$$

The products $\times \hat{\mathbf{n}}$ of (3.3b) become superfluous because \mathbf{t}_i is tangential to the metallic surface. Integrating the second term of (3.16) by parts,

$$\langle \mathbf{t}_i, \text{grad } \Phi_j \rangle = \int_{\partial S} \Phi_j \mathbf{t}_i \cdot \hat{\mathbf{n}}^s - \langle \text{div } \mathbf{t}_i, \Phi_j \rangle \quad (3.17)$$

The argument of (3.9–3.14) could now be repeated. In this case, the line integral is always zero because Φ_j is a scalar and because it is continuous in \mathbf{r} .

Substituting (3.14) into (3.17) and the result together with $\mathbf{A}_j = \bar{\bar{A}} * \mathbf{b}_j$ into (3.16), we arrive at the final reaction-type integrals.

$$\langle \mathbf{t}_i, \mathbf{E}_j \rangle = -j\omega \langle \mathbf{t}_i, \bar{\bar{A}} * \mathbf{b}_j \rangle \quad (3.18a)$$

$$- \frac{1}{j\omega} \langle \text{div } \mathbf{t}_i, \bar{\bar{\Phi}} * \text{grad}' \mathbf{b}_j \rangle \quad (3.18b)$$

$$+ \frac{1}{j\omega} \langle \text{div } \mathbf{t}_i, \int_{\partial S'} (\Phi_z^+ - \Phi_u) \lambda_{j+} - (\Phi_z^- - \Phi_u) \lambda_{j-} \rangle \quad (3.18c)$$

To compute each of (3.18) we conform to the following procedure:

P6 2.5D recipe for surface patches

1. All the vertical integrations (either in the convolution or in the test) are grouped together with the Green's function. Depending on the relative orientation of basis and test (half-)functions, once-, twice- or non-integrated Green's functions are produced. These vertical integrations are introduced under the Sommerfeld transform to operate on transmission line Green's functions, whose dependence on the vertical coordinates is known in closed form [cf §2.4 and (2.35)]. The vertical integrations are then performed *analytically* (§2.5).
2. The spatial-domain singularity or the most important quasi-singularity of the (integrated) Green's function is identified. This singularity has the form of a static free-space Green's function, or a sum of terms of that form. It is extracted from the (integrated) Green's function, either in the spectral domain or in the spatial domain, on convenience.
3. The extracted part is integrated over the source region analytically. The regular remainder is computed with numerical quadratures (§C).

The precise way in which this procedure is carried out depends on the relative orientation (horizontal, vertical) of both basis and test function, and the orientation of their support cell. It is important to remark that, if $\langle \mathbf{t}_i, \mathbf{E}_j \rangle$ is split

$$\langle \mathbf{t}_i, \mathbf{E}_j \rangle = \langle \mathbf{t}_{i+}, \mathbf{E}_{j+} \rangle - \langle \mathbf{t}_{i+}, \mathbf{E}_{j-} \rangle - \langle \mathbf{t}_{i-}, \mathbf{E}_{j+} \rangle + \langle \mathbf{t}_{i-}, \mathbf{E}_{j-} \rangle \quad (3.19)$$

each of the four terms in (3.19) contains both source and test line integrals *in every case*, even in free space. It is only when they are summed up that most (or, in free space or in special cases, all) of them cancel and it is possible to write (3.18). In other words, (3.18) is *not valid* for half-function/half-function reactions, not even when (3.18c) is zero. But the computation is to

be done by actually splitting (3.18) as in (3.19), and then adding the line integral if so needed, according to the matrix fill algorithm of [113, end of §II]. It is in this sense that

$$\begin{aligned} \langle \mathbf{t}_{i\pm}, \mathbf{E}_{j\pm} \rangle^* &\equiv -j\omega \langle \mathbf{t}_{i\pm}, \bar{A} * \mathbf{b}_{j\pm} \rangle \\ &\quad - \frac{1}{j\omega} \langle \text{div } \mathbf{t}_{i\pm}, \bar{\Phi} * \text{grad}' \mathbf{b}_{j\pm} \rangle \end{aligned} \quad (3.20)$$

must be understood, ie, the terms to be cancelled are not written.

In relation to the previous paragraph, a note on the application of reciprocity to the half-function to half-function reaction terms is in order. Because they are computed according to (3.20) and do not include the line integral terms, it is not necessarily true that

$$\langle \mathbf{t}_{i\pm}, \mathbf{E}_{j\pm} \rangle^* = \langle \mathbf{t}_{j\pm}, \mathbf{E}_{i\pm} \rangle^* \quad (3.21)$$

Only if the line integrals vanish in *both* complete reactions $\langle \mathbf{t}_i, \mathbf{E}_j \rangle$ and $\langle \mathbf{t}_j, \mathbf{E}_i \rangle$ does (3.21) hold for any of the terms of (3.19) separately. In particular, if the mixed potential expression of \mathbf{E}_j [from (3.7–3.7)] contains a line integral term, it is not possible to write

$$\langle \mathbf{t}_j, \mathbf{E}_j \rangle = \langle \mathbf{t}_{j+}, \mathbf{E}_{j+} \rangle^* - 2\langle \mathbf{t}_{j\pm}, \mathbf{E}_{j\mp} \rangle^* + \langle \mathbf{t}_{j-}, \mathbf{E}_{j-} \rangle^* \quad (3.22)$$

for the self-interaction, ie $\langle \mathbf{t}_{j+}, \mathbf{E}_{j-} \rangle^*$ and $\langle \mathbf{t}_{j-}, \mathbf{E}_{j+} \rangle^*$ will be different.

This will also mean that the matrix of moments may not be symmetrical because reciprocal elements are computed using different expressions [ie, with and without line integral, or using A_{zu} and Φ_u for type V (§3.2.5) and just Φ_z for type IV (§3.2.4) of table 3.1] that only give the same result when they are evaluated exactly. There should be no problem if they are evaluated with sufficient accuracy. However, if the test integral were approximated with a single sample, the numerical lack of symmetry could be problematic.

To solve this difficulty, a matrix symmetrization procedure has been developed in [18, (32–35)] that divides the line integral between source and observer basis functions; in practice, those elements that are non-symmetric when evaluated approximately are evaluated twice, and then averaged. Our matrix will always be symmetric by the simple expedient of never computing reactions $\langle \mathbf{t}_i, \mathbf{b}_j \rangle$ with $i < j$. A slight (and negligible) asymmetry due to numerical error will be apparent when solving mirrored problems. One such example is presented later (§P7).

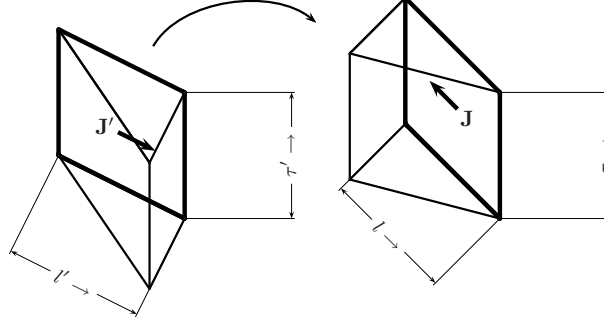
In the forecoming sections, the subindices $i\pm$ or $j\pm$ will be dropped when possible, ie $\mathbf{t}_{i\pm} \rightarrow \mathbf{t}$, or substituted by primes, ie $\tau_{j\pm} \rightarrow \tau'$. The source cell may be horizontal (1) or vertical, and in the latter case, the half-basis function may be oriented horizontally (2) or vertically (3). This gives three possibilities for the half-basis function; times the same three for the half-test function, there results a total of $3 \times 3 = 9$ reaction types. In the extraction of singular terms, factors Λ'_A and Λ'_Φ appear; these factors depend on the parameters of the medium and the position of z, z', τ and τ' relative to layer interfaces, as explained in §2.6.2.

3.2.1 Type I

This is when both observer and source cells are horizontal, $\lambda_{i\pm} = \lambda_{j\pm} = 0$. (3.20) becomes

$$\langle \mathbf{t}_{i\pm}, \mathbf{E}_{j\pm} \rangle = -j\omega \langle \mathbf{t}_{i\pm}, A_{uu} * \mathbf{b}_{j\pm} \rangle \quad (3.23a)$$

$$- \frac{\text{div } \mathbf{t}_{i\pm} \text{div}' \mathbf{b}_{j\pm}}{j\omega} \langle 1, \Phi_u * 1 \rangle \quad (3.23b)$$

Figure 3.2: A $\langle \mathbf{J}, \bar{\bar{E}}^J * \mathbf{J} \rangle$ interaction of type II.

This is also the general form of (3.20) in a free space medium, where $A_{uu} \rightarrow \mu\Psi$, $\Phi_u \rightarrow \Psi/\epsilon$, $\Psi = \frac{e^{-jkR}}{4\pi R}$. (3.23) may have a singularity or quasi-singularity given by

$$\begin{aligned} A_{uu} &= \frac{\Lambda'_A}{R} + A_{uu}^{\text{reg}} \\ \Phi_u &= \frac{\Lambda'_\Phi}{R} + \Phi_u^{\text{reg}} \end{aligned} \quad (3.24)$$

where A_{uu}^{reg} , Φ_u^{reg} are regular everywhere. This assumes that z and z' belong to the same dielectric layer, its boundaries included. The resulting singular or quasi-singular integrals have the same form as in free space and are computed likewise, with [146, (5,7)].*. The constant projection $\hat{\mathbf{e}}_{j\pm}\hat{\mathbf{e}}_{j\pm}$ in the rectangular rooftop (3.2b) can be simply taken out of the vector potential integral, ie

$$\int_{S'} A_{uu}(\mathbf{r} - \mathbf{r}_{j\pm}) \cdot \hat{\mathbf{e}}\hat{\mathbf{e}} = \hat{\mathbf{e}}\hat{\mathbf{e}} \cdot \int_{S'} A_{uu}(\mathbf{r} - \mathbf{r}_{j\pm}) \quad (3.25)$$

leaving the same integral as a triangular rooftop. Note that save the constant factor $\text{div } \mathbf{t}_{i\pm} \text{div}' \mathbf{b}_{j\pm}$, the fourfold integral (3.23b) is common to all half-functions defined over the pair of cells $i\pm, j\pm$, and thus need only be computed once for up to 16 half-test/half-basis reaction terms. On the filling of the moment matrix *by cells*, see the comments after P6 on page 57.

For reactions of this type, the functions

$$A_{uu}(P, z, z') \quad (3.26a)$$

$$\Phi_u(P, z, z') \quad (3.26b)$$

must be tabulated. The argument of these tables is only P ; z, z' are parameters, the vertical position of the cells.

3.2.2 Type II

This is when both observer and source cells are vertical, $\hat{\mathbf{n}} \cdot \hat{\mathbf{z}} = 0$, $\hat{\mathbf{n}}' \cdot \hat{\mathbf{z}}$, but the half-functions are oriented horizontally, that is, $\lambda = \lambda' = 0$, cf (3.13). (As per the 2.5D requirement, only

*For the self-interaction (same source and observer cell) the full integral $\int_S \int_S \mathbf{t}_{i\pm} \mathbf{b}_{j\pm} / R$ can be computed in closed form. For triangles, see [8, table I]; equivalent formulae had been published earlier by [31, (25-29)]. [8] includes useful convergence plots. For rectangles, for example [106, (10.33)], [96, (3.31)].

rectangles can be vertical cells.) The dependence along vertical and horizontal coordinates is separated,

$$\begin{aligned} \int_{S'} \mathbf{b}(\cdot) &= \int_{l'} \mathbf{b} dl' \int_{\tau'} (\cdot) dz' \\ \int_S \mathbf{t}(\cdot) &= \int_l \mathbf{t} dl \int_{\tau} (\cdot) dz \end{aligned} \quad (3.27)$$

and (3.20) can thus be written

$$\langle \mathbf{t}, \mathbf{E} \rangle = -j\omega \langle \mathbf{t}, \int_{\tau} \int_{\tau'} A_{uu} * \mathbf{b} \rangle \quad (3.28a)$$

$$- \frac{\text{div } \mathbf{t} \text{ div}' \mathbf{b}}{j\omega} \langle 1, \int_{\tau} \int_{\tau'} \Phi_u * 1 \rangle \quad (3.28b)$$

Both test and convolution integrals become one-dimensional. The functions

$$f_A(P, \tau, \tau') = \int_{\tau} \int_{\tau'} A_{uu} \quad (3.29a)$$

$$f_{\Phi}(P, \tau, \tau') = \int_{\tau} \int_{\tau'} \Phi_u \quad (3.29b)$$

must be tabulated in advance. These are functions of P only; the source and observer slices are fixed parameters for any given reaction term. The singular or quasi-singular parts of f_A and f_{Φ} can be obtained either by inversion of their asymptotic development when $k_p \rightarrow \infty$, or in a more straightforward way (§2.6), by spatial integration of the singular or quasi-singular parts of A_{uu} , Φ_u . The latter path yields the following:

- If $\tau \neq \tau'$, both f_A and f_{Φ} are regular when $P \rightarrow 0$.
- If $\tau = \tau'$, both f_A and f_{Φ} have a logarithmic singularity given by

$$\begin{aligned} f_A(P, \tau, \tau') &= -\Lambda'_A 2h' \log P + f_A^{\text{reg}} \\ f_{\Phi}(P, \tau, \tau') &= -\Lambda'_{\Phi} 2h' \log P + f_{\Phi}^{\text{reg}} \end{aligned} \quad (3.30)$$

The one-dimensional singular integrals $\int_{l'} \mathbf{b} \log P$, $\int_{l'} \log P$ that appear when one substitutes (3.30) into (3.28) are (surprisingly) typical of two-dimensional problems. Although they are immediate, they are also given by [146, (1,2)].

It is possible to go further and extract (and integrate analytically on l') the whole free-space static part of (3.29). This is advantageous mainly when $\tau \neq \tau'$, when the functions (3.30) are not strictly singular [instead of $\log P$, they have $\log(R + Z)$ with $Z > 0$; cf. (2.52)]. The necessary line and surface integrals can be found in §A. However, if the two interacting cells are not in the same dielectric layer, or even if they begin or end at an interface, the residual corresponding to homogeneous space cannot be used—that is valid only for the strictly singular case (see §2.6.3).

3.2.3 Type III

This is when both observer and source cells are vertical, $\hat{\mathbf{n}} \cdot \hat{\mathbf{z}} = 0$, and the half-functions are oriented vertically, $\lambda = \lambda' = 1$. The dependence along vertical and horizontal coordinates is separated [cf (3.27)]

$$\int_{S'} \mathbf{b}(\cdot) = \hat{\mathbf{z}} \int_{l'} dl' \int_{\tau'} b(z')(\cdot) dz' \quad (3.31a)$$

$$\int_S \mathbf{t}(\cdot) = \hat{\mathbf{z}} \int_l dl \int_{\tau} t(z)(\cdot) dz \quad (3.31b)$$

and (3.20) can now be written (the vector potential integral becomes a scalar integral, as $\hat{\mathbf{z}} \cdot \hat{\mathbf{z}} = 1$; we assume that there is no line integral)

$$\langle \mathbf{t}, \mathbf{E} \rangle = -j\omega \langle 1, \int_{\tau} t(z) \int_{\tau'} b(z') A_{zz} * 1 \rangle \quad (3.32a)$$

$$- \frac{\text{div } \mathbf{t} \text{ div}' \mathbf{b}}{j\omega} \langle 1, \int_{\tau} \int_{\tau'} \Phi_z * 1 \rangle \quad (3.32b)$$

The scalar potential integral (3.32b) is the same as in (3.28b), up to a constant factor. In the vector potential integral (3.32a), both convolution and test integrals become one-dimensional, as in §3.2.2. The function

$$f_A(P, \tau, \tau') = \int_{\tau} t(z) \int_{\tau'} b(z') A_{zz} \quad (3.33)$$

must be tabulated. As before, this is only function of P ; τ, τ' are fixed parameters for any given pair of observer and source cells. An important point is that (3.33) represents up to four functions, because on each slice $\tau = (z_0, z_1)$, $\tau' = (z'_0, z'_1)$ there are two possible vertically oriented half basis, viz

$$\begin{aligned} \overrightarrow{b}(z') &= \frac{l'}{A'}(z' - z'_0) & \overrightarrow{t}(z) &= \frac{l}{A}(z - z_0) \\ \overleftarrow{b}(z') &= \frac{l'}{A'}(z'_1 - z') & \overleftarrow{t}(z) &= \frac{l}{A}(z_1 - z) \end{aligned} \quad (3.34)$$

and (3.33) must be tabulated in advance for all four combinations. (Note that there are four even if $\tau = \tau'$).

It has been shown [see §2.6.3, (2.52)] that, like (3.29), (3.33) is regular whenever $\tau \neq \tau'$, and otherwise it has a logarithmic singularity, which in this case is given by

$$f_A(P, \tau, \tau') = -\frac{\Lambda'_A}{Q} h' \log P + f_A^{\text{reg}} \quad (3.35a)$$

$$(3.35b)$$

with the factor Q

$$\begin{aligned} +3 & \quad \text{if either } t = \overrightarrow{t}, b = \overrightarrow{b} \text{ or } t = \overleftarrow{t}, b = \overleftarrow{b} \\ -6 & \quad \text{if either } t = \overrightarrow{t}, b = \overleftarrow{b} \text{ or } t = \overleftarrow{t}, b = \overrightarrow{b} \end{aligned} \quad (3.35c)$$

as presented in table 2.4. The difference in sign for the second case is due to the different orientation of the rooftop here and the function $d(z)$ in that table.

3.2.4 Type IV

In this case, both source and observer cell are vertical, but $\lambda = 0$ and $\lambda' = 1$. The dependence of the half test function is separated like (3.27), while that of the half basis function is separated like (3.31).

$$\int_{S'} \mathbf{b}(\cdot) = \hat{\mathbf{z}} \int_{l'} dl' \int_{\tau'} b(z')(\cdot) dz' \quad (3.36a)$$

$$\int_S \mathbf{t}(\cdot) = \int_l \mathbf{t} dl \int_{\tau} (\cdot) dz \quad (3.36b)$$

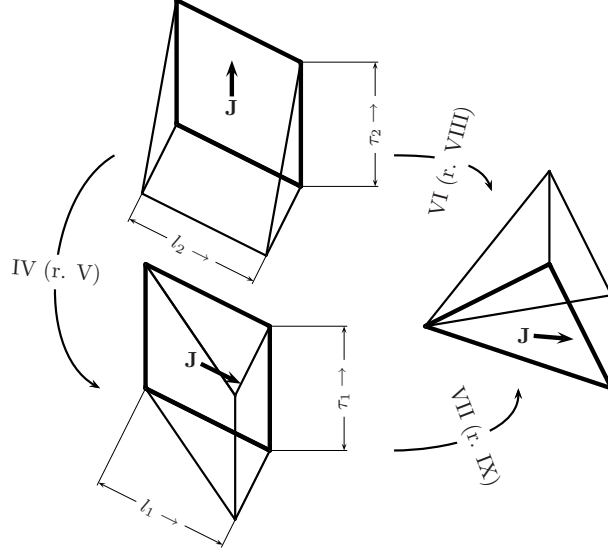


Figure 3.3: $\langle \mathbf{J}, \bar{\bar{E}}^J * \mathbf{J} \rangle$ interactions of types IV (recipr. V) VI (recipr. VIII) and VII (recipr. IX).

The salient characteristic of this type is that, due to Sommerfeld's Choice for the vector potential dyadic (§2.3) there is no vector potential term. Now (3.20) becomes

$$\langle \mathbf{t}, \mathbf{E} \rangle = -\frac{\text{div } \mathbf{t} \text{ div}' \mathbf{b}}{j\omega} \langle 1, \int_{\tau} \int_{\tau'} \Phi_z * 1 \rangle \quad (3.37)$$

which is the same scalar potential integral as (3.32b), up to a constant factor, and can be regularized in the same exact way.

3.2.5 Type V

This case is the reciprocal of type IV: both cells are similarly vertical, but here $\lambda = 1$ and $\lambda' = 0$. The separation is given by

$$\int_{S'} \mathbf{b}(\cdot) = \int_{l'} \mathbf{b} dl' \int_{\tau'} (\cdot) dz' \quad (3.38a)$$

$$\int_S \mathbf{t}(\cdot) = \hat{\mathbf{z}} \int_l dl \int_{\tau} t(z)(\cdot) dz \quad (3.38b)$$

The reaction (3.20) is now

$$\langle \mathbf{t}, \mathbf{E} \rangle = -j\omega \langle 1, \int_{\tau} t(z) \int_{\tau'} A_{zb} * b(l') \rangle \quad (3.39a)$$

$$- \frac{\text{div } \mathbf{t} \text{ div}' \mathbf{b}}{j\omega} \langle 1, \int_{\tau} \int_{\tau'} \Phi_u * 1 \rangle \quad (3.39b)$$

\mathbf{b} being $\hat{\mathbf{b}}b(l')$. The scalar potential term is like (3.28b). For the vector potential part, we have (cf [78, (54–55)])

$$A_{zb}(P) = -j \cos(\phi - \phi_b) \mathcal{S}_1 \{ A_{zu}(k_p) \} \quad (3.40)$$

with $\cos(\phi - \phi_b) = \hat{\mathbf{R}} \cdot \hat{\mathbf{b}}$. Therefore (3.39a) requires the tabulation of

$$f_A(P, \tau, \tau') = \int_{\tau} t(z) \int_{\tau'} \mathcal{S}_1\{A_{zu}\} \quad (3.41)$$

$$f_{\Phi}(P, \tau, z') = \int_{\tau} \int_{\tau'} \Phi_u \quad (3.42)$$

which represents two functions, depending on whether $t(z) = \overrightarrow{t}(z)$ or $t(z) = \overleftarrow{t}(z)$. These terms are not singular, and their spectral quasistatic part is not, in any case, invertible in closed form; it is no use extracting it.

3.2.6 Type VI

Here the source cell is vertical and the observer cell horizontal; on the source cell, we have $\lambda' = 0$. The separation is

$$\int_{S'} \mathbf{b}(\cdot) = \int_{l'} \mathbf{b} dl' \int_{\tau'} (\cdot) dz' \quad (3.43)$$

The reaction (3.20) becomes

$$\langle \mathbf{t}, \mathbf{E} \rangle = -j\omega \langle \mathbf{t}, \int_{\tau'} A_{uu} * \mathbf{b} \rangle \quad (3.44a)$$

$$- \frac{\text{div } \mathbf{t} \text{ div}' \mathbf{b}}{j\omega} \langle 1, \int_{\tau'} \Phi_u * 1 \rangle \quad (3.44b)$$

The required spatial-domain functions are

$$f_A(P, z, \tau') = \int_{\tau'} A_{uu} \quad (3.45a)$$

$$f_{\Phi}(P, z, \tau') = \int_{\tau'} \Phi_u \quad (3.45b)$$

If z touches τ' (ie, either $z = z'_0$ or $z = z'_1$) functions (3.45) have a logarithmic singularity when $P \rightarrow 0$, which is given by

$$\begin{aligned} f_A(P, z, \tau') &= -\Lambda'_A \log P + f_A^{\text{reg}} \\ f_{\Phi}(P, z, \tau') &= -\Lambda'_{\Phi} \log P + f_{\Phi}^{\text{reg}} \end{aligned} \quad (3.46)$$

3.2.7 Type VII

This case is like in §3.2.6, but $\lambda' = 1$. The separation is

$$\int_{S'} \mathbf{b}(\cdot) = \hat{\mathbf{z}} \int_{l'} dl' \int_{\tau'} b(z')(\cdot) dz' \quad (3.47)$$

There is no vector potential term, like in §3.2.4. The reaction takes the form

$$\langle \mathbf{t}, \mathbf{E} \rangle = - \frac{\text{div } \mathbf{t} \text{ div}' \mathbf{b}}{j\omega} \langle 1, \int_{\tau'} \Phi_z * 1 \rangle \quad (3.48)$$

which requires the tabulation of

$$f_A(P, z, \tau') = \int_{\tau'} \Phi_z \quad (3.49)$$

The singularity exists in the same cases and is extracted in the same exact way as (3.46), save that Φ_z takes the place of Φ_u .

3.2.8 Type VIII

This is the reciprocal of type VI. The separation is

$$\int_S \mathbf{t}(\cdot) = \int_l \mathbf{t} dl \int_\tau (\cdot) dz \quad (3.50)$$

The reaction takes the form

$$\langle \mathbf{t}, \mathbf{E} \rangle = -j\omega \langle \mathbf{t}, \int_\tau A_{uu} * \mathbf{b} \rangle \quad (3.51a)$$

$$- \frac{\text{div } \mathbf{t} \text{ div}' \mathbf{b}}{j\omega} \langle 1, \int_\tau \Phi_u * 1 \rangle \quad (3.51b)$$

which requires the tabulation of

$$f_A(P, \tau, z') = \int_\tau A_{uu} \quad (3.52a)$$

$$f_\Phi(P, \tau, z') = \int_\tau \Phi_u \quad (3.52b)$$

These are singular when $P \rightarrow 0$ if z' touches τ (ie, either $z' = z_0$ or $z' = z_1$); the regularization is

$$\begin{aligned} f_A(P, \tau, z') &= -\Lambda'_A \log P + f_A^{\text{reg}} \\ f_\Phi(P, \tau, z') &= -\Lambda'_\Phi \log P + f_\Phi^{\text{reg}} \end{aligned} \quad (3.53)$$

3.2.9 Type IX

The *last* case is the reciprocal of type VII (§3.2.7). The separation is

$$\int_S \mathbf{t}(\cdot) = \hat{\mathbf{z}} \int_l dl \int_\tau t(z)(\cdot) dz \quad (3.54)$$

The reaction term is much like that of type V (3.39),

$$\langle \mathbf{t}, \mathbf{E} \rangle = -j\omega \langle 1, \int_\tau t(z) (A_{zx} \hat{\mathbf{x}} + A_{zy} \hat{\mathbf{y}}) * \mathbf{b} \rangle \quad (3.55a)$$

$$- \frac{\text{div } \mathbf{t} \text{ div}' \mathbf{b}}{j\omega} \langle 1, \int_\tau \Phi_u * 1 \rangle \quad (3.55b)$$

If the half basis function is rectangular, the convolution of (3.55a) can be simplified to $\int_\tau t(z) A_{zb} * b(z')$, but not in general. Here we would use the cartesian components

$$\begin{aligned} A_{zx}(P) &= -j \cos(\phi) \mathcal{S}_1 \{ A_{zu}(k_p) \} \\ A_{zy}(P) &= -j \sin(\phi) \mathcal{S}_1 \{ A_{zu}(k_p) \} \end{aligned} \quad (3.56)$$

and the functions to be tabulated are now

$$f_A(P, \tau, z') = \int_\tau t(z) \mathcal{S}_1 \{ A_{zu} \} \quad (3.57a)$$

$$f_\Phi(P, \tau, z') = \int_\tau t(z) \Phi_u \quad (3.57b)$$

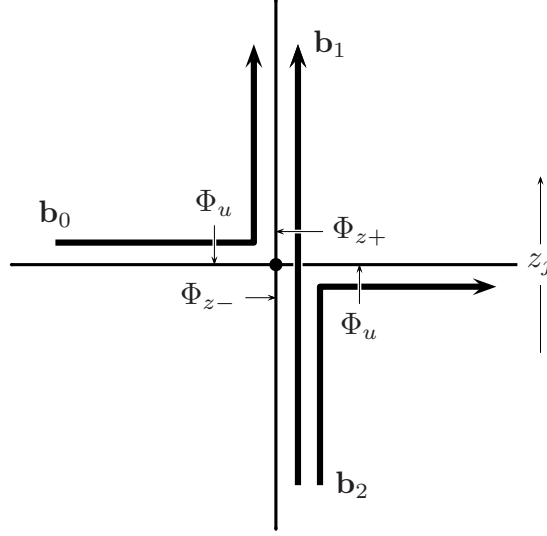


Figure 3.4: Three basis functions and three Φ Green's functions on a corner. With the restriction to 2.5D structures, no more than 4 cells can meet at a corner, that is, three basis functions (because of $\sum J = 0$ at the corner). The ones depicted here have: $\lambda_{0+} = 0, \lambda_{0-} = 1$; $\lambda_{1+} = 1, \lambda_{1-} = 1$; $\lambda_{2+} = 1, \lambda_{2-} = 0$ [cf (3.13, 3.58)].

3.2.10 Line integral

The line integral term (3.18c) can have two forms depending on the orientation of the observer cell. Adopting the re-simplified notation

$$\langle \text{div } \mathbf{t}_i, \int_{\partial S'} (\Phi_z^+ - \Phi_u) \lambda_{j+} - (\Phi_z^- - \Phi_u) \lambda_{j-} \rangle = \langle \text{div } \mathbf{t}, \int_{\partial S'} \Delta \Phi \rangle \quad (3.58)$$

If the observer cell is horizontal, (3.58) is

$$\text{div } \mathbf{t} \langle 1, \int_{\partial S'} \Delta \Phi \rangle \quad (3.59a)$$

and we need to tabulate

$$f_{\Delta \Phi}(P, z, z') = \Delta \Phi \quad (3.59b)$$

If the source cell is vertical, (3.58) becomes instead

$$\text{div } \mathbf{t} \langle 1, \int_{\partial S'} \int_{\tau} \Delta \Phi \rangle \quad (3.60a)$$

and need to tabulate

$$f_{\Delta \Phi}(P, \tau, z') = \int_{\tau} \Delta \Phi \quad (3.60b)$$

In fact (3.59b, 3.60b) represent three different tables, depending on whether

$$\pm \Delta \Phi = \begin{cases} \Phi_{z+} - \Phi_u \\ \Phi_{z-} - \Phi_u \\ \Phi_{z+} - \Phi_{z-} \end{cases} \quad (3.61)$$

(see fig. 3.4) where $\Phi_{z\pm}$ is $\lim_{u \rightarrow z'^{\pm}} \Phi_z(u)$. Each of (3.61) is a linear combination of the other two, so that in the worst case two tables would be required. Also, as explained above, these integrals are always regular.

3.2.11 Summary

The contents of §3.2.1–3.2.10 have been summarized in table 3.1.

3.3 Apertures

The problem of an arbitrarily shaped aperture in an infinite, thin conducting screen is most detailedly treated by [53] and in the review article [17] an extensive, if outdated, bibliography may be found. It is briefly reviewed here to establish the notation and as an introduction to the more general problem with both electric and magnetic currents (§3.3.1).

The continuity of the magnetic field can be guaranteed by enforcing continuity of its tangential component across the surface of the aperture.

$$\hat{\mathbf{n}} \times (\bar{\bar{H}}_+^M * \mathbf{M}_+ - \bar{\bar{H}}_-^M * \mathbf{M}_-) = -\hat{\mathbf{n}} \times (\mathbf{H}_+^i - \mathbf{H}_-^i) \quad (3.62a)$$

On the other hand, the tangential electric field on the aperture is represented by the magnetic currents through (1.3), because in the equivalent problem, fields on the other side are zero. It, too, must be continuous, which leads to the condition $\mathbf{M}_+ = -\mathbf{M}_-$. Thus (3.62a) becomes

$$\hat{\mathbf{n}} \times ([\bar{\bar{H}}_+^M + \bar{\bar{H}}_-^M] * \mathbf{M}_+) = -\hat{\mathbf{n}} \times (\mathbf{H}_+^i - \mathbf{H}_-^i) \quad (3.62b)$$

The magnetic current expansion

$$\mathbf{M} \equiv \mathbf{M}_+ = \sum_{j=0}^{m-1} \alpha_j \mathbf{b}_j \quad (3.63)$$

gives the decomposition of the scattered magnetic field (at each side of the aperture surface)

$$\bar{\bar{H}}_{\pm}^M * \mathbf{M}_{\pm} = \mathbf{H}_{\pm}^s = \sum_{j=0}^{m-1} \alpha_j \mathbf{H}_{j\pm} \quad (3.64)$$

where

$$\mathbf{H}_{j\pm} = -j\omega \mathbf{F}_{j\pm} - \text{grad } W_{j\pm} \quad (3.65)$$

In layered media, we shall consider only horizontal magnetic currents. (The general case does not present particular difficulty; the required developments are parallel to those in §3.2. In free space or homogeneous half space with perfect ground plane, however, just as with \mathbf{J} , arbitrary 3D orientation will be allowed for \mathbf{M}). With this restriction, $\bar{\bar{W}} \rightarrow W_u$ [cf (3.8)] and

$$\begin{aligned} \mathbf{F}_{j\pm} &= \pm \bar{\bar{F}}_{\pm} * \mathbf{b}_j \\ W_{j\pm} &= \pm \frac{1}{j\omega} (\text{grad}' W_{u\pm}) * \mathbf{b}_j \end{aligned} \quad (3.66)$$

A development identical to that leading to (3.18) yields here the linear system

$$\sum_{j=0}^{m-1} \alpha_j \langle \mathbf{t}_i, \mathbf{H}_{+j} - \mathbf{H}_{-j} \rangle = -\langle \mathbf{t}_i, \mathbf{H}_+^i - \mathbf{H}_-^i \rangle, \quad i = 0..n-1 \quad (3.67)$$

| <i>type</i> | <i>indices of</i> | <i>required tables</i> | <i>dT</i> | <i>dC</i> | <i>singular kernel</i> | <i>r-type</i> |
|-------------|-------------------|---|-----------|-----------|--|------------------|
| fs | - | | 2 | 2 | R^{-1} | fs |
| I | z, z' | A_{uu} Φ_u | 2 | 2 | R^{-1} | I |
| II | τ, τ' | $\int_{\tau} \int_{\tau'} A_{uu}$ $\int_{\tau} \int_{\tau'} \Phi_u$ | 1 | 1 | $-\log P (\tau = \tau')$ | II |
| III | τ, τ' | $\int_{\tau} \overrightarrow{t}(z) \int_{\tau'} \overrightarrow{b}(z') A_{zz}$ $\int_{\tau} \overrightarrow{t}(z) \int_{\tau'} \overleftarrow{b}(z') A_{zz}$ $\int_{\tau} \overleftarrow{t}(z) \int_{\tau'} \overrightarrow{b}(z') A_{zz}$ $\int_{\tau} \overleftarrow{t}(z) \int_{\tau'} \overleftarrow{b}(z') A_{zz}$ $\int_{\tau} \int_{\tau'} \Phi_z$ | 1 | 1 | $-\log P (\tau = \tau')$ | III ^a |
| IV | τ, τ' | $\int_{\tau} \int_{\tau'} \Phi_z$ | 1 | 1 | $-\log P (\tau = \tau')$ | V |
| V | τ, τ' | $\int_{\tau} \overrightarrow{t}(z) \int_{\tau'} \mathcal{S}_1\{A_{zu}\}$ $\int_{\tau} \overleftarrow{t}(z) \int_{\tau'} \mathcal{S}_1\{A_{zu}\}$ $\int_{\tau} \int_{\tau'} \Phi_u$ | 1 | 1 | (none) (none) $-\log P (\tau = \tau')$ | IV |
| VI | z, τ' | $\int_{\tau'} A_{uu}$ $\int_{\tau'} \Phi_u$ | 2 | 1 | $-\log P (z \in \tau')$ | VIII |
| VII | z, τ' | $\int_{\tau'} \Phi_z$ | 2 | 1 | $-\log P (z \in \tau')$ | IX |
| VIII | τ, z' | $\int_{\tau} A_{uu}$ $\int_{\tau} \Phi_u$ | 1 | 2 | $-\log P (z' \in \tau)$ | VI |
| IX | τ, z' | $\int_{\tau} \overrightarrow{t}(z) \mathcal{S}_1\{A_{zu}\}$ $\int_{\tau} \overleftarrow{t}(z) \mathcal{S}_1\{A_{zu}\}$ $\int_{\tau} \Phi_u$ | 1 | 2 | (none) (none) $-\log P (z' \in \tau)$ | VII |
| line Ia | z, z' | $\Phi_{z+} - \Phi_u$ | 2 | 1 | (none) | - |
| line IIa | τ, z' | $\int_{\tau} (\Phi_{z+} - \Phi_u)$ | 1 | 1 | (none) | - |
| line Ib | z, z' | $\Phi_{z-} - \Phi_u$ | 2 | 1 | (none) | - |
| line IIb | τ, z' | $\int_{\tau} (\Phi_{z-} - \Phi_u)$ | 1 | 1 | (none) | - |

^awith exchange of b and t

Table 3.1: Reaction terms of type $\langle \mathbf{J}, \bar{\bar{E}}^J * \mathbf{J} \rangle$. Legend: fs=free space; dC=dimension of spatial convolution integral; dT=dimension of spatial test integral; r-type=reciprocal type.

with the reaction terms

$$\langle \mathbf{t}_i, \mathbf{H}_{+j} - \mathbf{H}_{-j} \rangle = -j\omega \langle \mathbf{t}_i, (\bar{\bar{F}}_+ + \bar{\bar{F}}_-) * \mathbf{b}_j \rangle \quad (3.68a)$$

$$- \frac{1}{j\omega} \langle \text{div } \mathbf{t}_i, (W_{u+} + W_{u-}) * \text{div}' \mathbf{b}_j \rangle \quad (3.68b)$$

with the caveat that the inner product (test integral) in (3.68) is now

$$\langle \mathbf{t}_i, \mathbf{H}_j \rangle = - \int_S \mathbf{t}_i \cdot \mathbf{H}_j \quad (3.69)$$

due to the definition of the inner product as a reaction integral, cf (1.12). It will be assumed that magnetic currents only appear in layered media to model apertures on horizontal ground planes. There might n_a apertures sandwiched between $n_a + 1$ layered media; if so, there will be n_a equations (3.67), each with $[+ \rightarrow a+]$, $[- \rightarrow a-]$, where a is the (ordered) index of the aperture going from 0 to $n_a - 1$. The computation of the reaction terms of this system requires that

$$f_F(P, z, z') = (F_{uu+} + F_{uu-}) \quad (3.70a)$$

$$f_W(P, z, z') = (W_{u+} + W_{u-}) \quad (3.70b)$$

be tabulated for each couple of contiguous aperture layers $(z, z') = (z_a, z_{a+1})$. The regularization of (3.70) is handled in the same way as $\langle \mathbf{J}, \bar{\bar{E}}^J * \mathbf{J} \rangle$ reactions of type I [§3.2.1, (3.24)]. The medium $[+]$ will always be the medium *above* the aperture, and the medium $[-]$ the one below. Therefore the reference normal for the definition of $\mathbf{M}_+ \equiv \mathbf{M}$ will be $+\hat{\mathbf{z}}$, so $\mathbf{M} = \mathbf{E} \times \hat{\mathbf{z}}$.

3.3.1 Apertures and metallic scatterers

The coupled integral equations are directly obtained from (3.62b), enforced at apertures, by adding electric currents as sources of \mathbf{H}^s , and from (3.3b), enforced at the surface of metallic scatterers, by adding aperture magnetic currents as sources of \mathbf{E}^s (see fig. 3.5),

$$\begin{aligned} \hat{\mathbf{n}} \times ((\bar{\bar{H}}_a^M + \bar{\bar{H}}_{a-1}^M) * \mathbf{M}_a + \bar{\bar{H}}_a^J * \mathbf{J}_a - \bar{\bar{H}}_{a-1}^J * \mathbf{J}_{a-1}) \\ = -\hat{\mathbf{n}} \times (\mathbf{H}_a^i - \mathbf{H}_{a-1}^i), \quad a = 0 \dots n_a - 1 \end{aligned} \quad (3.71a)$$

$$\begin{aligned} \hat{\mathbf{n}} \times (\bar{\bar{E}}^J * \mathbf{J}_a + \bar{\bar{E}}_a^M * \mathbf{M}_a - \bar{\bar{E}}_a^M * \mathbf{M}_{a+1}) \\ = -\hat{\mathbf{n}} \times (\mathbf{E}_a^i - Z_s \mathbf{J}_a), \quad a = -1 \dots n_a \end{aligned} \quad (3.71b)$$

It is understood that all the Green's functions in (3.71) are zero if source and observer are not on the same side of *every* aperture. The magnetic and electric current distributions are then discretized in the same way as shown above (3.63–3.5). Now some of the basis functions \mathbf{b}_j will represent \mathbf{J} and others \mathbf{M} ; the distinction will be pointed out when needed. Still Galerkin ($\mathbf{t}_i = \mathbf{b}_i \forall i$) will be assumed.

(3.71) produces two new types of reaction terms,

$$\langle \mathbf{t}_i, \bar{\bar{H}}^J * \mathbf{b}_j \rangle = - \int_S \mathbf{t}_i \cdot \int_{S'} \bar{\bar{H}}^J \cdot \mathbf{b}_j \quad (3.72a)$$

$$\langle \mathbf{t}_i, \bar{\bar{E}}^M * \mathbf{b}_j \rangle = + \int_S \mathbf{t}_i \cdot \int_{S'} \bar{\bar{E}}^M \cdot \mathbf{b}_j \quad (3.72b)$$

Due to the reciprocity relation (1.13c), $\langle \mathbf{t}_j, \bar{\bar{H}}^J * \mathbf{b}_i \rangle$ and $\langle \mathbf{t}_i, \bar{\bar{E}}^M * \mathbf{b}_j \rangle$ are equal, so only one of them is needed; this will be $\langle \mathbf{t}_i, \bar{\bar{E}}^M * \mathbf{b}_j \rangle$.

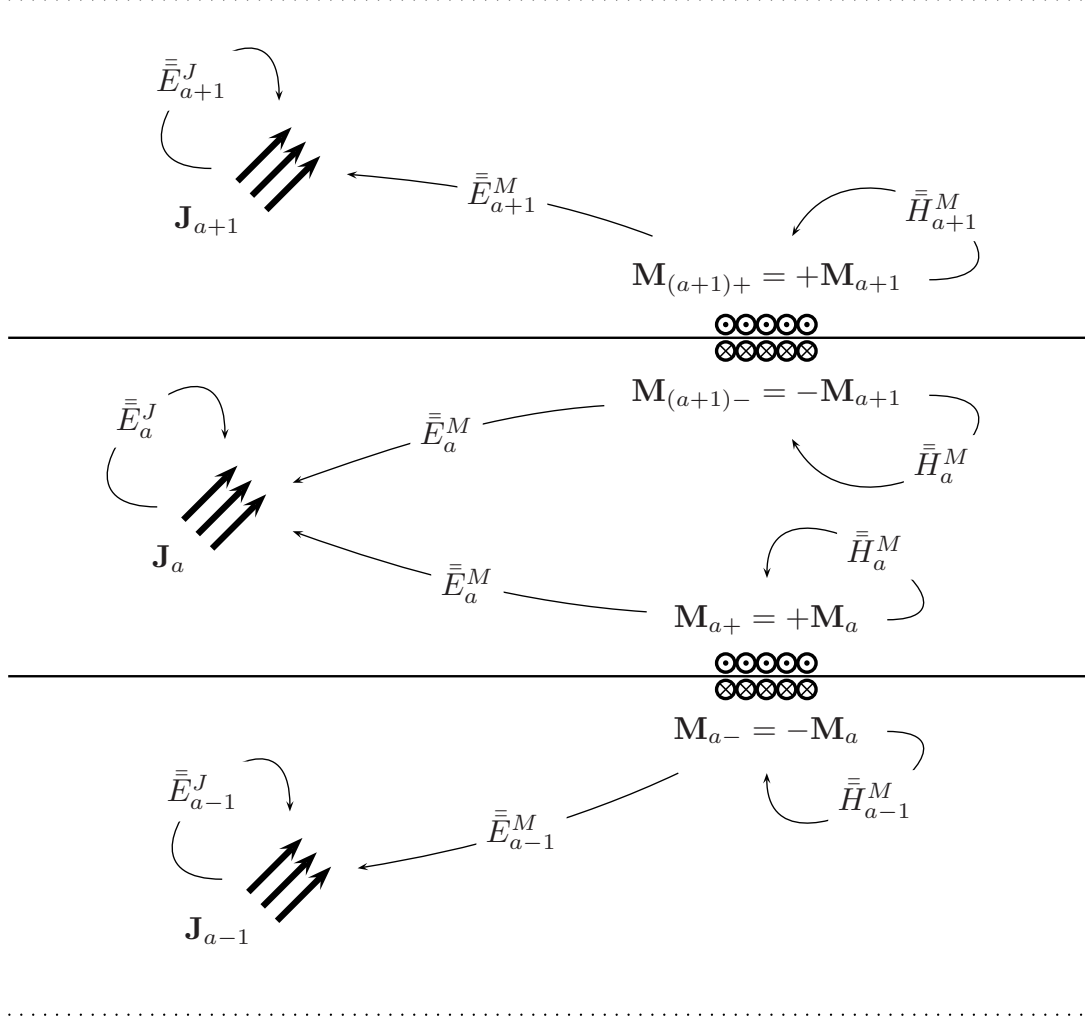


Figure 3.5: Multiple apertures with metallic scatterers, cf (3.71).

As in §3.2.1–3.2.9, it is necessary to consider different types according to the orientation of the observer cell and the test half-function. But to get a taste of the proceedings, we consider first the case of arbitrarily oriented \mathbf{J} and \mathbf{M} in free space. We shall deal with half bases; the test and basis subindices will be dropped when possible (see p. 58).

3.3.2 Free space

We have [50, table 3.1, pp. 98]:

$$\begin{aligned}\bar{\bar{E}}^M &= -\frac{1}{\epsilon} \text{curl } \bar{\bar{F}} = -\frac{1}{4\pi} \text{curl} \left[\frac{e^{-jkR}}{R} \bar{\bar{I}} \right] \\ &= -\frac{1}{4\pi} \text{grad} \frac{e^{-jkR}}{R} \times \bar{\bar{I}}\end{aligned}\tag{3.73}$$

Using $\text{grad } f(R) = -\text{grad}' f(R)$, the convolution integral of (3.72b) is

$$4\pi \mathbf{E} = 4\pi \bar{\bar{E}}^M * \mathbf{b} = \int_{S'} \text{grad}' \frac{e^{-jkR}}{R} \times \mathbf{b}\tag{3.74}$$

This is regularized by writing

$$e^{-jkR} = 1 - jkR - \frac{k^2}{2}R^2 + \dots \quad (3.75)$$

so that

$$4\pi\mathbf{E} = \int_{S'} \text{grad}' \frac{e^{-jkR} - 1 + k^2R^2/2}{R} \times \mathbf{b} \quad (3.76a)$$

$$+ \int_{S'} \text{grad}' \frac{1}{R} \times \mathbf{b} \quad (3.76b)$$

$$- \frac{k^2}{2} \int_{S'} \text{grad}' R \times \mathbf{b} \quad (3.76c)$$

(3.76a) is regular and can be computed with cubature rules for smooth integrands. (3.76b) and (3.76c) will be computed in closed form. Note that the integrand of (3.76c) is actually bounded for all \mathbf{r} ; its extraction is a matter of numerical convenience.

The algebra is quite different depending on whether \mathbf{b} is a triangular or a rectangular half function. Let \mathbf{p}, \mathbf{p}' be the projection of \mathbf{r}, \mathbf{r}' on the plane of S' . Also, let (inside the free space convolution only) $\hat{\mathbf{z}} := \hat{\mathbf{n}}', \hat{\mathbf{u}} := \hat{\mathbf{n}}'_s$. Then $Z = \mathbf{R} \cdot \hat{\mathbf{z}}$.

If S' is a triangle,

$$\mathbf{b} = \frac{l}{2A}(\mathbf{r}' - \mathbf{r} + \mathbf{r} - \mathbf{r}_{j\pm}) = \frac{l}{2A}(-\mathbf{R} + \mathbf{r} - \mathbf{r}_{j\pm}) \quad (3.77)$$

whence

$$\int_{S'} \text{grad}' \frac{1}{R} \times \mathbf{b} = -\frac{l}{2A}(\mathbf{r} - \mathbf{r}_{j\pm}) \times \int_{S'} \text{grad}' \frac{1}{R} \quad (3.78a)$$

$$\begin{aligned} \int_{S'} \text{grad}' R \times \mathbf{b} &= -\frac{l}{2A}(\mathbf{r} - \mathbf{r}_{j\pm}) \times \int_{S'} \text{grad}' R \\ &= +\frac{l}{2A}(\mathbf{r} - \mathbf{r}_{j\pm}) \times \left[\int_{S'} \frac{\mathbf{P}}{R} + Z\hat{\mathbf{z}} \int_{S'} \frac{1}{R} \right] \end{aligned} \quad (3.78b)$$

(3.78a) has been computed in [44, (25–33)]. (3.78b) has two terms which are, respectively, (6) and (5) of [146]. Note however that if S' is a triangle the whole electric field will be normal to the plane of S' (indeed, (3.74) is $-\frac{l}{2A}(\mathbf{r} - \mathbf{r}_{j\pm}) \times \int_{S'} \text{grad}'_s \frac{e^{-jkR}}{R}$, and the gradient is parallel to S') and the reaction term will vanish in the test whenever the test half function is on that plane. This includes the most common singular case, that is, when $\mathbf{r} \in \{S' - \partial S'\}$, and does not depend on whether the test half function is a triangular or a rectangular rooftop.

If \mathbf{b} is on a rectangle, the rooftop can be decomposed (recall §3.1)

$$\mathbf{b} = \frac{l}{A}\hat{\mathbf{e}}\hat{\mathbf{e}} \cdot (\mathbf{r}' - \mathbf{r}_{j\pm}) = \frac{l}{A}\hat{\mathbf{e}}\hat{\mathbf{e}} \cdot (-\mathbf{P} + \mathbf{p} - \mathbf{p}_{j\pm}) \quad (3.79)$$

and

$$\begin{aligned} \int_{S'} \text{grad}' \frac{1}{R} \times [\hat{\mathbf{e}}\hat{\mathbf{e}} \cdot (\mathbf{p}' - \mathbf{p}_{j\pm})] &= -\hat{\mathbf{e}} \times \left[\int_{S'} \text{grad}' \frac{1}{R} (\mathbf{p}' - \mathbf{p}_{j\pm}) \right] \cdot \hat{\mathbf{e}} \\ &= -\hat{\mathbf{e}} \times \left[\int_{S'} \text{grad}' \frac{1}{R} (\mathbf{p} - \mathbf{p}_{j\pm}) - \int_{S'} \text{grad}' \frac{1}{R} \mathbf{P} \right] \cdot \hat{\mathbf{e}} \end{aligned} \quad (3.80a)$$

The first term of (3.80a) is like (3.78a). Integration by parts in the second term gives

$$\begin{aligned} -\text{grad}' \frac{1}{R} \mathbf{P} &= \text{grad}' \frac{-\mathbf{P}}{R} + \frac{1}{R} \text{grad}' \mathbf{P} \\ &= \text{grad}' \frac{-\mathbf{P}}{R} + \frac{1}{R} (\bar{\bar{I}} - \hat{\mathbf{z}}\hat{\mathbf{z}}) \end{aligned} \quad (3.80b)$$

The term with $\bar{\bar{I}}$ will vanish after $\hat{\mathbf{e}} \times (\cdot) \cdot \hat{\mathbf{e}}$. The remaining integral is

$$\begin{aligned} \int_{S'} \text{grad}' \frac{-\mathbf{P}}{R} &= \int_{S'} \text{grad}'_s \frac{-\mathbf{P}}{R} + \hat{\mathbf{z}} \frac{\partial}{\partial z'} \frac{-\mathbf{P}}{R} \\ &= \int_{S'} \text{grad}'_s \frac{-\mathbf{P}}{R} - Z \hat{\mathbf{z}} \frac{\mathbf{P}}{R^3} \\ &= \int_{S'} \text{grad}'_s \frac{-\mathbf{P}}{R} - Z \hat{\mathbf{z}} \text{grad}'_s \frac{1}{R} \\ &= \int_{\partial S'} \hat{\mathbf{u}} \frac{-\mathbf{P}}{R} - Z \hat{\mathbf{z}} \int_{\partial S'} \hat{\mathbf{u}} \frac{1}{R} \\ &= \sum_i \hat{\mathbf{u}}_i \int_{\partial S'_i} \frac{-\mathbf{P}}{R} - Z \hat{\mathbf{z}} \sum_i \hat{\mathbf{u}}_i \int_{\partial S'_i} \frac{1}{R} \end{aligned} \quad (3.80c)$$

The final edge integrals in (3.80c) are immediate. A similar device can be used to obtain (3.76c); we write directly

$$\int_{S'} \text{grad}' R \times \mathbf{b} = -\frac{l}{A} \hat{\mathbf{e}} \times \left[\int_{S'} \text{grad}' R (\mathbf{p} - \mathbf{p}_{j\pm}) - \int_{S'} \text{grad}' (\mathbf{P} R) \right] \cdot \hat{\mathbf{e}} \quad (3.81a)$$

The first term is like (3.78b). The second is

$$\begin{aligned} -\int_{S'} \text{grad}' (\mathbf{P} R) &= -\int_{\partial S'} \hat{\mathbf{u}} \mathbf{P} R + \hat{\mathbf{z}} Z \int_{S'} \frac{\mathbf{P}}{R} \\ &= -\int_{\partial S'} \hat{\mathbf{u}} \mathbf{P} R - \hat{\mathbf{z}} Z \int_{S'} \text{grad}'_s R \\ &= -\sum_i \hat{\mathbf{u}}_i \int_{\partial S'_i} \mathbf{P} R - Z \hat{\mathbf{z}} \sum_i \hat{\mathbf{u}}_i \int_{\partial S'_i} R \end{aligned} \quad (3.81b)$$

where the line integrals are, again, immediate. As in the case of the triangle, the electric field on the plane of S' is normal to S' [there is a component $\hat{\mathbf{e}} \times \hat{\mathbf{z}}$ when the second term of (3.80c, 3.78b) is substituted into (3.80a), but it has Z as a factor] and the reaction term vanishes in the same way when \mathbf{t} and \mathbf{b} are on the same plane.

The accuracy gained by the extraction of the singular or quasi-singular terms of $\bar{\bar{E}}^M$ can be observed in figs. 3.7–3.10. We have computed the source integral $\int_{S'} \bar{\bar{E}}^M \cdot \mathbf{M}$ over either two right triangles (normalized short side lengths $kl = 1$ and $kl = .1$) and two squares (same normalized side lengths), for an observer point that moves away from the center along the perpendicular up to a normalized distance of $kR = .5$ (fig. 3.6).

On the triangle, a Gaussian rule of 13 points (7th degree) was used to compute the remainder of the integral after the extraction of 0, 1 or 2 terms. The relative error has been obtained by comparing these results to those obtained by using a rule of 20 points (8th degree) and the extraction of 2 terms. Therefore, the smallest errors on each plot (with extraction of 2 terms) may be inaccurate.

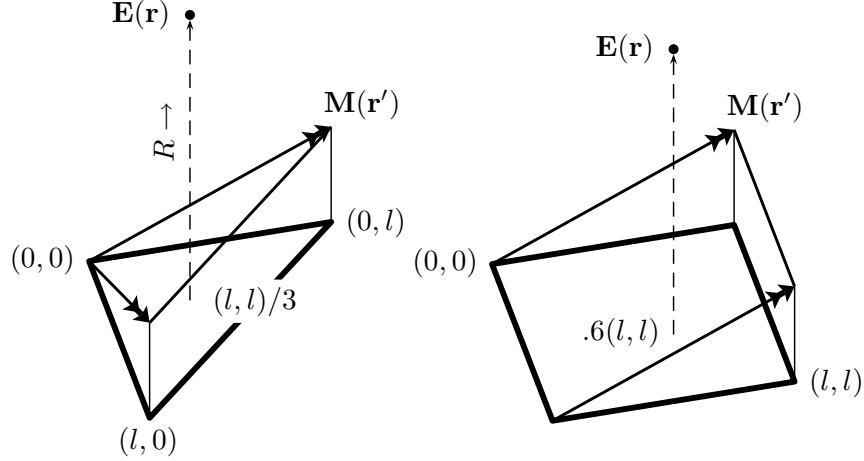


Figure 3.6: Disposition of source cell and observer point in the extraction tests of figs. 3.7–3.10.

On the square, the Gaussian rules used were of 20 points (9th order) for the plots and 40 points (13th order) for the reference. In this case the figures should be more accurate. We found that, on the plane of the source cell, the error was greatest at some distance off the center, and the observer point moves from that point upwards, instead of from the center of the rectangle; this is the reason why R (distance from the observer point to the center of the cell) does not begin at 0 in these plots.

The larger cells ($kl = 1$) are never used in practice, because they would produce too coarse a discretization. It is satisfying to see that when two singular terms are extracted the error is reasonably small even for that extreme case.

3.3.3 Homogeneous half-space bounded by ground plane

The Green's function for a perfect electric conductor (PEC) ground plane-bounded, homogeneous half-space can be obtained through image theory. If the ground plane has normal $\hat{\mathbf{z}}$ and contains the point \mathbf{o} , the images of elementary electric and magnetic sources are, respectively

$$\mathbf{J}\delta(\mathbf{r} - \mathbf{r}') \rightarrow -\mathbf{J} \cdot \bar{\bar{R}}\delta(\mathbf{r} - \mathbf{r}'') \quad (3.82a)$$

$$\mathbf{M}\delta(\mathbf{r} - \mathbf{r}') \rightarrow +\mathbf{M} \cdot \bar{\bar{R}}\delta(\mathbf{r} - \mathbf{r}'') \quad (3.82b)$$

where the position of the image is $\mathbf{r}'' = \bar{\bar{R}} \cdot \mathbf{r}' + 2\hat{\mathbf{z}}\hat{\mathbf{z}} \cdot \mathbf{o}$ and $\bar{\bar{R}} = \bar{\bar{I}} - 2\hat{\mathbf{z}}\hat{\mathbf{z}}$ is the reflection dyadic, which is symmetric [62, §2.8.2]. With (3.82), the potential Green's functions are

$$4\pi \begin{bmatrix} \bar{\bar{F}}/\epsilon \\ \bar{\bar{A}}/\mu \end{bmatrix} = \frac{e^{-jk|\mathbf{r}-\mathbf{r}'|}}{|\mathbf{r}-\mathbf{r}'|} \bar{\bar{I}} \begin{bmatrix} + \\ - \end{bmatrix} \frac{e^{-jk|\mathbf{r}-\mathbf{r}''|}}{|\mathbf{r}-\mathbf{r}''|} \bar{\bar{R}} \quad (3.83)$$

We have the following relationship for an arbitrary source distribution defined on a volume V :

$$\int_{V'} \frac{e^{-jk|\mathbf{r}-\mathbf{r}''|}}{|\mathbf{r}-\mathbf{r}''|} \bar{\bar{R}} \cdot \begin{bmatrix} \mathbf{M}(\mathbf{r}') \\ \mathbf{J}(\mathbf{r}') \end{bmatrix} dv' = \bar{\bar{R}} \cdot \int_{V'} \frac{e^{-jk|\mathbf{r}_p-\mathbf{r}'|}}{|\mathbf{r}_p-\mathbf{r}'|} \begin{bmatrix} \mathbf{M}(\mathbf{r}') \\ \mathbf{J}(\mathbf{r}') \end{bmatrix} dv' \quad (3.84)$$

with $\mathbf{r}_p = \bar{\bar{R}} \cdot \mathbf{r} + 2\hat{\mathbf{z}}\hat{\mathbf{z}} \cdot \mathbf{o}$. (It is trivial to show that $|\mathbf{r}_p - \mathbf{r}'| = |\mathbf{r} - \mathbf{r}''|$.) That is, the potential of a reflected current distribution is the same as the reflected potential of the original current distribution, computed at the reflection of the original observation point. The second computation is easier because only a point and a vector must be reflected, and not a whole current distribution.

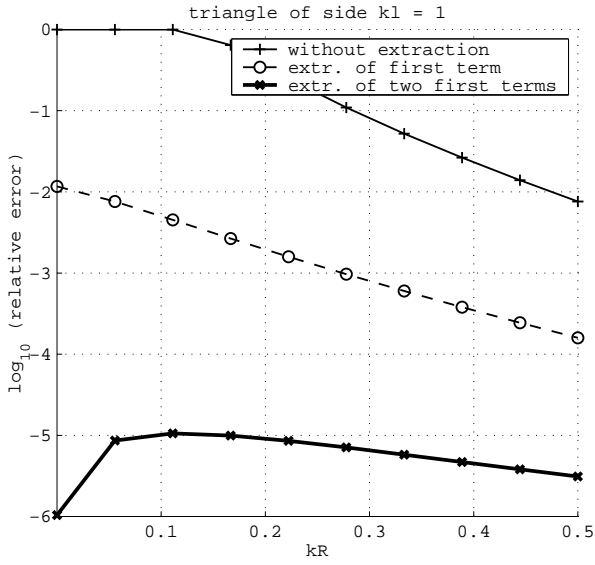


Figure 3.7: Relative error in the computation of the electric field produced by a magnetic current half-rooftop on a right triangle with vertices at $(0,0,0)$, $(1/k,0,0)$ and $(0,1/k,0)$, when the observer point moves from the center of the triangle up to a height of $.5/k$.

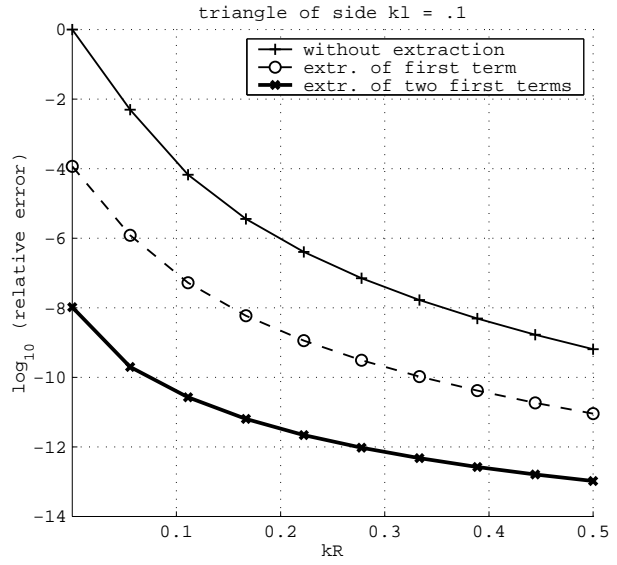


Figure 3.8: As in fig. 3.7, but now the sides of the triangle have sides of length $.1/k$.

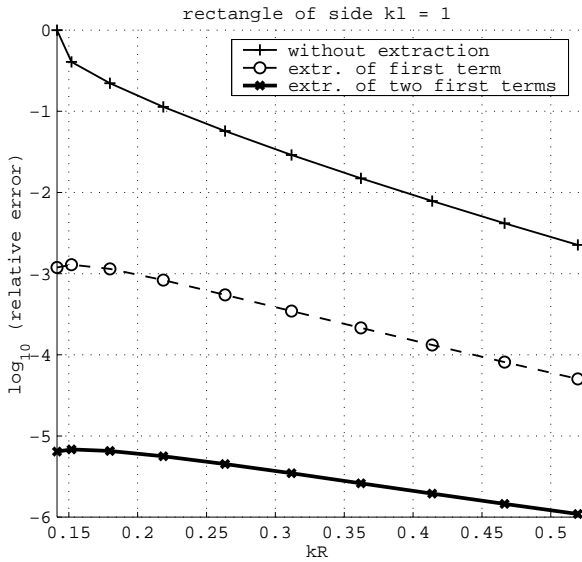


Figure 3.9: As in fig. 3.7, but the source cell is a rectangle with vertices at $(0,0,0)$, $(1/k,0,0)$, $(1/k,1/k,0)$, $(0,1/k,0)$.

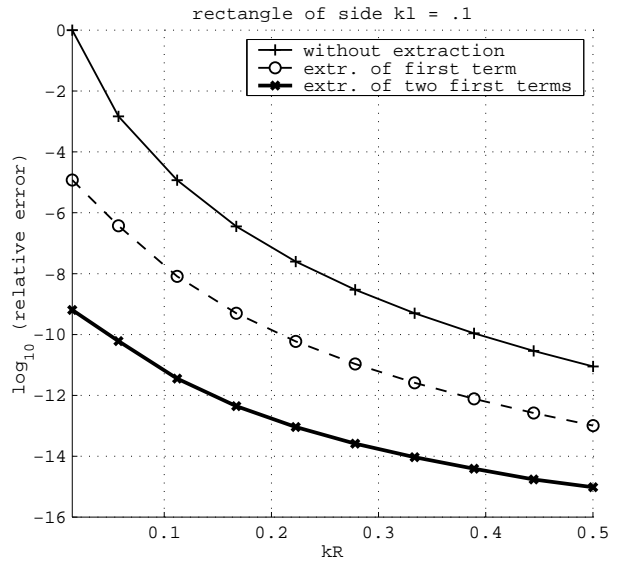


Figure 3.10: As in fig. 3.9, but now the sides of the rectangle have sides of length $.1/k$.

Similarly, we have for $\bar{\bar{E}}^M$ [cf (3.73)]

$$4\pi\bar{\bar{E}}^M = -\text{grad} \frac{e^{-jk|\mathbf{r}-\mathbf{r}'|}}{|\mathbf{r}-\mathbf{r}'|} \times \bar{\bar{I}} - \text{grad} \frac{e^{-jk|\mathbf{r}-\mathbf{r}''|}}{|\mathbf{r}-\mathbf{r}''|} \times \bar{\bar{R}} \quad (3.85)$$

the reflection property

$$\int_{V'} \text{grad} \frac{e^{-jk|\mathbf{r}-\mathbf{r}''|}}{|\mathbf{r}-\mathbf{r}''|} \times \bar{\bar{R}} \cdot \mathbf{M}(\mathbf{r}') dv' = -\bar{\bar{R}} \cdot \int_{V'} \text{grad} \frac{e^{-jk|\mathbf{r}_p-\mathbf{r}'|}}{|\mathbf{r}_p-\mathbf{r}'|} \times \mathbf{M}(\mathbf{r}') dv' \quad (3.86)$$

from $(\text{grad } g \times \bar{\bar{I}}) \cdot \bar{\bar{R}} = -\bar{\bar{R}} \cdot (\text{grad } g \times \bar{\bar{I}})$, because $\bar{\bar{R}}$ is symmetric and $\text{grad } g \times \bar{\bar{I}}$ is antisymmetric. The interpretation of property (3.86) is the same as that of (3.84), but note the sign change.

The expressions (3.84) and (3.86) are especially useful when computing costly closed form singular integrals like (3.76b) and (3.76c). These depend on a number of geometrical parameters that, using the reflection properties, do not need to be recomputed, nor reordered, nor inverted.

3.3.4 Type I

In this type, both observer and source cell are horizontal. (3.72b) retains the same form. To obtain the cartesian space-domain components $E_{xx}^M = -E_{yy}^M$, E_{xy}^M and E_{yx}^M it will be necessary to tabulate [cf table 2.1, (B.4)]

$$\begin{aligned} f_1(P, z, z') &= \mathcal{S}_0\{E_{uv}^M\} & f_3(P, z, z') &= \mathcal{S}_1\{k_p^{-1}E_{uv}^M\} \\ f_2(P, z, z') &= \mathcal{S}_0\{E_{vu}^M\} & f_4(P, z, z') &= \mathcal{S}_1\{k_p^{-1}E_{vu}^M\} \end{aligned} \quad (3.87)$$

The singular or strongest quasi-singular part of the convolution integral is the same as in free space (§3.3.2), provided that source and observer belong to the same dielectric layer. The convolution integral is regularized in that same way.

3.3.5 Type II

In this type, the observer cell is vertical, but the test half-function is horizontally oriented, $\lambda = 0 \rightarrow \mathbf{t} \cdot \hat{\mathbf{z}} = 0$. The test integral separates as type VIII of $\langle \mathbf{J}, \bar{\bar{E}}^J * \mathbf{J} \rangle$ reactions (§3.2.8). The generic reaction term (3.72b) takes the form

$$\langle \mathbf{t}, \bar{\bar{E}}^M * \mathbf{b} \rangle = \langle \mathbf{t}, \int_{\tau} \bar{\bar{E}}^M * \mathbf{b} \rangle \quad (3.88)$$

needing the tabulation of

$$\begin{aligned} f_1(P, \tau, z') &= \int_{\tau} \mathcal{S}_0\{E_{uv}^M\} & f_3(P, \tau, z') &= \int_{\tau} \mathcal{S}_1\{k_p^{-1}E_{uv}^M\} \\ f_2(P, \tau, z') &= \int_{\tau} \mathcal{S}_0\{E_{vu}^M\} & f_4(P, \tau, z') &= \int_{\tau} \mathcal{S}_1\{k_p^{-1}E_{vu}^M\} \end{aligned} \quad (3.89)$$

The singular or strongest quasi-singular part will be obtained by performing the integration \int_{τ} on the free-space static Green's function $\bar{\bar{E}}_{\text{static}}^M = -\frac{1}{4\pi} \text{curl} \frac{\bar{\bar{I}}}{R}$; this is the first term extracted in (3.76). The convolution integral [cf (3.88)] with such a kernel is

$$\frac{1}{4\pi} \int_{S'} \left[\int_{\tau} \text{curl}' \frac{\bar{\bar{I}}}{R} \right] \cdot \mathbf{b} = \frac{1}{4\pi} \int_{S'} \left[-\mathbf{b} \times \text{grad}' \int_{\tau} \frac{1}{R} \right] \quad (3.90)$$

The linear rooftops are irrotational, ie $\text{curl}' \mathbf{b} = 0$, whether \mathbf{b} is defined on a triangle or on a parallelogram. Also, the half basis function being horizontal, $\frac{\partial \mathbf{b}}{\partial z'} = 0$. Therefore the integrand of (3.90) can be written

$$\begin{aligned} -\mathbf{b} \times \text{grad}' f &= \text{curl}'(\mathbf{b}f) - f \text{curl}' \mathbf{b} \\ &= \hat{\mathbf{z}} \times \mathbf{b} \frac{\partial}{\partial z'} f + \text{curl}'_s(\mathbf{b}f) \end{aligned} \quad (3.91)$$

Because $\hat{\mathbf{z}} \times \text{curl}'_s(\mathbf{b}f) = 0$, the second term of (3.91) will disappear in the test integral (3.88). The significant part is written in full

$$\begin{aligned} -\mathbf{b} \times \text{grad}' \int_{\tau} \frac{1}{R} &\rightarrow \hat{\mathbf{z}} \times \mathbf{b} \frac{\partial}{\partial z'} \int_{z_0}^{z_1} dz \frac{1}{R} \\ &= \hat{\mathbf{z}} \times \mathbf{b} \left[-\frac{1}{R_1} + \frac{1}{R_0} \right] \end{aligned} \quad (3.92)$$

This is the sum of two potential-like terms, which are handled with [146, (5–6)]. We may note two facts. The first, trivial, is that only one of them can be singular (when $z' = z_0$ or $z' = z_1$), and it might be possible to get by without extracting the other if $|z_1 - z_0|$ is not very small. The second is that the singularity of $\int_{\tau} \bar{\bar{E}}^M$ is integrable for any position of the observer, whereas the singularity of the bare $\bar{\bar{E}}^M$ was not [cf (3.78a, 3.80a) and figs. 2.18, 2.24]. This will prove important when modelling apertures in thick metallic screens (§5.1).

3.3.6 Type III

This is like type II, save that $\lambda = 1$. The test integral separates as type IX of $\langle \mathbf{J}, \bar{\bar{E}}^J * \mathbf{J} \rangle$ reactions (§3.2.9). The generic reaction term (3.72b) can now be written

$$\langle \mathbf{t}, \bar{\bar{E}}^M * \mathbf{b} \rangle = \langle 1, \int_{\tau} t(z) (\hat{\mathbf{z}} \cdot \bar{\bar{E}}^M) * \mathbf{b} \rangle \quad (3.93)$$

Components E_{zx}^M, E_{zy}^M are to be obtained from the tables [cf (2.21)]

$$\begin{aligned} f_1(P, \tau, z') &= \int_{\tau} \overrightarrow{t}(z) \mathcal{S}_1\{E_{zv}^M\} \\ f_2(P, \tau, z') &= \int_{\tau} \overleftarrow{t}(z) \mathcal{S}_1\{E_{zv}^M\} \end{aligned} \quad (3.94)$$

The convolution integral is regularized as in §3.3.5. The singular part is

$$\frac{1}{4\pi} \int_{S'} \hat{\mathbf{z}} \cdot \left[\int_{\tau} t(z) \text{curl}' \frac{\bar{\bar{I}}}{R} \right] \cdot \mathbf{b} = \frac{1}{4\pi} \int_{S'} \hat{\mathbf{z}} \cdot \left[-\mathbf{b} \times \text{grad}' \int_{\tau} \frac{t(z)}{R} \right] \quad (3.95)$$

Because of the product $\hat{\mathbf{z}} \cdot$ in the test, only the second term of (3.91) (with $f = \int_{\tau} \frac{t(z)}{R}$) is now to be retained. Applying Stokes' theorem to the convolution integral (which is easily shown to be possible for that f)

$$\begin{aligned} \int_{S'} -\mathbf{b} \times \text{grad}' f &\rightarrow \int_{S'} \text{curl}'_s(\mathbf{b}f) \\ &= \sum_i \hat{\mathbf{n}}'_s \times \int_{\partial S'_i} (\mathbf{b}f) \end{aligned} \quad (3.96)$$

| <i>type</i> | <i>indices of</i> | <i>required tables</i> | <i>dT</i> | <i>dC</i> | <i>singular kernel</i> |
|-------------|-------------------|--|-----------|-----------|---|
| fs | - | | 2 | 2 | $\text{curl}(1/R - k^2 R/2)\bar{\bar{I}}$ |
| I | z, z' | E_{uv}^M E_{vu}^M $\mathcal{S}_1\{k_p^{-1}E_{uv}^M\}$ $\mathcal{S}_1\{k_p^{-1}E_{vu}^M\}$ | 2 | 2 | $\text{curl}'(1/R - k^2 R/2)\bar{\bar{I}}$ |
| II | τ, z' | $\int_{\tau} E_{uv}^M$ $\int_{\tau} E_{vu}^M$ $\int_{\tau} \mathcal{S}_1\{k_p^{-1}E_{uv}^M\}$ $\int_{\tau} \mathcal{S}_1\{k_p^{-1}E_{vu}^M\}$ | 1 | 2 | $\hat{\mathbf{z}} \times \bar{\bar{I}}/R$ |
| III | τ, z' | $\int_{\tau} \vec{t}(z) \mathcal{S}_1\{E_{zv}^M\}$ $\int_{\tau} \overleftarrow{t}(z) \mathcal{S}_1\{E_{zv}^M\}$ | 1 | 2 | $\hat{\mathbf{z}} \cdot \text{grad}' \log P \times \bar{\bar{I}}$ |

Table 3.2: Reaction terms of type $\langle \mathbf{J}, \bar{\bar{E}}^M * \mathbf{M} \rangle$. Legend: fs=free space; dC=dimension of spatial convolution integral; dT=dimension of spatial test integral.

Now there are two possibilities for $t(z)$, viz [see (3.34)]

$$\begin{aligned} \frac{A}{l} \vec{t}(z) &= Z + (z' - z_0) \\ \frac{A}{l} \overleftarrow{t}(z) &= \frac{l}{A}(z_1 - z') + Z \end{aligned} \quad (3.97)$$

z', z_0, z_1 are constants for both \int_{τ} and $\int_{S'}$, so we shall compute (3.96) for

$$f = \begin{cases} \int_{\tau} Z/R = R & \text{or} \\ \int_{\tau} 1/R = \log(Z + R). \end{cases} \quad (3.98)$$

When these are substituted into (3.96), and \mathbf{b} is split appropriately [cf (3.77, 3.77)] immediate segment integrals are obtained. Note that neither here nor in §3.3.5 has it been necessary to specify whether S' is a triangle or a rectangle. However, the edge integrals in (3.98) simplify differently in either case. Also, repeating the remark that concludes §3.3.5, (3.96) is seen to be absolutely integrable for any position of \mathbf{r} —actually, of \mathbf{p} and τ , with the restriction that $z_0 < z' < z_1$ (strictly) is, as usual, not allowed.

3.3.7 Summary

The contents of §3.3.2–3.3.6 have been summarized in table 3.2. The singular kernels are more indicative than exact, particularly for type III; see the corresponding section (§3.3.6) for details.

It should be mentioned that the regularization of the convolution integrals in (3.88) and (3.93) has already been published in [66, Appendix II]. The development presented here has two distinct advantages: first, the full static part is extracted, which accounts not only for the singular but also for quasi-singular cases, and is appropriate even when $h = |z_1 - z_0| > 0$ is small; second, it is valid for rectangles as well as for triangles, whereas the reference cited required S' to be a triangle.

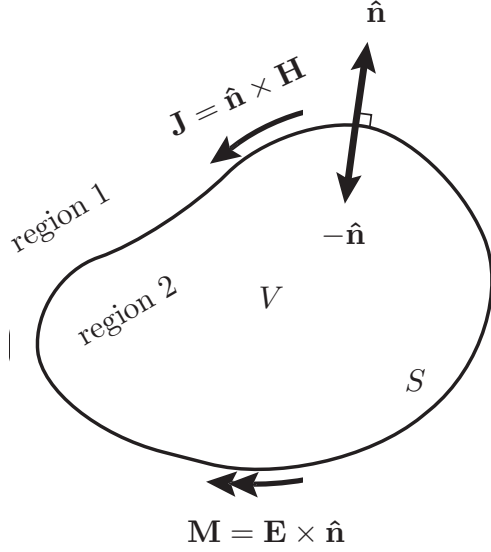


Figure 3.11: A penetrable homogeneous body.

3.4 Piecewise homogeneous dielectric bodies

In this case all magnetic and electric equivalent currents must be included, because 1) the equivalent problem's media are such that both currents radiate their due, and 2) none of the tangential fields is zero in the original problem. A closed homogeneous body with outward normal $\hat{\mathbf{n}}$ is considered (fig. 3.11).

Making use of the principle of equivalence, the tangential electric and magnetic fields just outside the body may be replaced by magnetic and electric currents

$$\mathbf{E} \times \hat{\mathbf{n}} = \mathbf{M} \quad \hat{\mathbf{n}} \times \mathbf{H} = \mathbf{J} \quad (3.99)$$

that will reproduce the previous situation outside the body, provided that the field inside the body is zero. The tangential fields are continuous across the interface and, as the normal is reversed, the equivalent currents inside (which reproduce the previous situation inside the body, provided that the fields outside are zero) are $\mathbf{M}_2 = -\mathbf{M} = -\mathbf{M}_1$ and $\mathbf{J}_2 = -\mathbf{J} = -\mathbf{J}_1$.

The total field outside is the sum of scattered and incident field, as usual

$$\bar{\bar{E}}^J * \mathbf{J} + \bar{\bar{E}}^M * \mathbf{M} + \mathbf{E}^i = \mathbf{E} \quad \bar{\bar{H}}^M * \mathbf{M} + \bar{\bar{H}}^J * \mathbf{J} + \mathbf{H}^i = \mathbf{H} \quad (3.100)$$

However, as the surface is approached from outside, we have the limits (cf [62, (6.89-90)])

$$\begin{aligned} \lim_{\mathbf{r} \rightarrow S^+} \mathbf{E}^{\text{tan}} &= \hat{\mathbf{n}} \times \mathbf{M} & \lim_{\mathbf{r} \rightarrow S^+} \mathbf{H}^{\text{tan}} &= \mathbf{J} \times \hat{\mathbf{n}} \\ \lim_{\mathbf{r} \rightarrow S^+} \int_S \bar{\bar{E}}^M \cdot \mathbf{M} &= \oint_S \bar{\bar{E}}^M \cdot \mathbf{M} + \frac{1}{2} \hat{\mathbf{n}} \times \mathbf{M} & \lim_{\mathbf{r} \rightarrow S^+} \int_S \bar{\bar{H}}^J \cdot \mathbf{J} &= \oint_S \bar{\bar{H}}^J \cdot \mathbf{J} + \frac{1}{2} \mathbf{J} \times \hat{\mathbf{n}} \end{aligned} \quad (3.101)$$

where \oint is a principal value integral. Therefore, just outside S , the pair (3.100) becomes

$$\bar{\bar{E}}_1^J * \mathbf{J} + \oint_S \bar{\bar{E}}_1^M \cdot \mathbf{M} - \frac{1}{2} \hat{\mathbf{n}} \times \mathbf{M} = -\mathbf{E}_1^i \quad (3.102a)$$

$$\bar{\bar{H}}_1^M * \mathbf{M} + \oint_S \bar{\bar{H}}_1^J \cdot \mathbf{J} - \frac{1}{2} \mathbf{J} \times \hat{\mathbf{n}} = -\mathbf{H}_1^i \quad (3.102b)$$

If the same procedure is carried out from (3.99) to (3.102), but now inside the dielectric body, we obtain:

$$-\bar{\bar{E}}_2^J * \mathbf{J} - \oint_S \bar{\bar{E}}_2^M \cdot \mathbf{M} - \frac{1}{2} \hat{\mathbf{n}} \times \mathbf{M} = -\mathbf{E}_2^i \quad (3.103a)$$

$$-\bar{\bar{H}}_2^M * \mathbf{M} - \oint_S \bar{\bar{H}}_2^J \cdot \mathbf{J} - \frac{1}{2} \mathbf{J} \times \hat{\mathbf{n}} = -\mathbf{H}_2^i \quad (3.103b)$$

The singular terms do not change sign, because both the normal and the equivalent currents do. The difference of (3.102) and (3.103) gives

$$\begin{aligned} \hat{\mathbf{n}} \times ([\bar{\bar{H}}_1^M + \bar{\bar{H}}_2^M] * \mathbf{M}_1 - [\bar{\bar{H}}_1^J + \bar{\bar{H}}_2^J] * \mathbf{J}_1) &= -\hat{\mathbf{n}} \times (\mathbf{H}_1^i - \mathbf{H}_2^i) \\ \hat{\mathbf{n}} \times ([\bar{\bar{E}}_1^M + \bar{\bar{E}}_2^M] * \mathbf{M}_1 - [\bar{\bar{E}}_1^J + \bar{\bar{E}}_2^J] * \mathbf{J}_1) &= -\hat{\mathbf{n}} \times (\mathbf{E}_1^i - \mathbf{E}_2^i) \end{aligned} \quad (3.104)$$

Principal value integrals are assumed in $\bar{\bar{E}}^M * \mathbf{M}$ and $\bar{\bar{H}}^J * \mathbf{J}$, according to (3.102–3.103). The system (3.104) is the CFIE (Combined Field Integral Equation) for the analysis of dielectric bodies, that was first used for arbitrarily shaped bodies with a surface patch discretization in [137]. For further details on the development of this equation see for example [62, §6.4.4], [109, §5.2.1, pp. 94–95] and [148, §2].

The CFIE can be combined with the EFIE (3.3b) for open conductor bodies and the MFIE for apertures (3.62b) to analyze many-body problems. A nice array of examples has been collected in [148, §6]. Although they do not offer any example that includes both dielectrics and apertures, these have also been analyzed using (3.104), for instance in [147].

3.5 Examples

P7 Vertical stake antenna The first example is a vertical cylindrical antenna partially buried in dry earth ($\epsilon_r = 16$) or in salted water ($\epsilon_r = 81$, $\sigma = 1 \text{ S/m}$), from [82, fig. 6]. The antenna has been discretized with the same number of vertical slices ($10 + 4$) as in [82]; the circumference is approximated with 4 patches. The model has 56 rectangles (fig. 3.12). The current along the dipole has been plotted in figs. 3.13 and 3.14, where a good agreement can be observed.

In addition, this example has been simulated in an inverted position, ie with the higher permittivity medium above. This allows to estimate the error produced by the numerical approximation of the matrix elements, because, as explained in p. 58, we force the symmetry in the matrix of moments by only computing the reactions where the source is above the observer. But the mixed potential expression for this reaction is different depending on the orientation and position of source and observer; specifically, is different in the straight-up and the inverted cases of fig. 3.12.

However, as can be seen in figs. 3.15–3.16, this ‘symmetry’ error is quite small, as must happen if the matrix elements are computed with sufficient accuracy. (Indeed, it would not be appreciated if both currents were plotted together with the reference curves). It does not come as a surprise that the error is greatest near the dielectric interface.

P8 Composite dielectric sphere This example has been analyzed by [148, §6.1, fig. 7], where it is used as a benchmark for the proper construction of rooftop junctions that enforce the continuity of tangential components of the field at an edge where three different dielectric regions meet. On the surface of both hemispheres, the cells have an arbitrary 3D orientation, and the object itself is placed in free space; it cannot, therefore, be treated (nor is there any

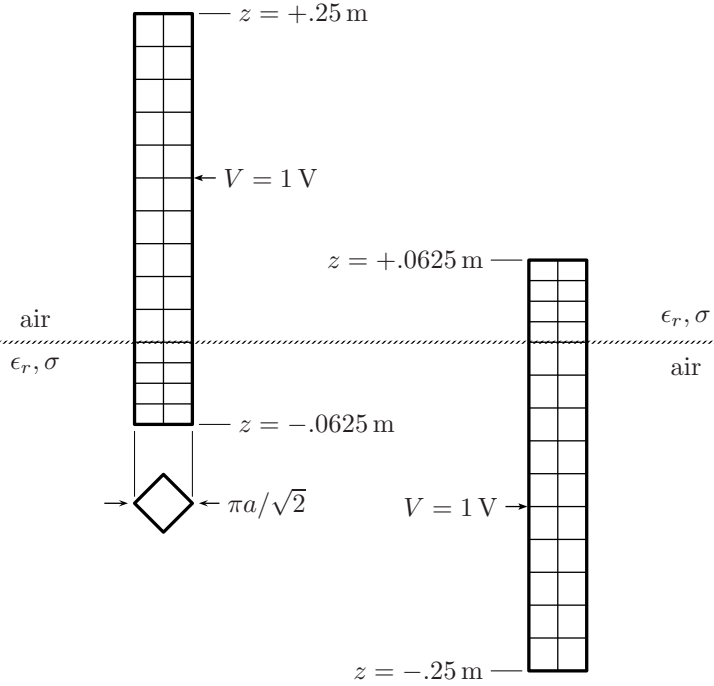


Figure 3.12: Vertical stake antenna, from [82, fig. (6b)]: straight up (left) and inverted (right). Excitation is by a δ voltage source at the indicated position ($z = \pm .125$ m), simulated radius of cylinder is $a = 10$ mm. This model has 14 slices and 56 cells. (The drawing is not to scale—the cylinder is thinner than it looks here.)

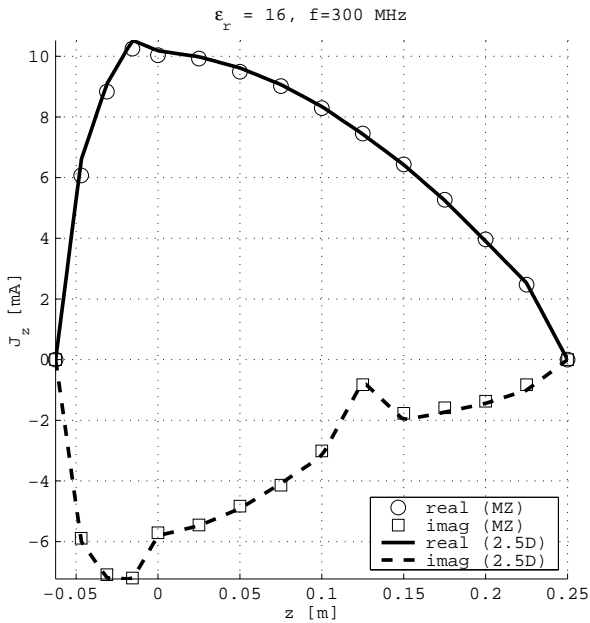


Figure 3.13: Current along a half-buried stake antenna, $\epsilon_r = 16$. MZ: results from [82, fig. 6(a)]. 2.5D: the 2.5D formulation presented here.

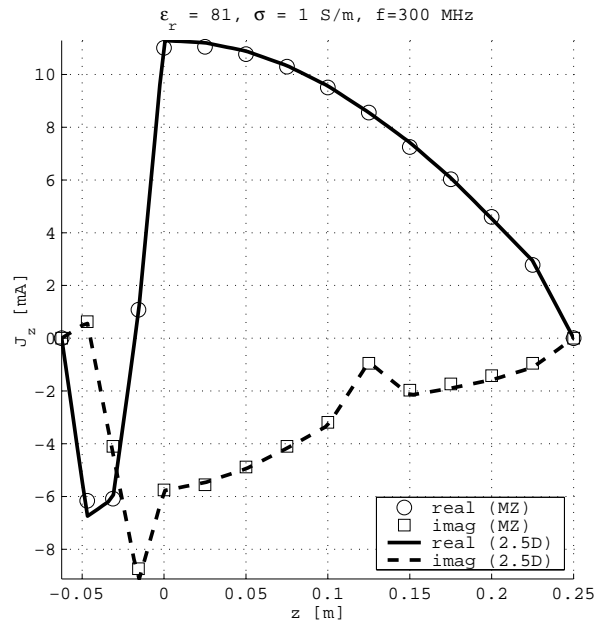


Figure 3.14: Current along a half-submerged stake antenna, $\epsilon_r = 81$, $\sigma = 1$ S/m. MZ: results from [82, fig. 6(b)]. 2.5D: the 2.5D formulation presented here.

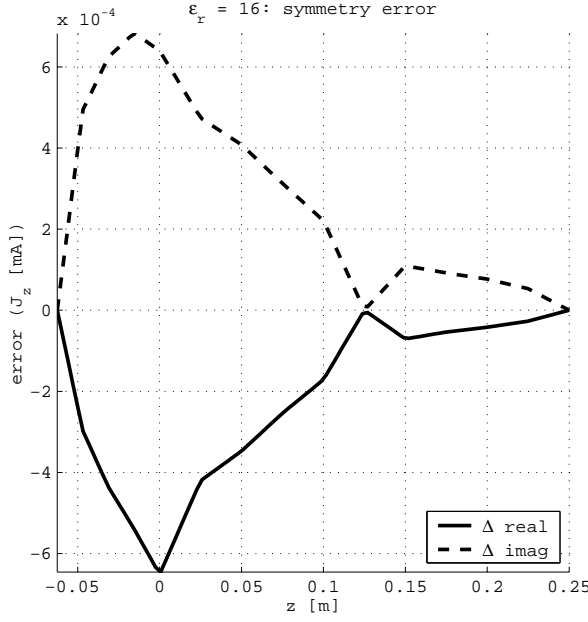


Figure 3.15: Difference between currents on the half-buried vertical antenna (earth, $\epsilon_r = 16$) computed straight up or reversed ($z \rightarrow -z$).

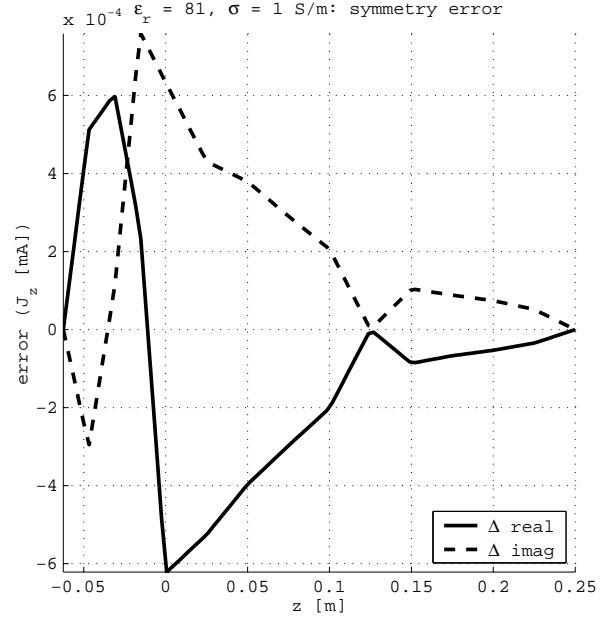


Figure 3.16: Same as fig. 3.15, but the antenna is now submerged on salted water with $\epsilon_r = 81$, $\sigma = 1$ [S/m].

need) with the 2.5D formulation. The justification for including it here is that it will be used to test the results of the volume integral equation, using polarization currents and a volume mesh, that will be presented in the next chapter.

The sphere itself is divided in two halves, rather like a Kinder egg (fig. 3.17). The problem contains three regions that are linked together and isolated from one another by three ‘interface’ surfaces. The hemispherical caps contain currents that radiate both inside and outside the sphere, while the currents of the ‘septum’ radiate only inside. The material of the upper half is fixed ($\epsilon_1 = 4$) while the material of the lower half is either $\epsilon_2 = 4$ or $\epsilon_2 = 8$. In the first case, the sphere is homogeneous and the results can also be compared against [137, fig. 5], where this example seems to have been used for the first time.

The surface equivalent currents have been plotted simply by sampling the rooftop basis functions along the paths indicated in figs. 3.18–3.21. It is easy to check the consistence of the results by comparing the currents at $\theta = 0^\circ$ and $\theta = 180^\circ$ between figs. 3.18–3.19 and figs. 3.20–3.21, respectively, because at these points the E and H plane cuts coincide.

3.6 Conclusion

In this chapter, the spatial domain integrated Green’s functions obtained in §2 have been applied to the computation of the reaction terms of the matrix obtained by expansion of the field integral equation (EFIE/MFIE) through a classic method-of-moments technique. Linear rooftops have been used to expand the unknowns, and either triangular or rectangular rooftops have been used in an unified way. We have made use of the information about the quasistatic behavior of the various Green’s functions obtained in §2 to extend the singularity extraction technique, customarily used to compute 3D potential and field self-interactions, to each of the spatial

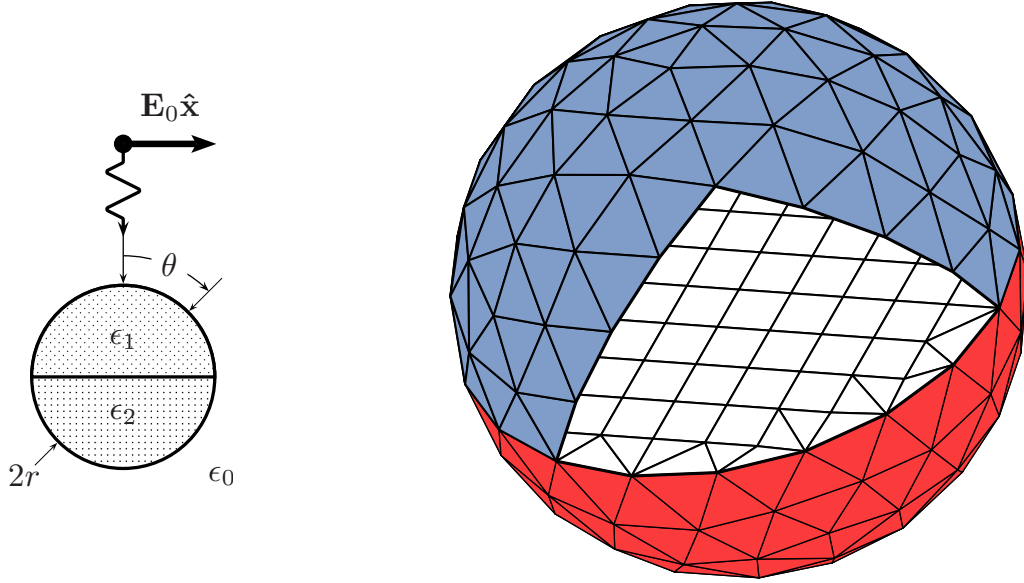


Figure 3.17: Composite sphere with halves of different dielectric material, excited with a linearly polarized plane wave coming from $\theta = 0$. Some triangles from the upper hemisphere have been taken apart to reveal the mesh of the septum. The sphere has radius $k_0 r = 1$. This mesh has $160 \times 2 + 104$ cells.

integrals that appear in the 2.5D approach. This work is original, and constitutes an essential part of the application of the 2.5D technique to some of the problems described in §5.

In addition, we have described summarily the method based on the Combined Field Integral Equations (CFIEs) for the analysis of arbitrarily shaped, composite metallic and homogeneous dielectric objects in 3D. Although this work is not original, by implementing it we have obtained a valuable tool for comparison between the results of a surface formulation, such as has been presented in this chapter, and a volume formulation, that is the subject of the next chapter.

The possibilities for further work are numerous, but probably the most immediate is the implementation of the CFIE method in layered media using the 2.5D technique. However, for the analysis of dielectric inhomogeneities in layered media, we decided to implement first the volume formulation.

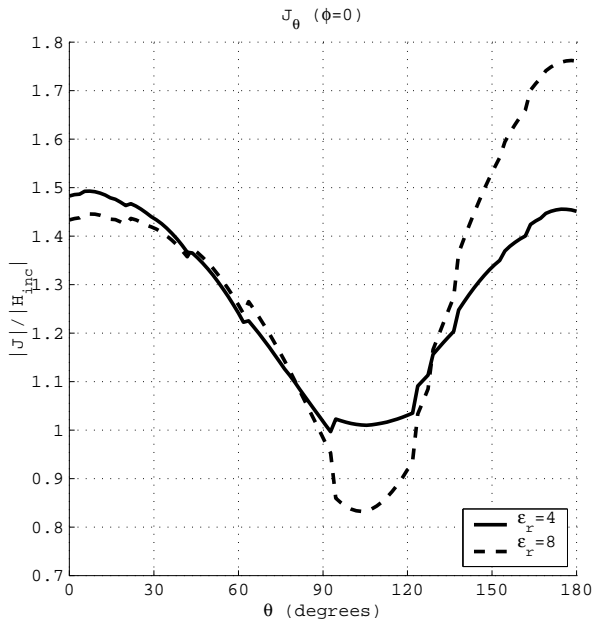


Figure 3.18: Composite sphere: J_θ along the E-plane cut $\phi = 0^\circ$.

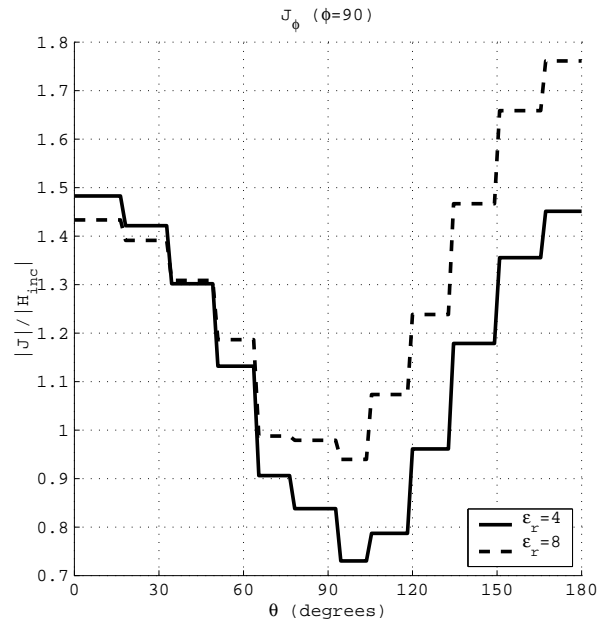


Figure 3.19: Composite sphere: J_ϕ along the H-plane cut $\phi = 90^\circ$.

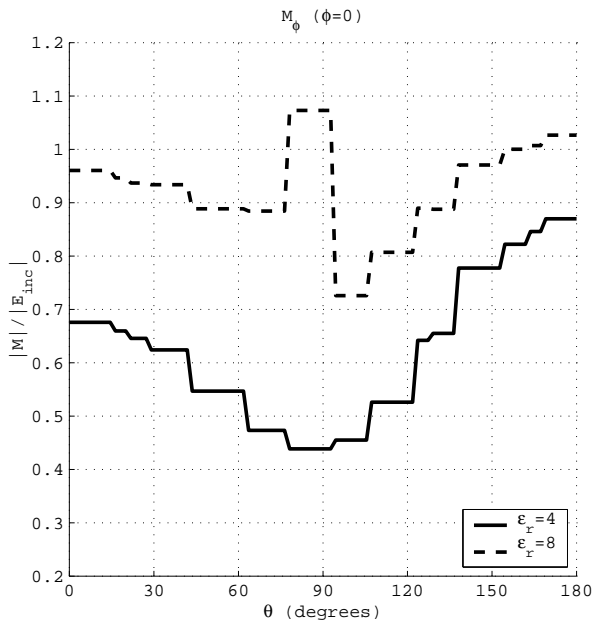


Figure 3.20: Composite sphere: M_ϕ along the E-plane cut $\phi = 0^\circ$.

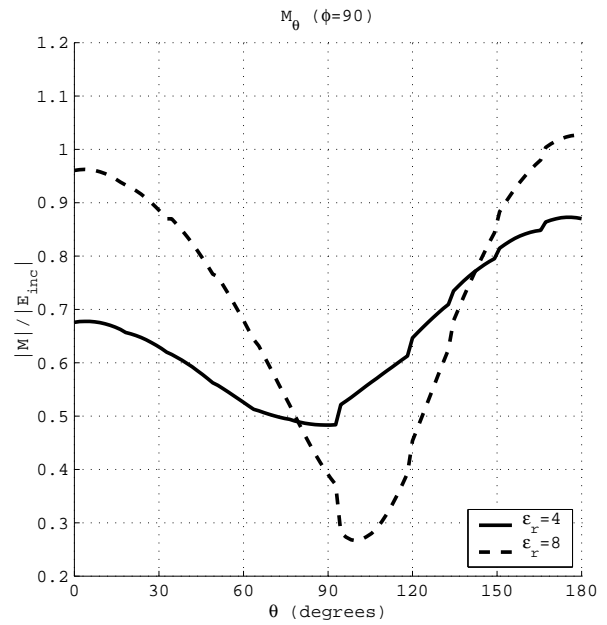


Figure 3.21: Composite sphere: M_θ along the H-plane cut $\phi = 90^\circ$.

4 Volume equivalence

In this chapter, we explore an possible alternative formulation for our problems, the so-called volume integral equation method. First, the theory is developed, and the volume elements (tetrahedra, prisms. . .) resulting from a 3D discretization and meshing are described. Preliminary results show the potentialities of this approach, and pave the way for a future combination and integration with the 2.5D approach mainly used in this thesis. In particular, the implementation of the volume integral equation in stratified media should be the next step to be considered, since it would provide a powerful systematic technique to analyze dielectric inclusions embedded in a layered environment.

4.1 Dielectric bodies

To extract a dielectric volume inclusion from the medium, the excess electric field in Ampère's law is transferred to the excitation term, so that the remaining electric field term is what it would be for the underlying medium, ie, with the dielectric inclusion removed.

$$\begin{aligned}\text{curl } \mathbf{H} &= j\omega\epsilon_0\mathbf{E} + j\omega(\epsilon - \epsilon_0)\mathbf{E} + \mathbf{J}_f \\ &= j\omega\epsilon_0\mathbf{E} + \mathbf{J}_p + \mathbf{J}_f\end{aligned}\tag{4.1}$$

The substitution (4.1) is sometimes called the ‘volume equivalence principle’ [10, §7.7]. If the *dielectric contrast*, or simply the *contrast*, is defined by

$$\kappa \equiv \frac{\epsilon - \epsilon_0}{\epsilon_0}\tag{4.2}$$

then the *polarization current* is

$$\mathbf{J}_p \equiv j\omega\kappa\mathbf{D}\tag{4.3}$$

The integral equation to be solved is [cf. (3.3)]:

$$\mathbf{E}^s(j\omega\kappa\mathbf{D}) - \mathbf{D}/\epsilon = -\mathbf{E}^i\tag{4.4}$$

This is a Fredholm equation of the second kind [110, §1.2] if the dielectric body is not a perfect conductor, ie $|\epsilon| \nrightarrow \infty$. For a numerical solution it is written in mixed potential form,

$$-j\omega\mathbf{A}(j\omega\kappa\mathbf{D}) - \text{grad } \Phi(j\omega\kappa\mathbf{D}) - \mathbf{D}/\epsilon = -\mathbf{E}^i\tag{4.5}$$

4.2 Discretization

The unknown \mathbf{D} will be expanded in a sum of subsectional divergence-conforming basis functions. These volume basis functions are defined over pairs of tetrahedra, wedges or cubes.

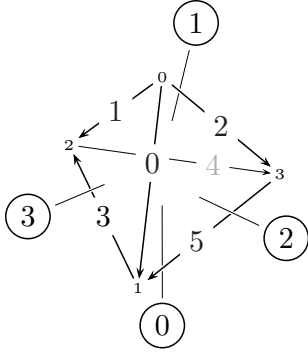


Figure 4.1: Numbering of nodes in tetrahedron.

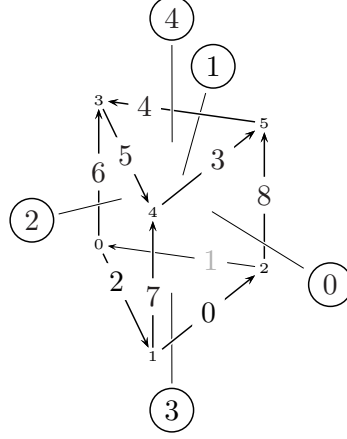


Figure 4.2: Numbering of nodes in parallel wedge.

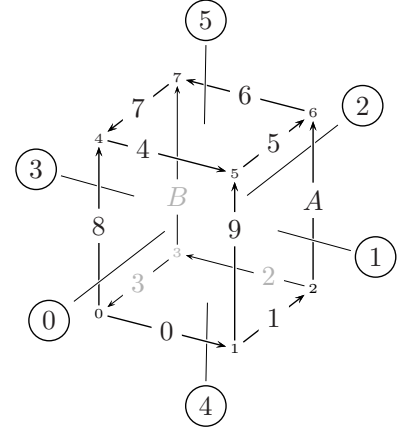


Figure 4.3: Numbering of nodes in parallel hexahedron.

The definition of linear, divergence-conforming basis functions on cube doublets is of course trivial. However, the first fully 3D solutions of the volume EFIE using subsectional basis functions did not use linear bases functions and Galerkin test, but rather pulse basis functions and point matching [63]. The corresponding basis functions for tetrahedra were first used in [120], shortly after the introduction of the RWG functions on triangular patches. In [35], the discretization consists solely of parallelepipeds, but in addition to linear rooftops, piecewise sinusoidal functions are also used. In [139], rooftops on parallelepipeds are used.

The wedges have seen little use, perhaps because they do not seem useful for general 3D structures and because automatic meshing with heterogeneous elements is difficult. In 2.5D problems, where these elements are essential, automatic meshing is simple, by extrusion. In [136], ground-plane connecting vias were modelled as wedges. The current was assumed constant and strictly vertical. This made sense because the vias were short and thin. In [145], wedges are used to discretize thin dielectric sheets. Linear functions are used for the horizontal bases, but the normal bases are constant. In [134, (4.48)], linear functions are defined on every face of the wedge, but they are not used thereafter (all the examples use parallelepipeds).

Of the works cited above, [35] and [139] considered the volume elements to be embedded in a layered medium, while in [136] they were placed in a parallel plate waveguide. The others assumed free space.

In this work, linear functions are used for every face of the wedge. These are defined as follows. First, for the functions to be linear, it is necessary that faces 4 and 3 of the wedge be parallel and similar, and that edges 6, 7 and 8 be parallel; the hexahedron must be a parallelepiped. It is recalled (§3.1) that a RWG doublet is the sum of two half functions defined on neighboring elements,

$$\mathbf{b}_{i\pm} = \mathbf{b}_{i-} - \mathbf{b}_{i+} \quad (4.6)$$

The two cells making up the i -th doublet share a face of area $A_i \rightarrow A$; let \mathbf{r}_{\pm} be a node of the $i\pm$ -th cell that does *not* belong to that common face. For tetrahedra, the half functions are then

$$\mathbf{b}_{\pm}(\mathbf{r}) = \frac{A}{3V_{\pm}}(\mathbf{r} - \mathbf{r}_{\pm}) \quad (4.7)$$

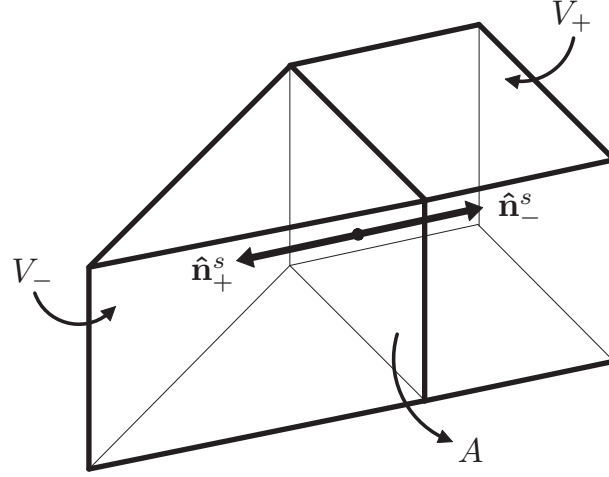


Figure 4.4: Volume rooftop made up of hexahedron and wedge.

In (4.7), the dependence of A , V_{\pm} and \mathbf{r}_{\pm} on i is assumed. Note that A is common to both half bases. In the wedge, there are two types. Let $\hat{\mathbf{e}}_{\pm}$ be a unit vector along any of the edges that connect the two triangles (6, 7 or 8 on fig. 4.2).

$$A \text{ is a triangle : } \mathbf{b}_{\pm}(\mathbf{r}) = \frac{A}{V_{\pm}}(\mathbf{r} - \mathbf{r}_{\pm}) \cdot \hat{\mathbf{e}}_{\pm} \hat{\mathbf{e}}_{\pm} \quad (4.8a)$$

$$A \text{ is a rectangle : } \mathbf{b}_{\pm}(\mathbf{r}) = \frac{A}{2V_{\pm}}(\mathbf{r} - \mathbf{r}_{\pm}) \cdot (\bar{\bar{\mathbf{I}}} - \hat{\mathbf{e}}_{\pm} \hat{\mathbf{e}}_{\pm}) \quad (4.8b)$$

In the hexahedron, let $\hat{\mathbf{e}}$ be a unit vector along any of the edges that connects face i to the face opposite (for example, edges 3, 1, 5 or 7 for face 0 in fig. 4.3).

$$\mathbf{b}_{\pm}(\mathbf{r}) = \frac{A}{V_{\pm}}(\mathbf{r} - \mathbf{r}_{\pm}) \cdot \hat{\mathbf{e}}_{\pm} \hat{\mathbf{e}}_{\pm} \quad (4.9)$$

The purpose of these definitions is to ensure continuity of normal component of the unknown across faces ($\mathbf{b}_i \cdot \hat{\mathbf{n}}_i = 1$ on face i). Therefore the three elements are compatible with each other and it is possible to have doublets where one of the cells is a cube and the other a wedge (fig 4.4), or one a wedge and the other a tetrahedron. This is equivalent to the compatibility of planar RWG functions on triangles or parallelograms in chap. 3.

4.3 Solution by the Method of Moments

Contrast is assumed to be constant on each cell. We take $\mathbf{J} = \mathbf{J}_p$; the presence of other current (for example, on surface patches) can be easily accounted for by using superposition. The electric displacement \mathbf{D} satisfies the same conditions as the RWG functions inside an inhomogeneous dielectric and is amenable to the expansion

$$\mathbf{D} = \sum_{j=0}^{n-1} D_j \mathbf{b}_j \quad (4.10)$$

The normal component of \mathbf{D} does *not* vanish at the boundary of a dielectric object unless extra conditions intervene. This means that (4.10) must include half-function terms there, ie either $\mathbf{b}_i = \mathbf{b}_{i+}$ or $\mathbf{b}_i = -\mathbf{b}_{i-}$ for certain i .

Each of the terms in (4.10) is also a polarization current that produces a scattered field [cf (3.7)]

$$D_j \mathbf{E}_j = D_j (-j\omega \mathbf{A}_j - \text{grad } \Phi_j) \quad (4.11)$$

with potential terms

$$\mathbf{A}_j = \bar{\bar{A}} * (j\omega \kappa_j \mathbf{b}_j) \quad (4.12a)$$

$$\Phi_j = \frac{1}{j\omega} (\text{div}' \bar{\bar{\Phi}}) * (j\omega \kappa_j \mathbf{b}_j) \quad (4.12b)$$

through the medium's Green's functions $\bar{\bar{A}}$, $\bar{\bar{\Phi}}$. For volume cells there is no need to distinguish between $\hat{\mathbf{n}}_\pm^s$ (normal to edge of cell) and $\hat{\mathbf{n}}$ (normal to cell), because the latter does not exist. The scalar potential can be integrated by parts [cf (2.18, 3.9)]

$$\Phi_j = -\frac{1}{j\omega} \bar{\bar{\Phi}} * \text{grad}'(j\omega \kappa_j \mathbf{b}_j) + \frac{1}{j\omega} \int_{\partial V'} [\bar{\bar{\Phi}} \cdot (j\omega \kappa_j \mathbf{b}_j)] \cdot \hat{\mathbf{n}}^s \quad (4.13)$$

The subdomain V' is made up of two cells, V'_+ and V'_- . Its boundary $\partial V'$ is $\partial V'_+ + \partial V'_-$. The boundary integral in (4.13) becomes

$$\int_{\partial V'_+} [\bar{\bar{\Phi}} \cdot (j\omega \kappa_{j+} \mathbf{b}_{j+})] \cdot \hat{\mathbf{n}}_{j+}^s - \int_{\partial V'_-} [\bar{\bar{\Phi}} \cdot (j\omega \kappa_{j-} \mathbf{b}_{j-})] \cdot \hat{\mathbf{n}}_{j-}^s \quad (4.14)$$

with the integration domain restricted to the common boundary. If a projection dyadic $\bar{\bar{P}}_j = \hat{\mathbf{n}}_{j+}^s \hat{\mathbf{n}}_{j+}^s$ is defined (and noting that for any 3D volume mesh $\mathbf{b}_{j+} \cdot \hat{\mathbf{n}}_{j+}^s = \mathbf{b}_{j-} \cdot \hat{\mathbf{n}}_{j-}^s = 1$ and $\hat{\mathbf{n}}_{j+}^s = -\hat{\mathbf{n}}_{j-}^s$ at the common face of \mathbf{b}_j , so $\bar{\bar{P}}_j$ is well defined), (4.14) becomes

$$j\omega \int_{\partial V'} [\kappa_{j+} \bar{\bar{\Phi}}^+ : \bar{\bar{P}}_j] - [\kappa_{j-} \bar{\bar{\Phi}}^- : \bar{\bar{P}}_j] \quad (4.15)$$

Both terms of the integrand in (4.15) will be equal unless

P9 Conditions under which the source boundary integral is $\neq 0$

1. One of them does not exist (half-function)
2. $\kappa_{j+} \neq \kappa_{j-}$ (boundary between regions of different contrast)

In the general layered-medium case ($\bar{\bar{\Phi}} = \bar{\bar{I}}_t \Phi_u + \hat{\mathbf{z}} \hat{\mathbf{z}} \Phi_z$), a 2.5D mesh is assumed, meaning that either $\mathbf{b}_{i\pm} \cdot \hat{\mathbf{z}} = 0$ or $\mathbf{b}_{i\pm} \times \hat{\mathbf{z}} = 0$ for every i . Also, unlike in 2.5D surface meshes, in a 2.5D volume mesh necessarily $\mathbf{b}_+ \cdot \hat{\mathbf{z}} \hat{\mathbf{z}} \cdot \hat{\mathbf{n}}_+^s = \mathbf{b}_- \cdot \hat{\mathbf{z}} \hat{\mathbf{z}} \cdot \hat{\mathbf{n}}_-^s$ if both \mathbf{b}_+ and \mathbf{b}_- exist (there can be no 'corner' functions). Accordingly, there is one additional case in which (4.15) does not vanish,

3. $\mathbf{b}_\pm \cdot \hat{\mathbf{z}} \hat{\mathbf{z}} \cdot \hat{\mathbf{n}}_\pm^s = 1$ (vertical doublet) and $\Phi_z^+ \neq \Phi_z^-$. This is equivalent to the second case of line integrals in surface patch interactions (P5 on page 56).

Once these precisions have been made, the potential terms (4.12) can be written out as

$$\mathbf{A}_j = j\omega \int_{V'} \kappa_j \bar{\bar{A}} \cdot \mathbf{b}_j \quad (4.16a)$$

$$\Phi_j = - \int_{V'} \kappa_j \bar{\bar{\Phi}} \cdot \text{grad}' \mathbf{b}_j + \int_{\partial V'} [\kappa_{j+} \bar{\bar{\Phi}}^+ : \bar{\bar{P}}_j] - [\kappa_{j-} \bar{\bar{\Phi}}^- : \bar{\bar{P}}_j] \quad (4.16b)$$

The two terms of the boundary integral (\pm), may be integrated separately, because unlike the terms of the line integral (3.10) these are absolutely integrable on their own (a surface integral with weakly $[1/R]$ singular integrand).

From (4.5) we obtain the expanded equation

$$-j\omega \sum_j \mathbf{A}_j - \text{grad} \sum_j \Phi_j - \sum_j \mathbf{D}_j / \epsilon_j = -\mathbf{E}^i \quad (4.17)$$

In the Galerkin solution, the traditional practice is apparently [120, (19)] to test (4.17) with \mathbf{D} (that is, with $\mathbf{t}_i \equiv \mathbf{b}_i$). Doing so has the inconvenient that the moments do not satisfy a reciprocity relation: $\langle \mathbf{t}_i, \mathbf{E}(\mathbf{b}_j) \rangle \neq \langle \mathbf{t}_j, \mathbf{E}(\mathbf{b}_i) \rangle$; the resulting matrix of moments will not be symmetric save in special cases. The reason is that $\mathbf{E}(\mathbf{b})$ is really $\mathbf{E}(\mathbf{J}(\mathbf{b})) = \mathbf{E}(j\omega\kappa\mathbf{b})$, and $\langle \mathbf{t}_i, \mathbf{E}(j\omega\kappa\mathbf{b}_j) \rangle$ is not a *reaction* according to the definition (1.12).

The other possibility is to test with $j\omega\kappa_i\mathbf{t}_i$ or with $\kappa_i\mathbf{t}_i$. The following points must be considered:

1. A symmetric matrix saves (almost) half the fill time. This would not be lost by testing with \mathbf{D} , because the reciprocal matrix elements are related by a constant factor, or are the sum of two terms that are related by a constant factor. However, keeping track of these relationships is obviously more complicated than if the reciprocal terms are, simply, equal.
2. A symmetric matrix saves half the storage and might be solved more efficiently. This advantage can only be exploited if the required matrix factorization routines are available.
3. A test function $\kappa_i\mathbf{t}_i$ does not fulfill normal continuity across the two component cells if these have different κ . This means that a boundary integral over ∂V will appear in that case, while it would not if the test function were simply \mathbf{t}_i . However, the boundary integral is always present if \mathbf{t}_i is a half-function, so the test boundary integral must be implemented all the same. The advantage is reduced to tiny savings in matrix fill time.

Our choice is to test with $\kappa_i\mathbf{t}_i$. The reaction terms are, if (4.16) is used for \mathbf{A}_j, Φ_j :

$$\langle \kappa_i\mathbf{t}_i, -j\omega\mathbf{A}_j \rangle = \omega^2 \int_V \kappa_i\mathbf{t}_i \cdot \int_{V'} \kappa_j \bar{\bar{A}} \cdot \mathbf{b}_j \quad (4.18)$$

$$\begin{aligned} \langle \kappa_i\mathbf{t}_i, -\text{grad} \Phi_j \rangle &= \int_V \kappa_i\Phi_j \text{div} \mathbf{t}_i - \int_{\partial V} \kappa_i\Phi_j \mathbf{t}_i \cdot \hat{\mathbf{n}}_i^s \\ &= - \int_V \kappa_i(\text{div} \mathbf{t}_i) \int_{V'} \kappa_j \bar{\bar{\Phi}} \cdot \text{grad}' \mathbf{b}_j \end{aligned} \quad (4.19a)$$

$$+ \int_V \kappa_i(\text{div} \mathbf{t}_i) \int_{\partial V'} [\kappa_{j+} \bar{\bar{\Phi}}^+ : \bar{\bar{P}}_j] - [\kappa_{j-} \bar{\bar{\Phi}}^- : \bar{\bar{P}}_j] \quad (4.19b)$$

$$- \int_{\partial V} (\kappa_{i+} - \kappa_{i-}) \int_{V'} \kappa_j \bar{\bar{\Phi}} \cdot \text{grad}' \mathbf{b}_j \quad (4.19c)$$

$$+ \int_{\partial V} (\kappa_{i+} - \kappa_{i-}) \int_{\partial V'} [\kappa_{j+} \bar{\bar{\Phi}}^+ : \bar{\bar{P}}_j] - [\kappa_{j-} \bar{\bar{\Phi}}^- : \bar{\bar{P}}_j] \quad (4.19d)$$

Integration by parts, and the fact that $\mathbf{t}_{i\pm} \cdot \hat{\mathbf{n}}_{i\pm}^s = 1$, were used in the derivation of (4.19). Its four terms (4.19a–4.19d) represent:

- (4.19a) is an interaction between volume charges.
- (4.19b) is an interaction between a source surface charge and a test volume charge. This will be zero unless one of the conditions stated above (P9 on the preceding page) holds.

- (4.19c) is an interaction between a source volume charge and a test surface charge. This will be $\neq 0$ in the same cases as the source surface charge, save the last one (P9/3), because $\bar{\bar{\Phi}}$ is always observer-continuous.
- (4.19d) is an interaction between source and test surface charges.

Now $\kappa \mathbf{t}$ is proportional to \mathbf{J} everywhere. The symmetry of the matrix of moments is thereby guaranteed.

4.3.1 Evaluation of reaction terms in free space

The numerical evaluation of the potential integrals (4.18–4.19), follows along the lines laid down in §3. We begin by assuming that the medium is homogeneous and unbounded and that the potential Green's functions are $\bar{A} = \mu \Psi \bar{I}$, $G^\Phi = \Psi/\epsilon$. The source integrals are singular when $V=V'$ (self-interaction, $i=j$) or $S=S'$ (which happens not only for the self-interaction, but also for the interaction between neighboring elements). Even when they are not, they may be difficult to evaluate numerically when the observation point \mathbf{r} is close to the source region.

Given the fact that the singular part of the integrand is known and can be integrated over the source region, volume or surface, with a closed formula, the extraction of the singularity seems the most efficient procedure. When the source region is a face charge [terms (4.19b, 4.19d)], the method is identical to that described in 3.2.1 for the computation of $\langle 1, \Phi_u * 1 \rangle$ on surface patches. Therefore only the case of a volume source region will be described here.

If the regularization (3.24) is applied to \bar{A} and $\bar{\bar{\Phi}}$, the singular parts to be computed analytically are [cf(4.16)]:

$$\mathbf{A}_{j\pm}^{\text{sing}} = j\omega \frac{\mu}{4\pi} \kappa_{j\pm} \int_{V'} \frac{1}{R} \mathbf{b}_{j\pm} \quad (4.20a)$$

$$\Phi_{j\pm}^{\text{sing}} = -\frac{1}{4\pi\epsilon} \kappa_{j\pm} \text{div} \mathbf{b}_{j\pm} \int_{V'} \frac{1}{R} \quad (4.20b)$$

The integral in (4.20b) is [146, (7)]; that formula is valid for any polyhedron. In the vector integral, the constant projections $\cdot \hat{\mathbf{e}}\hat{\mathbf{e}}$ of (4.8) and (4.9) are factored out and the result, the same for all three volume cells,

$$(\mathbf{r} - \mathbf{r}_{j\pm}) \int_{V'} \frac{1}{R} + \int_{V'} \frac{1}{R} (\mathbf{r}' - \mathbf{r}) \quad (4.21)$$

is solved with formulas [146, (7,8)]. The regular parts of (4.16),

$$\mathbf{A}_{j\pm}^{\text{reg}} = j\omega \frac{\mu}{4\pi} \kappa_{j\pm} \int_{V'} \frac{e^{-jkR} - 1}{R} \mathbf{b}_{j\pm} \quad (4.22a)$$

$$\Phi_{j\pm}^{\text{reg}} = -\frac{1}{4\pi\epsilon} \kappa_{j\pm} \text{div} \mathbf{b}_{j\pm} \int_{V'} \frac{e^{-jkR} - 1}{R} \quad (4.22b)$$

are computed numerically, with gaussian point rules. A list of point rules for volume regions, with references, is given in Appendix C.

4.4 Layered medium

In layered media, an application of the 2.5D formulation of §3 to the volume integral equation (4.4) is proposed. This imposes some constraints on the volume elements in addition to those stated in §4.2 for the free-space 3D formulation.

| <i>test function type & region</i> | <i>basis function type & region</i> | <i>integration of kernel</i> | <i>dimension</i> |
|--|---|----------------------------------|------------------|
| side-vol | side-vol | both | 2×2 |
| | side-face | both | 2×1 |
| | top/bottom-vol | both | 2×2 |
| | top-bottom-face | obs only | 2×2 |
| side-face | side-vol | both | 1×2 |
| | side-face | both | 1×1 |
| | top/bottom-vol | both | 1×2 |
| | top-bottom-face | obs only | 1×2 |
| top/bottom-vol | side-vol | (not used) | |
| | side-face | (not used) | |
| | top/bottom-vol | both | 2×2 |
| | top-bottom-face | obs only | 2×2 |
| top-bottom-face | side-vol | (not used) | |
| | side-face | (not used) | |
| | top/bottom-vol | src only | 2×2 |
| | top-bottom-face | none | 2×2 |

Table 4.1: Map of integrals in the interaction between volume elements in the 2.5D formulation.

P10 Constraints on volume elements in the 2.5D formulation

1. Tetrahedrons cannot be used.
2. The *top* and *bottom faces* (faces 3 and 4 of the wedge in fig. 4.2 and faces 4 and 5 of the hexahedron in fig. 4.3; naturally, the numbering is conventional) must be horizontal, and the *side faces* (every other) must be strictly vertical.
3. No pair of volume elements may overlap in z . (Any volume element will have a lowest (*bottom*) and a highest (*top*) z -coordinate. A *slice* is a pair of bottom and top coordinates, so that if two cells have the same bottom and top, they are in the same slice. Different slices are not allowed to overlap, so for any two slices either $(z_0, z_1) = (z'_0, z'_1)$ or, if $z_0 < z'_0$, necessarily $z_1 \leq z'_0$. This is dictated by the availability of integrated Green's function tables, as explained in chap. P3 on page 29.)

In free space, the integrals of (4.18, 4.19) are performed in exactly the same way whatever the orientation of basis or test functions. In the 2.5D formulation, the dimension of the integration domain (volume, surface, line) as well as the Green's function to be used, depend on this orientation.

Volume integrals become surface integrals in every case, and the integrated Green's function will carry the z -dependence (linear or constant) of the basis and test functions. Surface integrals may remain as surface integrals (when the surface was horizontal, ie the face charges of bottom and top functions) or become line integrals (when the surface was vertical, ie the face charges of the side basis and test functions).

This situation is presented in table 4.1. This table assumes that the integrals, which are terms from (4.18–4.19), are done ‘by cells’, that is, the surface integrals are split so that there is one integral per half-function. The actual Green's functions to tabulate and singular kernels can be looked up in table 3.1.

P11 Types of integrals for the interaction between volume elements in the 2.5D formulation

1. The *type* of function is ‘side’ (if $\lambda_{j\pm}$ or $\mathbf{b}_{j\pm} \cdot \hat{\mathbf{z}} = 0$) or ‘top/bottom’ (if $\mathbf{b}_{j\pm} \cdot \hat{\mathbf{z}} \gtrless 0$, respectively; here $\lambda_{j\pm} = 1$). The *region* is ‘vol’ (the volume of the element, $V \equiv V_{i\pm}$ or $V' \equiv V_{j\pm}$) or ‘face’ (one of the faces, only for scalar potential integrals).
2. The kernel is integrated when there is dependence of the basis or test function on the vertical coordinate. In practice this means for every combination of *type* and *region*, save top/bottom-face. Some of the interaction types are not used; this is because they are substituted for their reciprocals.
3. The dimension of the integral is determined by the original dimension of the regions (vg vol \times vol=3 \times 3) and the reduction by integration of the kernel, if any.

The singular kernels arise either from integration of the singular kernel of the 3D Green’s function, or from the identification of the singular part of the integrated 2.5D Green’s function. These functions have all been used already in §3.2 (see table 3.1). There are however a number of differences from the way things are done in the surface formulation.

P12 Peculiarities of the 2.5D formulation as applied to volume cell interactions

1. When extracting a singularity, the integrated singular kernel $\log P$ or (quasisingular) $\log(R + Z)$ needs to be integrated not over a segment, but rather over a triangle or a rectangle [actually this happened already for types VIII and IX of surface interactions (table 3.1) but in most cases reciprocity could be applied to use instead types VI and VII, which only require source integration over a segment]. The required integrals are solvable in closed form and can be found in P24 on page 133.
2. The boundary integrals (surface integrals) which result from application of integration by parts to the scalar potential terms are absolutely integrable (unlike in the surface case) and it is possible to integrate their terms separately. This means that the matrix can be filled cell-by-cell (half-function by half-function) in every case.

4.5 Examples

The following examples show the application of the volume formulation just presented to some classic examples from the literature. In every case, we compare equivalent currents or polarization currents, ie, the direct product of the solution of the integral equation by the method of moments. This is thought to be the more strict comparison criterion instead of secondary parameters, like far fields, in which the sensitivity to errors in the formulation (or in the numerical solution) is less.

P13 Two-layer dielectric sphere immersed in uniform field A dielectric sphere in uniform field is the ‘easiest’ problem of scattering by dielectrics in three dimensions. The dynamic solution is given by the theory of Gustav Mie[15, §14.5] in series form, but in the quasistatic case a closed form solution is possible, either for a homogeneous sphere, or a sphere made up of a number of concentric layers, by separation of variables in spherical coordinates. [142, §2.3] gives the expressions for a two-layer sphere.

For this comparison, a two-layered sphere with an inner core of radius $r = .458$ mm and $\epsilon_1 = 16$ and an outer shell with greater radius $r = 1$ mm and $\epsilon_2 = 9$, centered at the origin of

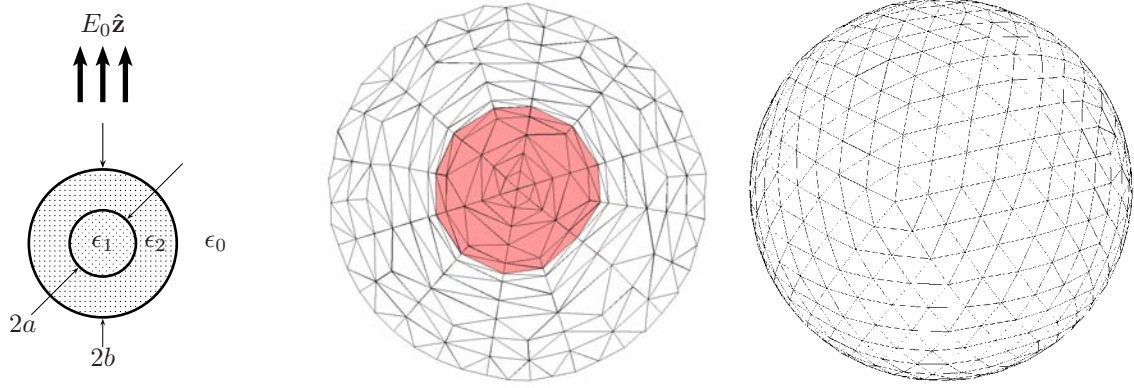


Figure 4.5: Two-layer dielectric sphere in uniform static field. The parameters are taken from [120, fig .6] and are: $a = 1$ mm, $b = .458$ mm, $\epsilon_1 = 16$, $\epsilon_2 = 9$. The densest mesh has 5000 tetrahedra, arranged in 5 layers for the inner core and 6 layers for the outer shell.

coordinates (fig. 4.5), was meshed with 4999 tetrahedra and simulated under normal plane wave incidence at a frequency of $47.7 \cdot 10^6$ Hz. (This sphere is the same as that used in the example of [120, fig. 6]). At this frequency, $k_0 = 1$ and the radius of the sphere is $\lambda_0/(2\pi 1000)$.

Although there are freely available programs that perform Delaunay ‘tetrahedralizations’ on any given closed polyhedron [2], the results are often highly irregular, much more so than in two-dimensional triangularizations. For this reason a specially tailored mesh was prepared. The mesh is inscribed in a sphere of radius somewhat larger than the figure given in the figures, to match the total volume of the mesh to the volume of the true sphere with nominal radius.

In the results of fig. 4.6 we see that the only component of the electric displacement is parallel to the ‘incident’ field. The static field is constant in the inner core. The jump in the tangential component of \mathbf{D} (along the line $z = 0$ or $\theta = \pi/2$) is as expected, while the normal component (along the line $P = 0$ or $\theta = 0$) is continuous. All these features are reproduced in the numerical solution. Overall, the agreement with the true fields is fairly good, considering the kind of discretization that was used.

The results of fig. 4.6 validate the symmetrization of the matrix of moments expressed in (4.18–4.19), because the internal discontinuity in the dielectric constant produces a test surface integral that is not present if the test is done with \mathbf{t} and not with $\kappa\mathbf{t}$.

P14 Two-layer dielectric sphere under plane wave excitation The same example just presented has been simulated at a frequency of 38.97 GHz. Here the electrical dimensions of the sphere of fig. 4.5 are $k_0a = .374$, $k_0b = .817$. (The figures given in the caption of fig. [120, fig. 6] are in error by a factor of 2π [119]). These results, obtained with a relatively crude mesh (fig. 4.7), are in good agreement with those of the reference. Therefore the symmetrization of (4.18–4.19) is validated also for the dynamic case.

P15 Dielectric cylinder under plane wave excitation: surface vs volume formulation This setup is represented in fig. 4.9. It has been analyzed with two different discretization densities, using

- the volume 3D (free space) formulation used for the spheres in the previous examples;

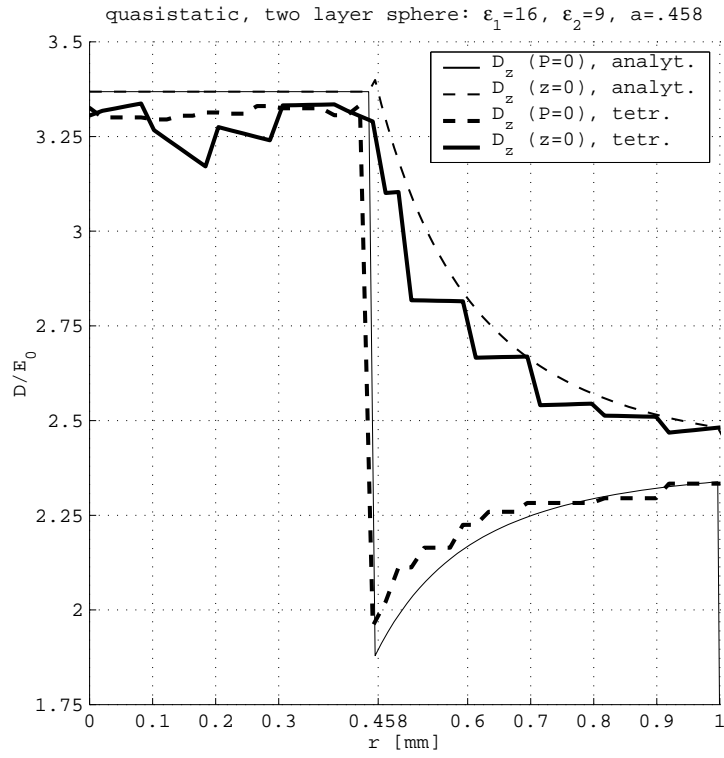


Figure 4.6: Two-layer dielectric sphere illuminated by very low-frequency plane wave (radius of outer shell is $< \lambda_0/6000$).

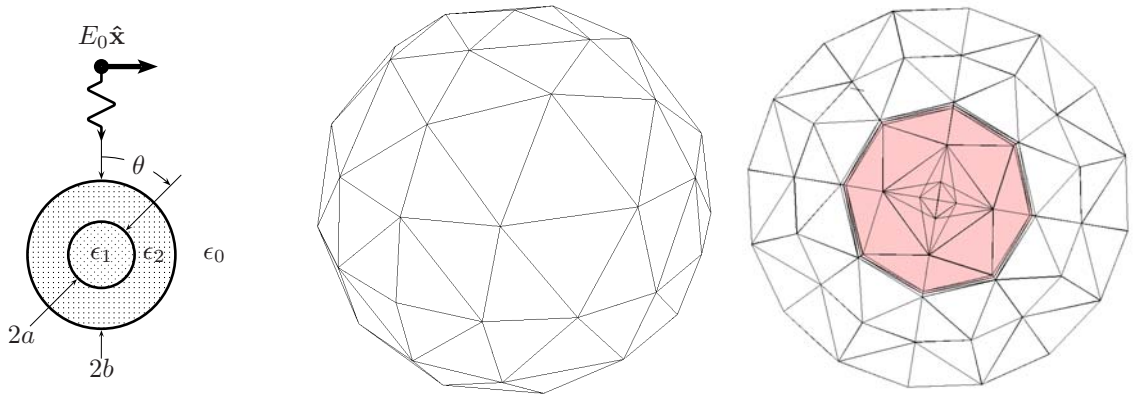


Figure 4.7: Mesh for the two-layer dielectric sphere under plane wave excitation: 888 tetrahedra. This is based on the subdivision of an octahedron. (The mesh used for the static case in fig. 4.5 is based on the subdivision of an icosahedron.)

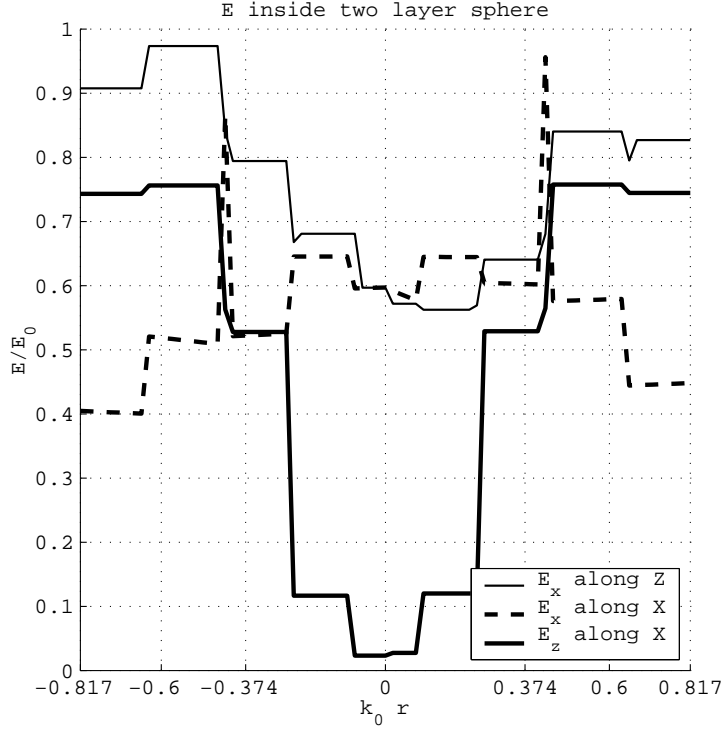


Figure 4.8: Electric field in a two-layer dielectric sphere subject to incident plane wave (top, fig. 4.8).

- the surface formulation presented in §3.4 and used to analyze a composite dielectric sphere in P8 on page 78.

The meshes for the cylinder are obtained by performing an extrusion on a planar mesh, in this case a circle (see fig. 4.10). This is in general true of 2.5D meshes, which are much simpler to generate than arbitrary 3D meshes. The extrusion produces, for the surface formulation, vertical rectangles, and for the volume formulation, separable (in the sense given in p. 28) wedges and hexahedra. The resulting mesh is therefore suitable for the application of the 2.5D techniques presented in this thesis. A comparison between the 3D and the 2.5D approaches is given in the next section.

Note that although only a view of the mesh from outside is presented in fig. 4.10, the meshes for the surface and the volume formulation are indeed different; the boundary is all there is in the surface formulation, while the mesh is solid in the volume formulation.

Here, the results of the volume and the surface formulation are compared on the surface of the cylinder. The solution of the surface problem gives the tangential field according to the relation $\mathbf{E} = \hat{\mathbf{n}} \times \mathbf{M}$, where the normal on the surface of the cylinder points outwards (this is actually a matter of convention). The solution of the volume problem gives the displacement $\mathbf{D} = \epsilon_1 \mathbf{E}$ inside the body, and this includes its surface. The representation of the field is, however, completely different, and this must be remembered when the respective results are compared.

Another possibility, not followed here, would be to compute the near field inside the body using the equivalent currents produced by the surface formulation, and compare this with the expansion of \mathbf{D} from the volume formulation [58, §6.29].

The results when a mesh of ~ 30 is used have been represented in figs. 4.11–4.12. The results with a mesh of ~ 70 cells/ λ_0 appear in figs. 4.13–4.14. The most noticeable feature of

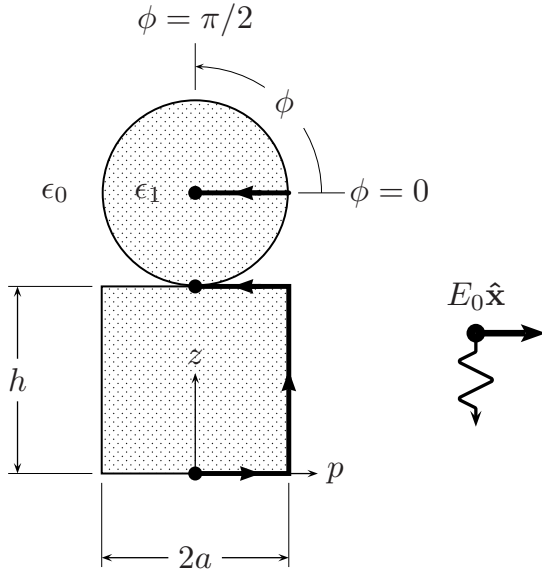


Figure 4.9: Homogeneous dielectric cylinder ($\epsilon_1 = 4$) in free space, under normal plane wave excitation, from [137, fig. 7] (also in [148, fig. 8], where a metallic cover is added). Electric field and equivalent magnetic currents are sampled along the indicated path and another similar at $\phi = \pi/2$ in figs. 4.11–4.14. Dimensions: $h = \lambda_0/5$, $a = \lambda_0/10$.

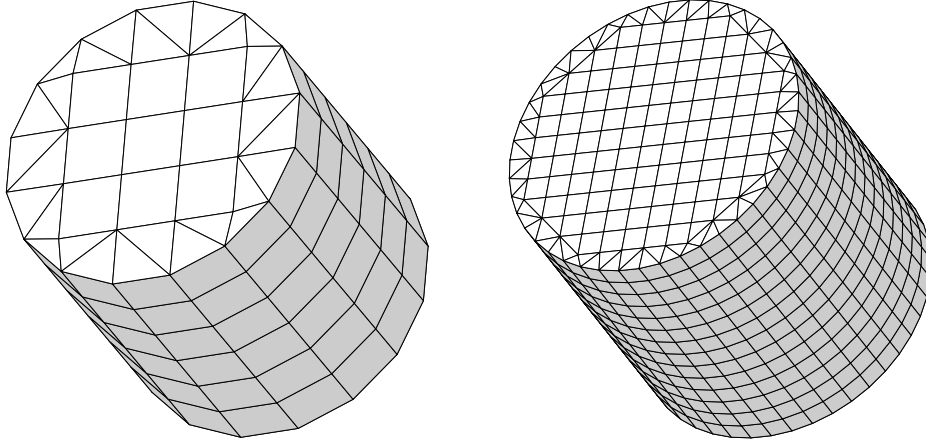


Figure 4.10: Two 2.5D volume (or surface) meshes for the homogeneous cylinder of fig. 4.9, with 30 and 70 cells/ λ_0 respectively.

these plots is the failure of the volume representation to capture the singular behavior of the radial component of the field near the edge of the cylinder [14, 4.13], which is not surprising, considering the type of discretization that is being used. Of course, along the vertical segment of the trace $s/\lambda_0 = (.1, .3)$, E_p is discontinuous; what is given is the value of the field *inside* the cylinder. Here $\hat{\mathbf{p}}E_p$ is normal to the cylinder and is not represented by any equivalent magnetic current.

P16 Dielectric cylinder under plane wave excitation: 3D vs 2.5D The homogeneous dielectric cylinder of the previous section has an appropriately orthogonal mesh, and can thus be analyzed with the 2.5D technique of §§2–3. In that technique, the mesh is considered to consist of horizontal layers and slices (a slice is the vertical extent of a cell which is not horizontal). In a problem in which there are no metallic patches and all the unknowns are polarization currents

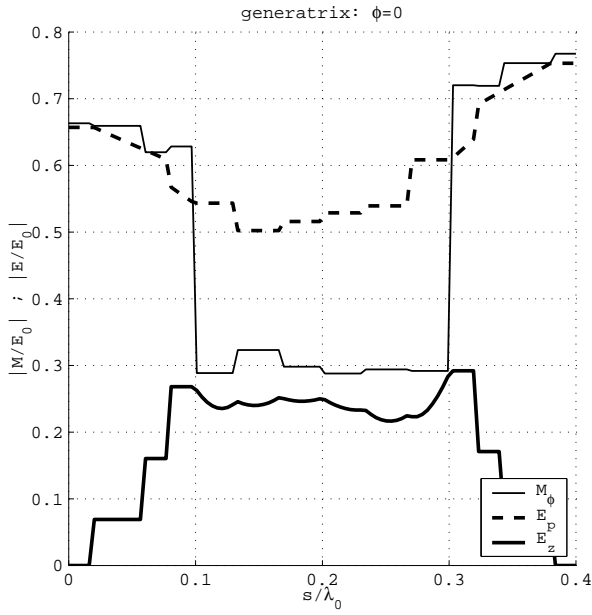


Figure 4.11: Electric field and equivalent magnetic current at the surface of the cylinder of fig. 4.9 under plane wave incidence, with a discretization ~ 30 cells/ λ_0 and along the cut of the plane $\phi = 0$ with the surface of the cylinder.

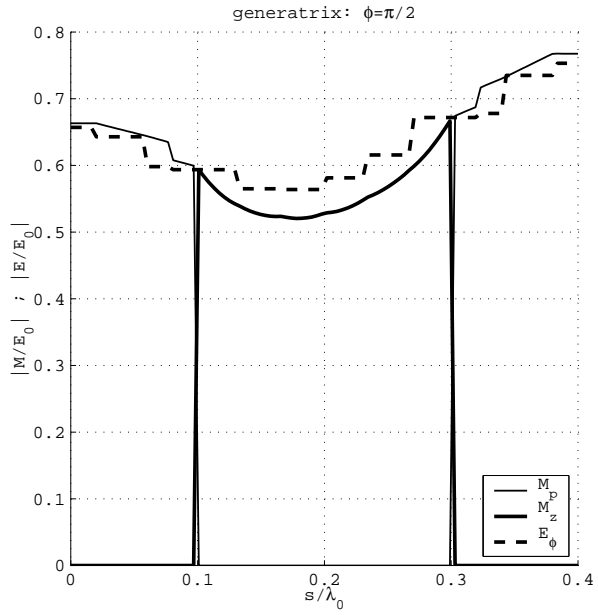


Figure 4.12: Same as in fig. 4.11, but along the cut $\phi = \pi/2$.

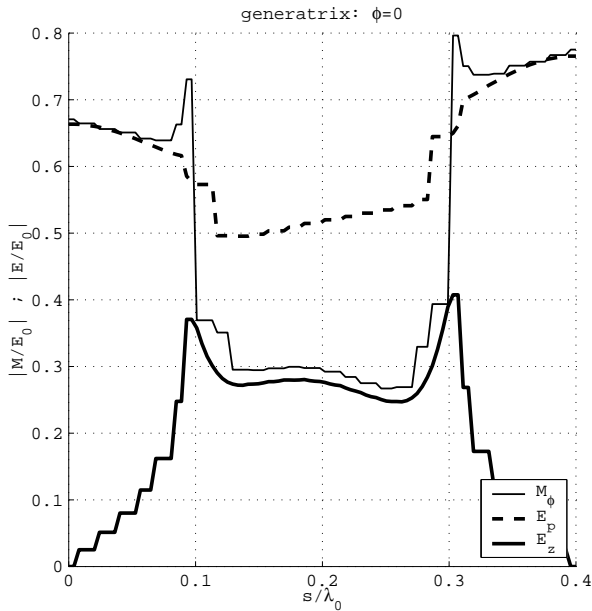


Figure 4.13: As in fig. 4.11, but the discretization is at ~ 70 cells/ λ_0 .

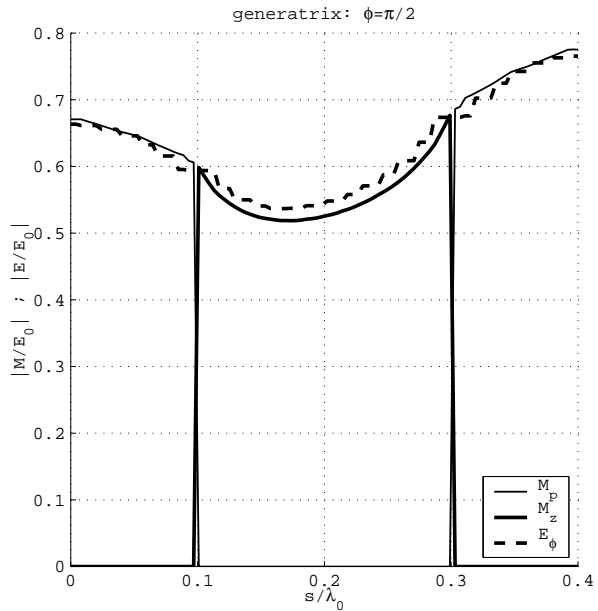


Figure 4.14: As in fig. 4.12, but the discretization is at ~ 70 cells/ λ_0 .

defined on dielectric bodies, there are no horizontal layers, only slices, because an element of finite volume must have a finite height. There are six slices in the coarser discretization of fig. 4.10.

The results obtained by either the 3D or the 2.5D formulation cannot be distinguished on a magnitude plot. For that reason, the absolute error between the 3D and the 2.5D formulation has been plotted instead, for both ~ 30 cells/ λ_0 and ~ 70 cells/ λ_0 discretizations. The excellent agreement serves as a validation of both the 3D and the 2D integration techniques used for linear rooftops defined on wedges and hexahedra.

4.6 Assessment

The final section of this chapter is not titled ‘conclusion’ and with good reason. So far only examples in free space have been presented, although we have introduced a formulation that, with the restrictions demanded by the 2.5D model, should retain its validity in layered media. Meanwhile, the symmetric formulation presented here has been validated in free space by analyzing composite and homogeneous bodies with a variety of meshes, using tetrahedra, wedges and hexahedra. We showed that there is only a small difference (error) in the method of moments solution when the reaction terms between volume cells are computed either

- as a double volume integral using point-to-point Green’s functions, or
- as a double surface integral, using integrated (slice-to-slice) Green’s functions.

This agreement validates, in particular, the singularity extraction procedure applied to the computation of these double surface integrals —the slice-to-slice Green’s function has a logarithmic-type singularity.

Other feature that would complete the implementation of the VEFIE-2.5D technique is the possibility of having interactions between polarization currents (volume cells) and electric or magnetic currents defined on surface patches (see [118] for a case without magnetic currents). In the general case of composite 3D objects with junctions between metallic parts, dielectric bodies and slots, the CFIE is clearly more economical in terms of unknowns and implementation complexity (because there are less types of interactions to program) and therefore preferable.

For peculiarly 2.5D problems, like the analysis of thin dielectric layers, where a single slice of volume cells may suffice, the volume formulation requires less unknowns. Also, the condition numbers associated to the matrix of moments are generally higher for the surface formulation.

To conclude, we note that if both the volume EFIE and the surface CFIE for dielectric bodies were to be implemented using the 2.5D technique, the precomputation of the vertical dependence of the Green’s functions would be independent of the permittivity of the dielectric body for the volume EFIE; for the surface CFIE, it would be necessary to decide whether to treat the interior problem with a 3D free-space Green’s function (in which case the Green’s kernels of the interior and the exterior problems could not be added) or to use there, also, a 2.5D technique. But then, the precomputation of the interior problem *would* depend on the dielectric permittivity of the interior medium.

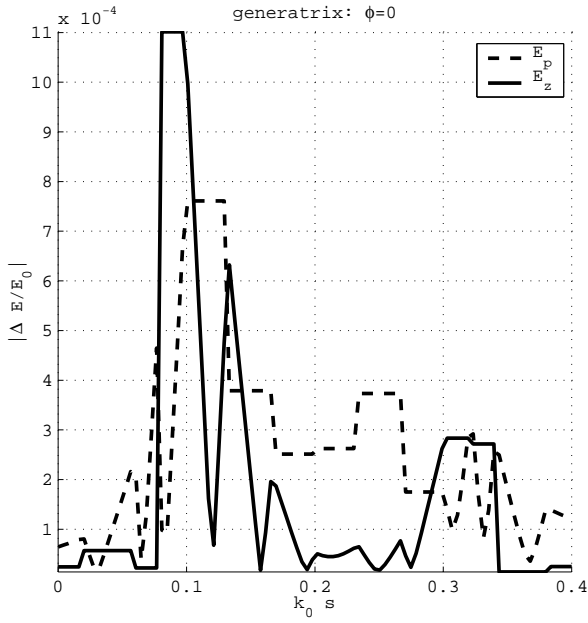


Figure 4.15: Absolute value of the difference between the electric field at the surface of the cylinder of fig. 4.9 obtained with a 3D volume MPIE in free space and a 2.5 volume MPIE in free space represented as a faked stratified medium.

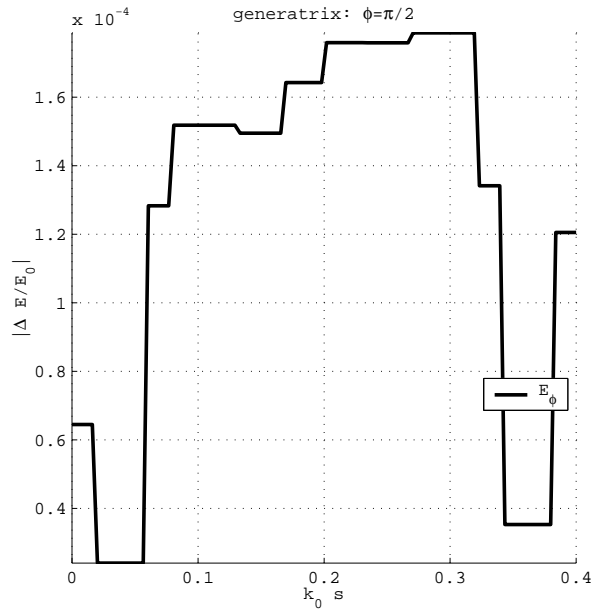


Figure 4.16: Same as in fig. 4.15, but along the cut $\phi = \pi/2$.

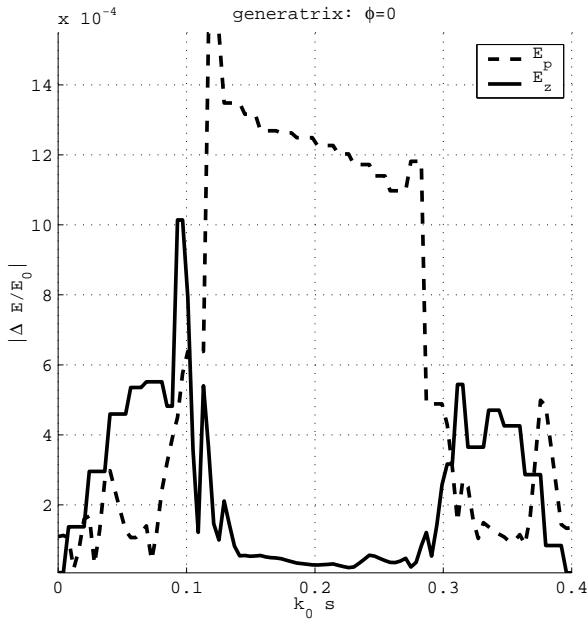


Figure 4.17: As in fig. 4.15, but the discretization is at ~ 70 cells/ λ_0 .

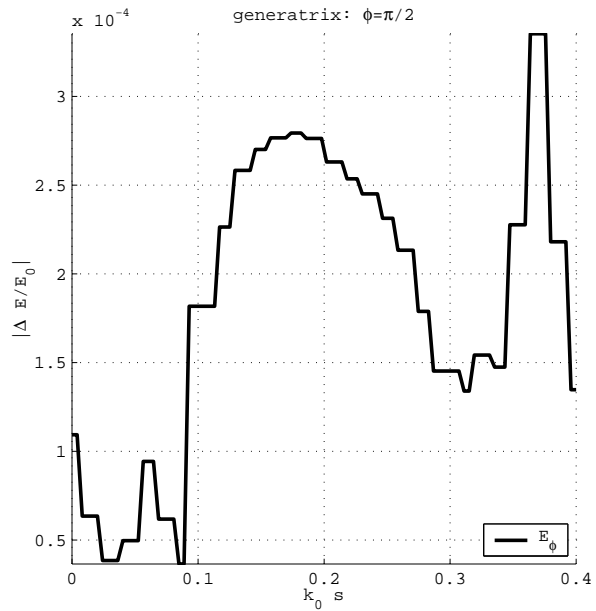


Figure 4.18: As in fig. 4.16, but the discretization is at ~ 70 cells/ λ_0 .

5 Applications

Three distinct applications of the theory and the numerical procedures presented up to now are studied in this chapter.

The first is a novel technique for the electromagnetic analysis of arbitrarily shaped apertures in thick metallic screens. This technique is made possible by the 2.5D integral equation approach developed in §§2–3. Although it is more efficient for small to moderate thicknesses (relative to λ_0), it is not an approximate method and will work for large thicknesses.

The second is the analysis of slot antennas with airbridges. A simple coplanar-waveguide (CPW) fed slot loop antenna is used as a prototype for some submillimeter-wave integrated receiver antenna designs. An airbridge over the radiating slots is required in these designs to provide DC return to the active element. The influence of these airbridges on the characteristics of the antenna is computed and compared to measurements (§5.2).

Finally, some of the work done in the frame of the IFER (Integrated Front-End Receivers) project [67] is summarily reviewed. An important part of this project involved the hybrid analysis of a planar feed antenna (using the Method of Moments and the results of this work) and a dielectric lens (using an advanced 3D ray-tracing method, developed at the University of Toronto). Only some aspects exclusively related to the analysis of the feed are touched upon (§5.3).

5.1 Apertures in thick metallic screens

Diffraction by an aperture in a black screen is a classical problem of optics [15, §VIII]. However, the black screen is not a very clear concept in rigorous electromagnetic theory, and it is impossible

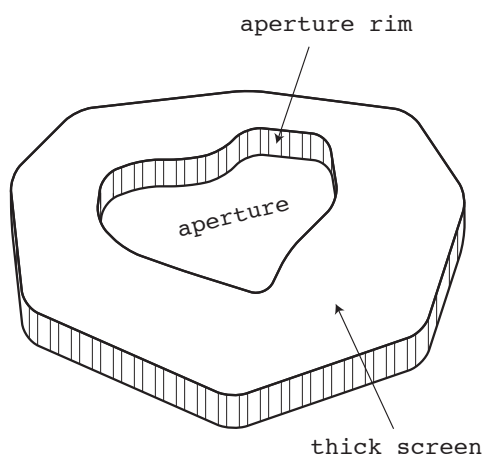


Figure 5.1: Arbitrarily shaped aperture in a thick (metallic) screen. The screen is infinitely wide.

to characterize with a simple choice of material parameters [15, §IX.1]; the simplest scatterer is a perfect (electric) conductor. Sommerfeld produced the first exact solution for the simplest diffraction problem (the half-plane) in 1896 [125, §38.A]. Since then, a number of approximations have been used to make more complicated situations, that do not have closed form solutions, manageable. We have the electrically small aperture [13], the infinitely thin aperture (which was treated in §3.3), the perfectly conducting aperture (idem); often these approximations are combined. Also, it is typical to assume a canonical shape for the aperture, and this is actually necessary if an exact solution is desired. If a numerical approximation is acceptable, the possibilities broaden considerably. The problem we shall attack in this section is that of an arbitrarily shaped aperture in an (in principle) arbitrarily thick, perfectly conducting plate of infinite lateral extent (fig. 5.1). Due to the open nature of the problem, its solution requires a proper use of the surface equivalence principle. Indeed there are a few alternatives even if we restrict ourselves to the integral equation technique, ie without resort to hybrid methods [40].

Consider the equivalent problem, given in §3.3, for the problem of an arbitrarily shaped aperture in an infinitely thin conducting screen. If the screen is now a thick plate, the equivalent problems above and below the plate should not change, because the equivalent magnetic currents will isolate the respective half-spaces. Now, naturally, the currents \mathbf{M}_u and \mathbf{M}_d do not occupy the same place, are not related to the same tangential electric field, and the relationship $\mathbf{M}_u = -\mathbf{M}_d$ holds no more (figs. 5.2 and 5.3). There is still a relationship, however, through the intervening space, which is necessary to model. Due to the use of the equivalence principle, this is now a parallel plate medium closed on every side by metallic walls —a cavity.

P17 Integral equation models for the aperture in thick screen

- A first possibility is to use modal expansions for the field in this cavity. This amounts to using the Green's functions of the cavity to obtain the magnetic field generated by each set of equivalent magnetic currents on the position of the other set, and then test as usual. This 'cavity model' is presented in fig. 5.3.

$$\begin{aligned} (\bar{\bar{H}}_{\text{cavity}}^M + \bar{\bar{H}}_{\text{above}}^M) * \mathbf{M}_u + \bar{\bar{H}}_{\text{cavity}}^M * \mathbf{M}_d &= -\mathbf{H}_u^{\text{exc}} \\ (\bar{\bar{H}}_{\text{cavity}}^M + \bar{\bar{H}}_{\text{below}}^M) * \mathbf{M}_d + \bar{\bar{H}}_{\text{cavity}}^M * \mathbf{M}_u &= -\mathbf{H}_d^{\text{exc}} \end{aligned}$$

The main inconvenient of the approach is the need to compute the Green's function for the cavity. This may be straightforward if the aperture has a regular shape (which means a rectangle or a circle, in practice), but it is not at all a simple matter otherwise. (A very interesting example is given in [16, §II]). On the other hand, the use of the cavity Green's function comes naturally to the problem and the results should arguably be faster and more accurate, although to verify this we shall wait and see the other techniques. Also, it seems reasonable to expect that the problem will not become more difficult to solve when the thickness of the plate increases, but rather the reverse, thanks to reduced coupling between high order modes at either end of the waveguide.

- A second possibility, and the one to be adopted here, is to leverage the 2.5D methods for open layered media that have been developed in §§2 and 3. The region between \mathbf{M}_{up} and \mathbf{M}_{dn} will be modelled as a laterally open parallel plate medium (or parallel plate waveguide, PPWG); the rim, then, is not included in the Green's function anymore and will be accounted for using equivalent electric currents (fig. 5.4). The integral equation is

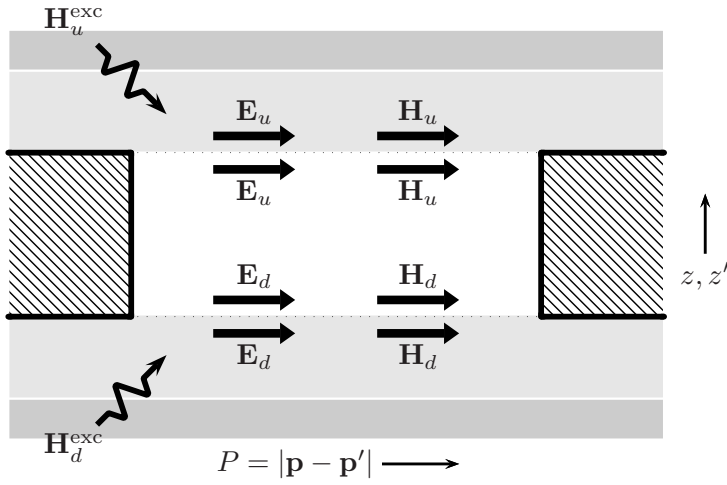


Figure 5.2: Aperture in thick screen: schematic view. Above, below or in the aperture itself are layered media.

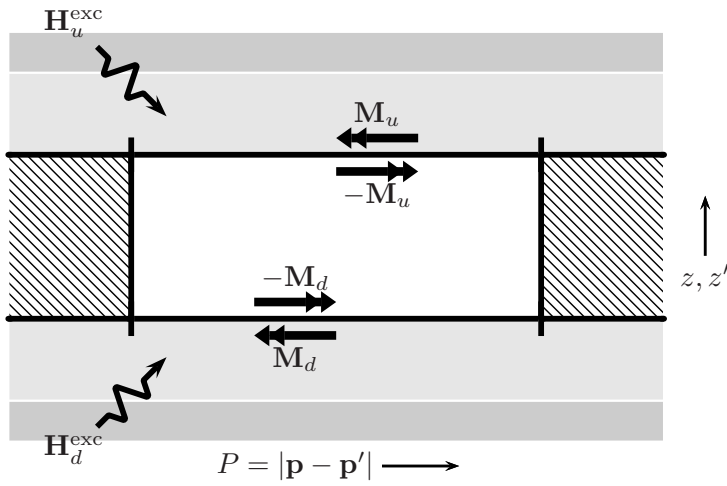


Figure 5.3: Modeling the aperture in a thick screen with a closed cavity and double equivalent magnetic currents.

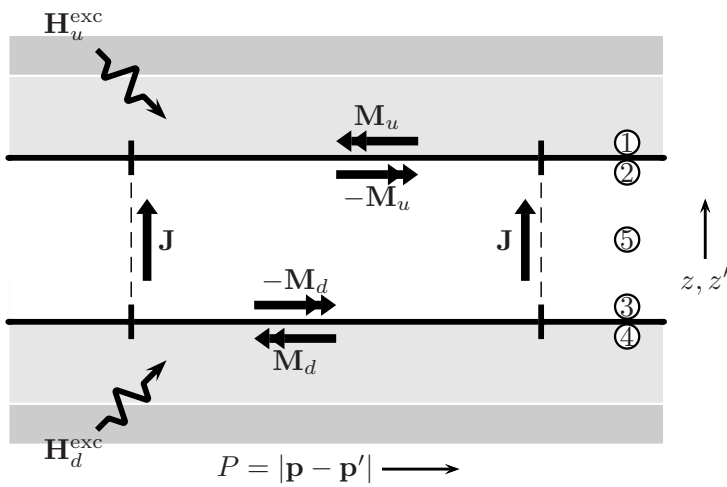


Figure 5.4: Modeling the aperture in a thick screen with a parallel plate waveguide, double equivalent magnetic currents, and electric walls along the rim of the aperture.

now

$$\begin{aligned}
(\bar{\bar{H}}_{\text{pp}}^M + \bar{\bar{H}}_{\text{above}}^M) * \mathbf{M}_u + \bar{\bar{H}}_{\text{pp}}^M * \mathbf{M}_d - \bar{\bar{H}}_{\text{pp}}^J * \mathbf{J} &= -\mathbf{H}_u^{\text{exc}} \\
(\bar{\bar{H}}_{\text{pp}}^M + \bar{\bar{H}}_{\text{below}}^M) * \mathbf{M}_d + \bar{\bar{H}}_{\text{pp}}^M * \mathbf{M}_u - \bar{\bar{H}}_{\text{pp}}^J * \mathbf{J} &= -\mathbf{H}_d^{\text{exc}} \\
\bar{\bar{E}}_{\text{pp}}^J * \mathbf{J} - \bar{\bar{E}}_{\text{pp}}^M * \mathbf{M}_u - \bar{\bar{E}}_{\text{pp}}^M * \mathbf{M}_d &= 0
\end{aligned} \tag{5.2a}$$

The most apparent difference between the cavity model and the PPWG model is that in the latter it is necessary to mesh the rim of the aperture, and this increases the complexity when the plate is very thick. On the other hand, most of the computation is dependent only on this thickness (the tabulation of Green's functions, according to the vertical discretization and to tables 3.1 and 3.2), and not on the shape of the aperture. This means that although changing thickness is expensive, changing shape has a low additional cost. This is precisely the opposite behaviour of the cavity Green's function technique. Therefore we see that our method is particularly adapted to printed circuit technology, where the vertical structure (number, type and thickness of layers) is more a technology constraint than a design parameter, and it is complementary to the other method, so that each has its domain of application.

The limitations of the PPWG model that are described now are forced upon us by the model itself: the purely numerical difficulties, such as the computation of the reaction terms, dealing with the singularity of $\bar{\bar{E}}^M$ in such a medium [electric and magnetic currents are actually in contact in fig. (5.4)]... have already been solved in §3.

5.1.1 Limitations of the 2.5D parallel-plate waveguide model

The first limitation is with *increasing* screen thickness. The reason why this is a limitation of the technique is that the walls (once rim) of the aperture are part of the structure, and they must be meshed. If the mesh density is to be kept constant, the number of cells and of basis functions grows linearly with the thickness. With plain integral equation solution techniques, this translates into quadratic storage increase and cubic time increase. It must however be remembered that for small problems (with current personal computers, up to a few thousand unknowns), complexity is dominated by matrix fill time. The cells of the walls are vertical, and consequently, thanks to the 2.5D formulation, it is only necessary to compute a 1D×1D integral for each interaction between them, in contrast to a 2D×2D integral in the general 3D case (see table 3.1: the integrals between vertical cells are of type II–V. Indeed, if the parallel plate medium is homogeneous, type V is equal to its reciprocal, type IV; A_{zp} is zero. See §3.2).

The second limitation is with *decreasing* screen thickness. This is most easily seen by writing the Green's function for the interaction between upper and lower magnetic current layers as an image series for the case of a homogeneous parallel plate waveguide, as in [89, §III, fig. 3]. As all the images have the same sign as the original source [cf (3.3.3)], they add constructively when $h \rightarrow 0$. It is thus clear that the method will break if an attempt is made to use that function directly. Indeed, the method will break much before the computation of $\bar{\bar{E}}^M$ becomes impossible. The appearance of many quasi-singular terms in the magnetic field convolution integral will make it difficult to evaluate, if the free space images are extracted one by one. A first solution would involve summing the whole static part of the series analytically, and extracting the static part not of the free space Green's function, but of the parallel plate Green's function; this can be derived in closed form (cf [88, (13)], [142, §1.7], [117, (5.44)]). In the limit, however, the reaction terms would still diverge.

The conclusion is not that the method is useless for any small thickness, but rather that the method is inaccurate for really, really small thicknesses. As the examples will show, it is possible to go down to $h \rightarrow \lambda/1000$ and obtain good accuracy, indeed obtain convergence with the ideal zero-thickness case. It may seem that this means that there is no practical limitation

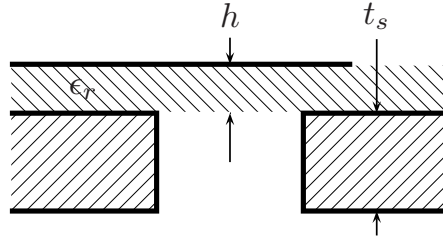


Figure 5.5: Vertical structure of microstrip-fed aperture in a thick screen, used in examples of figs. 5.6 and 5.13. The microstrip feed is assumed to be infinitely thin.

at all, because the difficult cases are devoid of interest! But the method requires a double discretization of the aperture, and there exists at least another technique that is ideally suited to small thickness, handles arbitrarily shaped apertures, and does not require double discretization. This is the “ δ -function” method, developed in our Laboratory in recent years [133, §5], [89, 129].

To demonstrate the possibilities of the approach adopted here, two sets of prototypes have been built. Both are microstrip-fed slot dipole antennas; the medium structure is that of fig. 5.5.

5.1.2 First prototype: rectangular aperture

The first is a microstrip-fed rectangular slot antenna. The geometry and the dimensions appear in fig. 5.6.

We start by considering the case of a ‘zero’ thickness metallic screen. The thickness of the metallization of the substrate ($35\ \mu\text{m}$, which is $\sim \lambda_0/1500$ at 6 GHz) can be safely neglected, and the methods of a §3.3 can be combined with a coarse mesh (fig. 5.7) to obtain the simulation results of fig. 5.8, that have been plotted together with measurements of the real structure from [133, figs. 5.26–5.28].

The aperture is rectangular and can also be modeled by the cavity Green’s function method, that can be expected to provide the best accuracy for thicknesses comparable to the wavelength. The cavity technique is described in [7, §5.3].

The agreement between simulation and measurements could be improved through a better mesh or an improved excitation model (a simple delta-gap at the start of the microstrip line was used). This is, however, not the main goal here. Rather, we want to see if the quality of the agreement is preserved when thicker screens and/or alternative simulation approaches are considered.

Figs. 5.9–5.12 show results for increasing screen thickness, from $\lambda/50$ up to $\lambda/5$. Now, in addition to measurements, we present three different theoretical predictions: the cavity model, the ‘delta’ technique [89] and the PPWG model, analyzed with the 2.5D techniques presented in this dissertation.

Experimentally, the resonant frequency seems to wander to and fro with increasing h ; it is apparent that a full-wave model is needed for this kind of structure.

For thin screens, all three simulations agree (essentially) and the difference with respect to measurements is essentially the same observed in the zero-thickness case of fig. 5.8. But as screen thickness is increased, a divergence appears between the numerical models. Obviously the cavity model is the most accurate, but we must be reminded of the difficulty of extending it to irregular aperture shapes. The δ -function method gives good results for the least thick screen, but quickly starts to drift off when h grows over about $\lambda/10$. The 2.5D results remain very close to those of the cavity model up to the greatest simulated thickness of $\lambda/5$, and are

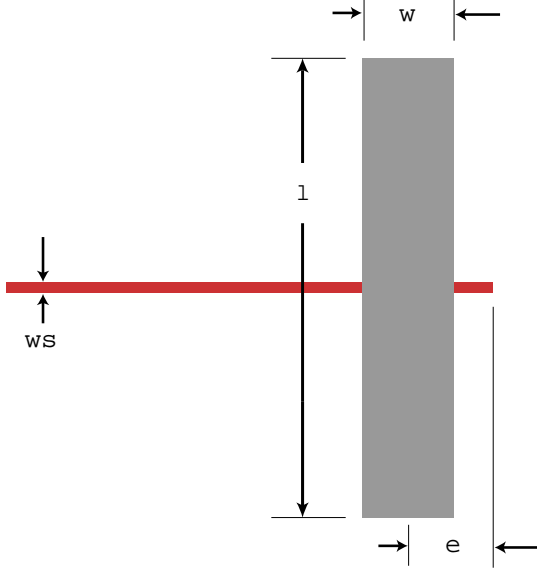


Figure 5.6: Rectangular aperture antenna in thick screen, fed by 50Ω microstripline. Dimensions: $l = 25$ mm, $w = 5$ mm, $e = 4.63$ mm, $w_s = .58$ mm. The substrate has $h = .635$ mm, $\epsilon_r = 10.5 \cdot (1 - j.0024)$. This design is from [133, fig. 5.23].

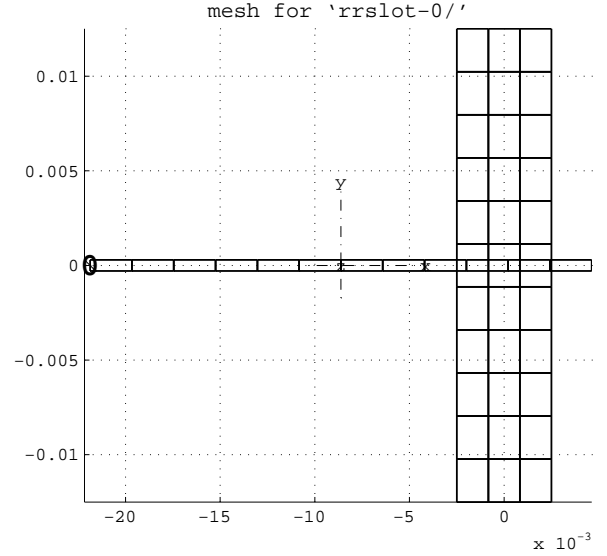


Figure 5.7: Mesh of the rectangular slot fed by microstripline whose dimensions are given in fig. 5.6.

clearly better than those of the ‘delta’ approach, that can be used for arbitrary shapes.

5.1.3 Second prototype: dogbone-shaped aperture

The second model is a dogbone-shaped slot antenna, also fed by coupling to a 50Ω microstrip line. Its dimensions are shown in fig. 5.13.

Fig. 5.14 shows the kind of mesh we used for the dogbone. This mixed triangular-rectangular mesh was prepared with a combination of the freely available TRIANGLE [3] and in-house tools.

The results are stable with increasing mesh density, as demonstrated by the comparison of simulated input impedance (fig. 5.15) for the two meshes of fig. 5.14. The meshes are for screen thickness of $t_s = 3$ mm. This stability is achieved thanks to the singularity and quasi-singularity extraction techniques developed for the 2.5D formulation in §3.

The breadboard series included screens of 0 mm (no screen, actually; the metallization of the substrate was $35\mu\text{m}$), 1 mm, 3 mm and 5 mm thick. They were made of brass and gold-plated for best contact with the printed antenna substrate; their size was $14\text{ cm} \times 14\text{ cm}$, large enough to avoid finite ground plane size influencing input impedance. Simulations and measurements are compared in figs. 5.16 to 5.19. The ‘dogbone’ resonates at 4.5 GHz if the thickness is $t_s = 35\mu\text{m}$ (fig. 5.16). For the other cases, the analysis with the present technique follows closely the behavior indicated by the measurements, as thickness increases. While a shape like the ‘dogbone’ does not add complexity to our approach, the cavity technique would become very cumbersome if practicable at all.

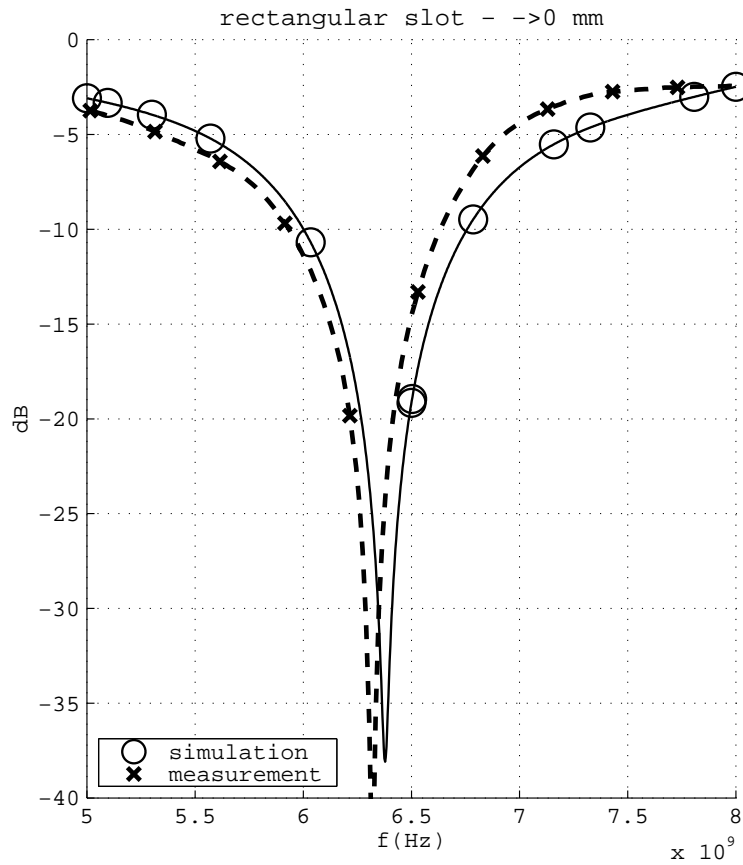


Figure 5.8: $|S_{11}|$ of the rectangular slot antenna: $t_s = 35 \mu\text{m} \approx \lambda/1500$ at 6 GHz. This was simulated using the infinitely thin screen approximation (§3.3).

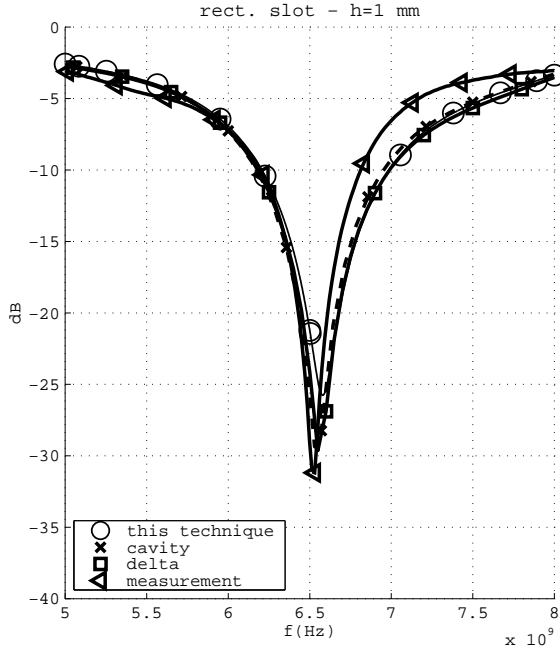


Figure 5.9: $|S_{11}|$ of rectangular slot antenna: $t_s = 1 \text{ mm} \approx \lambda/50$ at 6 GHz. The results of all simulations (PPWG, cavity and δ -approach) are very close. They all track precisely the marked displacement of the resonance, from 6.32 GHz (fig. 5.8) to 6.52 GHz here.

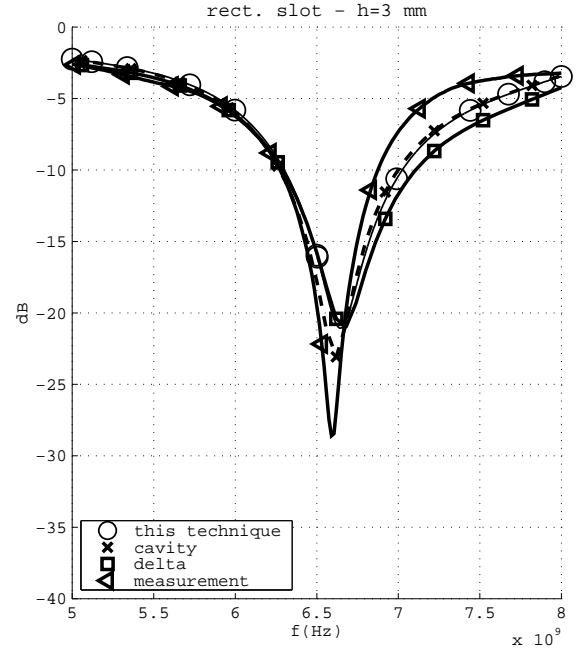


Figure 5.10: $|S_{11}|$ of rectangular slot antenna: $t_s = 3 \text{ mm} \approx \lambda/15$ at 6 GHz.

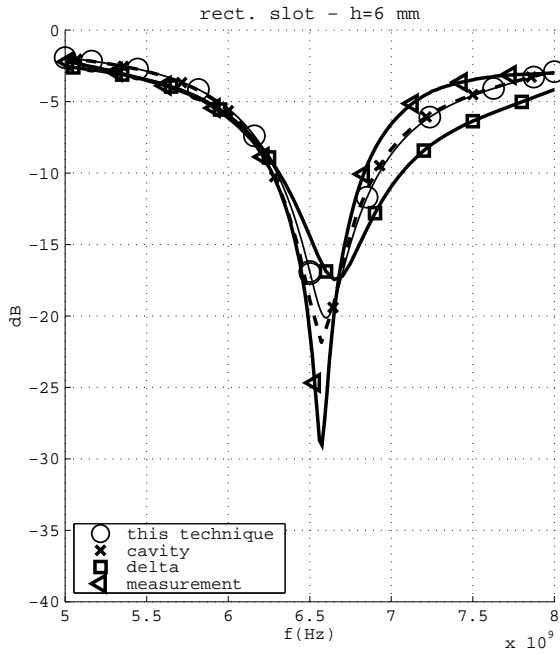


Figure 5.11: $|S_{11}|$ of rectangular slot antenna: $t_s = 6 \text{ mm} \approx \lambda/8$ at 6 GHz. The results from the δ -approach start to deviate.

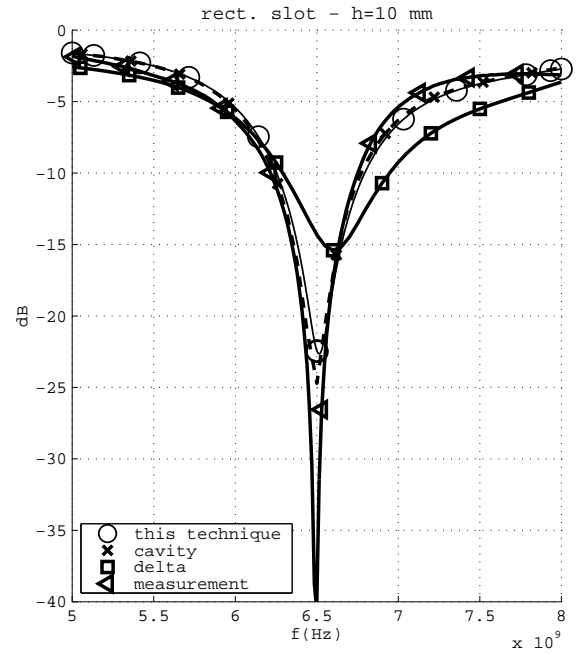


Figure 5.12: $|S_{11}|$ of rectangular slot antenna: $t_s = 10 \text{ mm} \approx \lambda/5$ at 6 GHz. The PPWG results are very close to the cavity method's. Both track correctly the measured resonant frequency.

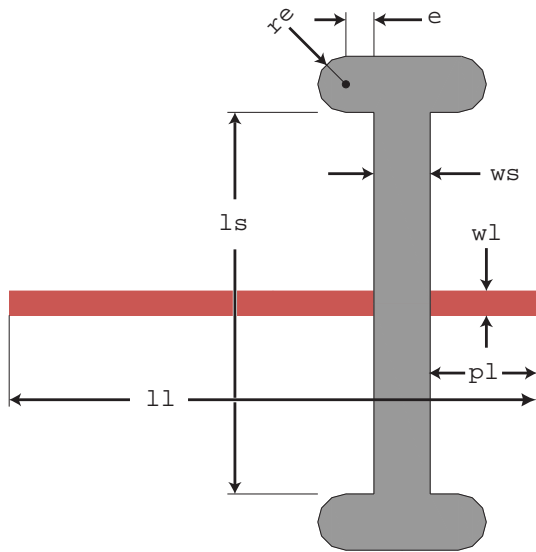


Figure 5.13: 'Dogbone' slot in thick screen, fed by $50\,\Omega$ microstripline. Dimensions in mm: $r_e = 2.5$, $e = 2.5$, $l_s = 34$, $w_s = 5$, $l_l = 47$, $w_l = 2.164$, $p_l = 9.5$. Microstrip substrate: $h = 0.76$ mm, $\epsilon_r = 2.485$.

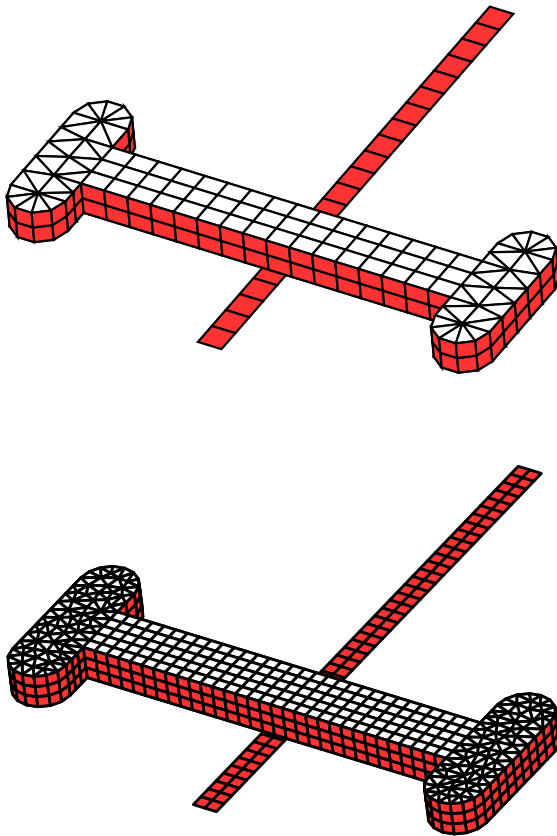


Figure 5.14: Two different density meshes for the 'dogbone' antenna. Above: ≈ 30 cells/ λ_0 . Below: ≈ 60 cells/ λ_0 . Magnetic cells in white; electric cells in grey/red. There is another layer of magnetic currents that is hidden in the figures.

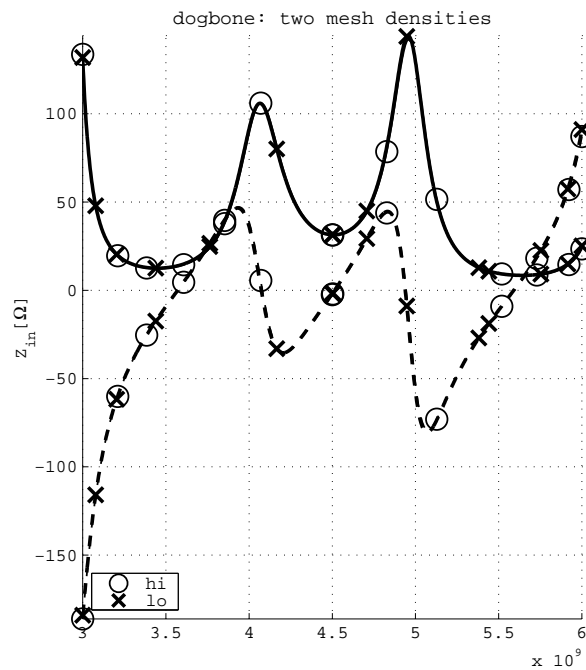


Figure 5.15: Convergence of analysis results with increasing mesh density, for 'dogbone' antenna. Real part —continuous line; imaginary part: —dashed line.

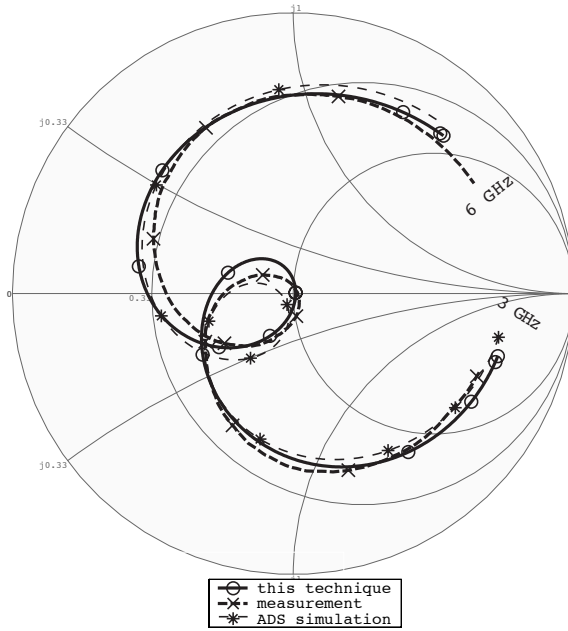


Figure 5.16: $|S_{11}|$ of 'dogbone' antenna: 'zero' thickness slot ($35 \mu\text{m} \approx \lambda/1700$ @5 GHz) simulated with infinitely thin screen approximation.

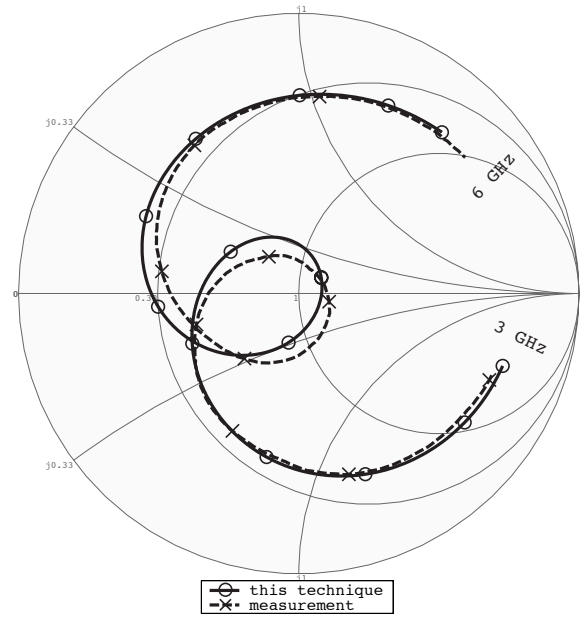


Figure 5.17: $|S_{11}|$ of 'dogbone' antenna: slot of thickness $\approx \lambda/60$ @5 GHz.

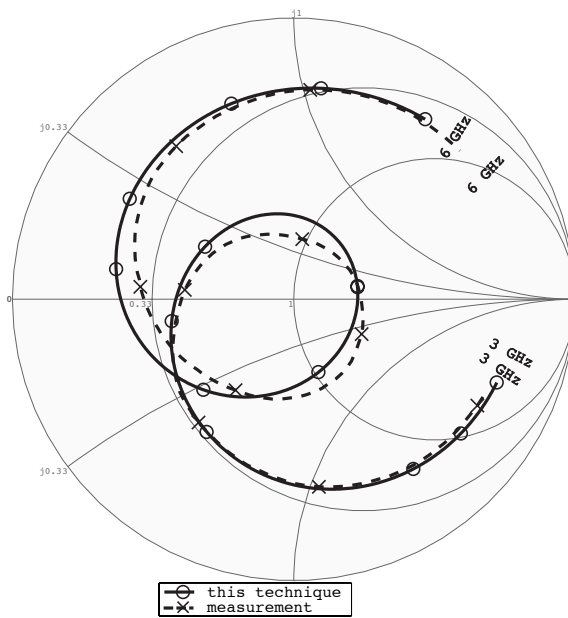


Figure 5.18: $|S_{11}|$ of 'dogbone' antenna: slot of thickness $\approx \lambda/20$ @5 GHz.

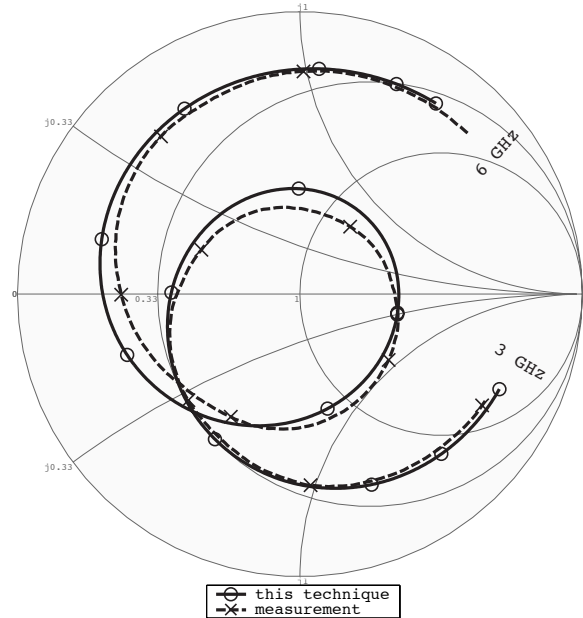


Figure 5.19: $|S_{11}|$ of 'dogbone' antenna: slot of thickness $\approx \lambda/12$ @5 GHz.

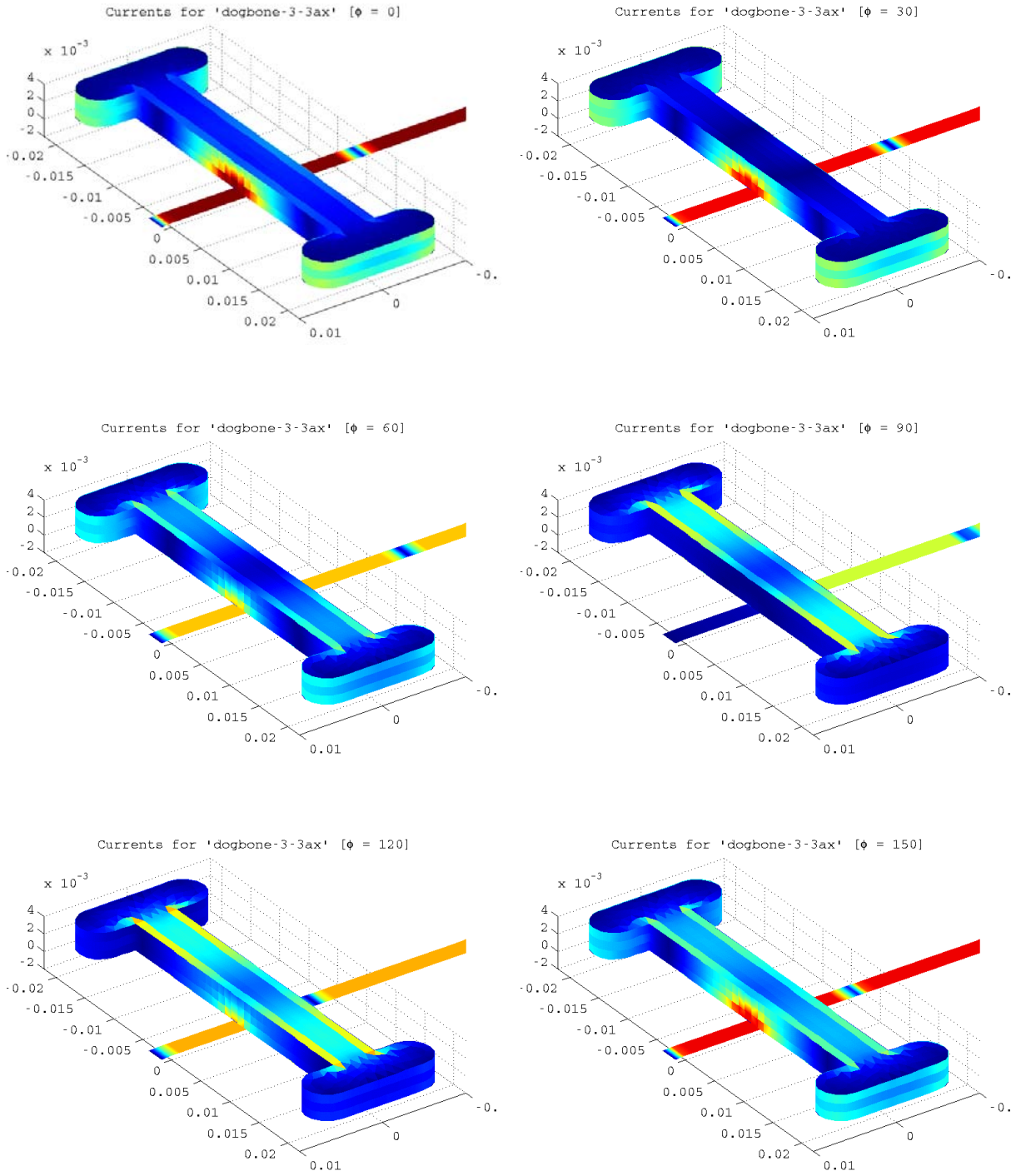


Figure 5.20: Color representation of electric (feed line, dogbone vertical walls) and magnetic (top of dogbone aperture) currents in the dogbone antenna over half a period. This has $t_s = 3\text{ mm}$ and the simulation is at 3 GHz. Excitation is a delta-gap voltage $V = 1$ at the other end of the strip, not shown in the figures. The magnitude of the current has been clipped to one fifth of its maximum value, which is the cause for the saturation on the feeding strip. Electric and magnetic currents are normalized (dimensions $\rightarrow \cdot k_0$, $\omega \rightarrow 1$, $c_0 = \epsilon_0 = \mu_0 \rightarrow 1$).

5.2 Airbridges in CPW and SL circuits

The coplanar waveguide (CPW) was first introduced in 1969 as a means to obtain an elliptically polarized field that could be used in non-reciprocal microwave devices [144]. Afterwards it came to be used more and more often for standard microwave and (especially) millimeter-wave printed circuit applications, which were once the domain of stripline and later of microstripline technology [123].

The main advantage of CPW lines is the possibility of connecting surface mounted elements either in series or in parallel; in microstrip it is necessary to drill via holes to make parallel connections. In addition to the fabrication worries, these vias add extra parasitics that become more and more troublesome as the frequency of operation increases.

The main inconvenient of CPW circuits *as such* is that, as the CPW transmission line consists of three conductors, it supports two quasi-TEM modes that propagate from zero frequency (fig. 5.21). One of them (the *even* or *antenna mode*) radiates by its very nature and is undesirable in circuit applications; this includes feed structures in slot antennas. Coupling between the *odd* (or *circuit*) mode and that unwanted mode will occur at any asymmetry of the structure (bends, forks, non-symmetrically connected devices, transitions). The even mode must be actively eliminated and this is done by means of *airbridges* that connect left and right ground planes of the CPW. In a conductor backed CPW, these airbridges may adopt the form of thru-vias [136] which eliminate also the parallel plate mode.

In antenna applications, an airbridge may have other purposes, such as

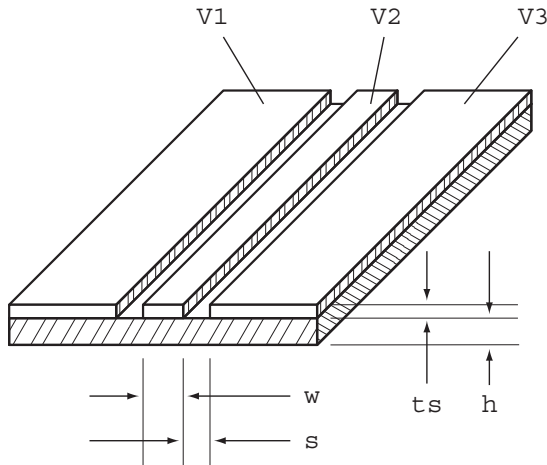
- Allow the connection of a hard-to-place lumped element.
- Provide DC return for active elements.
- Provide matching for active elements.
- Kill or create antenna resonance modes.
- Any combination of the above.

Besides, when the primary objective of an airbridge is to, say, provide DC return, it is important to assess its parasitic effect on the resonant modes of the antenna; indeed, this assessment is bound to be more critical than the quality of the DC return provided. Because these airbridges on extra duty are not placed systematically (as the ground plane equalizer airbridges are) and may need specific design (ie, specific values of parameters: height, distance from slots), and also because they may radiate, a full-wave analysis method is required. Integrated circuit technology produces regular shaped airbridges that can be appropriately analyzed by 2.5D methods. Some wire-bonding techniques may produce curved airbridges that require 3D methods.

5.2.1 CPW-fed slot loop antenna

The specific application we shall examine now has been inspired by work on antennas for integrated receivers in the millimeter- and submillimeter-wave bands [116], [121, §IV]. Typically, these are lens antennas fed in the focus by some sort of planar antenna or waveguide. This will be further discussed in §5.3; here we just point out that, because of considerable fabrication difficulties in these bands, and also because of the requirements of the lens system, the primary radiators, or feeds, are usually of the simplest kind. A quite popular one [98, 112, 128] is the slot ring antenna, often fed by CPW (figs. 5.22–5.23). This structure provides the easiest fabrication and excellent possibilities of integration with active devices.

The slot ring is almost always designed to radiate in its second resonant mode, where it is around a wavelength in circumference, because this mode produces the best radiation patterns



| | V_1 | V_2 | V_3 |
|--|-------|-------|-------|
| <i>even / balanced / antenna / slotline mode</i> | \pm | 0 | \mp |
| <i>odd / unbalanced / transmission line mode</i> | + | - | + |

Figure 5.21: Standard coplanar waveguide (CPW) and relative potentials for the two modes without cutoff frequency [48, §7.4.2].

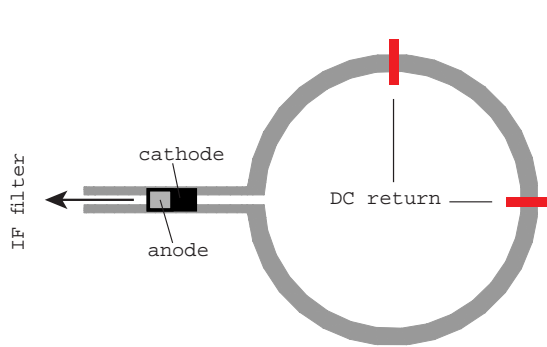


Figure 5.22: Integrated mixer design with diode in the feed line.

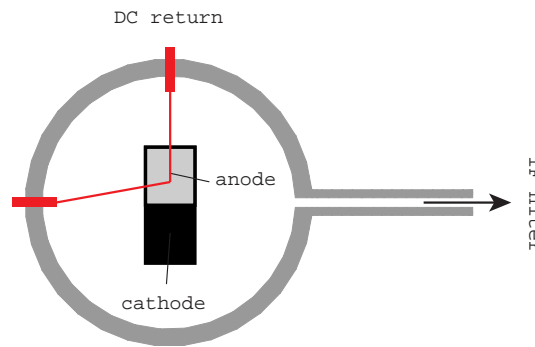


Figure 5.23: Integrated mixer design with centered diode.

(rotationally symmetric, with cancellation of the radiated fields at low elevation both in the E and the H planes) as well as broadband impedance behavior that allows good matching to the active element [96, §5.4].

One of the issues with these antennas is the placement of the active device. Because of their compact size, at very high frequencies (> 300 GHz) an integrated Schottky diode can be as big as the antenna itself [74], and often it cannot be placed in series in the input line as in fig 5.22. These considerations prompted the proposal of the configuration shown in fig. 5.23. Here the

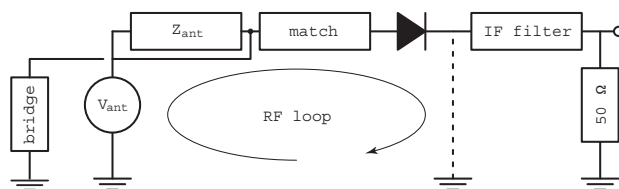


Figure 5.24: Equivalent circuit for fig. (5.22).

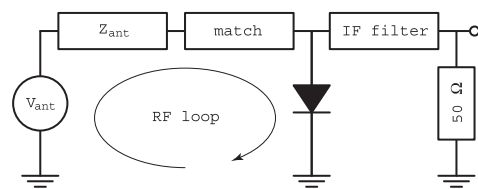


Figure 5.25: Equivalent circuit for fig. (5.23).

diode is placed in the middle, where there is plenty of space. It is also very close (cannot be more) to the antenna, and RF losses between the antenna and the mixer are minimized. Both in this design and in that of fig. 5.22, an airbridge is needed to provide DC return to the active element, so that it can be polarized. (Actually the configuration of fig. 5.22 only makes sense if a beam-lead diode is used; with a vertically mounted diode, the bridge would not be necessary (cf [70, §6.2.4]). This example is provided for illustration; the beam-lead diodes can be used for ‘low’ frequency models, but not for submillimeter wave applications).

With respect to the antenna, the airbridge has a different role in each of these designs. In the ‘centered’ design, fig. 5.23, the filter must present an open circuit to the loop, and the airbridge is part of the RF loop composed of antenna, matching structure (the bridge) and diode, all in series (fig. 5.25).

In the other design, the RF loop is closed by the filter; the sole purpose of the bridge is to provide DC return (fig. 5.24), and matching is provided by the section of CPW connecting the diode to the antenna.

In both cases the bridge should be designed so that it does not modify the characteristics of the antenna as a radiator. For example, in [96, §5.2.2], the bridge was designed by assimilating it to a short section of suspended microstrip line. This approximation may allow to match the diode, but does not provide precise information on the effect of the bridge on the slot loop itself.

To verify the capability of the methods presented in this work to analyze this kind of structure, a low frequency model (3 GHz) has been designed (fig. 5.26). Airbridges of different sizes (from $\sim \lambda_0/12$ to $\sim \lambda_0/4$) have been built (figs. 5.27–5.28) and placed in either the symmetrical or the asymmetrical positions of figs. 5.22–5.23.

These structures provide an excellent test case for the EM integral equation models and for the numerical techniques developed in previous chapters.

On one side we have both electric currents (used to represent the airbridges) and magnetic currents (on the CPW slots). On the other side both vertical and horizontal currents must be considered.

Finally, if the airbridge has a low height and/or is located close to the slots, strong coupling and quasi-singular interactions may arise, which will bear out the singularity extraction procedures applied to the computation of the elements of the matrix of moments.

An excellent agreement has been obtained for all lengths when the bridge is placed in the symmetrical position (figs. 5.29–5.36). As expected, the longest airbridge, which in circuit terms has the highest impedance, produces the smallest alteration respect to the bridge-less behavior (this is shown in dashed line in fig 5.37).

In the asymmetrical position, only the shortest airbridge was tested, with good agreement (fig. 5.37). Out of the design frequency of 3 GHz, the asymmetry introduced by the bridge causes multiple resonances, but the response at 3 GHz has barely changed.

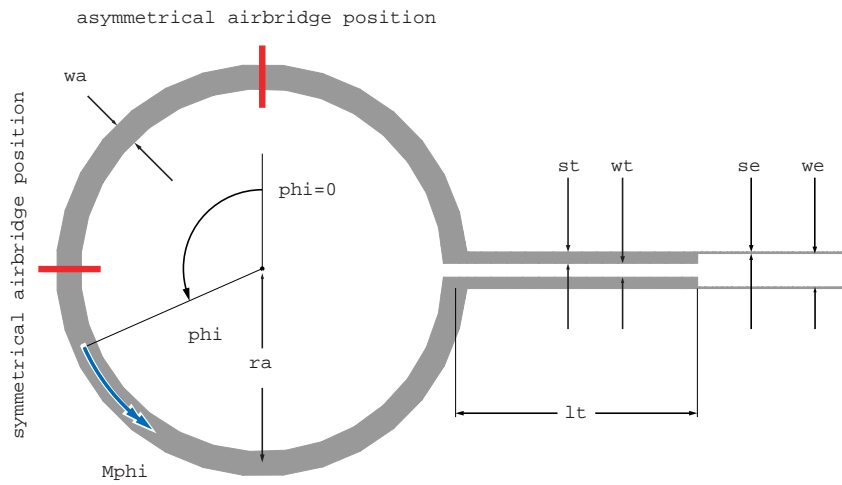


Figure 5.26: Air-bridged CPW-fed slot antenna: low frequency model, resonant at 3 GHz. Dimensions in mm: $r_a = 15.92$, $w_a = 2$, $l_t = 19.89$, $w_t = 1.140$, $s_t = 0.930$, $w_e = 0.126$, $s_e = 2.748$. The slot is printed on dielectric substrate with $h = 1.57$ mm, $\epsilon_r = 2.33$.

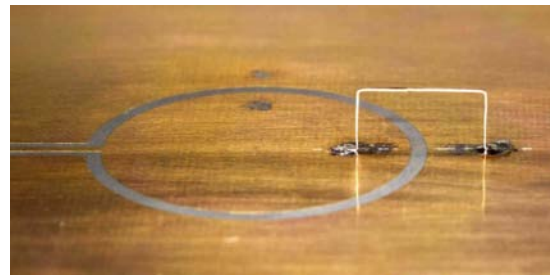
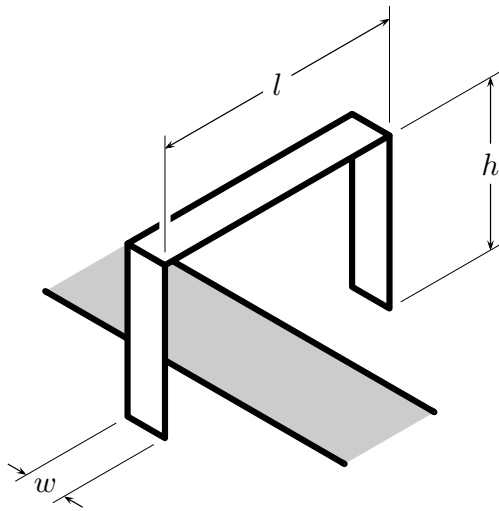
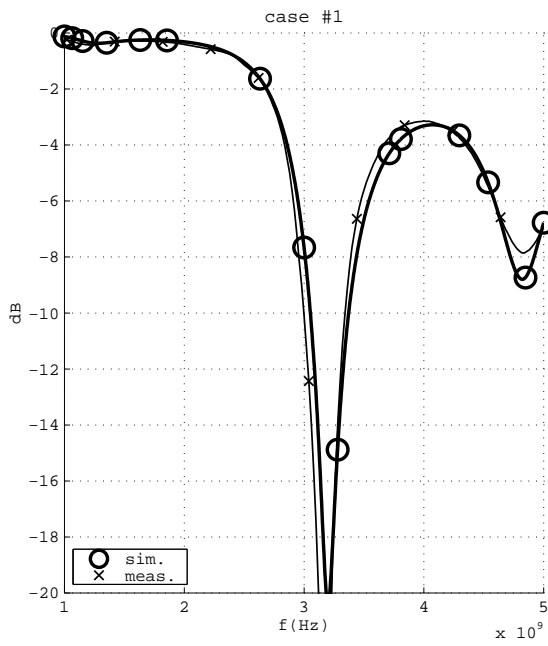
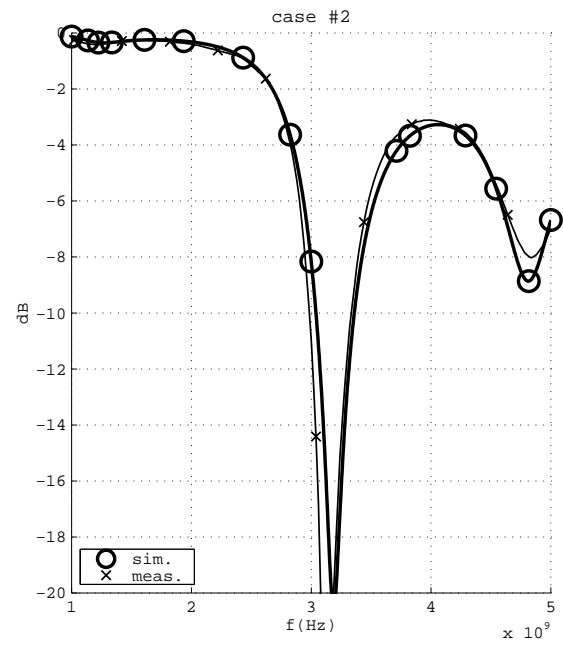
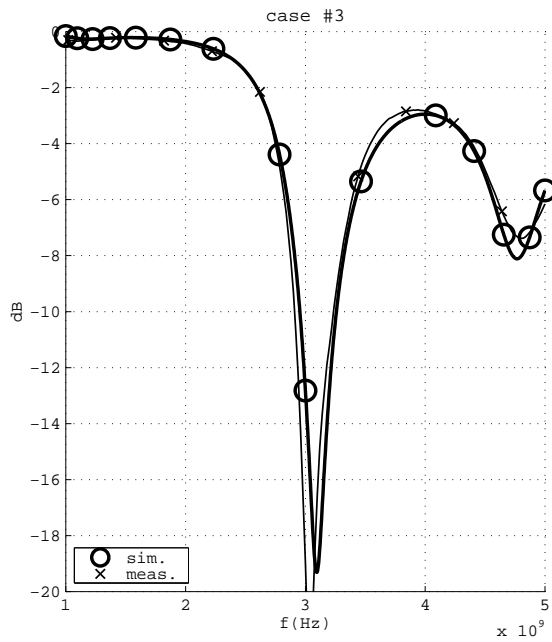
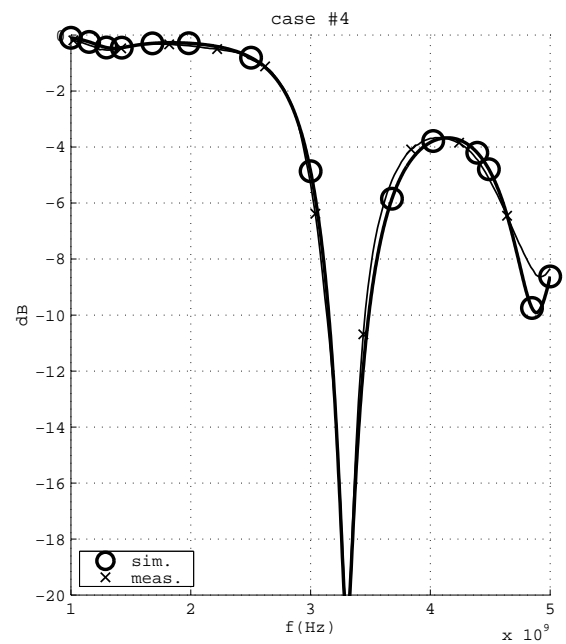


Figure 5.27: (above) Detail of airbridge #3 as mounted in the symmetric position.

| case # | l | h | w |
|--------|------|------|------|
| 1 | 6.1 | 5.95 | 0.98 |
| 2 | 12.1 | 3.2 | 0.95 |
| 3 | 12.1 | 5.95 | 0.85 |
| 4 | 12.1 | 1.4 | 1.0 |
| 5 | 6.05 | 3.0 | 1.05 |
| 6 | 6.2 | 1.0 | 1.55 |

Figure 5.28: (left) Measured dimensions (in mm) for each of the airbridges whose effect on the input impedance of the CPW-fed slot loop antenna is presented in figs. 5.29–5.34.

Figure 5.29: $|S_{11}|$ for case #1 of fig. 5.28.Figure 5.30: $|S_{11}|$ for case #2 of fig. 5.28.Figure 5.31: $|S_{11}|$ for case #3 of fig. 5.28.
This is the longest bridge.Figure 5.32: $|S_{11}|$ for case #4 of fig. 5.28.

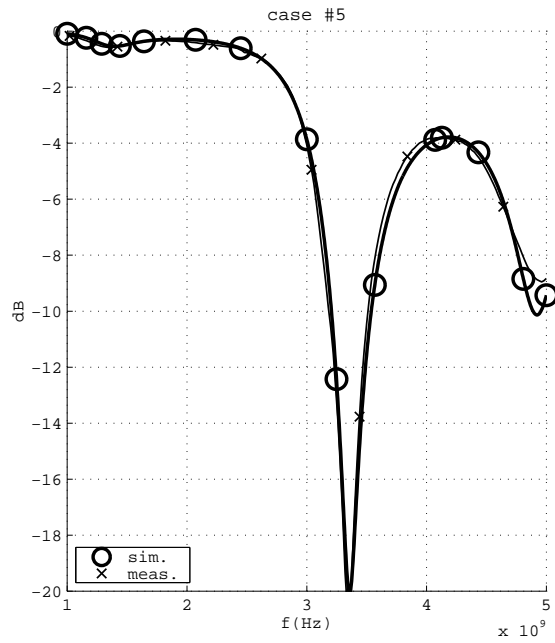
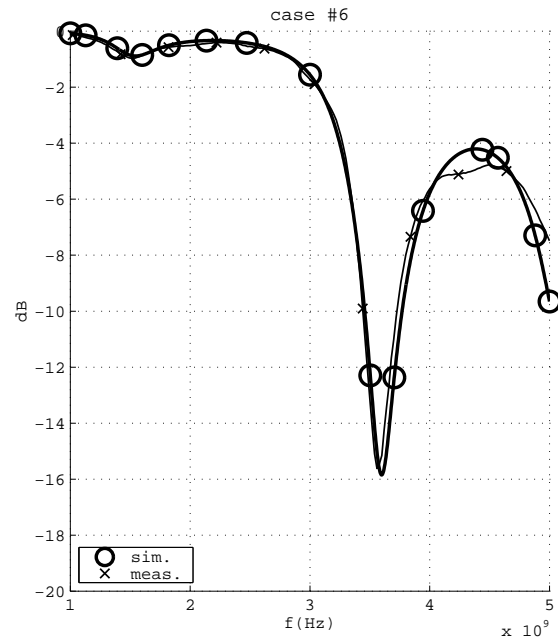
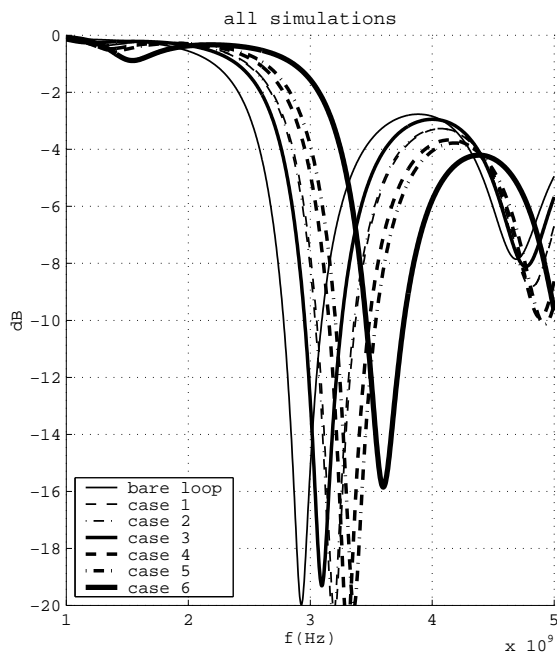
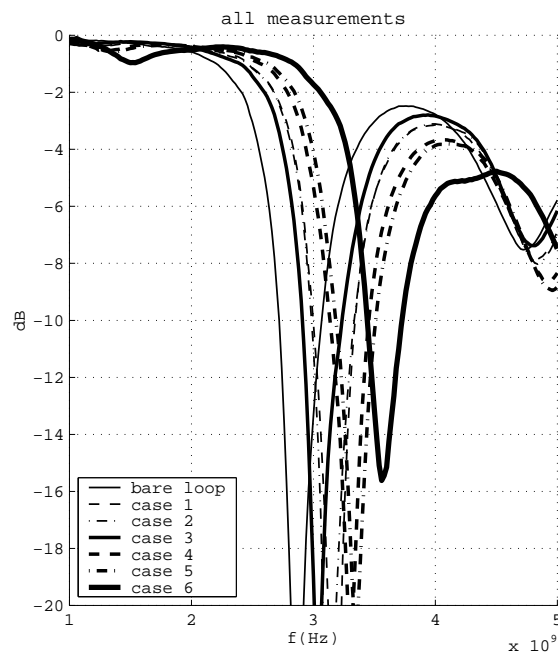
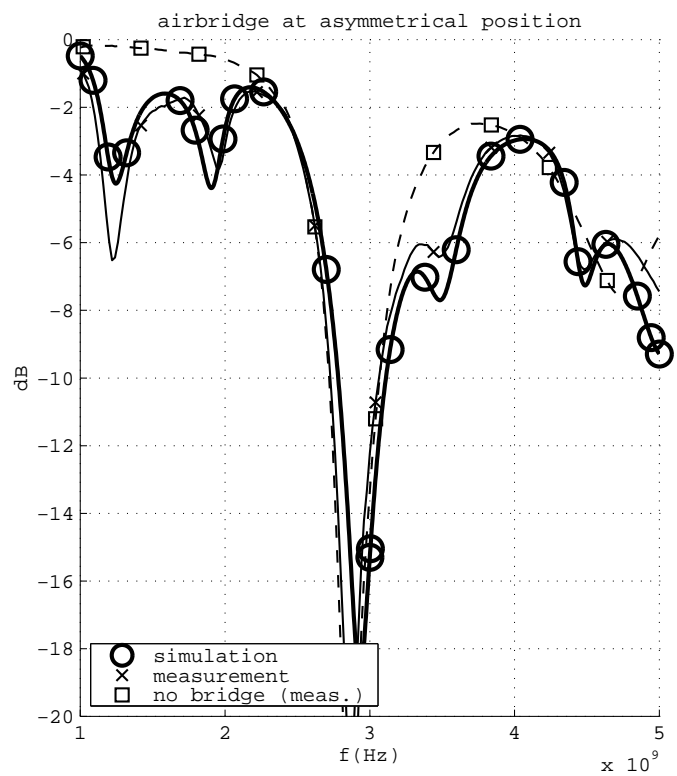
Figure 5.33: $|S_{11}|$ for case #5 of fig. 5.28.Figure 5.34: $|S_{11}|$ for case #6 of fig. 5.28. This is the shortest bridge.Figure 5.35: Simulated $|S_{11}|$ for all 6 cases of fig. 5.28.Figure 5.36: Measured $|S_{11}|$ for all 6 cases of fig. 5.28.

Figure 5.37: Return loss for CPW-fed antenna with asymmetrically placed airbridge. The main resonance (at 3 GHz) is not changed by the airbridge, because in that position ($\phi = 0^\circ$ in fig.5.26) and at that frequency there is a natural minimum of magnetic current in the slot loop.



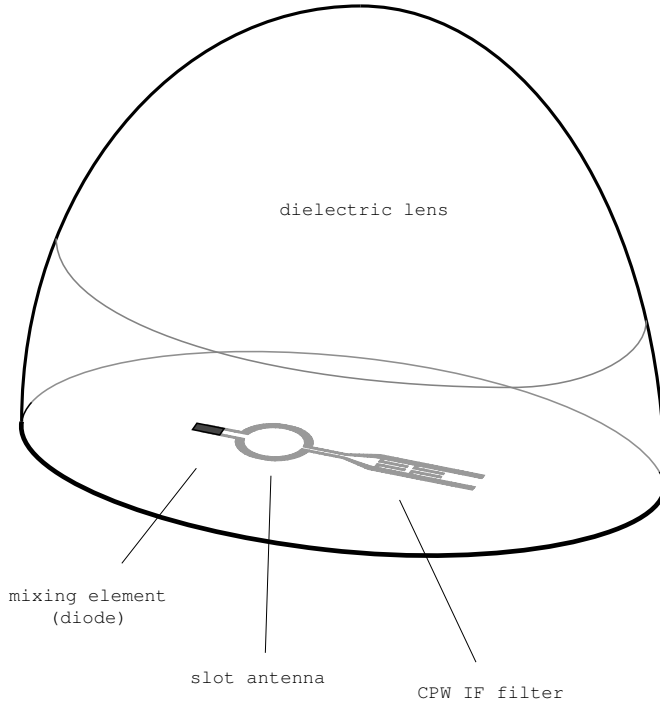


Figure 5.38: Schema of the integrated receiver on a substrate lens.

5.3 Integrated antennas in substrate lenses

Among the various possible architectures for a receiver frontend for atmospheric chemistry missions, room temperature frontends (as opposed to superconductor-based [151]) with integrated, reliable Schottky diode technology, seem among most promising [90], as evidenced by the sizable literature on the subject [6, 37, 38]. The basic structure of such a frontend is depicted in figure 5.38. It consists in a feed section (mixer with integrated antenna) coupled to a dielectric lens, and it is intended to work in the sub-millimeter waveband (up to 1 THz). The term ‘substrate lens’ is used because the lens is attached directly to the substrate of the planar antenna, so that the slots may radiate most of their power into it [59, (33)], [149, §E (37-38)]. The structure is also free from surface waves, because the slots see what amounts to a homogeneous half-space.

Part of the radiation produced by the feed is reflected back from the lens-air interface, and causes a change on the input impedance of the integrated antenna, which has been estimated by certain authors [138, §IV], [42, §II, fig. 4], and, at least for large lenses ($\varnothing > 10\lambda_0/\sqrt{\epsilon_r}$) is small. In principle, this effect is not taken into account in the present work.

Therefore, we postulate that the magnetic currents radiated by the slots into the lens are the same as they would be if the lens were replaced by a semi-infinite homogeneous medium of the same dielectric constant. This approximation effectively decouples feed and lens and allows for a much greater ease of analysis.

In an open structure receiver, all circuit elements (filter, diode matching network) are on the same plane as the antenna, and they produce parasitic radiation. To keep it within tolerable limits, a careful design of the receiver as a whole is required.

5.3.1 60 GHz models

The tools developed in §§ 2–3 have been used in the production of two different low-frequency (60 – 65 GHz) prototypes. They are all based around the IFER baseline design, which places the vertically-mounted diode at the end of a CPW tuning stub (fig. 5.39). This design was

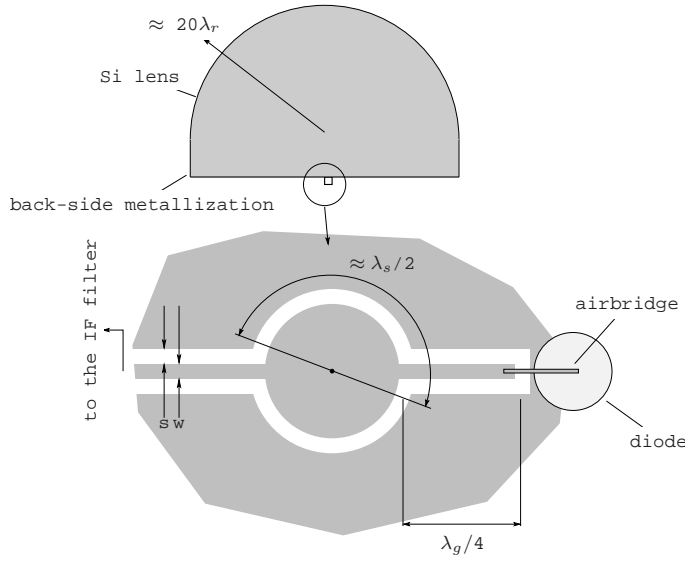


Figure 5.39: IFER baseline design.

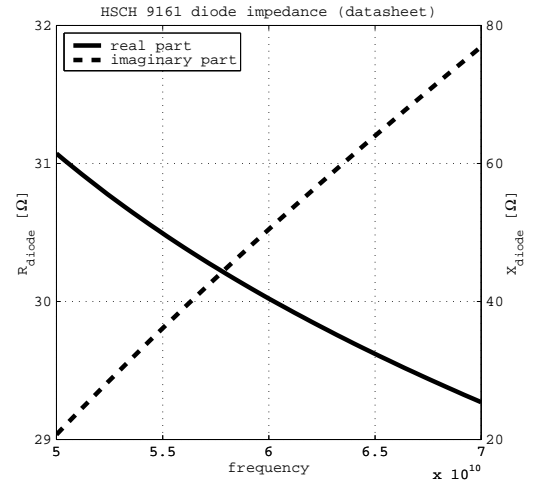


Figure 5.40: Input impedance of unpolarized Schottky diode (HSCH-9161) around 60 GHz, according to the data sheet.

studied, substituting a rectangular loop, in [98]. The diode may also be placed in the input line, in series, and then the stub must be shorted to provide the required DC return. However, as discussed above (p. 111), this configuration becomes less attractive at higher frequencies. One advantage of the tuning stub with the diode at the end is that the design is practically the same with either a beam-lead or a vertically mounted diode.

The prototypes are *subharmonically-pumped* mixers, which means that the RF signal is not mixed with a directly generated LO signal, but rather with a higher harmonic generated in the diode's nonlinear junction [70, §7.3.4]. In our measurement system (described in [96, §E]), this is the 16th harmonic for RF of 65 GHz. In the real-size system, the LO would be introduced quasi-optically.

The beam-lead Schottky GaAs diode HSCH-9161 from Hewlett-Packard was available in our Laboratory and was selected as the active element. The dimensions of this piece are approximately $250\ \mu\text{m} \times 250\ \mu\text{m}$ without the leads, which are $231\ \mu\text{m}$ long $\times 120\ \mu\text{m}$ wide. Its input impedance has been computed from the equivalent circuit in the datasheet [54], based on 1 GHz measurements (fig. 5.40).

The first design is shown in fig. 5.43. With the facilities of our lab, the minimum dimension of the layout was limited to $50\ \mu\text{m}$. This is the width of the slots (s_1, s_2) of the quarter-wavelength stubs of the IF filter in fig. 5.43. Because of the great difference between the RF (60.5 GHz) and the IF (330.11 MHz) the filter has been designed as a bandstop filter instead of as a low-pass filter. Compact CPW filters have become increasingly popular in recent years [127]. A 10 GHz standalone filter was designed, built and measured on the same principle, to verify the ability of our code to analyze it. The layout and the results appear in figs. 5.41–5.42. A frequency shift can be appreciated. The simulation was checked with commercial software (HPADS) and the results were very similar. Three causes appear as most likely.

- Conductor (ground plane) losses have not been taken into account. Indeed it is possible to

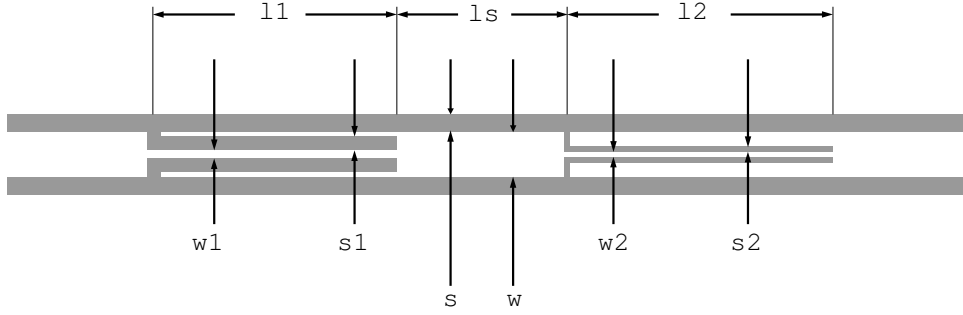


Figure 5.41: Above: test bandstop compact CPW filter at 10 GHz. Dimensions in mm: $l_1 = 2.81$, $w_1 = 0.091$, $s_1 = 0.154$, $l_s = 1.26$, $w = 0.5$, $s = 0.2$, $l_2 = 3.02$, $w_2 = 0.052$, $s_2 = 0.061$.

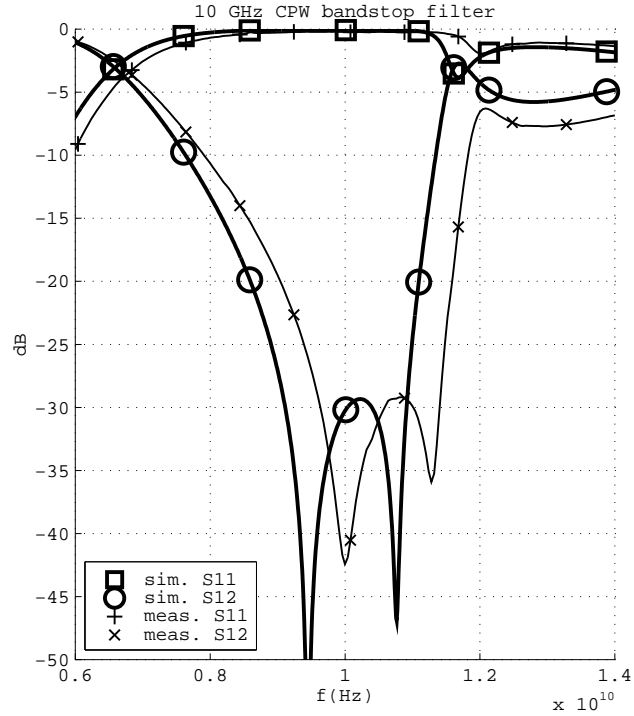


Figure 5.42: To the right: test bandstop compact CPW filter at 10 GHz. Measured and simulated $|S_{11}|$ and $|S_{12}|$.

make simulation and measurement agree slightly better by adding these losses, but not by much, and in any case the effect is not a frequency shift, but an adjustment of levels [67, fig. 4.3].

- Metalization thickness is not taken into account. This is thought to be the most important source of error. The overall effect is to lower the effective dielectric constant of the CPW lines, thus moving upward the resonances [19, §IV.4]. The effect may be specially important because the slots have widths comparable to the metallization thickness, vg $s_2 = 52 \mu\text{m}$ vs $t = 17 \mu\text{m}$. It is clear that this is more likely to happen as frequency increases and the same fabrication process is used. An extension of the technique demonstrated in §5.1 to the case of CPW excitation would be of help.
- There is a difference between the actual value of the permittivity of the substrate and the value introduced in the simulation. A slight adjustment of the permittivity does indeed produce a closer match between measurement and simulation. This source of error is difficult to separate from the precedent.

The radiation patterns for the first design, that of fig. 5.43, after the lens, appear in figs. 5.44–5.47. These patterns were measured on the final prototype. No simulation appears,

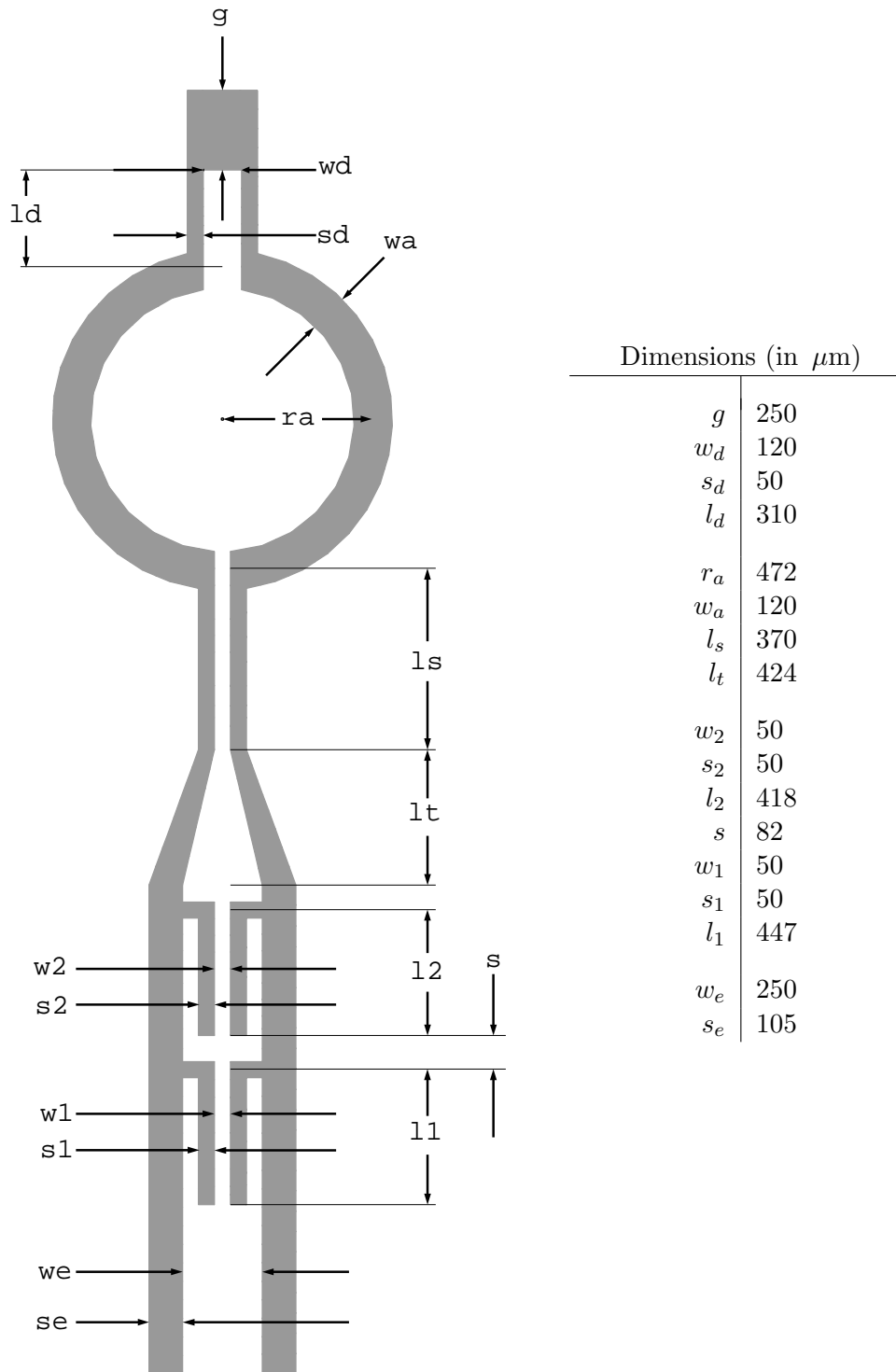


Figure 5.43: First IFER design for operation at 60.5 GHz with alumina ($\epsilon_r = 10$) lens, to scale. The tuning stub and the end gap have been sized to accommodate the HSCH-9161 diode ($g = 250 \mu\text{m}$ is the size of its body; $w_d = 120 \mu\text{m}$ is the width of the lead).

since ray-tracing from the complete current distribution would have required excessive computer resources. Simulations that do not include the lens have been reported in [67].

The extension (7.7 mm) of the alumina lens [104, §2.3] (radius 24.3 mm, $\epsilon_r = 10$) was hyperhemispherical [37, §1], and the lack of directivity in the patterns of figs. 5.44–5.45 is expected. On the other hand, they show good symmetry, particularly (again as expected) the H-plane patterns. It was discovered much later, after the IFER project ended, that the alumina lens was defective —a Rexolite antireflection layer had been attached, which hid an imperfectly smooth alumina surface. These defects should be taken into account when evaluating figs. 5.44–5.45.

The same design was also measured with a near-synthesized ellipsoidal lens (radius 25 mm, extension 8.5 mm; the synthesized-ellipsoidal extension being 9.1 mm) that had been built for a former effort [96, §5.5] in Stycast HI-K material of relative permittivity $\epsilon_r = 12$. The design is not meant for a lens of this permittivity, which is evident in the relatively high crosspolarization levels, in particular in the H-plane. However, considering that mismatch, the results obtained do not differ much from those of [96, (5.27–28)].

The main inconvenient of the simple design of fig. 5.43, apart from those inherent to the uniplanar structure, is the lack of parameters to match the diode with a relatively short stub ($l_d = \lambda/4$ at most). In an attempt to address this shortcoming, an improvement on traditional slot loops is proposed in fig. 5.48. The T-match for CPW-fed antennas [68, 105] has been shown to offer a wideband, compact matching solution with limited effect on the cross-polarization of slot loops. The T-match is used only in the tuning stub. However, the design rules would have to be forced down to $30\text{ }\mu\text{m}$ for this design. The simulated performance of this prototype has been reported in [67].

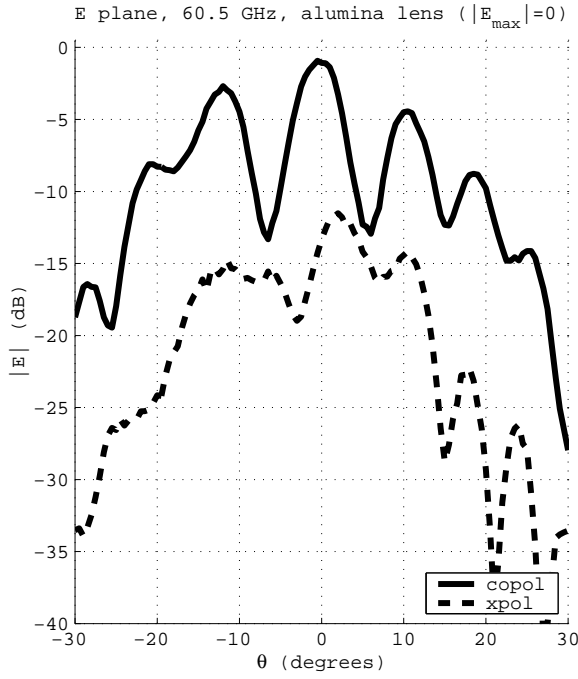


Figure 5.44: E-plane radiation pattern cut of first IFER design (fig. 5.43) using an alumina lens.

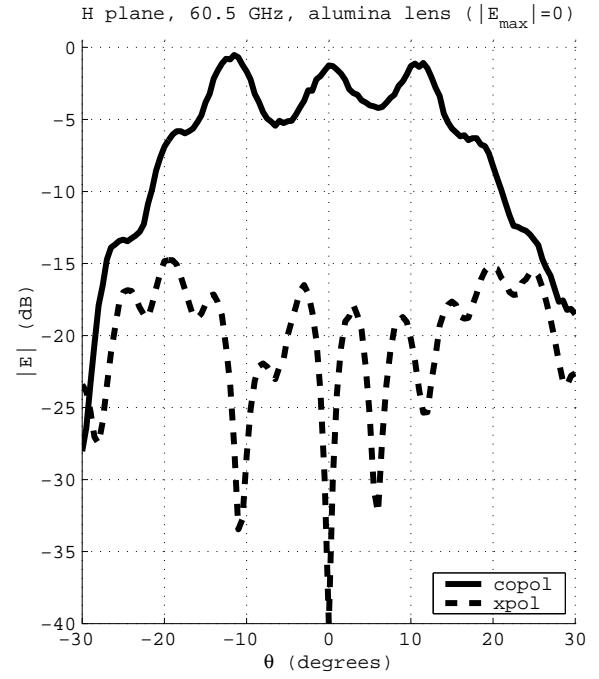


Figure 5.45: H-plane radiation pattern cut of first IFER design (fig. 5.43) using an alumina lens.

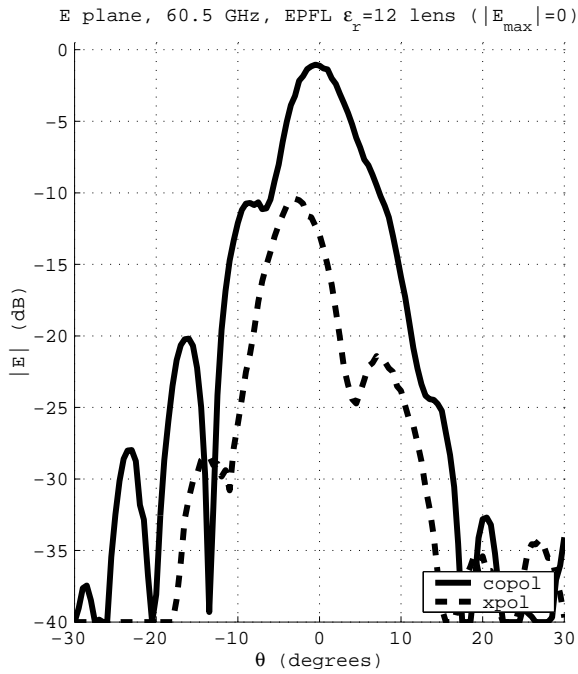


Figure 5.46: E-plane radiation pattern cut of first IFER design (fig. 5.43) using an $\epsilon_r = 12$ lens.

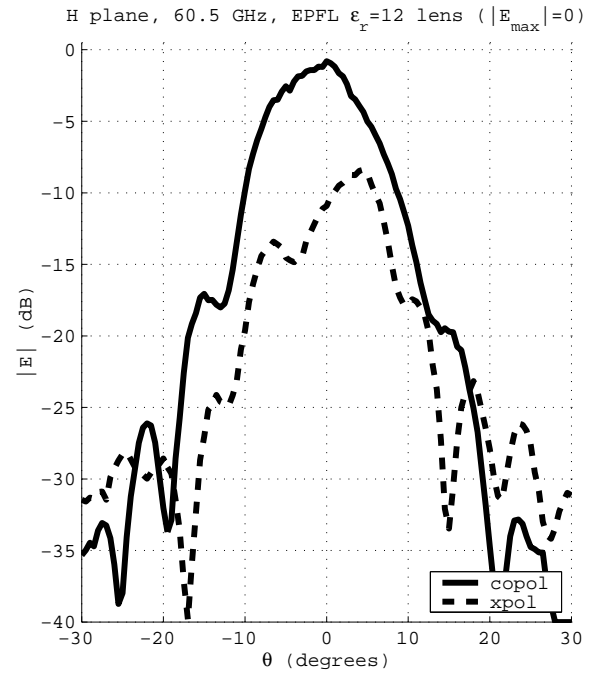
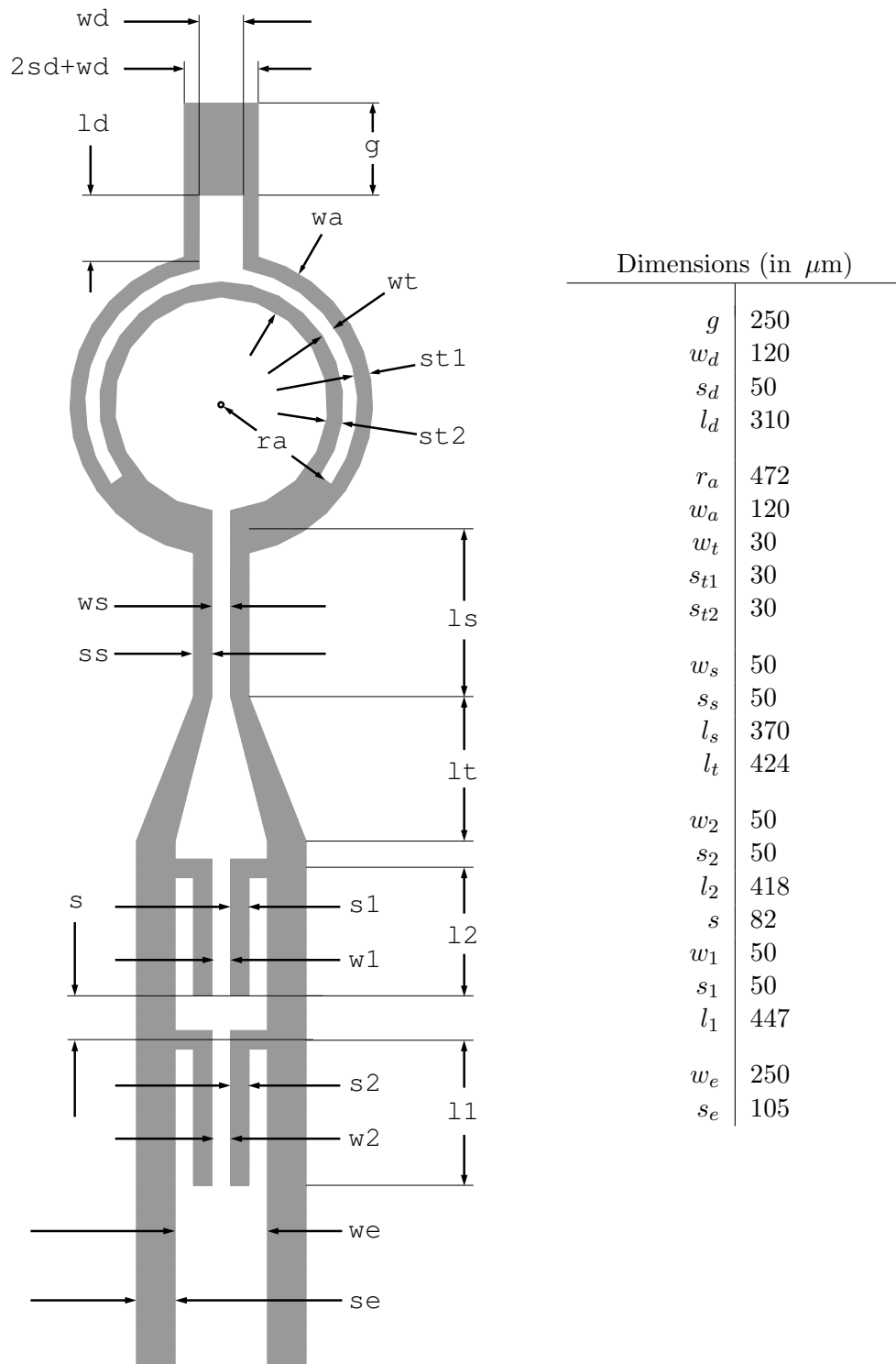


Figure 5.47: H-plane radiation pattern cut of first IFER design (fig. 5.43) using an $\epsilon_r = 12$ lens.

Figure 5.48: Second IFER design for operation at 65 GHz with silicon ($\epsilon_r = 12$ lens), to scale.

6 Perspectives

We have described the bases and the details of the implementation of a technique to precompute the vertical component of the general problem of a 3D scatterer embedded in stratified media. Actually, it was necessary, because of the characteristics of the technique, to restrict the scatterers that could be analyzed to be 2.5D —each part of the structure must either be parallel to the axis of stratification or form a right angle with it.

The main motivation for this development was to avoid the 3D tables and 3D interpolation required by a completely general spatial-domain integral equation technique. The precomputed dependence on the vertical component consists in a series of 1D tables, and only 1D interpolation (in P) is required during the evaluation of any of the reaction terms produced by the application of the method of moments to the integral equation. Therefore, there is an advantage in storage —because less tables are needed— and a double advantage in efficiency: first, 3D interpolation is reduced to 1D interpolation, and second, the dimension of the spatial integrals is reduced from 3 to 2 (for volume integrals) or from 2 to 1 (for surface integrals).

The main limitation of the technique is that it requires a careful and extensive analytical treatment of the Green's functions both in the spatial and the spectral domain, and to ease the implementation some simplifications had to be made. For example, the unknowns were expanded exclusively in combinations of linear rooftops. In these last years, when the use of higher-order basis functions in electromagnetics can finally be said to have arrived to its mature age, such simplification may seem outdated. However, it is easy to check in the recent literature the fact that almost all the development on higher order functions is restricted to methods that use only the free space Green's functions, or, if they concern layered media, the higher order bases are applied exclusively to horizontal unknowns.

The 2.5D technique has been explored quite extensively in this work; we have analyzed problems with electric and magnetic surface currents, where the electric currents could be defined on vertical patches, and electric polarization currents defined on volume elements. But the subject was not in any way exhausted. We have shown examples of extended formulations (analysis of composite dielectric objects in free space, with the CFIE) that could be reimplemented to some advantage using the semi-spectral method. In addition, a combination of all the methods presented here could also be used, in which any particular structure or inhomogeneity could be meshed using volume or surface elements according to its characteristics.

Preliminary results show the potentialities of this approach, and pave the way for a future combination and integration with the 2.5D approach mainly used in this thesis. In particular, the implementation of the volume integral equation in stratified media should be the next step to be considered, since it would provide a powerful systematic technique to analyze dielectric inclusions embedded in a layered environment.

A trend that together with the higher-order basis functions is being rapidly accepted by the electromagnetic modeling community is the multipole technique, that allows the analysis of large problems using a traditional moment-method approach. So far the multipole method has barely begun to be used for anything other than free space problems, and it would be daring indeed to propose its application to the 2.5D methods presented here, because we did not even attempt to

develop the asymptotic approximations for the far field, which the multipole method requires. However, it could be used in free space or in ground-plane bounded half-spaces to analyze, with a sort of hybrid method, such structures as the slot-antenna fed substrate lenses studied in the IFER project. The multipole technique is ideally suited to the treatment of electrically large problems in simple media, such as the lens, while the 2.5D technique can be used to analyze efficiently the feed.

Finally, an extremely important point that has been barely mentioned in this thesis is the treatment of excitations. We have used simple delta-gap (or combinations thereof) and plane wave excitations. It has long been evident, however, that the delta-gap model is not really accurate for the prediction of input impedances and circuit parameters. We were mostly concerned with other aspects of the method of moments technique. It is clear that the treatment of excitations would have been a favored area of work if this dissertation had not needed, at some point, a full stop.

A Vector relations

P18 Volume

$$\operatorname{div} \frac{\mathbf{R}}{3} (\log R - 1/3) = \log R \quad (\text{A.1a})$$

$$\operatorname{div} \frac{\mathbf{R}}{R} = 1/R \quad (\text{A.1b})$$

$$\operatorname{grad} R = \mathbf{R}/R \quad (\text{A.1c})$$

$$\operatorname{grad} \frac{1}{R} = -\mathbf{R}/R^3 \quad (\text{A.1d})$$

P19 Surface These are computed simply by noting that for a function $f(p, z)$ [50, (A-11)],

$$\operatorname{div}_s(\hat{\mathbf{p}}f) = \frac{1}{p} \frac{\partial}{\partial p}(pf)$$

$$\operatorname{grad}_s f = \hat{\mathbf{p}} \frac{\partial f}{\partial p}$$

$$\operatorname{div}_s \frac{R^3}{3P^2} \mathbf{P} = R \quad (\text{A.2a})$$

$$\operatorname{div}_s \frac{\mathbf{P}}{2} (\log P - 1/2) = \log P \quad (\text{A.2b})$$

$$\operatorname{div}_s \frac{\mathbf{P}}{2} \left(\log |R + Z| - \frac{R^2}{2P^2} + \frac{ZR}{P^2} \right) = \log |R + Z| \quad (\text{A.2c})$$

$$\operatorname{grad}_s \frac{R^3}{3} = \mathbf{P}R \quad (\text{A.2d})$$

$$\operatorname{grad}_s \frac{P^2}{2} (\log P - 1/2) = \mathbf{P} \log P \quad (\text{A.2e})$$

$$\operatorname{grad}_s \frac{1}{2} (P^2 \log |R + Z| + ZR - R^2/2) = \mathbf{P} \log |R + Z| \quad (\text{A.2f})$$

$$\operatorname{div}_s \frac{R}{P^2} \mathbf{P} = 1/R \quad (\text{A.2g})$$

$$\operatorname{grad}_s R = \mathbf{P}/R \quad (\text{A.2h})$$

$$\operatorname{grad}_s P \log |R + Z| = \mathbf{P}/R^2 \quad (\text{A.2i})$$

P20 Line

$$\frac{\partial}{\partial z} \log |Z + R| = 1/R \quad (\text{A.3a})$$

$$\frac{\partial}{\partial z} R = Z/R \quad (\text{A.3b})$$

$$\frac{\partial}{\partial z} (Z \log |R + Z| - R) = \log |R + Z| \quad (\text{A.3c})$$

$$\frac{\partial}{\partial z} (Z \log |R - Z| + R) = \log |R - Z| \quad (\text{A.3d})$$

$$\frac{\partial}{\partial z} \left(\frac{1}{4} ZR + \frac{1}{2} Z^2 \log |R - Z| - \frac{1}{4} P^2 \log |Z + R| \right) = Z \log |R - Z| \quad (\text{A.3e})$$

$$\frac{\partial}{\partial z} \left(-\frac{2}{9} P^2 R + \frac{1}{9} Z^2 R + \frac{1}{3} Z^3 \log |R - Z| \right) = Z^2 \log |R - Z| \quad (\text{A.3f})$$

$$\frac{\partial}{\partial z} \left(\frac{1}{2} ZR + \frac{1}{2} P^2 \log |R + Z| \right) = R \quad (\text{A.3g})$$

$$\frac{\partial}{\partial z} \frac{Z}{P^2 R} = 1/R^3 \quad (\text{A.3h})$$

$$\frac{\partial}{\partial z} \frac{1}{R} = Z/R^3 \quad (\text{A.3i})$$

$$\frac{\partial}{\partial z} \left(\frac{Z}{R} + \log |R + Z| \right) = Z^2/R^3 \quad (\text{A.3j})$$

In the following integrals, the source region is a line segment with orientation $\hat{\mathbf{e}}$ and normal $\hat{\mathbf{u}}$. It is contained on a plane with normal $\hat{\mathbf{z}} = \hat{\mathbf{u}} \times \hat{\mathbf{e}}$. It is assumed that:

$$\begin{aligned} \mathbf{R} &= Z\hat{\mathbf{z}} + \mathbf{P} = Z\hat{\mathbf{z}} - P_0\hat{\mathbf{u}} - l\hat{\mathbf{e}} \\ R_0^2 &= Z^2 + P_0^2 \end{aligned}$$

Then:

$$\int dl R = \frac{1}{2} (lR + R_0^2 \log |l + R|) \quad (\text{A.4a})$$

$$\int dl lR = \frac{1}{3} R^3 \quad (\text{A.4b})$$

$$\int dl \log |Z + R| = |P_0| \arctan \frac{l|P_0|}{R_0^2 + ZR} + l(\log(Z + R) - 1) + Z \log(l + R) \quad (\text{A.4c})$$

$$\int dl l \log |Z + R| = -\frac{R^2}{4} + \frac{1}{2}ZR + \frac{1}{2}(-Z^2 + R^2) \log(Z + R) \quad (\text{A.4d})$$

$$\int dl l^2 \log |Z + R| = -\frac{P_0^3}{3} \arctan \frac{P_0 l}{(R_0)^2 + ZR} + \frac{lP_0^2}{3} - \frac{l^3}{9} - \frac{lZR}{6} + \frac{l^3}{3} \log |R + Z| \quad (\text{A.4e})$$

$$-Z \left[\frac{P_0^2}{3} + \frac{R_0^2}{6} \right] \log |l + R| \quad (\text{A.4f})$$

$$\begin{aligned} \int dl P^2 \log |Z + R| &= \frac{2}{3} P_0^3 \arctan \frac{P_0 l}{(R_0)^2 + ZR} \\ &+ l \left[-\frac{2}{3} P_0^2 - \frac{l^2}{9} + \frac{ZR}{6} + \frac{P^2 + 2P_0^2}{3} \log |R + Z| \right] \\ &+ Z \left[\frac{P_0^2}{2} - \frac{Z^2}{6} \right] \log |R + l| \end{aligned} \quad (\text{A.4g})$$

$$\int dl P_0 \frac{R^2}{P^2} = P_0 l + Z^2 \arctan \frac{l}{P_0} \quad (\text{A.4h})$$

$$\int dl P_0 \frac{R}{P^2} = P_0 \log(l + R) + |Z| \arctan \frac{|Z|l}{P_0 R} \quad (\text{A.4i})$$

These are useful enough, when they apply:

$$\arctan x \pm \arctan y = \frac{x \pm y}{1 \mp xy} \quad (\text{A.5a})$$

$$\arctan \frac{l}{P_0} - \arctan \frac{Zl}{P_0 R} = \arctan \frac{P_0 l}{(R_0)^2 + ZR} \quad (\text{A.5b})$$

B..... Ancillary

P21 2D Fourier transform in cartesian and polar coordinates Assume $\mathbf{p}' = 0$; also $f(k_p, k_\phi) = f_p(k_p)f_\phi(k_\phi)$. Then

$$\int_{-\infty}^{+\infty} \int_{-\infty}^{+\infty} f(k_p, k_\phi) e^{-j\mathbf{k}_p \cdot \mathbf{p}} d\xi d\eta = \int_0^\infty dk_p k_p f_p \int_0^{2\pi} dk_\phi f_\phi e^{-jk_p p \cos(k_\phi - \phi)} \quad (\text{B.1a})$$

Let $f_\phi(k_\phi) = e^{jk_\phi n}$, n an integer. Substitution of [36, (5.2.7c)]

$$e^{-ja \cos b} = \sum_{m=-\infty}^{+\infty} (-j)^m J_m(a) e^{jmb} \quad (\text{B.1b})$$

into (B.1a) yields

$$\int_0^\infty dk_p k_p f_p \sum_{m=-\infty}^{+\infty} (-j)^m J_m(a) e^{-jmb} \int_0^{2\pi} dk_\phi e^{jk_\phi(n+m)} \quad (\text{B.1c})$$

The innermost integral of (B.1c) is zero unless $n = -m$. This reduces the sum to a single term, cf [78, (34)]:

$$\mathcal{F}^{-1}\{f_p(k_p) e^{jk_\phi n}\} = \frac{1}{2\pi} (-j)^n e^{jn\phi} \int_0^\infty dk_p k_p J_n(k_p p) f_p \quad (\text{B.1d})$$

Let us adopt the definition [124, (2.13-14)], [78, (35)], [107, (7)] (but see [87, 61])

$$\mathcal{S}_n[f_p] \equiv \frac{1}{2\pi} \int_0^\infty dk_p k_p J_n(k_p p) f_p \quad (\text{B.2})$$

With (B.1d) and the recurrence formula for Bessel functions [50, (D-16)]

$$B_n(x) = \frac{2(n-1)}{x} B_{n-1} - B_{n-2} \quad (\text{B.3})$$

we get (cf [45, table 6.8], [80, (65-70)]):

$$\begin{aligned} \mathcal{F}^{-1}\left\{\frac{j\xi}{k_p} f_p\right\} &= \cos(\phi) \mathcal{S}_1[f_p] \\ \mathcal{F}^{-1}\left\{\frac{j\eta}{k_p} f_p\right\} &= \sin(\phi) \mathcal{S}_1[f_p] \\ \mathcal{F}^{-1}\left\{\frac{\xi\eta}{k_p^2} f_p\right\} &= -\frac{\sin(2\phi)}{p} \mathcal{S}_1[k_p^{-1} f_p] + \frac{\sin(2\phi)}{2} \mathcal{S}_0[f_p] \\ \mathcal{F}^{-1}\left\{\frac{\xi\xi}{k_p^2} f_p\right\} &= -\frac{\cos(2\phi)}{p} \mathcal{S}_1[k_p^{-1} f_p] + \cos^2 \phi \mathcal{S}_0[f_p] \\ \mathcal{F}^{-1}\left\{\frac{\eta\eta}{k_p^2} f_p\right\} &= +\frac{\cos(2\phi)}{p} \mathcal{S}_1[k_p^{-1} f_p] + \sin^2 \phi \mathcal{S}_0[f_p] \end{aligned} \quad (\text{B.4})$$

P22 Extension of limits of integration to $\pm\infty$ in the Fourier-Bessel transform On occasion the integration limits of the Sommerfeld integral (B.2) are extended to $\int_{-\infty}^{+\infty}$. This is done by a procedure detailed in [36, 64–68], that depends on the relations

$$J_n(x) = \frac{1}{2} [H_n^{(1)}(x) + H_n^{(2)}(x)] \quad (\text{B.5a})$$

$$J_n(xe^{\pm j\pi}) = e^{\pm jn\pi} J_n(x) \quad (\text{B.5b})$$

$$H_n^{(1)}(xe^{+j\pi}) = -e^{-jn\pi} H_n^{(2)}(x) \quad (\text{B.5c})$$

$$H_n^{(2)}(xe^{-j\pi}) = e^{+jn\pi} H_n^{(1)}(x) \quad (\text{B.5d})$$

and on f_p of (B.2) being an even function of k_p [which is always the case for transmission line Green's functions (§2.4), that depend on k_p only through $\gamma = \sqrt{k_p^2 - k^2}$], and that results in

$$\mathcal{S}_n[f_p] = \frac{1}{4\pi} \int_{\infty e^{-j\pi}}^{+\infty} dk_p k_p H_n^{(2)}(k_p p) f_p \quad (\text{B.6})$$

If (B.6) rather than (B.2) is chosen, care must be taken to circumvent the branch cut of the Hankel function, which conventionally extends from 0 to $-\infty$ on the real axis. (On the other hand, J_n is entire).

P23 Source-continuous scalar potential Green's function for the charge associated with a vertical dipole We begin with the expression

$$\Phi_z(z, z') = \frac{\omega}{k_x} \int_{-\infty}^{z'} dz'' E_{zx}^M(z'', z) \quad (\text{B.7})$$

derived by reciprocity in [39], although any other integral expression will yield similar results. The lower limit of integration is not important, at least as far as we go low enough to ensure the desired continuity. If we substitute E_{zx}^M for its expression in terms of the TLGF's, we obtain [78, (28)]

$$\Phi_z(z, z') = - \int_{-\infty}^{z'} dz'' \frac{1}{\epsilon''} I_v^e(z'', z) \quad (\text{B.8})$$

(B.8) must be source continuous, because the integrand contains at most step discontinuities. Now, typical derivation follows taking $1/\epsilon''$ outside the integral. This is not valid when layers are crossed. The resulting expression (2.20f), [80, (32)], [45, (6.82)] is

$$\Phi_z(z, z') = \frac{j\omega}{\gamma^2} V_i^e(z', z) \quad (\text{B.9})$$

This expression remains valid within layers, however—but it is not source continuous and leads to a line integral term that, in principle, would be better to avoid. Therefore we proceed to compute (B.8) by making use of the TL equation (2.5a)

$$\frac{\partial V_i(z, z')}{\partial z} = -\gamma Z I_i(z, z') \quad (\text{B.10a})$$

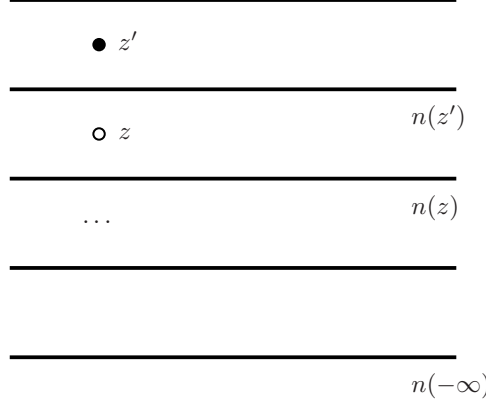
Exchanging variables and dividing by ϵ'

$$\frac{1}{\epsilon'} I_i(z', z) = \frac{1}{-\gamma' Z' \epsilon'} \cdot \frac{\partial V_i(z', z)}{\partial z'} \quad (\text{B.10b})$$

The second term can be integrated by parts (defining $A(z) = 1/[\gamma Z(z)\epsilon(z)]$)

$$\Phi_z(z, z') = \frac{V_i(z', z)}{A(z')} - \frac{V_i(\infty, z)}{A(\infty)} - \int_{\infty}^{z'} dz'' \left\{ V_i(z'', z) \frac{\partial A(z'')}{\partial z''} \right\} \quad (\text{B.10c})$$

To perform the derivative inside the integral, we note that γ'' , Z'' and ϵ'' are piecewise continuous functions of z'' .



$$\begin{aligned} \Phi_z(z, z') &= \frac{V_i(z', z)}{A(z')} - \frac{V_i(\infty, z)}{A(\infty)} \\ &\quad - \int_{\infty}^{z'} dz'' \left\{ V_i(z'', z) \sum_{n(-\infty)+1}^{n(+\infty)} \delta(z'' - z_n) [A(z_n^+) - A(z_n^-)] \right\} \end{aligned} \quad (\text{B.11a})$$

The sum extends over all layer discontinuities. Finally,

$$\begin{aligned} \Phi_z(z, z') &= \frac{V_i(z', z)}{A(z')} - \frac{V_i(\infty, z)}{A(\infty)} \\ &\quad - \sum_{n(-\infty)+1}^{n(z')} V_i(z_n, z) [A(z_n^+) - A(z_n^-)] \end{aligned} \quad (\text{B.11b})$$

We find that this is the same as (B.9), save for the addition of the discontinuity step at each layer interface. As for the implementation: the terms $V_i(z_n, z)$ have to be computed. They have an exponential dependence on z which is the same for them all; in fact it is the same as that of $V_i(z_n, z)$, so it is possible to factor it out.

However, without pursuing this work further, it seems that it will be more work to compute this source continuous scalar potential Green's function than to just accept the discontinuity in (B.9) and compute the line integral; the corner line integrals have to be implemented anyway. We have decided to go with (B.9).

P24 Integral of $\log(R+Z)$ over a triangle or a rectangle There are two cases of interest here, a) the factor function is constant or b) linear. The following two functions shall be used, from (A.2c) and (A.2f) respectively:

$$\mathbf{f} = -\frac{\mathbf{P}}{2} \left(\log(R+Z) - \frac{R^2}{2P^2} + \frac{ZR}{P^2} \right) \quad (\text{B.12a})$$

$$g = -\mathbf{f} \cdot \mathbf{P} \quad (\text{B.12b})$$

Before applying the appropriate integral theorem to transfer the integration from the surface of the polygon (S) to its contour (∂S), a small circle of radius ϵ centered at $P = 0$ is excluded, so that the integrand and its antidivergence or antigradient are regular on $S - S_\epsilon$.

If the log function is multiplied by a constant function, then,

$$\begin{aligned}
 \int_{S'} \log(R + Z) &= \int_{S'} \text{div}'_s \mathbf{f} \\
 &= \lim_{\epsilon \rightarrow 0} \left[\int_{\partial S' - \partial S'_\epsilon} \mathbf{f} \cdot \hat{\mathbf{n}} + \int_{S'_\epsilon} \log(R + Z) \right] \\
 &= \int_{\partial S'} \mathbf{f} \cdot \hat{\mathbf{n}} + \alpha(\mathbf{p}) \lim_{\epsilon \rightarrow 0} \left[-\epsilon \mathbf{f} \cdot (-\hat{\mathbf{P}}) + \int_0^\epsilon dP P \log(R + Z) \right] \\
 &= \int_{\partial S'} \mathbf{f} \cdot \hat{\mathbf{n}} + \alpha(\mathbf{p}) (-Z^2/2 + Z|Z|) \tag{B.13a}
 \end{aligned}$$

The angle $\alpha(\mathbf{p})$ is as in [146, 5] and is computed as indicated there. The remaining contour integral (over a polygonal contour) is doable in closed form by splitting \mathbf{P} in parts normal and tangential to each segment and using formulas from P20 on page 128.

If the log function is multiplied by a linear vector function,

$$\begin{aligned}
 \int_{S'} \mathbf{P} \log(R + Z) &= \int_{S'} \text{grad}'_s g \\
 &= \lim_{\epsilon \rightarrow 0} \left[\int_{\partial S' - \partial S'_\epsilon} g \hat{\mathbf{n}} + \int_{S'_\epsilon} \mathbf{P} \log(R + Z) \right] \\
 &= \int_{\partial S'} g \hat{\mathbf{n}} \tag{B.13b}
 \end{aligned}$$

The composition of (B.13a) and (B.13b) allows to compute the singular or quasi-singular integrals arising from the use of the z -integrated Green's functions, whose singularities or quasi-singularities are (for the potentials at least) of this type (tables 2.4 and 2.6). We note that the case $Z = 0$ is included in (B.13a–B.13b).

To estimate the need of computing the integrals of $\log |R+Z|$ over triangular and rectangular cells according to the exact formulas (B.13a–B.13b), the direct integration using a number of Gaussian rules on increasing order has been plotted on figs. B.1–B.4. (These Gaussian rules are given in tables C.1 and C.2). The disposition of source cells and observer points is the same as in fig. 3.6. Only the results for $\int_{S'} \log(R + Z)$ are shown; $\int_{S'} \mathbf{P} \log(R + Z)$ is (presumably) better behaved.

As discussed in §3.3.2 the case $kl = 1$ (figs. B.1 and B.3) is not representative of what is found in a typical mesh. In the more meaningful case $kl = .1$ (figs. B.2 and B.4), we see that except for $kR < .1$, a low (3-4 points) degree rule may be sufficient to compute accurately this type of integrals. On the other hand, when $Z = 0$, results are poor whatever the degree of the rule and the use of (B.13a) is imperative.

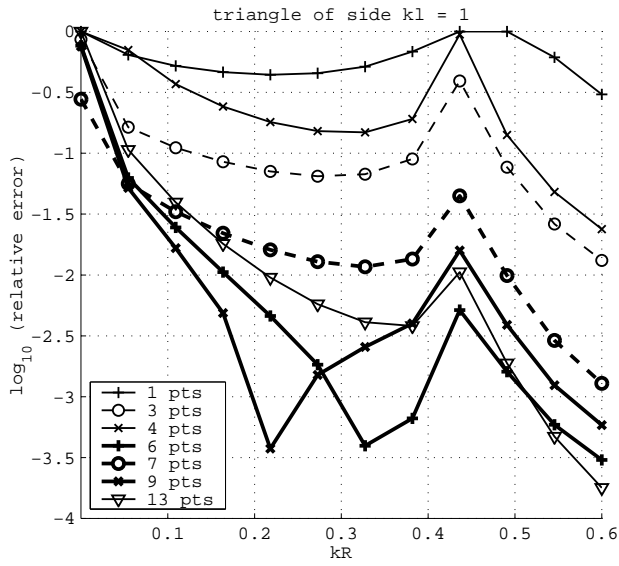


Figure B.1: Direct numerical computation of the integral of $\log(R + Z)$ over a large triangle.

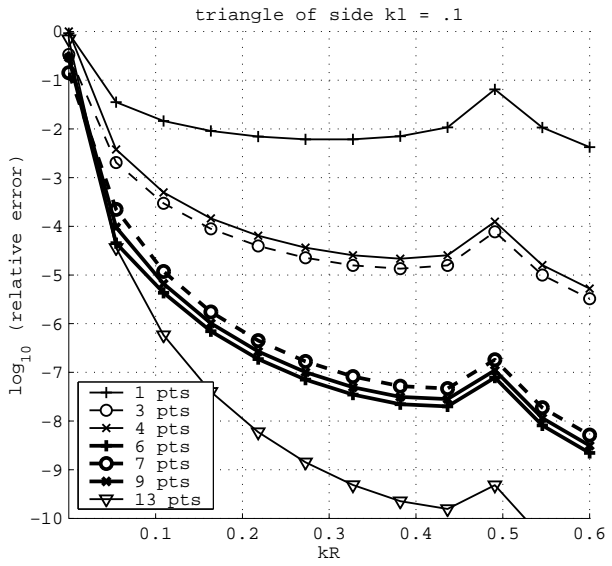


Figure B.2: Direct numerical computation of the integral of $\log(R + Z)$ over a small triangle.

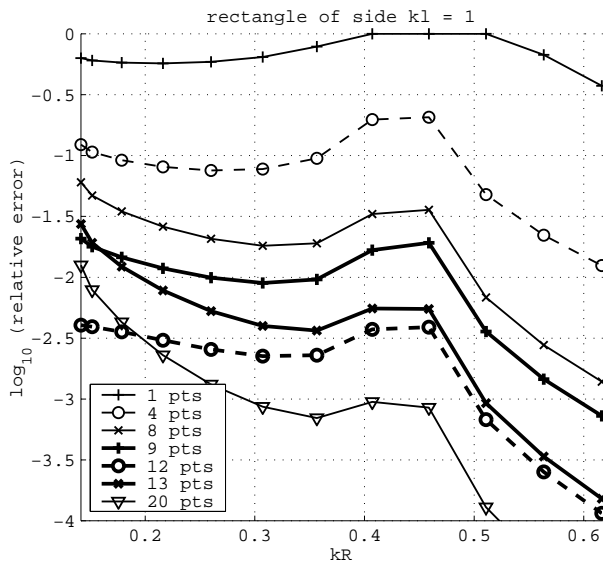


Figure B.3: Direct numerical computation of the integral of $\log(R + Z)$ over a large rectangle.

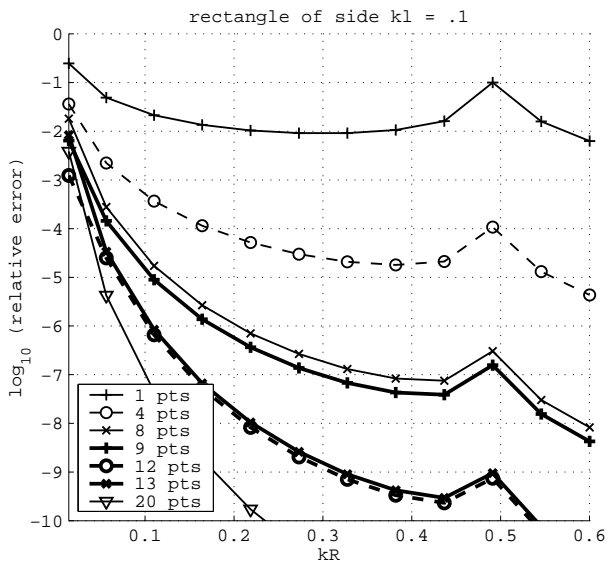


Figure B.4: Direct numerical computation of the integral of $\log(R + Z)$ over a small rectangle.

C Gaussian rules

The numerical integration with 2D or 3D quadrature rules is based on the following principle: there is an affine mapping that transforms certain ‘unit’ region (the *unit element*) in normalized coordinates $\mathbf{s} = (u, v, w)$ into the region of interest (the *element*) in real-world coordinates $\mathbf{r} = (x, y, z)$.

The unit elements are defined so that the transformation $T(\mathbf{s})$ is the same for all: triangle, parallelogram, tetrahedron, parallel wedge and parallelepiped. Because $T(\mathbf{s})$ is an affine transformation, the elements are completely specified by a position vector \mathbf{o} and two (three) edge vectors \mathbf{a} \mathbf{b} (\mathbf{c}). The position vector is any vertex of the element, and the edge vectors the two (three) vectors from \mathbf{o} to the two (three) *neighboring* vertices (figs. C.1 and C.2). Naturally we take $w = 0$ for the triangle and the parallelogram.

$$T(\mathbf{s}) = \mathbf{o} + u\mathbf{a} + v\mathbf{b} + w\mathbf{c} \quad (\text{C.1})$$

A point integration rule is defined over this unit region, and the integral is performed in normalized coordinates.

$$\int_R f(\mathbf{r}) = \int_{S=T^{-1}(R)} f(T(\mathbf{s})) \frac{A_R}{A_S} \approx \frac{A_R}{A_S} \sum_i \omega_i f(T(\mathbf{s}_i)) \quad (\text{C.2})$$

All the rules $\{\omega_i, \mathbf{s}_i\}$ that appear in this appendix are fully symmetric. This means that the position of the transformed integration points is as independent on the ordering of the nodes as

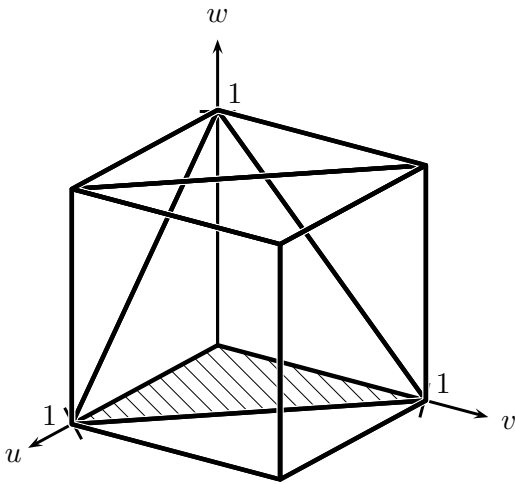


Figure C.1: The five unit elements. The unit triangle, base of tetrahedron and wedge, is shaded.

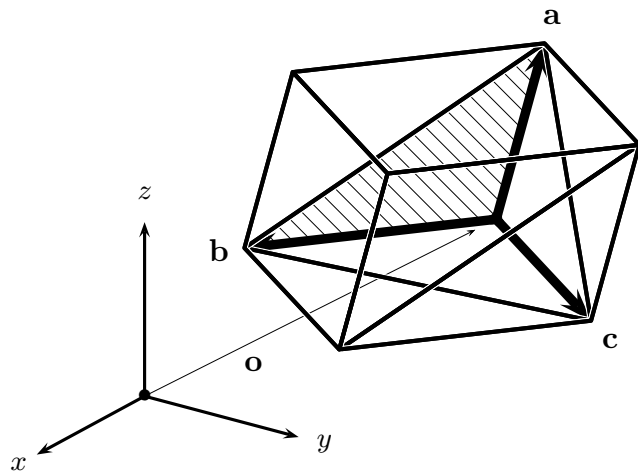


Figure C.2: The five elements defined by \mathbf{oabc} in real-world coordinates, according to (C.1). The triangle, base of tetrahedron and wedge, is shaded.

it can be. (In the rectangle, for instance, it does not matter whether the nodes are numbered cw or ccw, or which one is the first of the list —the transformed points fall in the same places.) This also means that the choice of origin and axes for the transformation is immaterial, and do not even need to be positively oriented, although this might be advisable on other grounds.

This rules should also be useful for general quadrilaterals [109] or hexahedra [93]. The rules are what in one dimension would be called Gauss-Legendre and perform best with smooth integrands. They are optimal, in the sense that they integrate exactly a monomial of higher or equal degree than any other rule with the same number of points.

P25 Triangle The unit triangle has its vertices at $\mathbf{s} = (0, 0), (0, 1), (1, 0)$. It is the base of the unit tetrahedron or the unit wedge and has area $A_S = .5$. The $\{\omega_i\}$ given here have been doubled so that the factor A_S^{-1} in (C.2) is already included.

The points \mathbf{s}_i are to be produced according to symmetry generators. There are three classes of symmetry for the triangle rules:

Class I produces $\mathbf{s}_0 = (1/3, 1/3)$.

Class II (vertices) produces $\mathbf{s} = (a, a), (a, 1 - 2a), (1 - 2a, a)$.

Class III (2×sides) produces $\mathbf{s} = (a, b), (b, a), (a, 1 - a - b), (1 - a - b, a), (b, 1 - a - b), (1 - a - b, b)$.

Coordinates and weights are listed in table C.1. The most complete reference for optimal rules on the triangle is [28], who gives rules up to order 20 (79 integration points) with up to 15 significant figures. Other accessible sources are [4, §25.4.63] (7p.).

To build denser rules by subdivision, it is preferable to split the triangle in four by the midpoint of each side. In this way the aspect ratio of the triangle and the symmetry of the rule are preserved.

P26 Rectangle The unit rectangle has its vertices at $\mathbf{s} = (0, 0), (0, 1), (1, 1), (1, 0)$ and has area 1. It is the base of the unit hexahedron.

The points \mathbf{s}_i are to be produced according to symmetry generators. There are four symmetry classes for the rectangle rules (take all sign combinations):

Class I produces $\mathbf{s}_0 = (.5, .5)$.

Class II (sides) produces $\mathbf{s} = (.5 \pm a/2, .5), (.5, .5 \pm a/2)$.

Class III (vertices) produces $\mathbf{s} = (.5 \pm a/2, .5 \pm a/2)$.

Class IV (2×sides) produces $\mathbf{s} = (.5 \pm a/2, .5 \pm b/2), (.5 \pm b/2, .5 \pm a/2)$.

Coordinates and weights are listed in table C.2. These rules can be gotten from [27]. Other accessible sources are [4, §25.4.62] (4 & 9p.).

P27 Tetrahedron The unit tetrahedron has its vertices at $\mathbf{s} = (0, 0, 0), (1, 0, 0), (0, 1, 0), (0, 0, 1)$. Its volume is 1/6 and a factor of 6 has already been included in the $\{\omega_i\}$ given here.

The points \mathbf{s}_i are to be produced according to symmetry generators. There are three symmetry classes for the tetrahedron rules.

Class I produces $\mathbf{s}_0 = (.25, .25, .25)$.

Class II (vertices) produces $\mathbf{s} = (a, a, a), (a, a, 1 - 3a), (a, 1 - 3a, a), (1 - 3a, a, a)$.

Class III (edges) produces $\mathbf{s} = (a, a, b), (b, b, a), (a, b, a), (b, a, b), (b, a, a), (a, b, b)$.

Coordinates and weights are listed in table C.3. These rules come from [41], save the 24 point rule [56].

| points | degree | symmetry | ω | a | b |
|--------|--------|----------|-------------------------|------------------------|------------------------|
| 1 | 1 | I | 1. | .33333333333333333333 | |
| 3 | 2 | II | .33333333333333333333 | .16666666666666666666 | |
| 4 | 3 | I | -.5625 | .33333333333333333333 | |
| | | II | .52083333333333333333 | .2 | |
| 6 | 4 | II | .109951743655321867638 | .091576213509770743459 | |
| | | II | .223381589678011465695 | .445948490915964886318 | |
| 7 | 5 | I | .225 | .33333333333333333333 | |
| | | II | .12593918054482715259 | .10128650732345633880 | |
| | | II | .13239415278850618073 | .47014206410511508977 | |
| 9 | 5 | II | .205950504760886603012 | .437525248383383867325 | |
| | | III | .063691414286223365160 | .037477420750087775659 | .165409927389841422924 |
| 13 | 7 | I | -.149570044467681750630 | .33333333333333333333 | |
| | | II | .175615257433207811754 | .260345966079039826926 | |
| | | II | .053347235608838491270 | .065130102902215811538 | |
| | | III | .077113760890257140260 | .048690315425316411793 | .312865496004873861407 |
| 16 | 8 | I | .072157803838893584126 | .33333333333333333333 | |
| | | II | .051608685267359125141 | .170569307751760206622 | |
| | | II | .016229248811599040155 | .050547228317030975458 | |
| | | II | .047545817133642312397 | .459292588292723156029 | |
| | | III | .013615157087217497132 | .728492392955404281241 | .263112829634638113422 |

Table C.1: Integration rules for the triangle.

P28 Wedge The unit wedge has its vertices at $\mathbf{s} = (0, 0, 0), (1, 0, 0), (0, 1, 0), (0, 0, 1), (1, 0, 1), (0, 1, 1)$. Its volume is $1/2$ and the $\{\omega_i\}$ given here have already been doubled.

Nobody seems to have produced optimal gaussian rules for the wedge. Therefore, I have used product rules of optimal gaussian rules on the triangular base \times linear Gauss-Legendre rules along its height, with number of points: $1 \times 1, 3 \times 2, 3 \times 3, 4 \times 3, 4 \times 4$ and 6×4 .

P29 Hexahedron The unit hexahedron has its vertices at $\mathbf{s} = (0, 0, 0), (1, 0, 0), (1, 1, 0), (0, 1, 0), (0, 0, 1), (1, 0, 1), (1, 1, 1), (0, 1, 1)$. Its volume is 1.

The points \mathbf{s}_i are to be produced according to symmetry generators. There are five symmetry classes for the hexahedron rules.

Class I produces $\mathbf{s}_0 = (.5, .5, .5)$.

Class II (faces) produces $\mathbf{s} = (.5 \pm a/2, .5, .5), (.5, .5 \pm a/2, .5), (.5, .5, .5 \pm a/2)$.

Class III (vertices) produces $\mathbf{s} = (.5 \pm a/2, .5 \pm a/2, .5 \pm a/2)$.

Class IV (edges) produces $\mathbf{s} = (.5 \pm a/2, .5 \pm a/2, 0), (.5 \pm a/2, 0, .5 \pm a/2), (0, .5 \pm a/2, .5 \pm a/2, 0)$.

Class V ($2 \times$ edges) produces $\mathbf{s} = (.5 \pm a/2, .5 \pm a/2, .5 \pm b/2), (.5 \pm a/2, .5 \pm b/2, .5 \pm a/2), (.5 \pm b/2, .5 \pm a/2, .5 \pm a/2)$.

Coordinates and weights are listed in table C.4; the rules come from [27].

| points | degree | symmetry | ω | a | b |
|--------|--------|----------|------------------------|------------------------|------------------------|
| 1 | 1 | I | 1. | 0. | |
| 4 | 3 | II | 0.25 | .57735026918962576450 | |
| 8 | 5 | II | .204081632653061224490 | .841565025531986612774 | |
| | | III | .045918367346938775510 | .940958551844098431750 | |
| 9 | 5 | I | .19753086419753086419 | 0. | |
| | | II | .12345679012345679012 | .774596669241483377036 | |
| | | III | .07716049382716049382 | .774596669241483377036 | |
| 12 | 7 | II | .06049382716049382716 | .92582009977255146157 | |
| | | III | .13014822916684861428 | .38055443320831565638 | |
| | | III | .05935794367265755855 | .80597978291859874371 | |
| 13 | 7 | I | .01234567901234567901 | 0. | |
| | | II | .15123456790123456790 | .585540043769119907613 | |
| | | IV | .04783950617283950617 | .929497072097828568789 | .579685425866102036070 |
| 20 | 9 | II | .071613424709810966785 | .984539811942252392433 | |
| | | II | .454090352551545224132 | .488886342842372416228 | |
| | | III | .042784615466778051169 | .939567287421521534134 | |
| | | IV | .215755803635932878957 | .836710325023988974095 | .507376773674613005277 |
| 40 | 13 | III | .190130011633091768921 | .551473280569941928827 | |
| | | III | .013028158998051469058 | .968340720218421941014 | |
| | | IV | .139527516092232388746 | .026667673869542453606 | .377724312589881160245 |
| | | IV | .137999398640593062673 | .235988332487411073425 | .793396171109383868545 |
| | | IV | .039497677876689456247 | .265486560240884896496 | .978761747825121715591 |
| | | IV | .081396322074913473345 | .702141598362496912618 | .913909457030225547757 |

Table C.2: Integration rules for the rectangle.

| points | degree | symmetry | ω | a | b |
|--------|--------|----------|------------------------|-------------------------|--------------------------|
| 1 | 1 | I | 1. | .25 | |
| 4 | 2 | II | 0.25 | .1381966011250105151796 | |
| 5 | 3 | I | .8 | .25 | |
| | | II | .45 | .16666666666666666666 | |
| 11 | 4 | I | -.07893333333333333333 | .25 | |
| | | II | .04573333333333333333 | .399403576166799204996 | |
| | | II | .14933333333333333333 | .100596423833200795004 | |
| 14 | 5 | II | .112687925718015850799 | .310885919263300609797 | |
| | | II | .073493043116361949544 | .092735250310891226402 | |
| | | III | .042546020777081466438 | .454496295874350350508 | .04550370412564964949188 |
| 24 | 6 | I | .03992275025816749210 | .214602871259152029289 | |
| | | II | .01007721105532064295 | .0406739585346113531156 | |
| | | II | .05535718154365472210 | .3223378901422755103440 | |
| | | III | .04821428571428571429 | .0636610018750175252992 | .2696723314583158080340 |

Table C.3: Integration rules for the tetrahedron.

D Documentation for TM

Perilous to us all are the devices of an art deeper than we possess ourselves.

J.R.R. TOLKIEN

TM is a software package intended to serve as simulation tool and demonstration benchmark for this thesis work. It is written in C++ [132] and is scriptable in Scheme [30]. It implements the conductor patch and aperture MPIE/CFIE (§§3.2, 3.3, 3.3.1), the dielectric-body volume MPIE (§4.2) and the dielectric-body surface CFIE (§3.4) in homogeneous (unbounded or perfect ground-plane bounded) space and, save the dielectric-body surface CFIE, in laterally unbounded layered media (§2).

TM is, as most overly ambitious software packages, a never-finished, never-correct piece of work. Somebody said that writing software documentation takes at least as much effort as actually writing the code; if it is true, it is proposed as an excuse for the roughness of these pages, whose purpose is not to teach to use the code, but to give a glimpse into its feature set.

Installation

TM compiles and runs in UNIX-style systems. A reasonably standards-conforming C++ compiler is required. The freely available GUILF package from the Free Software Foundation, v. 1.6 or above, must be installed.

TM requires two input files per simulation, one describing the medium, another the structure. The distinction is however not so clear-cut when dielectric bodies are analyzed with the surface equivalence principle; the specification of the different homogeneous regions is made in the structure file.

Medium description file

The medium file has extension `.in`. It contains a lists of blocks, each with the following format:

```
block number-of-block
base block-start-z
bottom-boundc
{ layer height  $\epsilon_r$   $\mu_r$   $\sigma$  }+
top-boundc
```

```

block 0
  base -1.51 mm
  infty
  layer 1 mm 1 0 1 0 0
  layer 0.51 mm 2.33 -0.0028 1 0 0
  ground

block 1
  base ontop
  ground
  layer 3 mm 1 0 1 0 0
  ground

block 2
  base ontop
  ground
  layer 1 mm 1 0 1 0 0
  infty

```

Figure D.1: The medium specification file for the microstrip-fed, dogbone-shaped aperture in a 3 mm thick screen of §5.1.3

number-of-block is present only to mark the sequence of blocks but it is not used otherwise. The first block (*number-of-block* = 0) must give a numeric value (with units) for *block-start-z*. The following blocks may just indicate *ontop*, which places them on top of the previous block. In this way it is possible to create multiple ground-plane media. The boundary conditions *bottom-boundc* and *top-boundc* can be:

- a complex number. Both TM and TE reflection coefficients are forced to this value in the modal representation.
- `cond < σ >` a conductivity. The surface impedance of a metal with this conductivity is used.
- `ground` the same as putting `-1`. This is a ground plane boundary.
- `infty` the same as putting `0`. This means to continue the adjacent layer (first or last of the block) to infinity, which produces a half-space.

The medium specification file for the microstrip-fed ‘dogbone’ shaped antenna (§5.1.3) is given in fig. D.1.

Structure file

The structure file has the extension `.mesh`. It is composed of four sections.

[**defs**] This contains the definition of the length unit in SI meters. For example `<unit 1e-3>` sets up the millimeter as the default unit.

[**nodes**] A numbered list of 3D nodes (`<x y z>`), one per line.

[**cells**] A list of cells. A group of these may be preceded by a ‘group definition’ which has the form

group *group-number* *group-name*
group-type *group-data* *region-spec*

The *group-type* can be one of **boundary**, **volume** or **volume**. For each of these, *group-data* has the format:

boundary $\langle \text{elec}|\text{magn} \{Z_s|Y_s|\sigma\} \rangle$ Z_s or Y_s are surface impedances or admittances (for the magnetic conductor boundary), σ (for electric conductor boundary) a conductivity. These provide for a Leontovich-type condition on the surface of the conductor. If *group-data* has this value, the cells following must be surface patches.

volume $\langle \epsilon_r \mu_r \sigma \rangle$ material parameters of a dielectric inclusion. If *group-data* has this value, the cells following must be volume elements.

interface $\langle \epsilon_r \mu_r \sigma \rangle$ material parameters. The cells following (which must be surface patches) bound a homogeneous dielectric body of that material. If *region-spec* allows, this group will create a *region* to which the other groups can refer.

The possibilities for *region-spec* are:

in $\langle \text{other-group-name} \rangle$ the group will not radiate in open space but inside a *region* bounded by an **interface** group named by *other-group-name*. There are a number of laterally *unbounded* implicit regions defined by the layered medium (the **block**'s in the description of the medium file format), and if a group has no *region-spec*, **in** **open** is assumed (**open** is a reserved name) which automatically makes the cells of the group radiate in the unbounded region that its vertical position places it in.

from $\langle \text{group-name-a to group-name-b} \rangle$ the group, which must be an **interface** or a horizontal **boundary magn** placed on the position of an infinite metallic ground plane, is a boundary between two *regions*. The integral equations to be solved will enforce the continuity of the tangential components of **E** and **H** (or only of **H** for a **boundary magn**) across this boundary. Either **from** or **to** may be omitted; in that case, **open** is assumed. The reference normal for the definition of equivalent currents is taken **from** the first region **to** the second region, or upwards if both are open (the unbounded **block**'s are ordered in the direction of increasing z). These *region-spec*'s provide support for the analysis of composite dielectric bodies and aperture-coupled dielectric resonators.

The list of cells, by itself, is simply a numbered list of lines of the form

index *number-of-nodes* { *node-index* }^{*number-of-nodes*}

where *node-index* is an index into the list of nodes given in the previous section of the file.

[**ports**] A list of edges (planar cell index plus two node indices) where delta-gap excitation can be impressed. (A plane wave excitation is indicated through configuration parameter **currents-exc**.)

[**metaports**] These group port edges to form multicell delta gaps [33, VII], differential ports, CPW ports (which are a type of differential port [97], [143, §II]), etc.

Two examples are given: the mesh for the composite sphere of P8 on page 78, and the first mesh for the 'dogbone' antenna of fig. 5.14 in p. 107 —see figs. D.2–D.3.

```

[defs]
unit 0.001

[nodes]
0 0 0 1
1 0 0.894427 0.447214
<...>

[cells]
  group 0 sphere-up
  interface (4,0) (1,0) 0
0 3 1 28 27
1 3 8 26 28
<...>

  group 1 sphere-dn
  interface (4,0) (1,0) 0
160 3 92 109 108
161 3 99 107 109
<...>

  group 2 midwall
  interface (4,0) (1,0) 0
    from sphere-dn
    to sphere-up
320 3 166 24 162
321 4 166 167 173 172
<...>

```

Figure D.2: Structure input file for two-material composite sphere of fig. 3.17 in p. 81.

```

[defs]
unit 0.001

[nodes]
0 -70 -1.082 -0.76
1 -67.7838 -1.082 -0.76
<...>

[cells]
  group 0 feed
  boundary elec (0,0)
0 4 0 1 39 38
1 4 2 3 41 40
<...>

  group 1 dogbone-bottom-cover
  boundary magn (0,0)
37 3 141 179 142
38 3 142 179 143
<...>

  group 2 dogbone-top-cover
  boundary magn (0,0)
144 3 254 292 255
145 3 255 292 256
<...>

  group 3 dogbone-extr-boundary
  boundary elec (0,0)
251 4 302 303 441 440
252 4 303 304 442 441
<...>

[ports]
0 0 0 38 % port-one, subport 0

[metaports]
simple const 50. 0 % port-one

```

Figure D.3: Structure input file for microstrip-fed 'dogbone' antenna of fig. 5.14 in p. 107.

Command line

TM's command line has 4 compulsory arguments, 1 optional argument, and an indeterminate number of **key=value** arguments in any position, that change the default configuration options documented in the next section. In addition to that, interpreted command scripts (written in Scheme) can be loaded, from which the simulation can be started and controled programmatically. If no scripts are given, a default script, that runs a standard simulation with the parametrized by default arguments, is started instead.

```
tm mesh-file start-freq end-freq number-of-samples [output-name]
    [- {var=value | scheme-file}+ [-] ]
```

output-name is used as prefix for all output files produced by TM. If it is not given, *mesh-file* is used. Depending on the frequency sampling mode (configuration option **sampling-method**), *mesh-file*, *start-freq* and *end-freq* may actually be ignored.

If the command line ends in a hyphen, the program will open a command line interface and show a prompt. From this prompt a series of commands (for instance (**help-tm** 'commands')) can be entered.

Configuration options

Some options have one or more aliases and these are listed between parentheses after the name of the option. False is to be indicated with 0 and true with 1.

use-packed-momm (**pm**, **use-bunch-kaufman-factor**) If this is false, solve the moment system using LU decomposition with partial pivoting, as implemented by the LAPACK routines **zgetrf**, **zgetrs** and **zgecon**. This requires that the whole system matrix be stored in memory.

If this is true, solve the moment system using the Bunch-Kaufman diagonal pivoting method, as implemented by the LAPACK routines **zsptf**, **zsptf** and **zsptf**. This method requires the system matrix to be symmetric and uses half the storage space of the previous method. Unfortunately it is much slower in practice, not because of any fault in the algorithm, but because the routines have not been so well optimized for each particular computer architecture as the LU routines have been [1].

sampling-method (**sm**) Select the method for sampling when doing a frequency sweep. The possibilities are:

uniform uniformly spaced sampling.

list an explicitly given list of points.

adaptive adaptive sampling based on the variation of the *S* parameters, with the algorithm given in [71, Part II].

reduce-rectangles-to-triangles (**r2t**) Divide every rectangle of the mesh in two triangles before starting the analysis. (Useful mainly for tests).

reduce-hexahedra-to-wedges (**h2p**) Divide every hexahedron of the mesh in two wedges before analysis.

reduce-hexahedra-to-tetrahedra (**h2t**) Divide every hexahedron of the mesh in six tetrahedra before analysis.

- reduce-wedge-to-tetrahedra (p2t)** Divide every wedge of the mesh in three tetrahedra before analysis.
- quad-eps-wav** The minimum relative error to be attained in the weighted averages algorithm, that is used to integrate the tail of the Sommerfeld transform.
- ellipse-convergence-precision (ecp)** The minimum relative error to be attained in the integration along the elliptic part of the Sommerfeld integration path.
- absolute-rhox (pmax)** Sets a minimum $k_0 P$ down to which to compute spatial domain Green's function tables that is independent of the mesh.
- absolute-rhox (pmax)** Sets a maximum $k_0 P$ up to which to compute spatial domain Green's function tables that is independent of the mesh.
- atar-file (af)** Name a file that contains a substrate (layered medium) specification. The use of this option is mandatory.
- always-extract-first-order-singularity (aes)** Always extract the first potential-type quasistatic term, no matter how far away the source and the observer cells are. Useful for tests.
- extract-field-cubic-singularity (ecs)** Always extract the first quasistatic term of $\bar{\bar{E}}^M$, no matter how far away source and observer cells are. Useful for tests.
- ms-extract-singularity (mses)** Always extract the first quasistatic term of $\int_{\tau} \bar{\bar{E}}^M$, no matter how far away source and observer cells are. Useful for tests.
- write-cache (wc)** Write the Green's function tables to a cache on disk. This is the default.
- use-cache (uc)** Try to read a cache of Green's function tables from disk. If they are found but they do not match the current medium and mesh, they will be discarded.
- radpat-include-groups (rp+)** This option takes a comma-separated list of cell groups, which are included in the computation of the radiated (far) field. The default is to include all groups. The interest of this and the next option (**rp-**) is to separate the radiation of main radiating elements from parasitic radiation.
- radpat-exclude-groups (rp-)** This option takes a comma-separated list of cell groups, which are excluded in the computation of the radiated (far) field. The default is to exclude no group. This option has priority over **rp+**.
- include-electric-radiation (erp)** If this is false, the electric currents will not be included in the computation of the radiated (far) field. Default is true.
- include-magnetic-radiation (mrp)** If this is false, the magnetic currents will not be included in the computation of the radiated (far) field. Default is true.
- use-free (uf)** Use closed form specializations for the Green's functions (and the reaction integrals) in unbounded and ground-plane bounded homogeneous media. These allow arbitrarily oriented cells. If this is not true, the medium will be treated as a general layered medium and a 2.5D mesh will be required.
- currents-exc (ce)** Set the excitation used to compute the current distribution on the structure. The default loads on the ports are given in the structure file; they can only be modified by using the script commands. The options are:

default excite the first port on the circuit with unit excitation, all else turned off.

all excite all ports with unit excitation. loads.

given *<list-of-excs>* a comma separated list of complex numbers gives the excitation of each one of the ports in the circuit.

- *< θ >* [ϕ [ζ [A]]] excite with a plane wave incident from (θ, ϕ) and polarization angle ζ ($\zeta = 0 \rightarrow$ TM polarization, $\zeta = 90 \rightarrow$ TE polarization); A is the amplitude of the wave and can be complex. This works also in layered media.

List of Figures

| | | |
|------|---|----|
| 1 | Side view of a complex 2.5D structure | 2 |
| 1.1 | A complicated medium with no embedded structure. | 8 |
| 1.2 | A manageable medium with an embedded structure. | 8 |
| 2.1 | Layered medium. | 13 |
| 2.2 | Characteristic parameters of a plane wave. | 15 |
| 2.3 | Natural axes of a plane wave. | 15 |
| 2.4 | Slices and layers. | 30 |
| 2.5 | Quasistatic images in the same-layer case. | 37 |
| 2.6 | Two half-spaces medium | 38 |
| 2.7 | A_{zp} in half space (from [83]). | 39 |
| 2.8 | A_{zp} in one-layer microstrip (from [83]). | 39 |
| 2.9 | A_{zp} in two-layer microstrip (from [83]). | 39 |
| 2.10 | Source and observer on different sides of a dielectric interface. | 40 |
| 2.11 | Sommerfeld integration path | 44 |
| 2.12 | Twice integrated singular free space potential Green's functions. | 46 |
| 2.13 | Once (z') integrated singular free space potential Green's functions. | 46 |
| 2.14 | Key for figs. 2.15–2.16. | 47 |
| 2.15 | Twice integrated non-singular free space potential Green's functions. | 48 |
| 2.16 | Once (z') integrated non-singular free space potential Green's functions. | 48 |
| 2.17 | Key for figs. 2.18–2.19. | 48 |
| 2.18 | Once (z) integrated components of $\bar{\bar{E}}^M$ in PEC-bounded free space, $\tau = z'$ | 49 |
| 2.19 | z -integrated components of $\bar{\bar{E}}^M$ in PEC-bounded free space, $\tau > z'$ | 49 |
| 2.20 | Key to layered media Green's functions | 49 |
| 2.21 | Twice integrated A_{zz} and A_{zz} for $\tau = \tau' = \tau_2$, for different z variation. | 50 |
| 2.22 | Twice integrated A_{zz} and A_{zz} for $\tau = \tau' = \tau_2$, for the same z variation. | 50 |
| 2.23 | Twice integrated singular Φ_z and Φ_u | 51 |
| 2.24 | Source integrated components of $\bar{\bar{E}}^M$ in microstrip medium: singular case. | 52 |
| 2.25 | Source integrated components of $\bar{\bar{E}}^M$ in microstrip medium: nonsingular case. | 52 |
| 3.1 | Parameters of the surface RWG function | 54 |
| 3.2 | A $\langle \mathbf{J}, \bar{\bar{E}}^J * \mathbf{J} \rangle$ interaction of type II. | 59 |
| 3.3 | Various types of electric-electric interactions. | 62 |
| 3.4 | Three basis functions and three Φ Green's functions on a corner. | 65 |
| 3.5 | Multiple apertures with metallic scatterers | 69 |
| 3.6 | Disposition of source cell and observer point in the extraction tests of figs. 3.7–3.10. | 72 |
| 3.7 | Relative error on extraction of $\bar{\bar{E}}^M$ singular terms (large triangle). | 73 |
| 3.8 | Relative error on extraction of $\bar{\bar{E}}^M$ singular terms (small triangle) | 73 |
| 3.9 | Relative error on extraction of $\bar{\bar{E}}^M$ singular terms (large rectangle). | 73 |

| | | |
|------|--|-----|
| 3.10 | Relative error on extraction of $\bar{\bar{E}}^M$ singular terms (small rectangle) | 73 |
| 3.11 | A penetrable homogeneous body. | 77 |
| 3.12 | Vertical stake antenna. | 79 |
| 3.13 | Current along a half-buried stake antenna, $\epsilon_r = 16$. MZ: results from [82, fig. 6(a)]. 2.5D: the 2.5D formulation presented here. | 79 |
| 3.14 | Current along a half-submerged stake antenna, $\epsilon_r = 81$, $\sigma = 1$ S/m. MZ: results from [82, fig. 6(b)]. 2.5D: the 2.5D formulation presented here. | 79 |
| 3.15 | Symmetry errors: stake antenna in earth. | 80 |
| 3.16 | Symmetry errors: stake antenna in salted water. | 80 |
| 3.17 | Composite sphere with halves of different dielectric material. | 81 |
| 3.18 | Composite sphere: J_θ along the E-plane cut $\phi = 0^\circ$ | 82 |
| 3.19 | Composite sphere: J_ϕ along the H-plane cut $\phi = 90^\circ$ | 82 |
| 3.20 | Composite sphere: M_ϕ along the E-plane cut $\phi = 0^\circ$ | 82 |
| 3.21 | Composite sphere: M_θ along the H-plane cut $\phi = 90^\circ$ | 82 |
| 4.1 | Numbering of nodes in tetrahedron. | 84 |
| 4.2 | Numbering of nodes in parallel wedge. | 84 |
| 4.3 | Numbering of nodes in parallel hexahedron. | 84 |
| 4.4 | Volume rooftop made up of hexahedron and wedge. | 85 |
| 4.5 | Two-layer dielectric sphere in uniform static field. The parameters are taken from [120, fig .6] and are: $a = 1$ mm, $b = .458$ mm, $\epsilon_1 = 16$, $\epsilon_2 = 9$. The densest mesh has 5000 tetrahedra, arranged in 5 layers for the inner core and 6 layers for the outer shell. | 91 |
| 4.6 | Two-layer dielectric sphere illuminated by very low-frequency plane wave (radius of outer shell is $< \lambda_0/6000$). | 92 |
| 4.7 | Mesh for the two-layer dielectric sphere under plane wave excitation: 888 tetra- hedra. This is based on the subdivision of an octahedron. (The mesh used for the static case in fig. 4.5 is based on the subdivision of an icosahedron.) | 92 |
| 4.8 | Electric field in a two-layer dielectric sphere subject to incident plane wave (top, fig. 4.8). | 93 |
| 4.9 | Homogeneous cylinder under plane wave excitation. | 94 |
| 4.10 | Two 2.5D volume (or surface) meshes for the homogeneous cylinder of fig. 4.9, with 30 and 70 cells/ λ_0 respectively. | 94 |
| 4.11 | Electric field and equivalent magnetic current at the surface of the cylinder of fig. 4.9 under plane wave incidence, with a discretization ~ 30 cells/ λ_0 and along the cut of the plane $\phi = 0$ with the surface of the cylinder. | 95 |
| 4.12 | Same as in fig. 4.11, but along the cut $\phi = \pi/2$ | 95 |
| 4.13 | As in fig. 4.11, but the discretization is at ~ 70 cells/ λ_0 | 95 |
| 4.14 | As in fig. 4.12, but the discretization is at ~ 70 cells/ λ_0 | 95 |
| 4.15 | Absolute value of the difference between the electric field at the surface of the cylinder of fig. 4.9 obtained with a 3D volume MPIE in free space and a 2.5 volume MPIE in free space represented as a faked stratified medium. | 97 |
| 4.16 | Same as in fig. 4.15, but along the cut $\phi = \pi/2$ | 97 |
| 4.17 | As in fig. 4.15, but the discretization is at ~ 70 cells/ λ_0 | 97 |
| 4.18 | As in fig. 4.16, but the discretization is at ~ 70 cells/ λ_0 | 97 |
| 5.1 | Aperture in thick screen. | 99 |
| 5.2 | Aperture in thick screen: schematic view. | 101 |
| 5.3 | Cavity model for aperture in thick screen. | 101 |
| 5.4 | Parallel plate waveguide model for aperture in thick screen. | 101 |

| | | |
|------|---|-----|
| 5.5 | Vertical structure of a microstrip-fed thick-screen aperture. | 103 |
| 5.6 | Dimensions of rectangular aperture antenna. | 104 |
| 5.7 | Mesh of rectangular slot fed by microstripline. | 104 |
| 5.8 | Input return loss of the rectangular slot antenna: $h \approx 0$ | 105 |
| 5.9 | Rectangular slot antenna: $t_s = 1$ mm. | 106 |
| 5.10 | Rectangular slot antenna: $t_s = 3$ mm. | 106 |
| 5.11 | Rectangular slot antenna: $t_s = 6$ mm. | 106 |
| 5.12 | Rectangular slot antenna: $t_s = 10$ mm. | 106 |
| 5.13 | Dimensions of ‘dogbone’ aperture antenna. | 107 |
| 5.14 | Two different density meshes for the ‘dogbone’ antenna. | 107 |
| 5.15 | Convergence with mesh density for ‘dogbone’ antenna. | 107 |
| 5.16 | $ S_{11} $ of ‘dogbone’ antenna: ‘zero’ thickness slot ($35 \mu\text{m} \approx \lambda/1700$ @5 GHz). | 108 |
| 5.17 | $ S_{11} $ of ‘dogbone’ antenna: slot of thickness 1 mm $\approx \lambda/60$ @5 GHz. | 108 |
| 5.18 | $ S_{11} $ of ‘dogbone’ antenna: slot of thickness 3 mm $\approx \lambda/20$ @5 GHz. | 108 |
| 5.19 | $ S_{11} $ of ‘dogbone’ antenna: slot of thickness 5 mm $\approx \lambda/12$ @5 GHz. | 108 |
| 5.20 | Color representation of currents in the dogbone antenna. | 109 |
| 5.21 | Standard coplanar waveguide (CPW) and relative potentials for the two modes without cutoff frequency [48, §7.4.2]. | 111 |
| 5.22 | Integrated mixer design with diode in the feed line. | 111 |
| 5.23 | Integrated mixer design with centered diode. | 111 |
| 5.24 | Equivalent circuit for fig. (5.22). | 111 |
| 5.25 | Equivalent circuit for fig. (5.23). | 111 |
| 5.26 | Air-bridged CPW-fed slot antenna | 113 |
| 5.27 | Photo of airbridge #3. | 113 |
| 5.28 | Dimensions of the six airbridge cases. | 113 |
| 5.29 | Airbridge case #1 | 114 |
| 5.30 | Airbridge case #2 | 114 |
| 5.31 | Airbridge case #3 | 114 |
| 5.32 | Airbridge case #4 | 114 |
| 5.33 | Airbridge case #5 | 115 |
| 5.34 | Airbridge case #6 | 115 |
| 5.35 | Airbridges, all simulations. | 115 |
| 5.36 | Airbridges, all measurements. | 115 |
| 5.37 | Return loss for CPW-fed antenna with asymmetrically placed airbridge. | 116 |
| 5.38 | Schema of the integrated receiver on a substrate lens. | 117 |
| 5.39 | IFER baseline design. | 118 |
| 5.40 | Input impedance of Schottky | 118 |
| 5.41 | Test bandstop compact CPW filter at 10 GHz, dimensions. | 119 |
| 5.42 | Test bandstop compact CPW filter at 10 GHz, S parameters. | 119 |
| 5.43 | First IFER design for operation at 60.5 GHz with alumina ($\epsilon_r = 10$) lens, to scale. The tuning stub and the end gap have been sized to accommodate the HSCH-9161 diode ($g = 250 \mu\text{m}$ is the size of its body; $w_d = 120 \mu\text{m}$ is the width of the lead). | 120 |
| 5.44 | E-plane radiation pattern cut of first IFER design (fig. 5.43) using an alumina lens. | 122 |
| 5.45 | H-plane radiation pattern cut of first IFER design (fig. 5.43) using an alumina lens. | 122 |
| 5.46 | E-plane radiation pattern cut of first IFER design (fig. 5.43) using an $\epsilon_r = 12$ lens. | 122 |
| 5.47 | H-plane radiation pattern cut of first IFER design (fig. 5.43) using an $\epsilon_r = 12$ lens. | 122 |
| 5.48 | Second IFER design for operation at 65 GHz with silicon ($\epsilon_r = 12$ lens), to scale. | 123 |
| B.1 | Direct numerical computation of the integral of $\log(R + Z)$ over a large triangle. | 135 |
| B.2 | Direct numerical computation of the integral of $\log(R + Z)$ over a small triangle. | 135 |

| | | |
|-----|---|-----|
| B.3 | Direct numerical computation of the integral of $\log(R + Z)$ over a large rectangle. | 135 |
| B.4 | Direct numerical computation of the integral of $\log(R + Z)$ over a small rectangle. | 135 |
| C.1 | The five unit elements. | 137 |
| C.2 | The five elements defined by oabc | 137 |
| D.1 | The medium specification file for the microstrip-fed, dogbone-shaped aperture in a 3 mm thick screen of §5.1.3 | 144 |
| D.2 | Structure input file for two-material composite sphere of fig. 3.17 in p. 81. | 146 |
| D.3 | Structure input file for microstrip-fed ‘dogbone’ antenna of fig. 5.14 in p. 107. | 146 |

List of Tables

| | | |
|-----|---|-----|
| 2.1 | Spectral Green's functions. | 21 |
| 2.2 | Notation for §2.4. | 22 |
| 2.3 | Integrals of exponential vs linear rooftop | 31 |
| 2.4 | Singularities of integrated free space Green's function. | 35 |
| 2.4 | Singularities of integrated free space Green's function. (cont.) | 36 |
| 2.5 | Singular images for point-source Green's functions | 42 |
| 2.6 | Singular cases for integrated Green's functions in layered media. | 43 |
| 3.1 | Reaction terms of type $\langle \mathbf{J}, \bar{\bar{E}}^J * \mathbf{J} \rangle$ | 67 |
| 3.2 | Reaction terms of type $\langle \mathbf{J}, \bar{\bar{E}}^M * \mathbf{M} \rangle$ | 76 |
| 4.1 | Map of integrals in the 2.5D volume formulation | 89 |
| C.1 | Integration rules for the triangle. | 139 |
| C.2 | Integration rules for the rectangle. | 140 |
| C.3 | Integration rules for the tetrahedron. | 140 |
| C.4 | Integration rules for the hexahedron. | 141 |

References

The numbers after each reference indicate the page where the citation is made.

- [1] ATLAS: Automatically tuned linear algebra software. <http://math-atlas.sourceforge.net/>. 147
- [2] TETGEN: 3D Delaunay tetrahedral mesh generator. <http://tetgen.berlios.de>. 91
- [3] TRIANGLE: A two-dimensional quality mesh generator and Delaunay triangulator. <http://www-2.cs.cmu.edu/~quake/triangle.html>. 104
- [4] Milton Abramowitz and Irene A. Stegun, editors. *Handbook of Mathematical Functions —with Formulas, Graphs and Mathematical Tables*. Dover, 1972. 45, 138
- [5] M. Irsadi Aksun and R. Mittra. Derivation of closed-form Green's functions for a general microstrip geometry. *IEEE Trans. on Microwave Theory Tech.*, 40(11):2055–2062, November 1992. 27, 34
- [6] Walid Y. Ali-Ahmad, William L. Bishop, Thomas W. Crowe, and Gabriel M. Rebeiz. An 86 – 106 GHz quasi-integrated low noise schottky receiver. *IEEE Trans. on Microwave Theory Tech.*, 41(4):558–564, April 1993. 117
- [7] Alejandro Álvarez Melcón. *Applications of the Integral Equation Technique to the analysis and Synthesis of Multilayered Printed Shielded Microwave Filters and Cavity Backed Antennas*. PhD thesis, Ecole Polytechnique Fédérale de Lausanne, LEMA-DE, 1998. no. 1901. 103
- [8] Paolo Arcioni, Marco Bressan, and Luca Perregrini. On the evaluation of the double surface integrals arising in the application of the boundary integral method to 3-D problems. *IEEE Trans. Antennas Propagat.*, 45(3):436–439, March 1997. 59
- [9] Mina Ayatollahi and S. Safavi-Naeini. A new representation for the Green's function of multilayer media based on plane wave expansion. *IEEE Trans. Antennas Propagat.*, 52(6):1548–1557, June 2004. 27
- [10] Constantine A. Balanis. *Advanced Engineering Electromagnetics*. John Wiley, 1989. 83
- [11] Lionel Barlatey. *Structures Rayonnantes en Milieu Stratifié Isotrope*. PhD thesis, Ecole Polytechnique Fédérale de Lausanne, LEMA-DE, 1991. no. 923. 1
- [12] Lionel Barlatey, Juan. R. Mosig, and Thomas Sphicopoulos. Analysis of stacked microstrip patches with a mixed potential integral equation. *IEEE Trans. Antennas Propagat.*, 38(5):608–615, May 1990. 14
- [13] Hans A. Bethe. Theory of diffraction by small holes. *Physical Review*, 66(8):163–182, October 1944. 100
- [14] J. Van Bladel. *Singular Electromagnetic Fields*. Oxford University Press, 1991. 94
- [15] Max Born and Emil Wolf. *Principles of Optics*. Cambridge University Press, 7th edition, 2002. 13, 90, 99, 100
- [16] Maurizio Bozzi, Luca Perregrini, Jochen Weinzierl, and Carsten Winnewisser. Efficient

- analysis of quasi-optical filters by a hybrid MoM/BI-RME method. *IEEE Trans. Antennas Propagat.*, 49(7):1054–1064, July 2001. 100
- [17] Chalmers M. Butler, Yahya Rahmat-Samii, and Raj Mittra. Electromagnetic penetration through apertures in conducting surfaces. *IEEE Trans. Antennas Propagat.*, 26(1):82–93, January 1978. 66
 - [18] Chi H. Chan and Robert A. Kipp. Application of the complex image method to characterization of microstrip vias. *Int. J. Microwave and Millimeter-Wave CAE*, 7(5):368–379, 1997. 38, 39, 58
 - [19] Michael W. Chapman and Sanjay Raman. A 60 GHz uniplanar MMIC $4\times$ subharmonic mixer. *IEEE Trans. on Microwave Theory Tech.*, 50(11):2580–2588, November 2002. 119
 - [20] Jingyang Chen, Ahmed A. Kishk, and Allen W. Glisson. A 3D interpolation model for the calculation of the Sommerfeld integrals to analyze dielectric resonators in a multilayered medium. *Electromagnetics*, 20(1):1–15, January 2000. 14, 28, 50
 - [21] Jingyang Chen, Ahmed A. Kishk, and Allen W. Glisson. Application of a new MPIE formulation to the analysis of a dielectric resonator embedded in a multilayered medium coupled to a microstrip circuit. *IEEE Trans. on Microwave Theory Tech.*, 49(2):263–279, February 2001. 19, 50, 56
 - [22] Weng Cho Chew. *Waves and Fields in Inhomogeneous Media*. Van Nostrand Reinhold, 1990. 20
 - [23] Y. Leonard Chow and Ibrahim N. El-Behery. An approximate dynamic spatial Green's function for microstriplines. *IEEE Trans. on Microwave Theory Tech.*, 26(12):978–983, December 1978. 27
 - [24] Y.L. Chow, N. Hojjat, S. Savafi-Naeini, and R. Faraji-Dana. Spectral Green's functions for multilayer media in a convenient computational form. *IEE Proc. H-Microw. Antennas Propag.*, 145(1):85–91, February 1998. 21, 22, 23
 - [25] Y.L. Chow, J.J. Yang, D.G. Fang, and G.E. Howard. A closed-form spatial Green's function for the thick microstrip substrate. *IEEE Trans. on Microwave Theory Tech.*, 39: 588–592, 1991. 27
 - [26] Phillip C. Clemmow. *The Plane Spectrum Representation of Electromagnetic Fields*. Oxford University Press/IEEE Press, 1996. 15, 16
 - [27] Ronald Cools. An encyclopaedia of cubature formulas. *J. Complexity*, 19:445–453, 2003. 138, 139
 - [28] D. A. Dunavant. High degree efficient symmetrical gaussian quadrature rules for the triangle. *Int. Journal for Num. Methods in Engineering*, 21:1129–1148, 1985. 138
 - [29] Gülbin Dural and M. Irsadi Aksun. Closed form Green's functions for general sources and stratified media. *IEEE Trans. on Microwave Theory Tech.*, 43(7):1545–1552, July 1995. 27
 - [30] R. Kent Dybvig. *The Scheme Programming Language*. The MIT Press, 3rd edition, 2003. 143
 - [31] Thomas F. Eibert and Volkert Hansen. On the calculation of potential integrals for linear source distributions on triangular domains. *IEEE Trans. Antennas Propagat.*, 43(12): 1499–1502, December 1995. 59
 - [32] Thomas F. Eibert and Volkert Hansen. 3-D FEM/BEM-hybrid approach based on a general formulation of Huygens' principle for planar layered media. *IEEE Trans. on Microwave Theory Tech.*, 45(7):1105–1112, July 1997. 14, 28, 47
 - [33] George V. Eleftheriades and Juan R. Mosig. On the network characterization of planar passive circuits using the methods of moments. *IEEE Trans. on Microwave Theory Tech.*,

- 44(3):438–445, March 1996. 145
- [34] D.G. Fang, J.J. Yang, and G.Y. Delisle. Discrete image theory for horizontal electric dipoles in a multilayered medium. *IEE Proc. H-Microw. Antennas Propag.*, 135(5):297–303, October 1988. 27
- [35] Marco Farina and Tullio Rozzi. A 3-D integral equation-based approach to the analysis of real-life MMICs —application to microelectromechanical systems. *IEEE Trans. on Microwave Theory Tech.*, 49(3):517–523, March 2001. 28, 84
- [36] Leopold B. Felsen and Nathan Marcuvitz. *Radiation and Scattering of Waves*. Prentice-Hall, 1973. 17, 20, 43, 44, 131, 132
- [37] Daniel F. Filipovic, Steven S. Gearhart, and Gabriel M. Rebeiz. Double-slot antennas on extended hemispherical and elliptical silicon dielectric lenses. *IEEE Trans. on Microwave Theory Tech.*, 41(10):1738–1749, November 1993. 117, 121
- [38] Gildas P. Gauthier, Walid Y. Ali-Ahmad, Thomas P. Budka, Daniel F. Filipovic, and Gabriel M. Rebeiz. A uniplanar 90 GHz Schottky-diode millimeter-wave receiver. *IEEE Trans. on Microwave Theory Tech.*, 43(7):1669–1672, July 1995. 117
- [39] Philippe Gay-Balmaz. *Structures 3-D Planaires en Milieux Stratifiés: Fonctions de Green et Application à des Antennes Incluant des Parois Verticales*. PhD thesis, Ecole Polytechnique Fédérale de Lausanne, LEMA-DE, 1996. no. 1569. 1, 44, 132
- [40] S.D. Gedney and R. Mittra. A hybrid method for the solution of the electromagnetic scattering by an inhomogeneously filled trough or slit in a thick conducting screen. In *AP-S International Symposium*, 1990, May 1990. 100
- [41] M. Gellert and R. Harbord. Moderate degree cubature formulas for 3-D tetrahedral finite-element approximations. *Comm. Appl. Num. Meth.*, 7:487–495, 1991. 138
- [42] Gaël Godi and Ronan Sauleau. FDTD analysis of reduced size substrate lens antennas. In *IEEE Ant. Prop. Soc. Intl. Symposium*, pages 667–670, 2004. 117
- [43] I.S. Gradshteyn and I.M. Ryzhik. *Table of Integrals, Series and Products*. Academic Press, sixth edition, 2000. 33, 39, 45
- [44] Roberto D. Graglia. On the numerical integration of the linear shape functions times the 3D Green’s function or its gradient on a plane triangle. *IEEE Trans. Antennas Propagat.*, 41(10):1448–1455, October 1993. 70
- [45] Tomasz M. Grzegorzcyk. *Integrated 3D Antennas for Millimeter-Wave Applications: Theoretical Study and Technological Realization*. PhD thesis, Ecole Polytechnique Fédérale de Lausanne, LEMA-DE, 2000. no. 2299. 1, 18, 26, 131, 132
- [46] Tomasz M. Grzegorzcyk and Juan R. Mosig. Line charge distributions arising in the integral equation treatment of bent scatterers in stratified media. *IEE Proc. H-Microw. Antennas Propag.*, 148(6):365–368, December 2001. 56
- [47] Tomasz M. Grzegorzcyk, Juan R. Mosig, and George Eleftheriades. IFER: Survey of existing designs and analysis tools. Propositions for future work / ESA-ESTEC contract 14062/00/NL/GD. Technical note, EPFL-LEMA / EM Group, University of Toronto, August 2000. 1
- [48] K.C. Gupta, Ramesh Garg, and I.J. Bahl. *Microstrip Lines and Slotlines*. Artech House, 1st edition, 1979. 111, 153
- [49] Richard C. Hall and Juan R. Mosig. The analysis of arbitrarily shaped aperture coupled patch antennas via a mixed potential integral equation. *IEEE Trans. Antennas Propagat.*, 44(5):608–614, May 1996. 14
- [50] Roger F. Harrington. *Time-Harmonic Electromagnetic Fields*. McGraw-Hill, 1961. 7, 9, 12, 41, 69, 127, 131

- [51] Roger F. Harrington. *Field Computation by Moment Methods*. Macmillan, 1968. 7, 11
- [52] Roger F. Harrington. Matrix methods for field problems. *Proceedings of the IEEE*, 55(2): 136–149, May 1968. 11
- [53] Roger F. Harrington and Joseph R. Mautz. Electromagnetic coupling through apertures. Technical Report TR-81-4, Department of Electrical and Computer Engineering, Syracuse University, August 1981. 9, 66
- [54] Hewlett-Packard. HSC-9161 zero bias beamlead detector diode, technical data. Technical Report 3-83. 118
- [55] Tatsuo Itoh. Spectral domain immittance approach for dispersion characteristics of generalized printed transmission lines. *IEEE Trans. on Microwave Theory Tech.*, 28(7):733–736, July 1980. 14
- [56] P. Keast. Moderate-degree tetrahedral quadrature formulas. *Comput. Methods Appl. Mech. Eng.*, 55:339–348, 1986. 138
- [57] Noyan Kinayman and M. Irsadi Aksun. Efficient use of closed-form Green’s functions for the analysis of planar geometries with vertical connections. *IEEE Trans. on Microwave Theory Tech.*, 45(5):593–603, May 1997. 14, 21, 27
- [58] B.M. Kolundžija and A.R. Djordjević. *Electromagnetic Modeling of Composite Metallic and Dielectric Structures*. Artech House, 2002. 93
- [59] Masanobu Kominami, David M. Pozar, and Daniel H. Schaubert. Dipole and slot elements and arrays on semi-infinite substrates. *IEEE Trans. Antennas Propagat.*, 33(6):600–607, June 1985. 117
- [60] Fred T. Kroghand and W. Van Snyder. A new representation of Patterson’s quadrature formulae (algorithm 699). *ACM Transactions on Mathematical Software*, 17(4):457–461, December 1991. 45
- [61] K. Kurokawa. Power waves and the scattering matrix. *IEEE Trans. on Microwave Theory Tech.*, 13(3):194–202, March 1965. 22
- [62] Ismo V. Lindell. *Methods for Electromagnetic Field Analysis*. IEEE Press, 1995. 17, 72, 77, 78
- [63] Donald E. Livesay and Kun Mu Chen. Electromagnetic fields induced inside arbitrarily shaped biological bodies. *IEEE Trans. on Microwave Theory Tech.*, 12(12):1273–1280, December 1974. 84
- [64] Daniel Llorens del Río, Tomasz M. Grzegorzczuk, and Juan R. Mosig. IFER: Survey of existing designs and analysis tools. Propositions for future work / ESA-ESTEC contract 14062/00/NL/GD. Technical note, EPFL-LEMA / EM Group, University of Toronto, August 2000. 1
- [65] Daniel Llorens del Río and Juan R. Mosig. IFER: Efficient full wave analysis of mixed metal/slot structures in stratified media, including vertical elements, and mixed port types / ESA-ESTEC contract 14062/00/NL/GD. Technical report, EPFL-LEMA, February 2003. 1
- [66] Daniel Llorens del Río and Juan R. Mosig. On the interaction of electric and magnetic currents in stratified media. *IEEE Trans. Antennas Propagat.*, 52(8):2100–2108, August 2004. 15, 76
- [67] Daniel Llorens del Río, Juan R. Mosig, Andrew Pavacic, and George Eleftheriades. Final technical report / ESA-ESTEC contract 14062/00/NL/GD. Technical report, EPFL-LEMA / EM Group, University of Toronto, February 2003. 1, 99, 119, 121
- [68] Daniel Llorens del Río, Julien Perruisseau-Carrier, and Juan R. Mosig. The T-match: an integrated match for CPW-fed antennas. In *Journées Internationales de Nice sur les*

- Antennes*, pages V2–347–350, November 2002. 121
- [69] Daniel Llorens del Río, Ivica Stevanović, and Juan R. Mosig. Analysis of printed structures including thick slots. In *Proceedings of COST-284 Meeting*, Budapest, April 2003. 15
 - [70] S. A. Maas. *Microwave Mixers*. Artech House, 2nd edition, 1993. 112, 118
 - [71] Michael Mattes. *Contribution to the Electromagnetic Modelling and Simulation of Waveguide Networks Using Integral Equations and Adaptive Sampling*. PhD thesis, Ecole Polytechnique Fédérale de Lausanne, LEMA-DE, 2003. no. 2693. 147
 - [72] Joseph R. Mautz and Roger F. Harrington. H -field, e -field and combined-field solutions for conducting bodies of revolution. *Arch. Elektron Übertragungstech.*, 32(4):157–164, April 1978. 55
 - [73] Joseph R. Mautz and Roger F. Harrington. Electromagnetic scattering from a homogeneous material body of revolution. *Arch. Elektron Übertragungstech.*, 33:71–80, 1979. 53
 - [74] J. Mees, A. Simon, C. Lin, P. Otero, J. Mosig, , T. Vaupel, V. Hansen, H. Merkel, E. Kollberg, P. Piironen, J. Louhi, V. Möttönen, A. Räisänen, and J. Zhang. Mm and sub-mm-wave open structure integrated receiver front end technology development. Baseline Design Report KASIMIR-BDR-DSS-01, Dornier Satellitensysteme GmbH, Technische Universität Darmstadt, École Polytechnique Fédérale de Lausanne, Bergische Universität Gesamthochschule Wuppertal, Chalmers University of Technology, Helsinki University of Technology, August 1998. 111
 - [75] Joaquín Bernal Méndez. *Aplicación del Método de las Imágenes Complejas al Análisis de Líneas de Transmisión en Medios Estratificados*. PhD thesis, Universidad de Sevilla, 1999. 45
 - [76] Krzysztof A. Michalski. Extrapolation methods for Sommerfeld integral tails. *IEEE Trans. Antennas Propagat.*, 46(10):1405–1418, October 1998. 45
 - [77] Krzysztof A. Michalski and Juan R. Mosig. Discrete complex image MPIE analysis of coax-fed coupled vertical monopoles in grounded dielectric substrate: two formulations. *IEE Proc. H-Microw. Antennas Propag.*, 142(3):269–254, June 1995. 27
 - [78] Krzysztof A. Michalski and Juan R. Mosig. Multilayered media Green’s functions in integral equation formulations. *IEEE Trans. Antennas Propagat.*, 45(3):508–519, March 1997. 14, 17, 18, 20, 21, 23, 26, 62, 131, 132
 - [79] Krzysztof A. Michalski and Juan R. Mosig. Multilayered media Green’s functions in integral equation formulations (draft). *IEEE Trans. Antennas Propagat.*, 1997. 34
 - [80] Krzysztof A. Michalski and Dalian Zheng. Electromagnetic scattering and radiation by surfaces of arbitrary shape in layered media, part I: Theory. *IEEE Trans. Antennas Propagat.*, 38(3):335–344, March 1990. 14, 19, 20, 56, 131, 132
 - [81] Krzysztof A. Michalski and Dalian Zheng. Electromagnetic scattering and radiation by surfaces of arbitrary shape in layered media. part I: Theory and part II: Implementation and results for contiguous half-spaces. *IEEE Trans. Antennas Propagat.*, 38(3):335–352, March 1990. 14
 - [82] Krzysztof A. Michalski and Dalian Zheng. Electromagnetic scattering and radiation by surfaces of arbitrary shape in layered media, part II: Implementation and results for contiguous half-spaces. *IEEE Trans. Antennas Propagat.*, 38(3):345–352, March 1990. 14, 78, 79, 152
 - [83] Adel A.K. Mohsen and Alaa K. Abdelmageed. An efficient evaluation of the nonsymmetrical components of the Green’s function for multilayered media. *Microwave and Opt. Tech. Letters*, 28(3):199–202, February 2001. 38, 39, 151

- [84] G.D. Monteath. *Applications of the Electromagnetic Reciprocity Principle*. Pergamon, 1st edition, 1973. 23
- [85] Juan R. Mosig. *Les Structures Microruban: Analyse au Moyen des Équations Intégrales*. PhD thesis, Ecole Polytechnique Fédérale de Lausanne, LEMA-DE, 1983. no. 511. 44
- [86] Juan R. Mosig. Integral equation technique. In Tatsuo Itoh, editor, *Numerical techniques for microwave and millimeter-wave passive structures*, chapter 3. John Wiley, 1st edition, 1989. 7, 10, 20, 34, 44, 45
- [87] Juan R. Mosig. On the calculation of Green's functions arising in the mixed potential integral equation formulation of multilayered printed antennas. Internal report, EPFL-LEMA, May 1996. 17, 18, 26, 131
- [88] Juan R. Mosig. Static Green's functions with conformal mapping and MATLAB. *IEEE AP Magazine*, 45(5), October 2003. 102
- [89] Juan R. Mosig. Scattering by arbitrarily-shaped slots in thick conducting screens: An approximate solution. *IEEE Trans. Antennas Propagat.*, accepted for publication. 102, 103
- [90] Juan R. Mosig and George V. Eleftheriades. Integrated Front End Receivers (IFER). Unsolicited proposal to ESA/ESTEC, EPFL-LEMA /EM Group, University of Toronto, November 1999. 1, 117
- [91] Juan R. Mosig and Fred E. Gardiol. A dynamic radiation model for microstrip structures. In P.W. Hawkes, editor, *Advances in Electronics and Electron Physics*, pages 139–237. Academic Press, 1982. 1, 14
- [92] Juan. R. Mosig and Fred E. Gardiol. General integral equation formulation for microstrip antennas and scatterers. *IEE Proc. H-Microw. Antennas Propag.*, 132:424–432, December 1985. 28
- [93] B.M. Notaroš and Branko D. Popović. General entire-domain method for analysis of dielectric scatterers. *IEE Proc. H-Microw. Antennas Propag.*, 143(6):498–504, December 1996. 138
- [94] Vladimir I. Okhmatovski and Andreas C. Cangellaris. A new technique for the derivation of closed form electromagnetic Green's functions for unbounded planar layered media. *IEEE Trans. Antennas Propagat.*, 50(7):1005–1016, July 2002. 27
- [95] Vladimir I. Okhmatovski and Andreas C. Cangellaris. Evaluation of layered media Green's functions via rational function fitting. *IEEE Microw. and Wireless Comp. Letters*, 14(1): 22–24, January 2004. 27
- [96] Pablo Otero. *Slot Antennas on Substrate Lenses for the Millimeter- and Submillimeter Wave Bands*. PhD thesis, Ecole Polytechnique Fédérale de Lausanne, LEMA-DE, 1998. no. 1834. 59, 111, 112, 118, 121
- [97] Pablo Otero, George V. Eleftheriades, and Juan R. Mosig. Modeling the coplanar transmission line excitation of planar antennas in the method of moments. *Microwave and Opt. Tech. Letters*, 16(4):219–225, November 1997. 145
- [98] Pablo Otero, George V. Eleftheriades, and Juan R. Mosig. Integrated modified rectangular loop slot antenna on substrate lenses for millimeter- and submillimeter-wave frequencies mixer applications. *IEEE Trans. Antennas Propagat.*, 46(10):1489–1497, October 1998. 110, 118
- [99] Wolfgang K.H. Panofsky and Melba Phillips. *Classical Electricity and Magnetism*. Addison-Wesley, 1962. 5, 38, 41
- [100] Joel Pasvolksky, Raphael Kastner, Ehud Heyman, and Amir Boag. Electromagnetic analysis of an antenna embedded in a composite environment. *IEEE Trans. Antennas Propagat.*,

- 49(5):681–687, May 2001. 8
- [101] T. N. L. Patterson. Algorithm for automatic numerical integration over a finite interval [D1] (algorithm 468). *Commun. ACM*, 16(11):694–699, 1973. 45
 - [102] Andrew Pavacic, George Eleftheriades, Daniel Llorens del Río, and Juan R. Mosig. IFER-CCN: Technical report TR300. Technical report, EM Group, University of Toronto / EPFL-LEMA, March 2004. 1
 - [103] Andrew P. Pavacic, George V. Eleftheriades, Daniel Llorens del Río, and Juan R. Mosig. Technical report - milestone M7 / ESA-ESTEC contract 14062/00/NL/GD. Technical note, EPFL-LEMA / EM Group, University of Toronto, August 2002. 1
 - [104] Andrew P. Pavacic, Daniel Llorens del Río, George V. Eleftheriades, and Juan R. Mosig. IFER: Technical note 2200. / ESA-ESTEC contract 14062/00/NL/GD. Technical note, EPFL-LEMA / EM Group, University of Toronto, October 2001. 1, 121
 - [105] Julien Perruisseau-Carrier, Daniel Llorens del Río, and Juan R. Mosig. A new integrated match for CPW-fed antennas. *Microwave and Opt. Tech. Letters*, 42(6):444–448, September 2004. 121
 - [106] Andrew F. Peterson, Scott L. Ray, and Raj Mittra. *Computational Methods for Electromagnetics*. IEEE press, 1988. 59
 - [107] Gonzalo Plaza, Francisco Mesa, and Francisco Medina. Treatment of singularities and quasi-static terms in the EFIE analysis of planar structures. *IEEE Trans. Antennas Propagat.*, 50(4):485–491, April 2002. 38, 42, 131
 - [108] Branko D. Popović. *Introductory Engineering Electromagnetics*. Addison Wesley, 1971. 15, 16
 - [109] Branko D. Popović and B.M. Kolundžija. *Analysis of Metallic Antennas and Scatterers*. IEE, 1st edition, 1994. 78, 138
 - [110] David Porter and David S.G. Stirling. *Integral Equations — a Practical Treatment, from Spectral Theory to Applications*. Cambridge University Press, 1990. 83
 - [111] Alexander D. Poularikas, editor. *The Transforms and Applications Handbook*. CRC Press & IEEE Press, 1st edition, 1996. 33
 - [112] Sanjay Raman and Gabriel M. Rebeiz. Single and dual-polarized millimeter-wave slot-ring antennas. *IEEE Trans. Antennas Propagat.*, 44(11):1438–1444, November 1996. 110
 - [113] S.M. Rao, D.R. Wilton, and A.W. Glisson. Electromagnetic scattering by surfaces of arbitrary shape. *IEEE Trans. Antennas Propagat.*, 30(3):409–418, March 1982. 54, 55, 58
 - [114] Raúl Rodríguez-Berral, Francisco Mesa, and Francisco Medina. Systematic and efficient root finder for computing the modal spectrum of planar layered waveguides. *Int. J. Microwave and Millimeter-Wave CAE*, 14(1):73–83, 2004. 44
 - [115] V. H. Rumsey. Reaction concept in electromagnetic theory. *Physical Review*, 94(6):1483–1491, June 1954. 12
 - [116] David B. Rutledge, Dean P. Neikirk, and Dayalan P. Kasilingam. Integrated circuit antennas. In Kenneth J. Button, editor, *Infrared and millimeter waves*, chapter 1. Academic Press, 1983. 110
 - [117] Matthew O. Sadiku. *Numerical Techniques in Electromagnetics*. CRC press, 1992. 102
 - [118] Tarpan K. Sarkar and Ercument Arvas. Integral equation approach to the analysis of finite microstrip antennas: Volume/surface formulation. *IEEE Trans. Antennas Propagat.*, 38(3):305–312, March 1990. 96
 - [119] Daniel H. Schaubert. Personal communication, August 2004. 91

- [120] Daniel H. Schaubert, Donald R. Wilton, and Allen W. Glisson. A tetrahedral modeling method for electromagnetic scattering by arbitrarily shaped inhomogeneous dielectric bodies. *IEEE Trans. Antennas Propagat.*, 32(1):77–85, January 1984. 84, 87, 91, 152
- [121] Felix K. Schwing. Millimeter wave antennas. *Proceedings of the IEEE*, 80(1):92–102, May 1992. 110
- [122] J. Sercu, N. Fache, F. Libbrecht, and P. Lagasse. Mixed potential integral equation technique for hybrid microstrip-slotline multilayered circuits using a mixed rectangular-triangular mesh. *IEEE Trans. on Microwave Theory Tech.*, 43(5):1162–1172, May 1995. 14
- [123] Rainee N. Simons. *Coplanar Waveguide Circuits, Components and Systems*. John Wiley and Sons, 1st edition, 2001. 110
- [124] Ian N. Sneddon. *Fourier Transforms*. Dover, 1995. 33, 131
- [125] Arnold Sommerfeld. *Optics*. Academic Press, 1954. 100
- [126] Arnold Sommerfeld. *Partial Differential Equations in Physics*. Academic Press, 1964. 18
- [127] James Sor, Yongxi Qian, and Tatsuo Itoh. Miniature low-loss CPW periodic structures for filter applications. *IEEE Trans. on Microwave Theory Tech.*, 49(12):2336–2341, December 2001. 118
- [128] K. D. Stephan, N. Camilleri, and T. Itoh. A quasi-optical polarization-duplexed balanced mixer for millimeter-wave applications. *IEEE Trans. on Microwave Theory Tech.*, 83(2):164–170, February 1983. 110
- [129] Ivica Stevanović and Juan R. Mosig. Efficient electromagnetic analysis of line-fed aperture antennas in thick conducting screens. *IEEE Trans. Antennas Propagat.*, 52(11):2896–2903, November 2004. 103
- [130] Gilbert W. Stewart. *Matrix Algorithms. Vol. I: Basic Decompositions*. SIAM, 1998. 12
- [131] Julius Adams Stratton. *Electromagnetic Theory*. McGraw-Hill, 1941. 9
- [132] Bjarne Stroustrup. *The C++ Programming Language*. Addison-Wesley, 3rd edition, 2000. 143
- [133] Eric Suter. *Efficient Numerical Modelling of Large Scale Planar Antennas Using a Sub-domain Multilevel Approach*. PhD thesis, Ecole Polytechnique Fédérale de Lausanne, LEMA-DE, 1998. no. 2286. 103, 104
- [134] Ferdinando Tiezzi. *Planar Antennas with Inhomogeneities: Numerical Techniques and Software Engineering*. PhD thesis, Ecole Polytechnique Fédérale de Lausanne, LEMA-DE, 2002. no. 2706. 84
- [135] Alireza Torabian and Y. Leonard Chow. Simulated image method for Green’s function of multilayer media. *IEEE Trans. on Microwave Theory Tech.*, 47(9):1777–1781, September 1999. 14, 27
- [136] Ming-Ju Tsai, Chinglung Chen, Nicolaos G. Alexopoulos, and Tzvy-Sheng Horng. Multiple arbitrary shape via-hole and air-bridge transitions in multilayered structures. *IEEE Trans. on Microwave Theory Tech.*, 44(12):2504–2511, December 1996. 14, 84, 110
- [137] Korada Umashankar, Allen Taflov, and Sadasiva Rao. Electromagnetic scattering by arbitrary shaped three-dimensional homogeneous lossy dielectric objects. *IEEE Trans. Antennas Propagat.*, 34(6):758–766, June 1986. 78, 80, 94
- [138] Maarten J. M. van der Vorst, Peter J.I. de Maagt, and Matti H.A.J. Herben. Effect of internal reflections on the radiation properties and input admittance of integrated lens antennas. *IEEE Trans. on Microwave Theory Tech.*, 47(9):1696–1704, September 1999. 117

- [139] Thomas Vaupel and Volkert Hansen. Electrodynamic analysis of combined microstrip and coplanar/slotline structures with 3-D components based on a surface/volume integral-equation approach. *IEEE Trans. on Microwave Theory Tech.*, 47(9):1788–1800, September 1999. 84
- [140] Mark Vrancken and Guy A. E. Vandenbosch. Hybrid dyadic-mixed potential and combined spectral-space domain integral-equation analysis of quasi 3-D structures in stratified media. *IEEE Trans. on Microwave Theory Tech.*, 51(1):216–225, January 2003. 2, 14, 46
- [141] James R. Wait. *Electromagnetic Waves in Stratified Media*. Pergamon Press, 2nd edition, 1970. 13
- [142] James R. Wait. *Electromagnetic Wave Theory*. Harper & Row, 1985. 20, 90, 102
- [143] Chi-Hsueh Wang, Huei Wang, and Chun-Hsiung Chen. A full wave analysis for uniplanar circuits with lumped elements. *IEEE Trans. on Microwave Theory Tech.*, 51(1):207–215, January 2003. 145
- [144] Cheng P. Wen. Coplanar waveguide: A surface strip transmission line suitable for nonreciprocal gyromagnetic device applications. *IEEE Trans. on Microwave Theory Tech.*, 17(12):1087–1090, December 1969. 110
- [145] Donald R. Wilton and Michael A. Khayat. Electromagnetic scattering by thin dielectric sheet using integral equation techniques. In *IEEE AP Society Int. Symposium*, Houston, Texas, USA, July 2004. 84
- [146] Donald R. Wilton, S.M. Rao, Allen W. Glisson, Daniel H. Schaubert, O.M. Al-Bundak, and Chalmers M. Butler. Potential integrals for uniform and linear source distributions on polygonal and polyhedral domains. *IEEE Trans. Antennas Propagat.*, 32(3):276–281, March 1984. 59, 60, 70, 75, 88, 134
- [147] D. Yau and N.V. Shuley. Numerical analysis of an aperture coupled rectangular dielectric resonator antenna using a surface formulation and the method of moments. *IEE Proc. H-Microw. Antennas Propag.*, 146(2):105–110, April 1999. 78
- [148] Ylä-Oijala, M. Taskinen, and J. Sarvas. General surface integral equation method for composite metallic and dielectric structures. Technical Report Report 419, Helsinki University of Technology, December 2003. 78, 94
- [149] Cheuk yu Edward Tong and Raymond Blundell. An annular slot antenna on a dielectric half-space. *IEEE Trans. Antennas Propagat.*, 42(7):967–974, July 1994. 117
- [150] Aiming Zhu and Stephen Gedney. Comparison of the Müller and PMCHWT surface integral formulations for the locally corrected Nyström method. In *AP-S International Symposium*, Monterey, California, June 2004. 53
- [151] J. Zmuidzinas and P.L. Richards. Superconducting detectors and mixers for millimeter and submillimeter astrophysics. *Proceedings of the IEEE*, 92(10):1597–1616, October 2004. 117

Index

- airbridges, 110–112
- basis functions
 - higher order, 125
 - linear, *see* rooftop
- convergence
 - of \bar{E}^M integrals, 71
 - of logarithmic integrals, 134
 - with mesh density, 104
- CPW, 110
- dielectric contrast, 83
- EFIE, *see* integral equation
- factorization, *see* separability
- free space, 7
- Green's function, 7
 - plots, 46
 - spectral, 18
- hexahedron
 - basis function, 85
 - figure, 84
 - rules, 139
- homogeneous half-space, 117
- IFER, 117
 - baseline design, 117
- incident field, 9
- inner product, 12
- integral equation, 1, 10
 - aperture, 66
 - dielectric interface, 78
 - EFIE, 10
 - electric conductor, 55
 - MFIE, 10
 - MPIE, 10
 - MPIE vs plain EFIE, 14
 - volume, 83
 - volume vs surface, 96
- layered medium, 34, 41, 88
- lens, 117
 - substrate \cdot , 117
- line integral, 55
 - corner, 56
 - crossing interface, 56
- Lorenz's gauge, 19
- MPIE, *see* integral equation
- multipole method, 125
- orichalcum, 5
- polarization current, 83
- prism, *see* wedge
- quasistatic
 - collapse of \cdot terms, 37
 - layered medium
 - z and z' in the same layer, 34
 - z and z' in adjacent layers, 39
- reaction, 12, 87
- reciprocity
 - and line integrals, 58
 - transmission line Green's functions, 23
 - VEFIE reaction terms, 87
- rectangle
 - basis function, 54
 - rules, 138
- reflection on ground plane
 - A, Φ , 72
 - \bar{E}^M , 74
- rooftop, 30
 - surface, 54
 - volume, 85
- separability
 - of z, z' exponential integrals, 31
 - of expansion functions, 14, 28

- of vertical dependence in Green's functions, 2, 14, 21, 28
- singularity
 - on dielectric edge, 94
- slice
 - conditions on, 29
 - definition, 28
- Sommerfeld
 - choice, 18
 - conditions, 10
 - identity, 32
 - integral, 43
 - transform, 32
- spatial domain approach, 11
- spectral domain approach, 11
- superposition, 7
- surface impedance, 17, 22, 37, 55, 144
- surface waves, 117
- tetrahedron
 - basis function, 84
 - figure, 84
 - rules, 138
- thick metallizations
 - apertures, 99
- triangle
 - basis function, 54
 - rules, 138
- wedge
 - basis function, 85
 - figure, 84
 - rules, 139

Curriculum Vitae

Daniel Llorens del Río was born August 13, 1975 in the city of Valencia, Spain. He obtained the degree of ‘Ingeniero de Telecomunicación’ from University of Málaga, Spain, in 2000, with a thesis entitled *Antena de ranura alimentada por CPW para las bandas de GSM-e y DCS1800/DECT*, on the design of a dual band slot loop antenna. Since then he has been an assistant in the Laboratoire d’Électromagnétisme et d’Acoustique, EPFL. There he worked on the ESA project *Integrated Front End Receivers* (IFER) in collaboration with a team of the University of Toronto. His task was the development of code for the analysis of integrated antenna feeds that could be coupled to 3D ray-tracing software.

Journal publications

- [1] Daniel Llorens del Río, Pablo Otero Roth, and Carlos Camacho Peñalosa. Dual band, single port, planar slot antenna. *IEEE Trans. Antennas Propagat.*, 51(2):137–138, January 2003.
- [2] Daniel Llorens del Río and Juan R. Mosig. On the interaction of electric and magnetic currents in stratified media. *IEEE Trans. Antennas Propagat.*, 52(8):2100–2108, August 2004. 15, 76
- [3] Julien Perruisseau-Carrier, Daniel Llorens del Río, and Juan R. Mosig. A new integrated match for CPW-fed antennas. *Microwave and Opt. Tech. Letters*, 42(6):444–448, September 2004. 121
- [4] Andrew Pavacic, Daniel Llorens del Río, George V. Eleftheriades, and Juan R. Mosig. Internal reflections in integrated lens antennas with off-axis feeds. In preparation.

Congress meetings

- [1] Michael Mattes, Roger Abächerli, Daniel Llorens del Río, and Juan R. Mosig. Minimizing the number of sampling points using the model-based parameter estimation and the survival-of-the-fittest principle of the genetic algorithm. In *18th Annual Review of Progress in Applied Computational Electromagnetics*, pages 71–78, March 2002.
- [2] Daniel Llorens del Río, Julien Perruisseau-Carrier, and Juan R. Mosig. The T-match: an integrated match for CPW-fed antennas. In *Journées Internationales de Nice sur les Antennes*, pages V2–347–350, November 2002. 121
- [3] Michael Mattes, Daniel Llorens del Río, Francisco Núñez, and Juan R. Mosig. Optimization of an antenna in the wideband using adaptive frequency sampling. In *Journées Internationales de Nice sur les Antennes*, pages V1–59–62, November 2002.
- [4] Francisco Núñez, Daniel Llorens del Río, Jean-François Zürcher, and Anja Skrivervik. Optimization of a tri-band mobile communication antenna using genetic algorithms. In *Journées Internationales de Nice sur les Antennes*, pages V2–65–68, November 2002.
- [5] Daniel Llorens del Río, Ivica Stevanović, and Juan R. Mosig. Analysis of printed structures including thick slots. In *Proceedings of COST-284 Meeting*, Budapest, April 2003. 15

- [6] Daniel Llorens del Río, Ivica Stevanović, and Juan R. Mosig. Analysis of apertures of arbitrary shape in thick metallic screens. In *International ITG-Conference on Antennas*, Berlin, September 2003.
- [7] Juan R. Mosig and Daniel Llorens del Río. Full-wave models for analyzing thick screens in printed structures. In *Encuentro Ibérico de Electromagnetismo Computacional*, Burgos, Spain, December 2003.
- [8] Daniel Llorens del Río and Juan R. Mosig. Analysis of slot antennas with airbridges. In *Journées Internationales de Nice sur les Antennes*, pages 54–55, November 2004.

Technical Reports

- [1] Daniel Llorens del Río and Juan R. Mosig. IFER: Efficient full wave analysis of mixed metal/slot structures in stratified media, including vertical elements, and mixed port types / ESA-ESTEC contract 14062/00/NL/GD. Technical report, EPFL-LEMA, February 2003. 1
- [2] Daniel Llorens del Río, Juan R. Mosig, Andrew Pavacic, and George Eleftheriades. Final technical report / ESA-ESTEC contract 14062/00/NL/GD. Technical report, EPFL-LEMA / EM Group, University of Toronto, February 2003. 1, 99, 119, 121